ulm university universität
uulm

Model Studies on the Anode|Electrolyte Interphase Formation in Lithium-Ion- and Secondary Metal Batteries

Universität Ulm

Institut für Oberflächenchemie und Katalyse

Dissertation

Zur Erlangung des Doktorgrades Dr. rer. nat.
der Fakultät für Naturwissenschaften der Universität Ulm

vorgelegt von

Isabella Katharina Weber

(Bonn)

2021

Amtierender Dekan: Prof. Dr. Thorsten Bernhardt

Erster Gutachter: Prof. Dr. R. Jürgen Behm
Zweite Gutachterin: apl. Prof. Dr. Christine Kranz

Tag der Promotion: 30. September 2021

‘God made the bulk; the surface was invented by the devil.’

W. Pauli

Table of Contents

List of Abbreviations

18-c-6 / 18c6	18-crown-6 ether
AE	Auxiliary electrode, also see: CE
AFM	Atomic force microscopy
ASF	Atomic sensitivity factor
BE	Binding energy
BMP^+	1-Butyl-1-methylpyrrolidinium cation
CCD	Charge-coupled device
CE	Counter electrode
CV	Cyclic voltammogram
CELEST	Center for Electrochemical Energy Storage Ulm-Karlsruhe
CEI	Cathode|electrolyte interphase
CIP	Contact ion pair
$DEME^+$	N,N-diethyl-N-methyl (2-methoxyethyl) ammonium cation
DFT	Density functional theory
DME	Dimethyl ether
DMF	Dimethyl formamide
DMC	Dimethyl carbonate
EC	Ethylene carbonate
EEI	Electrode|electrolyte interphase
ESCA	Electron spectroscopy for chemical analysis
$EMIm^+$	1-Ethyl-3-methylimidazolium cation
FKM75	Fluoroelastomere, O-ring material
FSI^-	Bis (fluorosulfonyl) imide anion
FWHM	Full width at half maximum
GC	Glassy carbon
HOPG	Highly oriented pyrolytic graphite
HIU	Helmholtz Institute Ulm Electrochemical Energy Conversion
IL	Ionic liquid
IR	Infrared spectroscopy
j	Current density
KEL-F	Commercial name for PCTFE (Polychlorotrifluoroethylene) (cell material)
KS6(L)	Types of commercial graphite
LIB	Lithium-ion battery
$LiPF_6$	Lithium hexafluorophosphate (electrolyte salt)
LP30	Battery electrolyte, 1 M $LiPF_6$ + EC/DMC (1 : 1 v/v)

MAGE	Commercial artificial graphite	SEI	Solid electrolyte interphase
MD	Molecular dynamics	SEM	Scanning electron microscopy
ML	Monolayer	SNG	Spheroidized natural graphite
MLE	Monolayer equivalents	SiC	Silicon carbide
MPP^+	1-Methyl-1-propylpyrrolidinium cation	SSIP	Solvent-separated ion pair
$MPPp^+$	1-Methyl-1-propylpiperidinium cation	STM	Scanning tunneling microscopy
NMR	Nuclear magnetic resonance (spectroscopy)	TEM	Transmission electron microscopy
OCP	Open circuit potential (also: OCV, open circuit voltage)	$TFSI^-$	Bis (trifluoromethylsulfonyl) imide anion
$OMIm^+$	1-Octyl-3-methylimidazolium cation	THF	Tetrahydrofurane
PEEK	Polyether ether ketone (cell material)	$TMHA^+$	Trimethyl-n-hexylammonium cation
PEO	Polyethylene oxide	UHV	Ultrahigh vacuum
PES	Photoelectron spectroscopy	V	Volt (unit)
PTFE	Polytetrafluoroethylene (O-ring material)	WE	Working electrode
PVDF	Polyvinylidene difluoride (binder)	XPS	X-ray photoelectron spectroscopy
RE	Reference electrode	ZSW	Zentrum für Sonnenenergie- und Wasserstoff-Forschung
RTIL	Room temperature ionic liquid		

1. Introduction

1.1. Batteries

The topic of renewable energy has been growing in importance for the past years, especially in the light of the increasing awareness of the impact of anthropogenic climate change. However, certain natural energy sources like solar and wind power are intermittent. Similarly, alternatives for internal combustion engines in automotive applications are now more important than ever. A solution to both challenges requires easy-to-use, effective and, most importantly, low-cost energy storage devices. Batteries fulfil the first two of three requirements, and the cost of, for instance, battery packs for electric vehicles, is estimated to drop by 50 % between 2018 and 2030 due to the economy of scale, reaching 124 $ per kilowatt hour.[1] At the same time, they are key components for the portable communication, entertainment and computing devices which characterize today's society.

Differently to fuel cells, which transform chemical energy from external sources to electric energy, or power plants, in which energy conversion occurs via intermediate steps and thus with a significantly lower efficiency, a rechargeable battery converts chemical energy directly to electric energy upon discharge and vice versa upon charge. A typical battery setup consists of two electrodes, the anode and the cathode. They are connected by an electrolyte, which carries the internal current but does not conduct electrons. The cell voltage depends on the difference between the oxidation and reduction potential of the anode and the cathode under working conditions and may be calculated from the thermodynamic properties of any given material as shown in Equation (1)

$$E = \frac{\Delta G}{-n \cdot F} \tag{1}$$

with E being the resulting cell voltage, n the number of electrons transferred during the redox reaction, F the Faraday constant (96500 C mol^{-1}) and ΔG the difference between the Gibbs free energy of the cathode and the anode material.

Historically, the term 'battery' refers to a number of combined cannons or similar heavy ordnance in military jargon. Later, it became a synonym for the coupled connection of several electrochemical cells and is nowadays used as a general term even for single primary (non-rechargeable) or secondary (rechargeable) cells (also termed accumulators).

The Italian physician Luigi Galvani first reported electric interactions while studying now-famous dead frogs and thus became the eponym of the galvanic, i.e., electrochemical, cell. The

first representatives of such systems evolved all the way into the familiar, commercialized primary alkaline-manganese batteries using Zn anodes, MnO_2 cathodes and a potassium hydroxide electrolyte.[2] The first secondary battery was the lead-acid battery developed in 1859 by Gaston Planté,[3] which is still used as car starter battery today. The more practical rechargeable nickel-cadmium (NiCd) cells are descendants of alkaline-manganese cells, as well, and the toxic cadmium anode was replaced with a hydrogen-adsorbing alloy for metal hydride (NiMH) cells.[2,4] By the early 2000s, NiMH batteries were commonly used in consumer electronics – especially in high-drain devices like cameras – as well as in the first generation of electric hybrid vehicles like the Toyota Prius.[5]

Soon, however, the need for a rechargeable battery with a higher energy density led to the study of non-aqueous electrolytes, which offer higher voltages as they are not restricted by the rather narrow potential window of water splitting. Due to their high solubility and mobility in organic solvents, Li salts were used as charge carriers. In 1976, Whittingham *et al.* reported on a rechargeable Li battery consisting of a lithium metal anode and a titanium disulfide (TiS_2) cathode.[6] However, the use of lithium – despite its low weight, high cell potential, high gravimetric and volumetric capacity and high power density – encountered certain shortcomings. For example, uneven growth of the re-plated Li over multiple charge / discharge cycles caused dendrite formation and posed serious safety issues.[7] Substituting the Li metal anodes with Li-Al alloys solved the problem of internal short-circuits due to Li dendrite growth, however, the alloy anodes were subjected to strong volume changes during the charge and discharge cycles, and were by far outlived by Li metal anodes.[8] The obstacles posed by both by Li metal and Li alloys were finally overcome by using graphitic intercalation materials.[9] These substrates allow Li^+ ions[10,11] to move reversibly into and out of the anode material (and vice versa at the cathode), based on the so-called rocking chair principle of insertion (intercalation, i.e., charge process) and de-insertion (de-intercalation, i.e., discharge process). Furthermore, they intercalate Li^+ reversibly without significant volume changes and, most importantly, without Li plating. This resulted in a rechargeable battery with a potential >3.6 V and gravimetric energy densities of about 120-150 Wh kg^{-1} on the cell level, which is about two to three times higher than those of a common NiCd battery.[7]

This next generation of high-energy-density accumulators was developed during the 1970s and 1980s by John B. Goodenough, M. Stanley Whittingham and Akira Yoshino, who, together, received the 2019 Chemistry Nobel Prize 'for the development of lithium-ion batteries'.[12] Lithium-ion batteries (LIBs, see **Figure 1-1**) are characterized by a high specific energy, long

cycle life and low self-discharge; traits which may have been the reason why portable electronic communication devices have today become both omnipresent and irreplaceable. Moreover, their importance has long since expanded to automotive, military, aerospace and stationary applications.[7,13-20] LIBs nowadays are comprised of an electrolyte which consists of blends of carbon-containing solvents mixed with Li-containing salts[21,22] and additives for, e.g., enhanced anode stability.[23] Lithium-based layered oxides ($LiCoO_2$), spinel structures ($LiMn_2O_4$) or phospho-olivines ($LiMPO_4$, M being a metal) are employed as cathode materials.[24] Typical LIB anodes, finally, still consist of Li^+-hosting graphite compounds made up of a blend of active material, conductive carbon and binder.[13,25-28]

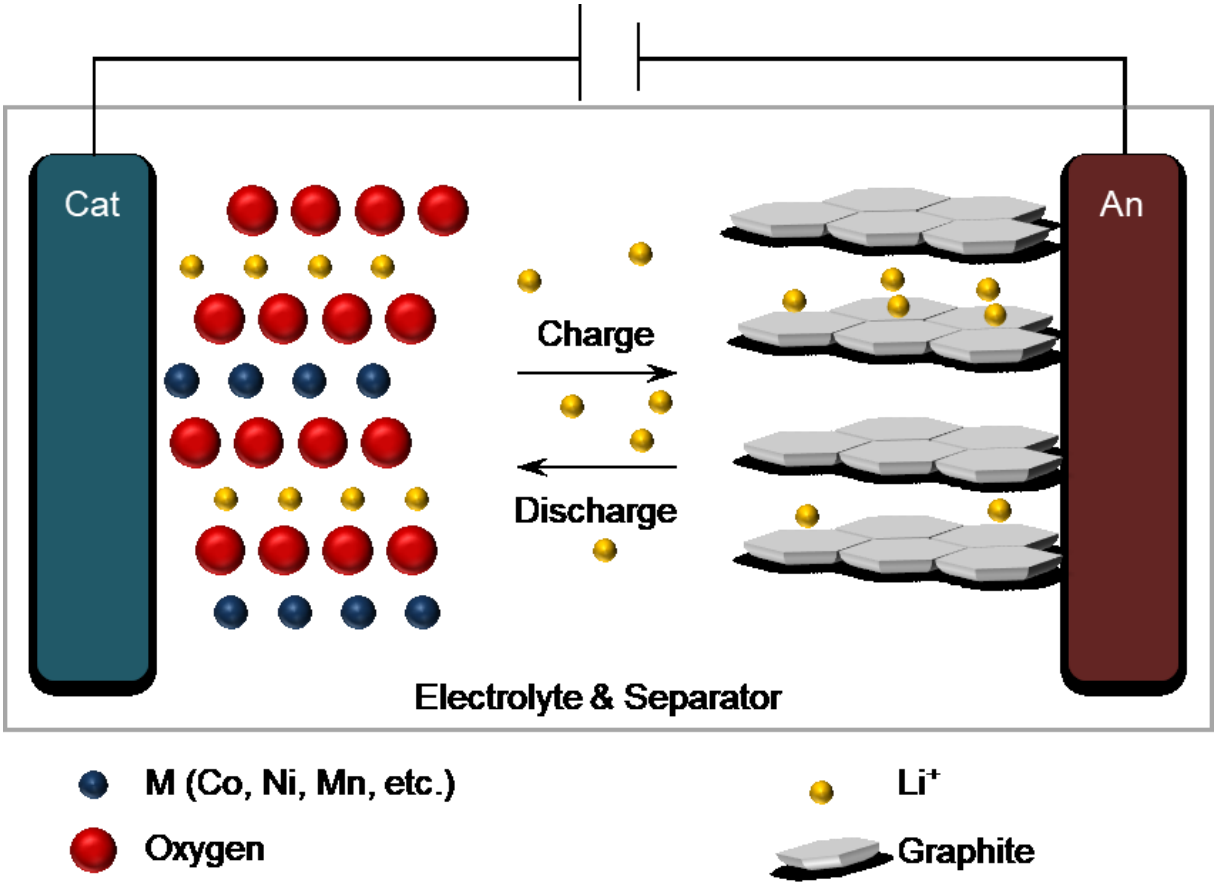

Figure 1-1. Schematic of a lithium-ion battery (LIB). Graphite is used as anode material (right), while lithium metal oxides form the cathode (left). Both are separated by the electrolyte. During charge (discharge), Li^+ is inserted into (de-inserted from) the graphite anode.

Despite the outstanding performance of LIBs, however, the demand for even better storage technologies still persists. It is based on several considerations: for one, while a significant shortage of Li is unlikely in the near future,[29] natural resources still need to be observed carefully.[30] Next, the LIB recycling rate is low to date, as it is complex due to the toxic battery components[31,32] and the equally complex and, furthermore, varying, cathode composition.[1]

And finally, both the political considerations, e.g., in the case of the cobalt necessary for cathode materials,[33] and the high cost for alternative methods of Li sourcing[34] have to be considered. All of the above deliberations result in an ongoing search for post-lithium battery systems. A possible alternative to lithium is magnesium. Its ubiquity, abundance, non-toxicity and recyclability, as well as its low price, make it an ideal candidate as shuttle ion. However, the development of secondary Mg ion batteries has encountered several challenges. On the negative side, differently to the LIB anodes, the insertion / de-insertion processes of the Mg^{2+} ion are aggravated due to its higher charge density. In consequence, no suitable active materials with good charge-transfer properties and an ability to withstand the more pronounced volume changes within the magnesiated anode material have been found so far.[35-43] On the positive side, however, Mg may be used in its metallic state. Due to its divalent nature, it possesses a higher volumetric capacity (3832 mAh cm^{-3} vs. 2061 mAh cm^{-3} for Li, referred to the pure metal anodes) despite its slightly lower-than-half gravimetric capacity (2205 mAh g^{-1} vs. 3862 mAh g^{-1} for Li).[38] Unlike Li metal, Mg is less prone to dendrite formation during deposition. This might be due to its low atom surface diffusion barrier, which results in a high mobility on the surface and, possibly, in the formation of even surface layers.[44] However, the smoothness of the Mg plating layers very likely depends on the nature of the salt or solvent plated from.[45,46]

Primary Mg metal batteries were commercialized in 1943 as reserve batteries, i.e., the cells consisting of a Mg anode and a metal halide or metal thiocyanate cathode were assembled, hermetically sealed and stored for later use and the electrolyte – water – was added when necessary to render them active.[47] During discharge, Mg ions are dissolved (stripped) from the Mg anode. Consequently, in order to realize rechargeable Mg batteries, Mg must be (re-)deposited (plated) onto the anode in order for the battery to (re-)charge. This, incidentally, poses perhaps the greatest challenge to researchers working on secondary Mg batteries. Aurbach *et al.* first reported on the prototype of a rechargeable Mg battery in 2000. It consisted of a Mg anode, a Chevrel-type Mo_6S_8 cathode and an organohaluminate-containing tetrahydrofurane (THF) electrolyte[48] (see **Figure 1-2**). Several other systems have been proposed since then, which will be briefly discussed in Chapter 1.3. Nevertheless, research continues, and as of now (2021), no commercializable secondary Mg battery has been developed for reasons that will be explained in the next chapter.

1.2. The Anode|Electrolyte Interface

Essentially, both the success of the lithium-ion battery and the difficulty in developing a rechargeable magnesium battery are based on one and the same issue, which, interestingly, works out very differently for the respective battery systems.

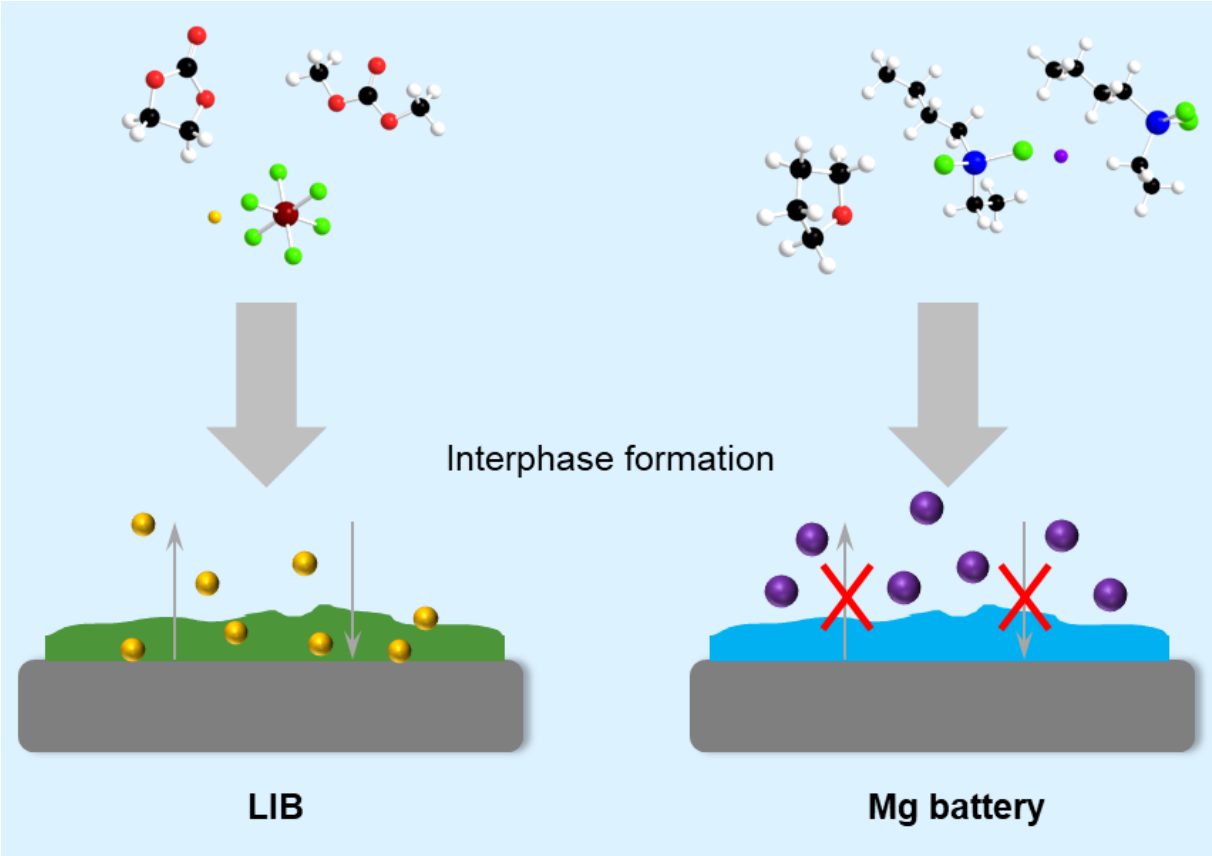

Figure 1-2. Comparison of the cation transport ability of the passivation layers formed at the anode|electrolyte interface of LIBs (left) and Mg batteries (right) from a LP30 (EC/DMC 1 : 1 + 1 M $LiPF_6$) and an organohaluminate salt ($Mg(AlCl_2BuEt)_2$) in THF, respectively. Li^+ is presented by yellow spheres, Mg^{2+} by violet ones.

For LIBs, the potential necessary to lithiate the graphite anode material is so low that it surpasses the reductive stability of the electrolytes; hence, reductive decomposition takes place during the first charge / discharge cycle(s). The passivating surface layer forming at the anode is referred to as the solid electrolyte interphase (SEI), as it exhibits the characteristics of a solid electrolyte.[49] It protects the battery from electrolyte depletion by continuous decomposition and the anode substrate from corrosion via solvent co-intercalation and prohibits Li dendrite formation. It is, however, still capable of Li^+ transport, allowing continuous diffusion of the charge carrier and thus continued inter- and de-intercalation.[50-55] The formation of the SEI is greatly influenced by the nature of electrode material[56-61] and the electrolyte, i.e., by the solvent,[62-68] the electrolyte salt,[60,63,69-73] and additives (for example, for improved SEI

formation, Li salt stability, cathode protection and enhanced safety[74]) as well as by contaminants[75] and the cycling time.[76]

It is generally agreed upon that the SEI formed in electrolytes containing ethylene carbonate consists of lithium oxides (Li_2O), lithium fluoride (LiF) and lithium alkyl carbonates, i.e., semicarbonates like $(H_2COCO_2Li)_2$, as well as polyethylene oxide (PEO).[56,58,71,77-80] However, there is a certain disagreement in regard to the SEI structure and formation process, and several models have been postulated over the course of the years.[54] Peled *et al*. suggested a mosaic structure, in which products from electrolyte decomposition form at the anode|electrolyte interface and precipitate as heterogeneous microphases.[56,58,81] In contrast, Kanamura *et al.* proposed a multilayer model on Li metal anodes in which inorganic species – mainly LiF – initially form a porous SEI just by chemical reaction of Li with residual HF. This can still be penetrated by solvent molecules, resulting in an SEI with higher concentrations of inorganic products at the anode surface and an increasing amount of organic solvent decomposition products at the electrolyte-near side of the SEI.[82-84] The Edström group, finally, blended both models into a combined multilayer and mosaic model in which the graphite substrate is covered by a homogeneous layer of inorganic products in the electrode-near and by an inhomogeneous porous layer of organic products in the electrolyte-near region, with mosaic-like pieces of LiF distributed throughout both layers.[71,85-87] However, due to the complexity of the LIB system, the individual influences have yet to be elucidated and no agreement regarding the exact SEI structure has been reached.

Similar to Li, Mg metal is highly active by nature. It immediately reacts with traces of oxygen, moisture from the surrounding environment,[88,89] and with possible contaminants in the electrolyte. Differently, though, the resulting passivating interphase successfully blocks Mg^{2+} ion migration. In other words, the SEI-like surface layer formed on Mg anodes is both electronically and ionically non-conducting and the reversible Mg plating and stripping which is essential for a functioning secondary battery does not take place.

While the SEI forming at the anode|electrolyte interface of the LIB anode has been studied diligently for about 40 years now, fewer studies have been conducted on the interactions and processes at the Mg electrode|electrolyte interface so far. There have been calls for more detailed studies, especially of the anode|electrolyte interface.[38,90] However, differently from LIB studies in which functioning processes are being investigated for detailed understanding and possible improvement, Mg battery research currently focusses first and foremost on identifying functioning systems.[41,91]

1.3. Electrolytes

For studies of the anode|electrolyte interface and surface processes in both Mg and Li-ion batteries, the choice of the electrolyte is crucial. In a well-functioning LIB, it influences the formation of a stable, Li^+-conducting and protecting SEI on the anode, which is a major factor for optimal battery operation. A LIB thus requires an electrolyte that is reductively decomposed into film-forming products on the anode at potentials higher than that of Li^+ intercalation. The most promising among the many solvents studied are alkyl carbonates like ethylene carbonate (EC), dimethyl carbonate (DMC) and diethyl carbonate (DEC).[21,22] A commercially available electrolyte, nowadays often termed LP30 (the name given to it by its original manufacturers), consists of a blend of 1 M $LiPF_6$-containing EC and DMC (1 : 1 v/v, **Figure 1-2**). EC has proven uniquely effective for SEI formation: it is highly viscous and, subsequently, has a poor ion conductivity even at ambient temperatures.[64] However, it can be easily mixed with all kinds of other alkyl carbonates with lower viscosity, and its reductive decomposition leads to the formation of a SEI which allows highly reversible intercalation and de-intercalation processes also in combination with other carbonate solvents.[50,62,69,92] DMC, on the other hand, is a linear carbonate characterized by a good ionic conductivity, but also by rigorous solvent co-intercalation observed in particular in combination with $LiClO_4$ salt[64] which results in surface exfoliation. In Chapter 3 and 4, we study the influences of the individual LP30 components EC and DMC on the SEI formation using cyclic voltammetry, *ex situ* X-ray photoelectron spectroscopy and depth profiling by Ar^+ sputtering, beginning at basic model substrates like highly oriented pyrolytic graphite (HOPG) and moving on to graphite powder film electrodes, both from artificial and from natural graphite.

Unfortunately, the carbonate electrolytes typically used for LIBs cannot be employed in Mg batteries, as, at contact, the Mg metal electrode passivates instantly. Moreover, the harder, double-charged Mg^{2+} ions are not able to diffuse through the resulting interphase. Thus, Mg batteries require an electrolyte which does not form such interphases on either of the electrodes. Mostly solutions which neither donate nor accept protons, e.g., etheric solvents (tetrahydrofurane, glymes, etc.), have proven suitable as Mg battery electrolytes so far.[37-39,48,91,93] However, THF suffers from high volatility and a tendency towards peroxide formation, low polarity and thus-decreased Mg salt dissociation and dissolution, and a poor anodic stability.[37] Furthermore, Mg salts like $Mg(BF_4)_2$ and $Mg(ClO_4)_2$ react with the surface and form a passivating layer.[40] On the other hand, organohaluminates, i.e., Grignard reagents (RMgX, R = alkyl, aryl groups, and X = halide, also see **Figure 1-2**) like the ones used by Aurbach *et al.*[48] have been shown to enable reversible Mg plating / stripping, but

simultaneously corrode other cell components.[44,93] Several solvent-salt combinations have been studied, among them organometallic-based complex salts like MgAlCl complexes in non-Grignard-based solutions which require certain conditioning steps before exhibiting nearly 100 % of Mg plating / stripping reversibility,[94,95] boron-based salt and complexes[96,97] like $Mg(BH_4)_2$ in dimethylether (DME),[98] as well as organometallic complexes like Mg hexafluoroisopropoxide ($Mg[Al(hfip)_4]_2$)[99] and Mg tetrakis (hexafluoroisopropyloxy) borate ($Mg[B(hfip)_4]_2$)[100] in ethereal solvents. Magnesium bis (trifluoromethylsulfonyl) imide ($MgTFSI_2$) is one of the few ether-soluble salts that allows Mg deposition / dissolution (semi-)reversibly given the right conditions, for example in $MgCl_2$-containing DME.[101] Interestingly, it has been shown that the addition of complexing additives like crown ethers may enhance Mg deposition / dissolution from $MgTFSI_2$.[45,46] In comparison to LIBs, thus, Mg battery electrolytes still pose a significant challenge and present one of the key issues of future research.

Both for LIBs and for Mg batteries, ionic liquids (ILs, also molten salts or room temperature ionic liquids, RTILs) are being discussed as promising electrolytes due to their favorable physico-chemical properties.[102-108] Many ILs display a low volatility, low flammability and high electrochemical stability – and, thus, enhanced overall safety characteristic – in comparison to ether-based electrolytes. However, as well-summarized by MacFarlane *et al.*, '…there is no IL that is generically non-volatile, non-flammable, intrinsically green, highly electrochemically stable, highly thermally stable, and is comprised of simple, ionic species.'[103] Overall, the main defining properties of an IL are twofold: i) the substance is liquid at ambient temperatures, and ii) the substance contains only ions.[109] Especially the idea of tailoring ILs to specific designs and purposes, as well as the promise of inherent conductivity paired with increased battery safety, make them promising research subjects both for LIB[102,106,108,110-112] and Mg battery applications.[113-121]

The ionic liquid 1-butyl-1-methylpyrrolidinium bis (trifluoromethylsulfonyl) imide (BMP-TFSI) has been studied thoroughly in the Behm group before.[122-134] It combines many traits which make it favorable for investigation in the battery field: an electrochemical window of about 5.5 V, which is one of the widest yet observed for ILs;[135,136] apparent stability at potentials more negative than the Li plating potential,[103] the highest conductivity observed for ILs of the pyrrolidinium family,[135,136] and a thermal stability even up to 100 °C in ultrahigh vacuum (UHV).[103,136] In Chapter 5 and 6, we employ BMP-TFSI as a possible solvent for

battery electrolytes and study the SEI formation on HOPG and graphite powder films and the Mg deposition and dissolution in Li and Mg battery model systems, respectively.

1.4. Model Studies at the Interface

The electrode|electrolyte – more specific, the anode|electrolyte – interface and the formation of a passivating interphase in both LIBs and Mg batteries play a crucial role for the reversibility of the Li^+ intercalation (Mg^{2+} plating) reaction, as well as for the overall battery performance. In order to improve the existing LIB and the current state of secondary Mg batteries, it is necessary to obtain a detailed and comprehensive understanding of the processes occurring at the interface, the mechanisms leading to the formation of the passivation layer, and, finally, the composition of the SEI. However, an unobstructed view often is hampered by the complexity of the cell components involved. A LIB anode, for example, consists of graphite powder with an already heterogeneous distribution of particle sizes and orientations, conductive carbon and a binder material which allows an improved adhesion towards the current collector material. The Mg metal anode for Mg batteries, on the other hand, may be of a simpler make-up but is covered by a native passivation layer even before cycling. Furthermore, complex electrolyte blends and/or procedures are necessary both for LIB and Mg battery to reach an optimal coulombic efficiency. Consequently, it is difficult to disentangle the influences and impacts from the many components and to gain an unhampered view on the individual processes taking place at the anode|electrolyte interface.

Surface science studies are designed to investigate the influence of specific aspects of complex systems under greatly idealized conditions, e.g., on well-defined surfaces at low pressure and temperature. Exemplary investigations, for example, were conducted by Uhl *et al.* on the structure formation of BMP-TFSI on noble metal single crystal surfaces in UHV,[122,123,137] as well as by Hausbrand *et al.*[138] and Ross *et al.*[52] on the cathode|electrolyte interface (CEI) and the SEI in LIBs, respectively. However, the gap between surface science studies and realistic systems – i.e., systems investigated at ambient temperature and pressure as well as under potential control – is significant. Therefore, the electrochemical model studies described here, using setups from half-cells and single-solvent electrolytes with increasingly more complex and realistic electrodes (HOPG, glassy carbon and binder-free graphite powder film electrodes), may be considered bridging sections between surface science and industrial battery research.

In order to obtain information on the impact of the individual cell components, we studied different graphite substrates (HOPG, artificial graphite, natural graphite) and electrolyte

solvents (ethylene carbonate, dimethyl carbonate), moving from model substrates to more realistic, but still simplified, and, finally, to binder-containing graphite powder electrodes, in Chapter 3 and 4. Furthermore, we investigated the chemical formation of a SEI from BMP-TFSI on HOPG under surface science conditions, followed by the SEI formed electrochemically via potentiodynamic cycling on the same substrate and, in the next step, on artificial powder film electrodes, in Chapter 5. In Chapter 6, finally, we studied the influence and synergies of the additives $Mg(BH_4)_2$ and 18-crown-6 ether on the reversibility of the Mg deposition / dissolution reaction from $MgTFSI_2$-containing BMP-TFSI on glassy carbon and on Mg electrodes, using cyclic voltammetry and molecular dynamics (MD) calculations.

1.5. Thesis Outline and Objective

This thesis consists of four publications, where two of them (Chapter 3 and 4) are interrelated, while the other two (Chapter 5 and 6) are independent. However, while the details of the studies (e.g., electrode material, electrolyte, battery system) might differ, all four papers are connected by a comprehensive topic and present different aspects of my study on the SEI formation in model systems for LIBs and Mg batteries with increasingly more pragmatic features. As to the overall structure of this work, an overview on the experimental techniques, procedures and evaluation methods will be given in Chapter 2 which will summarize the experimental sections of the four publications. The following chapters (Chapter 3 to 6) will contain the individual studies. A brief specific introduction for each topic or system is given in each of the chapters in terms of the Introduction paragraph of the respective publication.

In Chapter 3, we begin with the electrochemical and *ex situ* XP spectroscopic characterization of HOPG model electrodes in single-solvent carbonate electrolytes (EC + 1 M $LiPF_6$ and DMC + 1 M $LiPF_6$) and, consequently, move on to the more realistic (but still simplified, as they are binder-free) graphite powder film anodes of both artificial (MAGE) and spheroidized natural graphite (SNG) in single-solvent electrolyte (EC + 1 M $LiPF_6$ and DMC + 1 M $LiPF_6$) in Chapter 4. We aim to more specifically identify the influences of anode substrate and solvent, as well as the scan rate as a model for charge / discharge processes, on the formation and composition of the SEI formed in LIB. In the following chapter, Chapter 5, we begin even more fundamentally, i.e., by studying the chemical SEI formation of a possible LIB electrolyte IL, BMP-TFSI, before and after Li deposition on HOPG via XPS in ultrahigh vacuum. Then, we proceed with the electrochemical SEI formation in 0.1 M LiTFSI-containing BMP-TFSI at ambient temperature and pressure, both on HOPG and on binder-free graphite powder film substrates, and finally characterize the thus-formed SEI via XPS and sputter depth profiling.

Chapter 6 again employs the possible battery electrolyte BMP-TFSI, though this time for an electrochemical and theoretical study of Mg deposition / dissolution in the presence of $MgTFSI_2$. We aim for a more detailed view on the interactions between $TFSI^-$ and both the additives $Mg(BH_4)_2$ and 18-crown-6 ether for a better understanding of the Mg^{2+} coordination and interaction in $TFSI^-$- containing ionic liquid and their influence on the reversibility of the Mg plating / stripping process. In Chapter 7, finally, we will assess the model systems studied and compare the implications of the results obtained.

2. Experimental

2.1. Methods

2.1.1. Cyclic Voltammetry

Electrochemical studies focus on charge transfer processes across phase boundaries, e.g., between an electrode and an electrolyte. Such interfacial reactions may involve a wide variety of dynamic processes of which electron transfer reactions, ion diffusion (induced by a concentration gradient) and migration (induced by an external electrostatic field), deposition and dissolution, insertion and de-insertion and solvation and de-solvation processes are only a few examples. An electrochemical process is characterized by a thermodynamic equilibrium, i.e., a zero current situation, which may be shifted towards the cathodic process if the electrode potential is lower than the equilibrium potential and vice versa. Thus, the application and/or measurement of electrode potentials and of the resulting currents, as well as the study of the relationship between both, enables the investigation of a given electrode's kinetics in the presence of electroactive species as a subject of time (chronoamperommetry).

One of the classically applied electrochemical methods for the characterization of surface processes is cyclic voltammetry, also known as potentiodynamic scanning.[139-142] Here, the potential is scanned linearly between an upper and a lower potential limit, which results in a characteristic triangle shape of the potential–time response. The peaks which appear in the current–potential chart correspond to the respective electrochemical processes taking place at the electrode|electrolyte interface. This so-called cyclic voltammogram (CV) provides information – albeit indirectly – on the interaction between electrode material and electrolyte (and additives); on adsorption and desorption processes; on electron transfer reactions taking place at the interface and, even more indirectly, on the substrate morphology – in short: it offers insight on a system's current–time–potential behavior.

A cyclic voltammetry, or potentiodynamic, experiment is typically conducted in a three-electrode-configuration. A potential is applied to the electrode whose characteristics are supposed to be studied, i.e., the working electrode (WE). The counter electrode (CE, sometimes auxiliary electrode, AE) acts as the opposing side, balancing the charge – i.e., closing the electrical circuit. The third electrode, the reference electrode (RE), has an established redox potential. Thus, it is able to place the WE's potential into context by referencing it to its own redox potential, which is constant (and known on a relative scale, e.g., vs. H_2/H^+). For electrochemical studies in non-aqueous electrolytes, a metallic electrode (Pt, Li, Mg, etc.) or a silver wire coated with silver chloride (Ag/AgCl) may be used as quasi-

reference. Quasi-REs are poorly defined reference electrodes which may be used in the case that no essential change of the bulk solution occurs during the measurement. If this is the case, the potential of the RE will remain stable and may be calibrated by comparison with a known redox couple under the same circumstances.[143,144] In the case of this work, both Li and Mg and Ag/AgCl quasi-REs were used. The pure metal quasi-electrodes proved stable even in between measurements, while the potential of the Ag/AgCl quasi-reference shifted by, in our experience, about 0.2 eV between measurements. However, it was generally stable during one and the same cycling experiment. In the measurements conducted in Chapter 3 to 5 (Li salt-containing electrolytes), we employed a lithium quasi-reference (potential vs. Li/Li^+) as, in the case of possible dissolution, it should not impact the model system too much. Its reference value of 0 V vs. Li/Li^+ is determined by the processes of Li^+ deposition and dissolution. In the measurements conducted in ionic liquid in Chapter 6, we first employed an Ag/AgCl reference electrode for the experiments conducted in non-Mg salt-containing IL. For the later experiments in Mg-containing solution, Mg quasi-REs (0 V vs. Mg/Mg^{2+}: Mg deposition / dissolution) were used. And finally, despite the brief use of Ag/AgCl REs, all potentials in Chapter 6 are given versus Mg/Mg^{2+} using a conversion factor of E(Ag/AgCl)=1.55 V vs. Mg/Mg^{2+}.

Cyclic voltammetry is a popular and effective technique for electrochemical studies of battery (model) systems, as it allows a view of electrode|electrolyte interactions at the interface, e.g., charge storage mechanisms, charge diffusion, capacity, cyclability and stability, as well as the processes that precede, lead to and accompany SEI formation.[145,146] However, neither can it identify the individual processes taking place nor can it characterize the (side) products of interfacial reactions. Thus, for a more complete picture it should ideally be combined with other surface characterization techniques (like *ex situ* X-ray photoelectron spectroscopy, which will be discussed in more detail in Chapter 2.1.2), which allows a more detailed look on surface processes on a molecular level and, subsequently, on the interaction between the individual components.

2.1.2. X-Ray Photoelectron Spectroscopy

X-ray photoelectron spectroscopy (XPS), also known as ESCA (electron spectroscopy for chemical analysis), is a technique used for the elemental characterization of surfaces.[87,107,146,147] It involves sample irradiation with mono-energetic X-rays (Mg K_α: 1253.6 eV or Al K_α: 1486.6 eV). One X-ray photon may cause a core-level electron to be ejected; the difference between the photon's energy (hν), the electron's binding energy (BE) and the work function Φ

(i.e., the energy necessary to distance the electron far enough from the bulk for it not to experience any interactions anymore) is the kinetic energy (KE) of the emitted electron which is detected by the analyzer. As the BE is element-specific, the core levels appearing as peaks in the measured electron spectra offer information on the chemical composition and state of the probed surface. While X-ray photons have a penetration depth of 1-10 µm,[147] the interaction between electrons and matter is much stronger and their range is limited to 5-25 Å (depending on their kinetic energy). This short mean free path is the reason for the intrinsically high surface sensitivity of the technique, which allows the analysis of the first few nanometers of the material surface and sub-surface.

In battery (model) studies, *ex situ* XPS is commonly used to characterize the elemental composition of the passivation layers formed on the electrodes during cycling.[56,58,71,72,77,80,83,87,146,148-150] However, peak assignment can be challenging, especially as charging effects caused by non-conducting components may additionally affect the measured kinetic energies. Oswald *et al.* have pointed out the difficulties of binding energy referencing, especially for alkali metal-based battery materials, in detail.[151,152] For that reason, the C 1s signal at 284.8 eV[147] for the C–C species present in a variety of short-chained hydrocarbons typically found on the surface of most air-exposed XPS samples is commonly used for BE calibration. However, the composition of the so-called adventitious carbon may vary, thus leading to a shift in the C 1s binding energy. For the studies presented in Chapter 3 and 4 of this work, we have therefore employed the LiF peak in the F 1s (685.0 eV[147]) spectrum for BE referencing. For the study of the chemical and electrochemical passivation layer formed in ionic liquid electrolyte in Chapter 5, the F_{TFSI} signal (689.5 eV[153]) in the F 1s spectrum was employed as internal reference.

Aside from the compositional characterization, the peaks observed in XPS may also be used for quantitative analysis. In the simplest case, the peak areas of the respective signals for elemental compounds within one molecule mirror the elemental ratio, e.g., the N 1s region for the IL employed in Chapter 5, BMP-TFSI, displays two signals of which one is due to the nitrogen atom in the BMP^+ cation and one due to the nitrogen atom in the $TFSI^-$ anion. Accordingly, they display a peak area ratio of 1 : 1. In order to compare compounds from different elements and BE regions, the signal intensities of the spectra are normalized using the atomic sensitivity factors (ASFs). The element-specific ASFs depend on the photoelectric cross-section of the atomic orbital in question, the angular efficiency factor of the instrumental arrangement and the photoelectron's mean free path and may be used to quantify the XPS

signals, as was attempted in Chapters 3, 4 and 5. Note that the ASFs, as stated above, differ for different analyzers, and thus are different for the XPS system used in Chapters 3 and 4 and the one used in Chapter 5, respectively. We have found that the quantification of surface species is best possible in the case of un-decomposed, i.e., not potentiodynamically cycled, species, much like the vapor-deposited IL studied in UHV in Chapter 5. The electrochemical SEIs produced on HOPG and graphite powder electrodes in Chapter 3 and 4, on the other hand, feature a broad mixture of decomposed (and perhaps still un-decomposed) carbonate species with very similar functional groups. We have thus developed a semi-quantitative evaluation technique that takes into account a certain number of expected SEI components (for details, see Supporting Information in Chapter 3, section 3.5.5), as well as the un-decomposed IL in Chapter 5. While we may not be able to give a complete picture of the SEI composition due to the numerous parameters, we can still make reasonable assumptions on both quantitative and qualitative aspects and components of the SEIs formed.

In order to study the lower regions of, e.g., surface layers, depth profiling is often attempted by controlled surface erosion via Ar^+ sputtering. As sputtering may change both the surface composition as well as the chemical states of the surface species, however, the obtained results need to be interpreted cautiously. The use of soft X-ray photoelectron spectroscopy (SOXPES) and hard X-ray photoelectron spectroscopy (HAXPES), in contrast, allows the non-destructive analysis of the first few surface layers and the analysis of both sample surface and bulk, respectively, but requires synchrotron-based X-rays.[86,87,154] Still, useful information may be obtained from Ar^+ surface erosion, so the technique remains popular.[58,60,85,92,150] We, too, have employed sputter depth profiling of the surface layers investigated in Chapters 3, 4 and 5.

2.2. Setups, Cell Components and Procedures

The following paragraphs describe the experimental setups used for the model investigations, as well as the procedures followed. They present the accumulation of the experimental parts of all publications collected in this thesis.

2.2.1. Cell Setup

For the electrochemical experiments described in Chapter 3 to 6, two different half-cells were used which are displayed in **Figure 2-1**. Basically, both cells consist of a self-designed Kel-F cell body with individual, interconnected compartments. One of the compartments is open at the bottom, allowing the placement of various kinds of working electrode materials (HOPG, GC, Cu foil coated with active material, etc.) on the aluminum plate below the cell body.

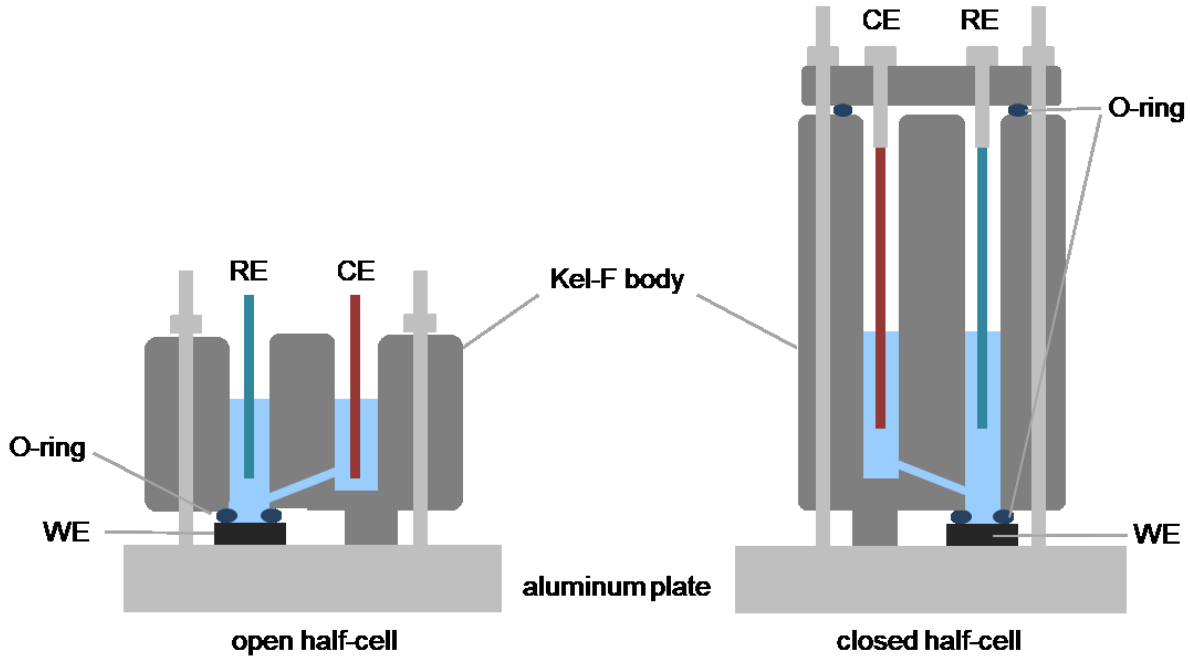

Figure 2-1: Open and closed half-cells used for the electrochemical experiments in this work. Both cells are assembled in a three-electrode-setup with a counter electrode (CE), a reference electrode (RE) and a working electrode (WE) of which the latter is placed on the aluminum plate below the Kel-F cell bodies.

Depending on the solvent, a Viton (FKM) or PTFE O-ring (inner diameter 5 mm, cross section 1 mm) was used to prevent leakage, as we have experienced a visible degradation of the Viton O-ring when in contact with dimethyl carbonate solvent.

The open cell (**Figure 2-1**, on the left) was used for short experiments and/or for electrolytes with a low vapor pressure (ethylene carbonate, ionic liquid). It consists of three compartments (the third is not shown in the figure), of which only two were used for the experiments described in Chapter 3, 4 and 5. The reference and counter electrodes are fastened into each one of the two cell compartments from the outside using two screws, which are then contacted by the crocodile clamps of the potentiostat's cables. The working electrode is contacted via copper tape from below. A closed beaker cell similarly designed from Kel-F (**Figure 2-1**, on the right) was used for long-term experiments and for studies with electrolyte with high vapor pressure, i.e., dimethyl carbonate. Its cylindrical shape, larger volume and covered opening aside, its general design is the same as the one of the open cell. However, it has only two compartments. Again, the working electrode is contacted via a piece of copper tape from below, while reference and counter electrode are connected to the two contacts in the cell cover.

Before use, the Kel-F cell body, the O-rings and glassy carbon substrates were cleaned with Caroic acid ($H_2O_2 : H_2SO_4$, 1 : 1), rinsed, sonicated and boiled in demineralized water three times. The clean components were then rinsed with acetone (VWR, 99.8+ %, AnalaR Normapur ACS, Reag. Ph. Eur.) and dried under a nitrogen stream. In the next step, the cells (with the exception of the ones mounted with Mg disk electrodes) were assembled under atmospheric conditions (with the WE, but without electrolyte and RE / CE) and subsequently dried in the glove box antechamber at 100 °C for 16 h. (For detailed preparation procedures of the different working electrodes and the electrolytes, we refer to sections 2.2.3 and 2.2.4, respectively.) The RE and CE were added inside the Ar-filled glove box (MBraun LabStar, H_2O ≤1 ppm / O_2 ≤0.5 ppm). The Li foil used for the $LiPF_6$- and LiTFSI-containing electrolytes was roughened with weighting paper in order to remove the native lithium oxide layer. The Mg rod for the Mg salt-containing electrolyte was similarly polished with emery paper before assembly. The electrolyte was stirred on a stirring plate for 15 minutes and pipetted into the assembled cell, which was then connected to the potentiostat.

2.2.2. Electrode Materials

2.2.2.1. Highly Oriented Pyrolytic Graphite (HOPG)

Highly oriented pyrolytic graphite (HOPG) is a graphite substrate with a highly anisotropic structure. The basal plane, i.e., the surface parallel to the c-axis, possesses well-defined edge and basal planes and is easily formed and cleaned by cleaving the surface layers using adhesive tape. However, even the optically smooth surface will still feature a low concentration of defect sites, e.g., steps and grain boundaries.[70,155-157] In contrast, the cross-sectional plane (edge plane) normal to the c-axis consists of a mixture of zigzag and armchair planes and is highly active in a variety of electrochemical systems.[157,158]

Earlier studies in the Behm group have used HOPG as a reliable, easy-to-prepare and well-defined model substrate for surface science studies under UHV conditions.[127,128,130,159] As the basal plane only offers a limited capability for Li^+ (de-)intercalation,[160,161] HOPG constitutes an ideal model electrode for electrochemical SEI model studies on simplified surfaces, a fact that has been taken advantage of by several groups already.[68,70,76,85] Among these ones was the work of Peled *et al.*, who have demonstrated the different reactivity of the basal versus the cross-sectional plane in regard to SEI formation.[56,58] A general disadvantage of HOPG for SEI formation, however, is its susceptibility towards solvent co-intercalation, which results in surface exfoliation.[64]

2.2.2.2. Artificial Graphite

In comparison to HOPG, artificial graphite powder displays a less ordered structure. In essence, the crystal planes of the basal structures are not aligned anymore (turbostratic disorder), which makes them more stable upon cycling because exfoliation by solvent co-intercalation is not easily possible anymore.[11] Due to the powder morphology, it is characterized by a broad distribution of sites. The graphite particles possess various orientations and do not only expose the relatively stable π electronic system (equivalent of the basal HOPG plane), but also the more reactive edge planes (equivalent of the cross-sectional HOPG plane). The latter undergo oxidation easily, which allows surface functionalization and significantly influences the reversibility of the (de-)intercalation process.

The artificial graphite powder used in Chapter 4 and 5 is MAGE, a commercial graphite produced by Hitachi Chemical Co., Ldt. It is generally employed for anodes in high-energy LIBs. Its production includes graphitization and mechanic shaping into sphere-like particles ('spheroidization'). That way, a 'folded' inner layer structure is created. In addition, the surface of the spherical particles is coated with amorphous carbon in order to alleviate solvent co-intercalation and subsequent exfoliation. MAGE has an average d_{50} particle size of 24.4 µm, a specific surface area of 3.5 $m^2 g^{-1}$ and an increased reversible capacity of 365 mAh g^{-1} compared to its predecessor, MAGD (362 mAh g^{-1}).[162]

2.2.2.3. Natural Graphite

Natural graphite, finally, is even more ordered than artificial graphite. This, however, once again allows for exfoliation of the electrode. The spheroidized natural graphite (SNG) powder used in Chapter 4 is a material prepared from the by-product of industrial spheroidization of natural graphite flakes. Normally, during the industrial procedure, 50 % of the initially applied material is lost. In order to improve these numbers, either a significant upgrade of the process is necessary, or the 'waste' graphite needs to be recycled efficiently, which was attempted with the preparation of said electrode material.[163-165]

The natural graphite by-product was processed by the Zentrum für Sonnenenergie- und Wasserstoff-Forschung (ZSW). Several spheroidizing steps were applied until the particles had an average d_{50} particle size of 12.8 µm and a specific surface area (via N_2 sorption) of 8.6 $m^2 g^{-1}$. Their reversible capacity of 366 mAh g^{-1}, on the other hand, is fairly similar to the one of MAGE.[164]

2.2.3. Sample Preparation

The HOPG substrates for both the electrochemical model studies conducted in Chapter 3 to 5 and the UHV experiments in Chapter 5 were prepared by cleaving the uppermost graphene layers from the crystal using adhesive tape. For the electrochemical experiments, the crystal was placed between the aluminum cell-holder and the cell body and dried in the glove box antechamber in Ar atmosphere at 100 °C for 16 hrs, before the cell was transferred to the glove box.

For the graphite powder electrodes employed in Chapter 4 and 5, aqueous suspensions (4 mg ml^{-1}) of the respective powders (commercial MAGE and spheroidized natural graphite, SNG) were prepared in ultrapure water (MilliQ, 18.2 MΩ cm). Cylindrical glassy carbon blocks (HTW, height: 4 mm, diameter: 8 mm) were polished in H_2O on carbide emery paper (particle density of 600, 2400 and 4000 cm^{-2}), rinsed, cleaned with Caroic acid, boiled in water and dried. 50 µl of the sonicated graphite suspension was deposited on the substrate, which was then dried under a weak nitrogen stream. The mass loading reached was approximately 0.4 mg cm^{-2}. The graphite powder thin film electrode on glassy carbon was assembled in the electrochemical half-cell, dried in Ar atmosphere at 100 °C for 16 hours and subsequently transferred to the glove box.

The binder-containing electrodes used in Chapter 4 were prepared by our partners at ZSW. MAGE and SNG electrode inks were prepared from the respective graphite powders, polyvinylidene difluoride binder (PVDF, Solvay) and N-methyl-2-pyrrolidone (NMP, Sigma Aldrich, 99.5 %) by adding an 8 wt.% solution of PVDF in NMP to the graphite material, reaching a graphite-to-binder ratio of 95 : 5. The resulting ink was homogenized and coated onto a dendritic Cu foil (Schlenck Metallfolien) by doctorblading. The approximate mass loading of the binder-containing electrodes, in comparison to the binder-free, GC-supported electrodes, was about 3.5 mg cm^{-2}. Finally, the electrodes were dried at 40 °C for 2 hrs and at 60 °C for 4 hrs before they were assembled in the cell and dried one final time at 100 °C for 16 h in the Ar-filled glove box antechamber.

For the surface science studies of the chemically formed surface layer in Chapter 5, the HOPG substrate was fixed on a tantalum sample plate using conductive silver paste and heated under nitrogen atmosphere for 30 min at 450 °C. Prior to its use, the IL was carefully degassed in UHV at around 400 K for 24 hrs, resulting in pure, water-free IL. To generate BMP-TFSI adlayers on HOPG, the IL was deposited on the HOPG at an evaporation temperature of 450 °K with a deposition rate of 0.1 ML min^{-1}, with one monolayer (ML) being defined as a

layer saturating the surface. Lithium deposition was carried out by a Li dispenser (SAES Getters, U=1.1 V / I=7.1 A) mounted ~6 cm above the HOPG sample with a deposition rate of ~0.04 MLE min^{-1} (MLE – monolayer equivalents).

LiTFSI, as a reference sample for the electrochemical experiments described in section 2.2.5.2, was mounted on a conductive carbon sticker on top of a tantalum sample holder inside the glove box and transferred to the UHV chamber under inert conditions.

The glassy carbon substrates studied in Chapter 6 were polished, cleaned, dried and assembled as described for the substrates for the powder graphite thin film electrodes in Chapter 4 and 5. The magnesium disks were polished with SiC 600 paper, then transferred to the antechamber of the glove box, dried under Ar (100 °C, 16 hrs) and finally polished a second time inside the glove box. Next, the open cell was assembled as described above; however, the third compartment was used for the CE, a gold wire (rinsed with Caroic acid, sonicated and boiled, rinsed with acetone). A Mg rod was polished with emery paper and used as RE. Cell assembly for the Mg electrodes took place as quickly as possible: the electrolyte was added immediately after cell assembly was finished. Then, the Mg working electrode surface was again roughened using a sharp glass tip before starting the measurement.

Finally, selected graphite anodes (HOPG and MAGE/SNG on glassy carbon) were selected for XP spectroscopic characterization of the SEI formed. Still within the cell, the SEI-covered substrates were rinsed by exchanging the electrolyte four times with DMC; then, the sample electrode was immersed in DMC for 45-60 min. This solvent exchange-and-soaking cycle was repeated four times in total, followed by a 45 min drying period after the last exchange. Then, the electrochemical cell was disassembled, the electrode mounted on a tantalum sample holder inside the glove box using a carbon sticker, and finally transferred directly to the XP spectrometer in a hermetically sealed transport box without any contact to ambient atmosphere.

2.2.4. Electrolyte Preparation

For the single-solvent carbonate electrolytes used in Chapter 3 and 4, a small amount of EC (Sigma Aldrich, 99.0 %, ≤50 ppm H_2O) was melted at 65 °C. DMC (Sigma Aldrich, 99.9 %, ≤20 ppm H_2O) did not require melting and was used as received. 1 M $LiPF_6$ (Sigma Aldrich, 99.99+ %) was placed in a Teflon beaker and the appropriate solvent volume added. The EC mixture was left to cool down while stirring for 45-60 min, the DMC mixture was stirred for approximately the same amount of time. LP30 electrolyte (1 M $LiPF_6$ in EC/DMC, 1 : 1 v/v, Solvionic, 99.9 %, ≤20 ppm H_2O) was employed as received. A volume of 0.3 ml of electrolyte

was used for the open cell if only two compartments were used, 0.7 ml if all three compartments required filling. 0.5 ml of electrolyte was employed for the closed half-cell.

For the IL-based electrolyte used in Chapter 5, 0.1 M Li bis (trifluoromethylsulfonyl) imide (LiTFSI, Solvionic, 99.9 %) in 1-butyl-1-methylpyrridinium bis (trifluoromethylsulfonyl) imide (BMP-TFSI, Solvionic, 99.9+ %, ≤20 ppm H_2O) was prepared in the atmosphere of the glove box and stirred until the salt was completely dissolved. Again, a volume of 0.3 ml of electrolyte was used.

For the IL electrolytes used in Chapter 6, finally, the appropriate amounts of $Mg(BH_4)_2$ (Sigma Aldrich, 95 %), $MgTFSI_2$ (Solvionic, 99.5 %, ≤250 ppm H_2O) and 18-crown-6 (Alfa Aesar, 99.0+ %, ≤0.29 % H_2O) were dissolved in 1-butyl-1-methylpyrrolidinium bis (trifluoromethylsulfonyl) imide (BMP-TFSI, Solvionic, 99.9+ %, ≤20 ppm H_2O) via stirring. Of the following solutions, 0.7 ml were employed in the open cell: BMP-TFSI with

a) 0.1 M $Mg(BH_4)_2$,
b) 0.1 M $Mg(BH_4)_2$ + 0.1 M 18-crown-6,
c) 0.05 M $Mg(BH_4)_2$ + 0.05 M $MgTFSI_2$ + 0.1 M 18-crown-6,
d) 0.01 M $Mg(BH_4)_2$ + 0.09 M $MgTFSI_2$ + 0.1 M 18-crown-6, and
e) 0.01 M $Mg(BH_4)_2$ + 0.09 M $MgTFSI_2$ + 0.2 M 18-crown-6.

2.2.5. Experimental Protocol

The following paragraph describes the individual preparation and measurement protocols used for the studies described in detail in Chapters 3 to 6. An overview depicting which electrodes were investigated in which electrolyte and which methods (CV/XPS) were applied in the respective investigations is given in **Figure 2-2**. For a better overview, the UHV samples (monolayers of BMP-TFSI deposited on HOPG before and after Li post-deposition) studied in Chapter 5 and the different magnesium salt and concentration variations in Chapter 6 were omitted in this overview.

2.2.5.1. Physical Characterization

For microscopic characterization of the optically smooth and the roughened HOPG substrate in Chapter 3, scanning electron microscopy (SEM) was conducted with a Zeiss Leo 1550 microscope with a field emission cathode. The smooth HOPG substrate was prepared as described above. The roughened surface was stripped with adhesive tape until it was optically smooth and then scratched multiple times using the tip of a scalpel.

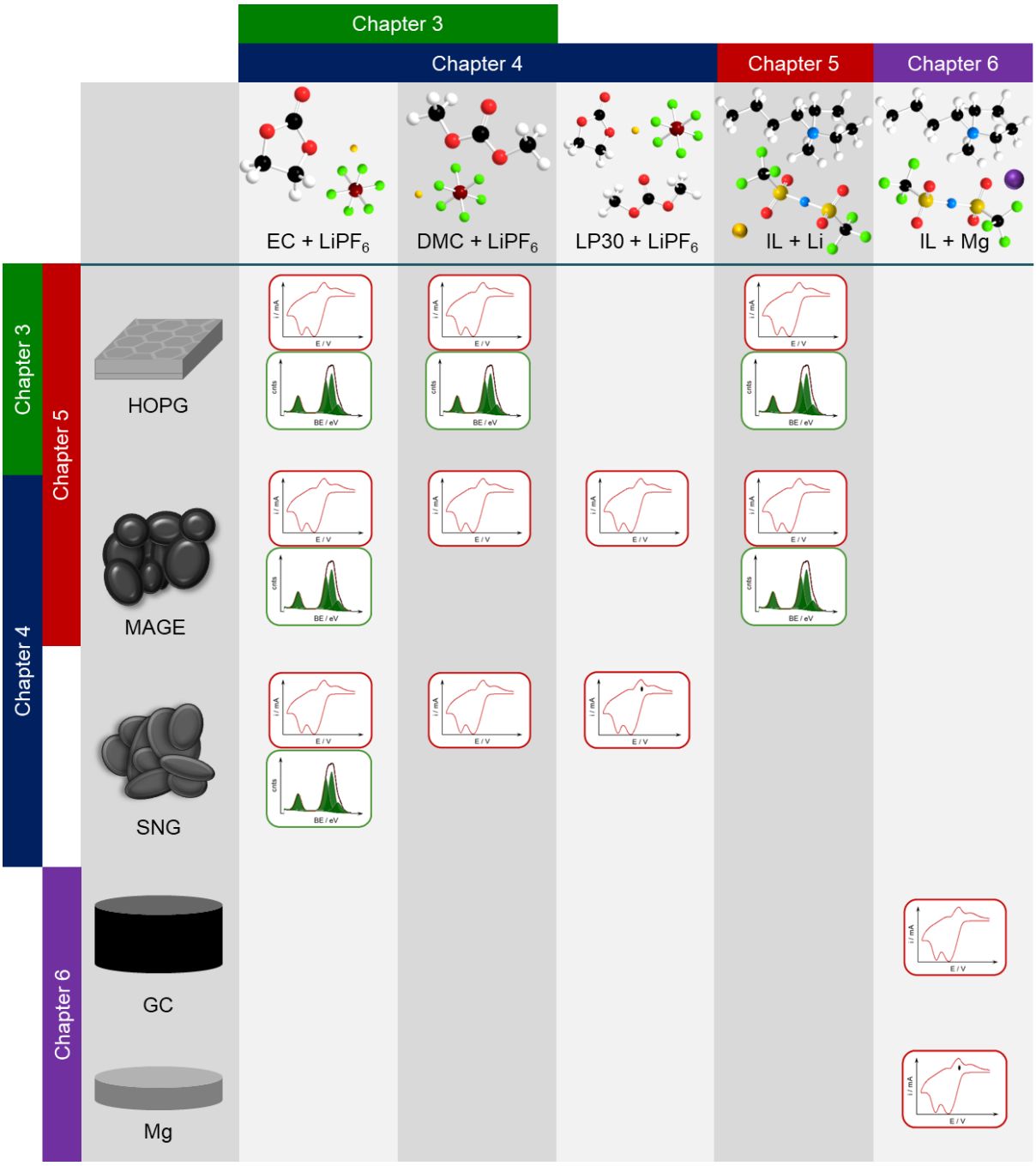

Figure 2-2. Overview on the model systems investigated experimentally in the thesis at hand, and of the respective characterization techniques employed. The red CV icon denotes electrochemical measurements, the green XPS icon (*ex situ*) XPS studies. The IL is BMP-TFSI.

Transmission electron spectroscopy (TEM) was employed for a comparison of the artificial and natural graphite powders (MAGE and SNG) used in Chapter 4 and 5, using a JEOL1400 bright-field transmission electron microscope equipped with a CCD camera (electron energy 90 keV). A droplet of ethanol (Merck Emsure) containing the graphite powder (ca. 1 mg ml^{-1}) was pipetted on a carbonized copper grid (Plano, Mesh 300) and transferred to the microscope after evaporation of the solvent.

2.2.5.2. Electrochemical Characterization

The anode substrates and electrochemical cells were prepared and assembled as described in sections 2.2.1 and 2.2.3. After immersing the samples at the open circuit potential (OCP), the potential was stepped to the upper potential limit and held for 60 seconds. Cycling was always started in the negative-going (cathodic) direction.

The cyclic voltammograms of HOPG and (binder-free) graphite powder substrates shown in Chapter 3 and 4, respectively, were recorded at scan rates of 0.1, 1 and 10 mV s^{-1} in a potential window of 1.5–0.02 V vs. Li/Li^+ or, for selected samples, cycled in DMC-based electrolyte in a potential window of 3.0–0.02 V vs. Li/Li^+ (Chapter 3) using a Princeton (PAR 263A) (Chapter 3) or a Solartron Analytical Modulab (Pstat 1MS/s) (Chapter 4, 5 and 6) potentiostat. For the experiments conducted in Chapter 5, CVs were recorded at a scan rate of 0.1 mV s^{-1} in a potential window of 1.5–0.02 V vs. Li/Li^+ using a Princeton potentiostat (PAR 263A). In Chapter 6, finally, the glassy carbon and Mg substrates in Mg-salt containing IL were cycled between 1.5 and -1.0 V vs. Mg/Mg^{2+} at 10 mV s^{-1} for at least 25 and a maximum of 100 cycles.

All currents were normalized by the geometric surface area of the electrode (SA_{geo}=0.196 cm^2).

2.2.5.3. XPS Characterization

The resulting SEI layers (i.e., the electrochemically formed SEI) of selected electrodes cycled at either fast (10 mV s^{-1}) or slow (0.1 mV s^{-1}) scan rate described in Chapter 3, 4 and 5 were characterized by X-ray photoelectron spectroscopy (XPS). In preparation, the samples were cleaned of excess salt and electrolyte by exchanging the electrolyte as described in section 2.2.3.

XPS measurements of the samples cycled in single-solvent, battery-relevant electrolytes described in Chapter 3 and 4 were conducted using a PHI 5800 Multi Technique ESCA System from Physical Electronics with monochromatic Al K_α (1486.6 eV) radiation at a detection angle of 45 °. The pass energy at the analyzer for survey spectra (detail spectra) was set to 93.9 eV (29.35 eV). Successive Ar^+ sputtering (I_{sp}~1 µA; U_{sp}=5 kV) was used to gradually remove the top-most surface layers in order to obtain a depth profile of the SEI. Spectra were taken after 2, 4, 6 and 18 minutes of sputtering, equivalent to a total sputtering time of 2, 6, 12 and 30 minutes. For the parameters used, the sputter rate is specified as approximately 1 nm min^{-1} by the manufacturer. A strong charging effect was observed for the substrates cycled in EC- and DMC-based single-solvent electrolyte. For compensation, the samples were neutralized (I_{neutr}=3 µA) during the XPS measurements. While this was sufficient in the case of EC-based electrolytes, severe charging effects in the case of DMC-based electrolytes could not

always be sufficiently compensated. In Chapter 4, thus, only the results of the XP analysis of the graphite powder film electrodes cycled in EC-based electrolyte are presented.

All experiments described in Chapter 5 – both the chemically formed and the electrochemically formed SEI, as well as the sample aged at OCP and the neat LiTFSI salt – were performed in a commercial UHV system (SPECS) equipped with an X-ray source (SPECS XR50, Al K_α and Mg K_α) and a hemispherical analyzer (SPECS, DLSEGD-Phoibos-Has3500) and a base pressure of $2 \cdot 10^{-10}$ mbar. An Al K_α or a Mg K_α X-ray source (1486.6 and 1253.6 eV, respectively) was employed, operated at a power of 250 W (U=14 kV, I=17.8 mA). The *ex situ* XP spectra after the electrochemical measurements were recorded with a pass energy of 100 eV at emission angles of 0° (information depth 6-9 nm) with respect to the surface normal and in grazing emission (80°, surface sensitive mode, information depth of 1-2 nm) in the UHV adsorption experiments. To minimize beam damage during X-ray exposure, we reduced the number of scans for all detail spectra to one or a few scans.

Evaluation of the XP spectra was conducted by first calibrating the binding energy (BE) scale. The commonly used peak for BE calibration, the C 1s main peak at 284.8 eV assigned to graphite, was not suitable in our case since carbide species appeared in the C 1s spectra of the sputtered sample, hindering an unequivocal peak fit (see Chapter 3, section 3.3.4). Consequently, the F_{LiF} signal at 685.0 eV[147] (Chapter 3 and 4) or the F_{TFSI} signal at 689.5 eV[153] (Chapter 5) in the F 1s BE region were used as binding energy reference. For the peak fit, a Shirley-type background was subtracted and the peaks fitted using a weighed least-square fitting of model curves (70 % Gaussian, 30 % Lorentzian).

Further details about the semi-quantitative fit procedure employed for the experimental evaluation of the XPS results obtained in Chapter 3 and 4 are given in the supporting information of Chapter 3 (section 3.5.5). Quantification of atomic concentrations was performed on the basis of the atomic sensitivity factors (ASF) given in **Table S3-2**, Chapter 3, section 3.5.5. XPS interpretation in Chapter 5 was approached with fewer restraints in regard to the product species. Atomic concentrations were again quantified on the basis of the ASFs, which, however, were calculated from a reference sample (Sample A in **Table S5-1**, Chapter 5, section 5.5.3) of multilayers of BMP-TFSI on HOPG after deposition of 10 ML of BMP-TFSI (Sample A) and correlated according to the nominal atomic ratios within the ionic liquid ($N_{BMP} : N_{TFSI}$ 1 : 1, $C_{TFSI} : C_{hetero} : C_{alkyl}$ 2 : 4 : 5, $F_{TFSI} : C_{TFSI}$ 6 : 2, $C_{TFSI} : O_{TFSI}$ 1 : 2 and $O_{TFSI} : S_{TFSI}$ 2 : 1).

2.2.6. Computational Methods

Chapter 6 consists of a joint manuscript co-authored with Johannes Ingenmey, M.Sc., from Prof. Dr. Barbara Kirchner's group from the Mulliken Center of Theoretical Chemistry, Bonn University. The combined electrochemical and theoretical study is based on CV measurements (I. Weber, Ulm University) and molecular dynamics (MD) simulations (J. Ingenmey, Bonn University), of which the protocol of the former is described in the prior sections and the latter is described in the following. The following paragraph was written by Johannes Ingenmey, was printed in Ref. 166 and is reprinted with permission from John Wiley and Sons.

'Classical molecular dynamics (MD) simulations of $MgTFSI_2$ in BMP-TFSI in the presence and absence of 18-crown-6 were performed using the LAMMPS program package (version 17th of Nov, 2016),[167] employing the OPLSA-AA force field[168] for Mg^{2+} and 18-crown-6 and the CL&P force field for the ionic liquid (BMP-TFSI).[169] In these simulations, the solvent was represented by 256 BMP-TFSI ion pairs. For selected compositions, clusters were cut from these simulations using the post-processing tool TRAVIS.[170,171] The cluster structures were geometrically optimized to the local energy minimum using density functional theory (DFT) with the ORCA program package,[172] the BP86 functional[173,174] and def2-SVP[175] basis set with Grimme's D3 dispersion correction.[176] Geometrical counterpoise (gCP) correction was applied to deal with the intermolecular as well as intramolecular basis set superposition error (BSSE).[177] Tight SCF convergence criteria were applied in each geometry optimization. Solvent effects were considered via the MD simulation; furthermore, they were considered explicitly in the DFT calculations by BMP-TFSI ion pairs in the cluster and implicitly by the conductor-like polarizable continuum model (CPCM);[178] setting the dielectric constant to 14.7[179] and the refractive index to 1.423.[180] Note that, while electrostatic interactions are the dominant attractive force between Mg^{2+} and oxygen, covalent interactions may also contribute to this, leading to delocalization of electron density to the cation's empty 3s and 3p orbitals. Such effects are not included in our classical MD simulations, which serve as starting point, but are fully considered in the subsequent DFT optimizations. Cluster coordination energies and ligand binding energies were obtained by performing single-point calculations of isolated parts of the optimized clusters at the same level of theory, maintaining their frozen structure (see also Chapter 6.3.2). Electron affinities E_A and the equilibrium potential for reduction E_{red} of the respective clusters were obtained by explicitly calculating the adiabatic energy difference between a cluster R and its reduced form R^- (all geometry-optimized) via Equation (2)

$$E_{\mathrm{A}}(\mathrm{R}) = E(\mathrm{R}) - E(\mathrm{R}^{-}) \quad (2)$$

And (3)

$$E_{\mathrm{red}}(\mathrm{R}) = \frac{E_{\mathrm{A}}(\mathrm{R})}{nF} - E_{\mathrm{ref}} \quad (3)$$

where E(R) and E(R^-) are the electronic energies of the solvated clusters, n is the number of exchanged electrons, F is the Faraday constant and E_{ref} is the reference potential calculated for Mg/Mg^{2+}. This yields values very close to those obtained by via the thermodynamic cycle method.[181-184],

2.3. Chemicals

Table 2-1. List of chemicals employed in the course of the preparation, setup, and both electrochemical as well as UHV-related investigations described in this work.

Chemicals	Formula	In Chapter	Provider	Purity	Specifi-cations
1-butyl-1-methylpyrrolidinium bis (trifluoromethyl-sulfonyl) imide (BMP-TFSI)	$C_{11}H_{20}N_2F_6S_2O_4$	5, 6	Solvionic	99.9 %	≤20 ppm H_2O
	$C_{11}H_{20}N_2F_6S_2O_4$	5	Merck	99.0+ %	≤10 ppm H_2O
18-crown-6 ether (18-c-6)	$C_{12}H_{24}O_6$	6	Alfa Aesar	99.0 %	≤0.29 % H_2O
Acetone	CH_3COCH_3	3, 4, 5, 6	VWR	99.8+ %	
Argon	Ar	3, 4, 5, 6	Westfalen	5.0	
Artificial graphite (MAGE)	C	4, 5	Hitachi Chemical Co., Ltd.		See chapters
Dimethyl carbonate (DMC)	$C_3H_6O_3$	3, 4, 5	Sigma Aldrich	99.9 %	≤0 ppm H_2O
Ethylene carbonate (EC)	$C_3H_4O_3$	3, 4	Sigma Aldrich	99.0 %	≤50 ppm H_2O
Ethanol	C_2H_5OH	4	Merck	99.9+ %	
Glassy carbon (GC)	C	4, 5, 6	HTW GmbH	Sigradur G	h=4mm, dia=8 (+0/-0.05) mm
Hydrogen peroxide	H_2O_2	3, 4, 5, 6	VWR	33 %	Unstabilized
Highly oriented pyrolytic graphite (HOPG)	C	3, 4, 5	MaTeck	ZYA	1x10x10 mm, mosaic spread 0.4 ± 0.1 °
Lithium foil	Li	3, 4, 5	Alfa Aesar	99.99+ %	
Lithium bis (trifluoromethyl-sulfonyl) imide (LiTFSI)	$LiC_2F_6NO_4S_2$	5	Solvionic	99.9 %	≤5000 ppm H_2O
Lithium hexafluorophosphate	$LiPF_6$	3, 4	Sigma Aldrich	99.99+ %	

Chemicals	**Formula**	**In Chapter**	**Provider**	**Purity**	**Specifi-cations**
LP30	1 M $LiPF_6$ + EC/DMC 1 : 1 v/v	4	Solvionic	99.9 %	≤20 ppm H_2O
Magnesium bis (trifluoromethyl-sulfonyl) imide ($MgTFSI_2$)	$MgC_4F_{12}N_2O_8S_4$	6	Solvionic	99.5 %	≤250 ppm H_2O
Magnesium borohydride	$Mg(BH_4)_2$	6	Sigma Aldrich	95.0 %	
Magnesium disk	Mg	6	Good-fellow	99.9 %	h=1.5 mm, dia=8 mm
Magnesium rod	Mg	6	Good-fellow	99.9 %	l=15 mm, dia=3.2 mm
N-Methyl-2-pyrrolidone (NMP)	C_5H_9NO	4	Sigma Aldrich	99.5 %	
Polyvinylidene difluoride (PVDF)	$(CH_2CF_2)_n$	4	Sigma Aldrich		
Spheroidized natural graphite (SNG)	C	4	ZSW		
Sulfuric acid	H_2SO_4	3, 4, 5, 6	Merck	95-97 %	

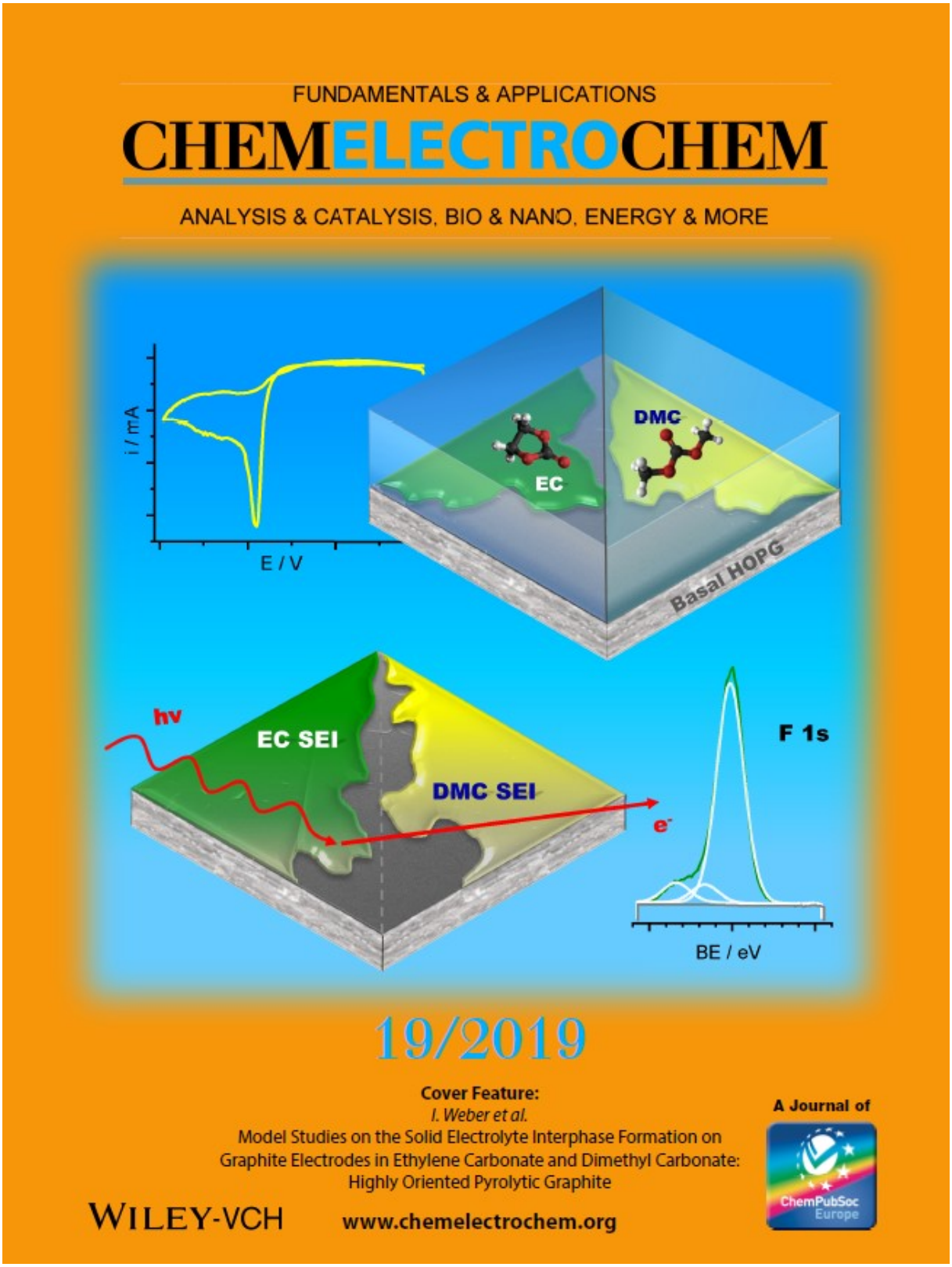

Reprinted with permission from John Wiley and Sons.

3. Model Studies on the Solid Electrolyte Interphase Formation on Graphite Electrodes in Ethylene Carbonate and Dimethyl Carbonate I: Highly Oriented Pyrolytic Graphite

The content of the following chapter, including the graphical abstract (Figure 3-0), was published in ChemElectroChem 2019, volume 6 pp. 4985-4997, and is reprinted here with permission from John Wiley and Sons.[185]

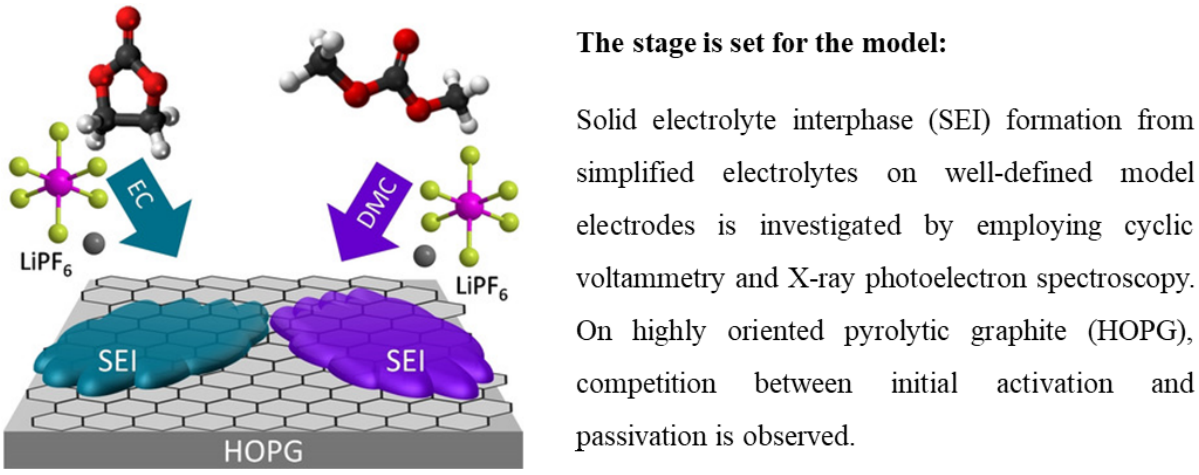

Figure 3–0. Graphical abstract.

In order to avoid duplication, the experimental part (section 4 of the publication) was removed and is instead referred to in detail in Chapter 2 of this thesis. The style, spelling, sections, enumeration, references and figures were adapted to fit the current layout. Finally, the figures from the supporting information were added at the end of the chapter.

The electrochemical data presented in this chapter was collected by B. Wang (Institute of Surface Chemistry and Catalysis, Ulm University) in the course of his Master Thesis, and by myself. Dr. T. Diemant (Institute of Surface Chemistry and Catalysis, Ulm University) conducted the *ex situ* XPS measurements, while the SEM micrographs were recorded by A. Minkow (Institute of Functional Nanosystems, Ulm University). I evaluated the experimental data and was heavily involved in the creative process of the publication.

Financial support for the research reported here was granted by the German Federal Ministry of Education and Research (BMBF) in the project 03X4636C (‘Li-EcoSafe – Entwicklung kostengünstiger und sicherer Lithium-Ionen-Batterien’). This work contributes to the research performed at CELEST (Center for Electrochemical Energy Storage Ulm-Karlsruhe).

3.1. Abstract

Aiming at a deeper understanding of the solid electrolyte interphase (SEI) formation on carbon anodes in lithium-ion batteries, we performed a combined electrochemical and spectroscopic model study using structurally well-defined graphite model electrodes (highly oriented pyrolytic graphite, HOPG) and simplified model electrolytes (ethylene carbonate (EC)+1 M $LiPF_6$ or dimethyl carbonate (DMC)+1 M $LiPF_6$). In cyclic voltammetry measurements, we find initial activation of the reductive electrolyte decomposition at faster scan rates (1 or 10 mV s^{-1}), whereas this is not the case at a slower scan rate (0.1 mV s^{-1}). This activation effect, which is more pronounced for DMC, is explained by an increase in the HOPG surface area, presumably by electrode exfoliation; it is not observed on surface-defect-rich samples. XPS analysis shows that, regardless of the solvent and the scan rate, the SEI is mainly composed of LiF and only small amounts of solvent and other salt decomposition products.

3.2. Introduction

Lithium-ion batteries (LIBs) have long become the dominant system for electrochemical energy storage, ubiquitously employed for portable electronic devices and increasingly also for automotive applications.[7,15] Of utmost importance for the performance of LIBs is the interphase layer formed at the interface between the anode and the organic electrolyte during the first charge / discharge cycles, the so-called solid electrolyte interphase (SEI). It affects the self-discharge characteristics, cycle life, rate capability and safety by passivating the electrode surface, protecting it from corrosion and hindering further electrolyte decomposition, while still allowing Li^+ diffusion and (de-)intercalation.[51,54,55] Typically, different graphite composite materials are used as anodes, mostly in combination with a conductive carbon and a binder.[13,186] The organic electrolytes consist of solvent blends mixed with Li^+ salts, the most common one being LP30, a 1 : 1 (v/v) blend of ethylene carbonate (EC) and dimethyl carbonate (DMC) with 1 M $LiPF_6$.[13,21,22,65] Although there is a vast number of studies and information available (for reviews see Refs. 7, 15, 51, 54, 55, 87, and 187-189), a clear identification of the different processes contributing to the formation of the passivation layer has not been possible so far. This is mainly due to the complexity of the system, which arises from the variety of often poorly defined features or parameters such as the nature and morphology of the electrode material, the exact solvent composition, the electrolyte salt, additives, or the cycling rate. On the other hand, a fundamental understanding of the reactions

responsible for the formation of the SEI and its composition is vital in order to systematically increase battery lifetime and capacity.

This is topic of the present model study, where we present results of combined electrochemical and *ex situ* spectroscopy measurements on the SEI formation in single-solvent electrolytes (EC and DMC, respectively, mixed with $LiPF_6$) on a highly oriented pyrolytic graphite (HOPG) model electrode. The electrochemical measurements were performed in a three-electrode half-cell configuration. The surface and sub-surface composition of the SEI resulting for different cycling rates was characterized by X-ray photoelectron spectroscopy (XPS). Furthermore, depth information was obtained by recording spectra before and after partial sputter removal of the topmost part of the SEI. Based on the binding energies (BEs) and the intensity ratios of the different elements, we can derive detailed information on the nature of the species contributing to the SEI and on the SEI formation process.

While there is a large number of model studies on the general topic of SEI formation,[56,58,59,63,68,69,155,190,191] the number of such studies on the interaction of the individual LP30 components EC and DMC with structurally well-defined model electrodes is much less. Jeong *et al.* studied the interplay between HOPG and $LiClO_4$-containing EC (DMC) electrolyte by electrochemical measurements and *in situ* atomic force microscopy (AFM), focusing on the effect of the co-solvent on the SEI formation.[64] Employing also *in situ* AFM, Cresce *et al*. followed the development of an SEI film in EC + LiTFSI on a HOPG electrode.[192] Closely related is an *in situ* scanning tunneling microscopy (STM) study on the SEI formation on HOPG in LP30 and in DMC conducted by Wang *et al.*, which focused on morphological aspects.[190]

Changing to the chemical composition of the SEI formed on graphite electrodes, previous studies revealed that it consists of decomposition products of salt and solvent, where the amount of these products and their vertical distribution is affected by a variety of different parameters,[60,66,70,71,73,76,77,85,193] such as the concentration of defect sites.[56,58] Going to well-defined anode materials, it was shown that the main decomposition product of carbonate-based electrolytes for defect-rich HOPG cuts about perpendicular to the basal plane (cross-sectional or edge plane) is LiF, where the F results from the decomposition of the $LiPF_6$ anion. The basal plane, in contrast, was found to favor the formation of solvent decomposition products, such as carbonates or polymers. Specifically mentioned were $(CH_2OCO_2Li)_2$ and polyethylene oxide (PEO) as EC decomposition products.[56,58] These assignments have to be regarded with caution,

however, since the above spectroscopic studies were conducted in solvent mixtures rather than in single-solvent electrolytes, which renders a clear identification of the underlying decomposition mechanism difficult.

Highly relevant for the present study of the SEI formation process are also results obtained in recent surface science-type model studies in our group, which were performed under ultrahigh vacuum (UHV) conditions and at low temperatures (80–300 K) using well-defined model surfaces and single-solvent compounds.[159] Studying the interaction between basal HOPG and EC, we obtained detailed insight into the chemical interaction and the decomposition processes taking place in the absence and presence of co-adsorbed lithium.[159]

In the first part of this work, we describe results of the electrochemical characterization of the model system via cyclic voltammetry (sections 3.3.1 to 3.3.3). This is followed by the XPS analysis of the SEI layers formed on the HOPG surface, including depth profiles created by successive Ar^+ sputtering (section 3.3.4). After an overview on the elemental composition of the SEIs, we discuss possible components of the passivation layers based on the binding energies and the intensity ratios of the respective signals and their depth distribution. These results will be used to derive a more detailed picture of the different processes occurring during SEI formation at the HOPG|electrolyte interface during the first cycles, which can serve as a simplified model for graphite|electrolyte interfaces in general.

3.3. Results and Discussion

3.3.1. Reductive EC and DMC Decomposition at 0.1 mV s^{-1}

Figure 3-1 displays a cyclic voltammogram (CV) recorded on the basal HOPG plane in the potential window of 1.5–0.02 V vs. Li^+/Li in EC; in b) we show the same potential range of a CV recorded on a HOPG electrode in DMC-based electrolyte during cycling in a wider potential window (3.0-0.02 V) (scan rate 0.1 mV s^{-1}).

In the HOPG|EC + $LiPF_6$ system, a first cathodic peak appears at 0.6 V. This agrees with a previous report, where reductive EC decomposition on basal HOPG was found to begin at ~0.7 V (CV at 0.5 mV s^{-1}, 2.9–0.0 V, EC + 1 M $LiClO_4$).[65] Qualitatively similar CVs were obtained also when EC was mixed with diethyl carbonate (DEC) (CV at 20 mV s^{-1}, 3.0–0.0 V, EC/DEC (1 : 1 v/v) + 1 M $LiClO_4$[155]) and DMC (CV at 5 mV s^{-1}, 3.0–0.0 V, EC/DMC (1 : 1 w/w) + 1 M $LiClO_4$[76]) as solvent, although the peak potentials differ somewhat. After the main peak, the reductive processes continue with decreasing rate down to the lower potential limit.

In this region, the current signal is slightly noisy, probably due to the evolution of ethylene gas or hydrogen, with the former being a product of EC decomposition and the latter a side-product caused by H_2O impurities in the electrolyte,[11,35,75] in our case approximately 20-50 ppm for the solvents.

For graphite materials used in realistic batteries, one usually observes a strong increase of the reduction current below 0.2 V in the cathodic scan, often together with distinct peaks which reflect staged lithium intercalation (0.2–0.02 V), and corresponding oxidation currents for de-intercalation up to 0.4 V in the anodic scan.[11] Basal HOPG surfaces, in contrast, are supposed to be incapable of rapid Li^+ intercalation.[160,161] This agrees with the above current traces recorded on HOPG|EC+$LiPF_6$, where no notable peaks are observed at the potentials expected for Li^+ (de-)intercalation. In contrast, Jeong *et al.* reported peaks in the CV close to 0.0 V in the cathodic scan and between 0.5 and 1.0 V in the anodic scan on basal HOPG and assigned them to a combination of irreversible solvent decomposition as well as Li^+ (de-)intercalation.[64] Interestingly, their CV for HOPG|EC + $LiClO_4$ is similar to current traces we obtained on 'scratched' HOPG (see below, **Figure 3-3**).

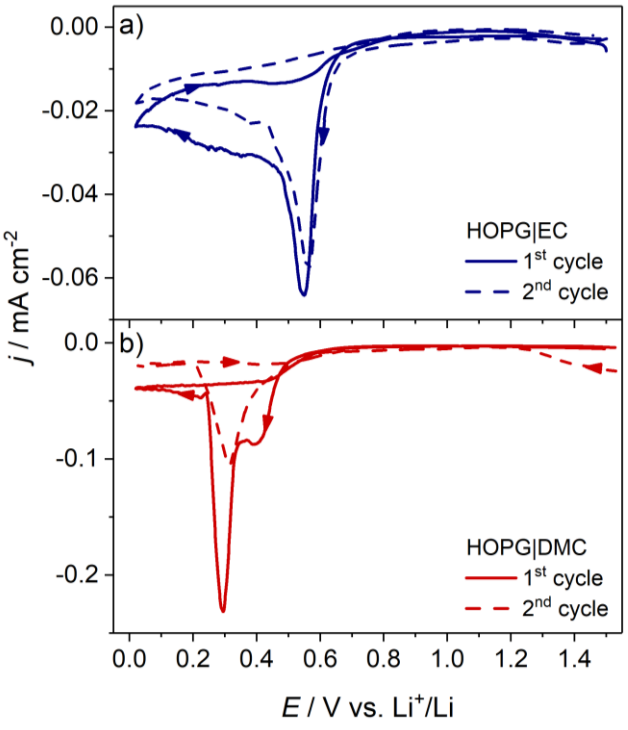

Figure 3-1. Cyclic voltammograms recorded on HOPG (basal plane) in a) EC + 1 M $LiPF_6$ and b) DMC + 1 M $LiPF_6$ at 0.1 mV s^{-1}.

On the other hand, surface science-type experiments of our group indicated that Li^+ intercalation occurs even on well-defined HOPG after deposition of small amounts of Li^0 under UHV conditions.[159] Taken together, it appears that Li^+ intercalation into basal HOPG is possible with measurable rates only on defective surfaces. In the first anodic scan, the reduction current forms a plateau between 0.2 and 0.5 V, indicating ongoing reductive processes (electrolyte decomposition). At the same time, we cannot exclude minor contributions from oxidative processes.

The second cycle of the CV in **Figure 3-1** shows the same characteristics as the first one, albeit with a slightly shifted onset (from 0.9 to 1.1 V) and peak potential (0.6 instead of 0.5 V) and a somewhat lower current density. According to the literature, formation of the SEI on HOPG electrodes and subsequent surface passivation in EC-containing electrolytes is largely completed in the first cathodic scan, regardless of the exact electrolyte composition (e.g., HOPG|EC+$LiClO_4$,[64] HOPG|EC/DMC+$LiPF_6$,[68] and HOPG|EC/DEC+$LiClO_4$[155]). Therefore, further reduction currents are usually not observed in the second and following cycles. Alliata *et al.,* though, observed incomplete surface passivation in a single cycle on basal HOPG, while on cross-sectional HOPG this was completed after one cycle.[76] In consequence, the different behavior in the present measurements may be an effect of the low defect density of the HOPG model electrode surface. It could also be related, however, to the much higher amount of electrolyte in our beaker cell compared to battery cells, which might cause dissolution and migration effects that delay complete surface passivation. These aspects will be discussed further with **Figure 3-3** (section 3.3.3).

The CVs for HOPG in DMC-based electrolyte (**Figure 3-1**) were recorded in a broader potential window (3.0–0.02 V), since in some of our measurements a peak around 0.08 V appeared in the cathodic scan, along with a broad signal at 1.9 V (see Supporting Information section 3.5.2, **Figure S3-2**). The latter peak has previously been attributed to reductive processes caused by O_2 or H_2O contaminations in the electrolyte.[68,70,194] This is reasonable, considering the rather high water content in our solvents. The next reductive Faradaic process with a pre-peak at 0.4 V is found at 0.3 V. Considering also the previous report by Jeong *et al.*,[64] we assign these peaks to the reductive decomposition of the DMC-based electrolyte. Jeong and coworkers reported the onset of DMC reduction at ~0.7 V (HOPG|DMC + $LiClO_4$, 5 mV s^{-1}, 3.0–0.0 V), which led to a sharp reduction peak at 0.3-0.2 V.[64] This agrees well with our observations. After the reductive decomposition, the cathodic current density

decreases until the lower potential limit and then remains constant on the subsequent anodic scan, forming a plateau much like the one observed for HOPG in EC-based electrolyte.

In the second cycle, the cathodic scan again shows a broad maximum at 1.9 V. After that peak, reductive currents appear again at about 0.5 V, which agrees with the trend in the first cycle. In this case, however, the pre-peak has vanished. Overall, the current density is only half of that recorded in the first cycle. Thus, in contrast to the EC-based electrolyte, we find a significant surface passivation for the HOPG|DMC system in the first two cycles.

3.3.2. Influence of Scan Rate and Cycling Time

To obtain more information on the kinetics of the processes contributing to the potentiodynamic SEI formation, we performed additional CV measurements with different scan rates (1 and 10 mV s^{-1}) in addition to the slow-scan measurements described above (0.1 mV s^{-1}).

In **Figure 3-2** we present selected cathodic scans (1st to 3rd in all cases, plus 5th and 10th/50th in some cases) of the potentiodynamic cycles measured in EC- and DMC-based electrolyte, respectively, which illustrate the difference in trends with varying scan rate. (The complete first cycles are presented and briefly discussed in **Figure S3-2**, Supporting Information, section 3.5.2 in this work.) In general, the scans support the previous conclusion (see section 3.3.1) that electrolyte decomposition (EC: 0.6–0.4 V, DMC: 0.4–0.3 V) continues past the first cycle and that therefore surface passivation / SEI formation is not completed at that point. At 0.1 mV s^{-1}, as discussed above with **Figure 3-1**, we mainly find a steady decrease of the cathodic current density for both electrolytes. At 1 and 10 mV s^{-1}, however, the behavior is more complex. For HOPG|EC + $LiPF_6$, we find a change in the peak current density and a shift in the peak position in the region of 0.7 to 0.2 V. Both effects appear to be linked, i.e., a decrease in current density is combined with a potential up-shift. For the fastest scan rate of 10 mV s^{-1} we find a steady decay of the reduction peak and a shift to higher potentials.

Furthermore, a pre-peak at higher potentials, which is visible only as weak shoulder in cycles one and two, becomes more dominant with increasing cycle number. From these observations we conclude that the apparent peak shift is mainly due to a pronounced increase of the relative intensity of the high potential peak / relative decrease of the low potential peak, while the actual shifts in the potentials of the individual peaks are rather small.

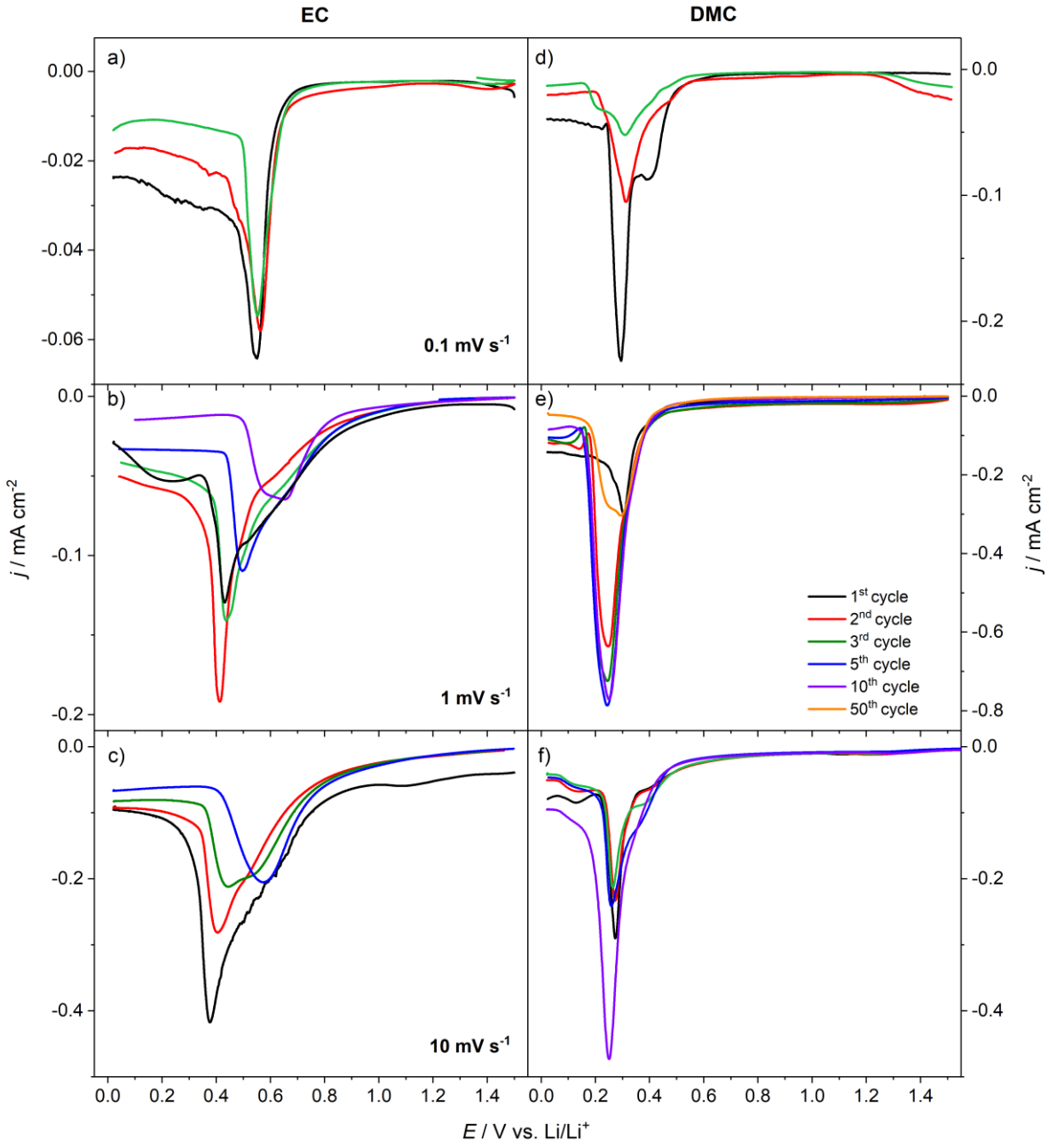

Figure 3-2. Cathodic scans between 1.5 and 0.02 V of HOPG in (a-c) EC- and (d-f) DMC-based electrolyte at 0.1, 1 and 10 mV s 1. From the scans indicated in the legend, we only show those which demonstrate best the activation effect for the respective series.

This indicates that two different processes are responsible for the two peaks, whose contributions change with increasing cycle number. Obviously, the process reflected by the lower potential peak is more strongly affected by the ongoing SEI formation than the higher-potential process.

Most complex, however, is the behavior observed at 1 mV s^{-1}. Under these conditions, the reduction peak first increases in intensity from cycle one to cycle two and subsequently decays. This demonstrates an initial activation effect, which, to the best of our knowledge, has not been reported before. At the same time, also the peak potential shifts to slightly lower values. Afterwards, the current density decreases, following the trend observed at 10 mV s^{-1}. The same is also true for the shift to higher potentials and for the appearance and relative growth of the second peak at higher potential.

For HOPG|DMC + $LiPF_6$, the trends for the current densities and the evolution of the higher-potential peak at 1 and 10 mV s^{-1} are rather similar to the ones observed in EC-based electrolyte (for the behavior at 0.1 mV s^{-1} see section 3.3.1), while the peak shifts are less pronounced. Also, the activation behavior at 1 mV s^{-1} is observed again, and it is even more pronounced than in EC-based electrolyte. In the present case, the activation continues up to the fifth cycle before the current density decreases again. After 30 cycles (not shown), we also find the double-peak feature which in EC-based electrolyte appeared already after ten cycles at the same scan rate.

Furthermore, in DMC-based electrolyte, we find an activation effect also at 10 mV s^{-1}. In contrast to the slower scan rate, though, it does not start right from the beginning but only after the first four cycles. Here it should be noted that, in some similar-type measurements, we also found activation right from the beginning. Most likely, these discrepancies result from differences in the quality of the HOPG model electrode surface, indicating that the activation effect depends sensitively on the defect density of the HOPG electrodes. This will be discussed in more detail in the next section.

3.3.3. Influence of the Surface Preparation

As a last point, we explored the influence of surface defects on the SEI formation. Scanning electron microscopy (SEM) micrographs of the optically smooth and the roughened HOPG surface are displayed in the Supporting Information (section 3.5.1 in this work), **Figure S3-1**. These show that the scratches in the HOPG surface exhibit a vastly increased number of cross-sectional sites. **Figure 3-3** displays CVs recorded on deliberately damaged HOPG in EC- and DMC-based electrolyte and, for comparison, the corresponding ones recorded on optically smooth HOPG (see also **Figure 3-1** and **Figure S3-3**). For both electrolytes, the CVs recorded on the two different surfaces differ significantly, with much higher currents on the defective surfaces. For the defective HOPG|EC+$LiPF_6$ system (**Figure 3-3**) we find a pronounced

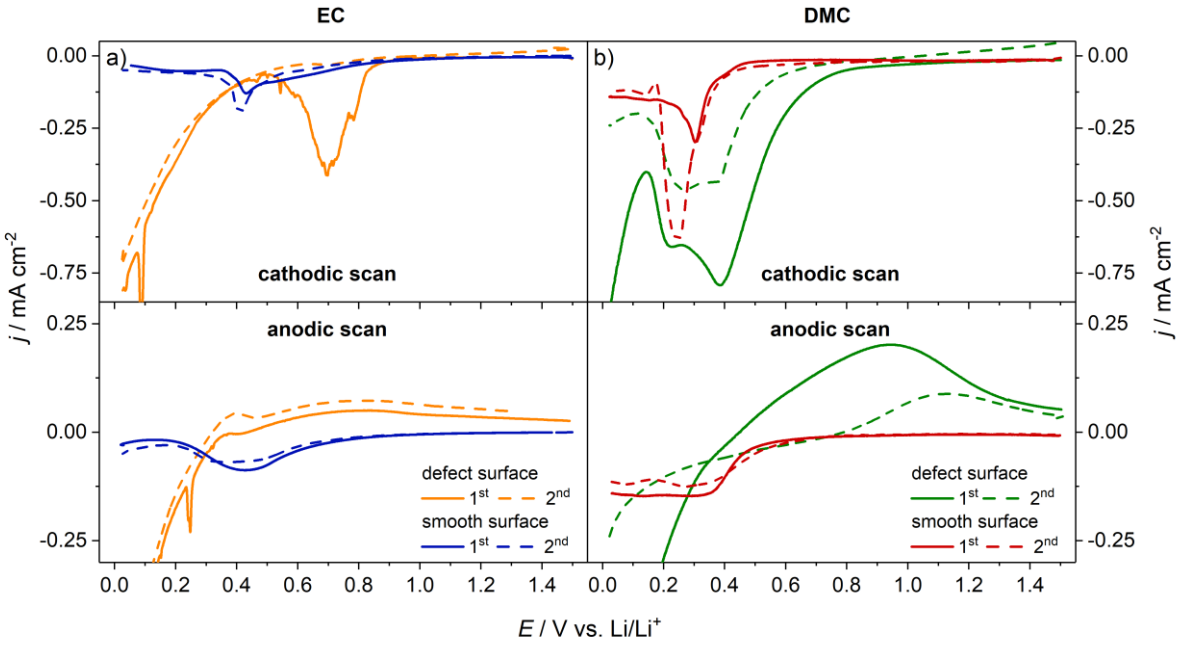

Figure 3-3. Cathodic (above) and anodic (below) scans of an optically smooth and a defective basal HOPG plane in a) EC + $LiPF_6$ and b) DMC + $LiPF_6$ at 1 mV s^{-1}. Straight lines present the first cycle, dashed lines the second.

reduction peak with a maximum at 0.7 V, at potentials considerably higher than the reduction peak on the smooth HOPG surface. The main decomposition process occurs in the potential range where, on smooth HOPG, the pre-peak is located, but with considerably higher currents. Below 0.5 V, the current increases continuously towards the lower potential limit. This is most likely due to Li^+ intercalation via the surface defects. In agreement with that, the anodic scan of the first cycle exhibits a small peak for Li^+ de-intercalation at 0.4 V. The second cycle exhibits no significant current signal except in the Li^+ (de-)insertion region. Hence, the first cycle is sufficient for complete passivation towards further (reductive) electrolyte decomposition.

Comparing the characteristics of our CVs recorded on smooth and damaged HOPG with the one reported by Jeong *et al.*[64] (HOPG|EC + $LiClO_4$), we find their CV to agree closer with that measured on the damaged substrate with respect to the decomposition potential, the Li^+ (de-)intercalation, and the overall passivation behavior. Most likely, that sample had a considerable density of surface defects. This agrees also with the absence of an activation effect in the measurements by Jeong and coworkers.[64]

A similar experiment performed in DMC-based electrolyte (**Figure 3-3**b) also shows a significant shift of the onset potential for electrolyte reduction to higher potentials and a broader and much more intense reduction peak compared to smooth HOPG (~1.1 V vs.

~0.6 V). In addition, it exhibits a side maximum at the lower potential side (0.2 V). At potentials below 0.1 V the current density increases steadily, which again is assigned to Li^+ intercalation. The corresponding, very broad Li^+ de-intercalation peak in the anodic scan is in the range 0.5–1.4 V. Note that the Li^+ de-intercalation charge is much higher than in EC-based electrolyte. In the second cycle, the general shape of the curves is maintained. The currents, however, are considerably lower than in the first scan, both those for electrolyte reduction and those for Li (de-)intercalation. Hence, also in this electrolyte there is no activation observed for the defective electrode surface, different from the optically smooth sample cycled under similar conditions (1 mV s^{-1}). The effect seems to be a unique aspect of the smooth, basal HOPG model electrode. We tentatively explain this by an increase in the electrochemically active surface area and/or the formation of surface sites with higher activity, caused, e.g., by surface exfoliation.[195] Such processes have been reported upon cycling of graphite electrodes in propylene carbonate electrolyte and were explained by solvent co-intercalation into defect sites[196] connected with the build-up of a passivation layer (SEI formation). Assuming different kinetics for these two counteracting processes, with activation being faster but with passivation prevailing as the dominant process in the long run, we can explain the complex behavior observed experimentally for the different scan rates as follows: at 0.1 mV s^{-1}, the scan rate is sufficiently slow that there is enough time for passivation before the second cycle is recorded, and passivation is the dominant effect. At 1 mV s^{-1}, in contrast, this is no more the case and the current densities in the second cycle exceed those in the first cycle in both electrolytes. Hence, activation is dominant at the beginning. Only after a number of cycles (~two for EC electrolyte reduction, ~ten for DMC electrolyte reduction) the thickness of the SEI is sufficient to negate the activating process and the current densities decrease again. The discrepancy in the time needed until passivation takes over is in line with the earlier onset for EC decomposition observed in the cathodic scan. Both effects point to a more facile decomposition and passivation process in EC than in DMC. Furthermore, it is likely that the processes leading to activation and passivation start at different potentials. Assuming that the passivating electrolyte decomposition is related to the peaks around 0.5 to 0.3 V and that the activation due to an increased surface via exfoliation sets in at lower potentials (during the rather flat region below the peak), the different behavior at 0.1 and 1 mV s^{-1} can be rationalized: at 0.1 mV s^{-1}, there is enough time for the electrolyte decomposition to form a passivation layer which hinders the exfoliation process before the potentials needed for the latter are reached. In contrast, at higher

scan rate, the passivation is not yet complete when the lower potentials trigger the activation process.

At a scan rate of 10 mV s^{-1}, finally, the behavior of both HOPG in EC- and DMC-based electrolyte is even more complex. The CVs show decreasing current densities for a certain amount of cycles, until the activating effect sets in and current densities increase again. In the picture discussed above this would mean that the time spent at low potentials is too short for significant activation, which involves also structural modifications, while electrolyte decomposition and passivation is still possible to some extent. A more detailed discussion is, however, not possible from the present data. This is particularly true as the number of cycles necessary until activation sets in was found to differ greatly, indicating distinct effects of the defect density of the HOPG surface. Likewise, no activation effects were found on deliberately damaged HOPG electrodes at 1 mV s^{-1}. Finally, focusing on the role of the different electrolytes in the passivation process on the damaged surfaces, it occurs faster in EC-based than in DMC-based electrolyte. In the former, only a single cycle is required for complete passivation, while SEI formation in single-solvent DMC electrolyte it is not yet completed after five cycles.

3.3.4. Chemical Composition of the SEI – Ex Situ XPS Characterization

The chemical (surface) composition of the SEI was characterized by XPS. Spectra were recorded on selected HOPG samples, 1) on the as-prepared SEI surface (t=0) and 2) after subsequent sputtering of the topmost layers (total sputter times two, six, 12 and 30 minutes, sputter rate ~1 nm min^{-1} as specified by the manufacturer).

The spectra will be shown in **Figure 3-5** and **Figure 3-6** for the non-sputtered electrodes (t=0) and for samples sputtered for six minutes (t=6) after cycling at a scan rate of 0.1 mV s^{-1}. Corresponding spectra recorded after longer sputtering times and upon cycling at 10 mV s^{-1} are included in the Supporting Information (**Figures S3-4** to **S3-11**, section 3.5.3).

3.3.4.1. Depth-Dependent Elemental Composition of the SEI Surface in EC- and DMC-Based Electrolyte at 0.1/10 mV s-1

Before discussing the spectra in detail, we will begin with the resulting elemental composition (Li, P, C, O and F) of the passivation layer, which can be derived from the peak intensities using the respective atomic sensitivity factors (ASFs, see **Table S3-2**, SI) without any ambiguities imposed by peak fitting / peak deconvolution procedures.

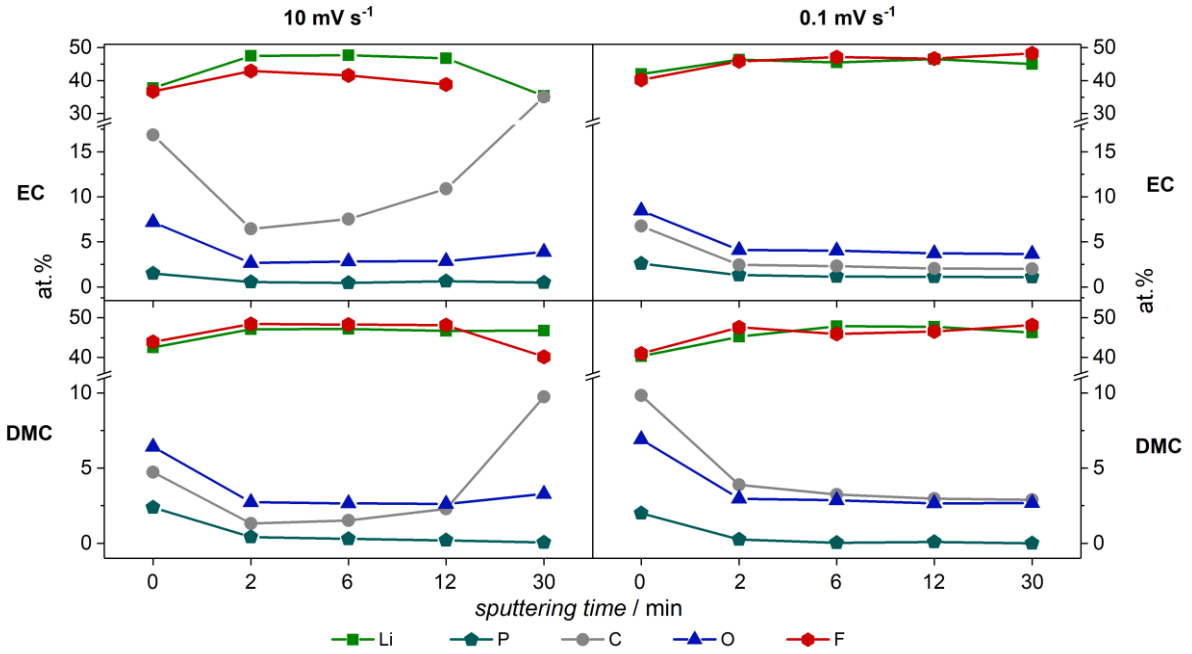

Figure 3-4. Elemental composition of the SEI formed on HOPG in EC- (above) and DMC-based (below) electrolyte, respectively, at scan rates of 10 mV s^{-1} (left) and 0.1 mV s^{-1} (right).

The depth-dependent compositions of the SEIs formed in EC- and DMC-based electrolytes obtained after different sputtering times are illustrated schematically in **Figure 3-4**. The elements with the highest concentrations in the surface and bulk regions of the SEI layer are Li and F (~40-50 at.%). The ratio of both elements is about 1 : 1. During sputtering, their atomic percentages remain more or less constant over the total sputtering time (30 min) for HOPG electrodes cycled at 0.1 mV s^{-1} regardless of the electrolyte. For samples cycled at 10 mV s^{-1}, the F concentration decreases slightly during the last 18 min of sputtering. Apparently, the majority of Li- and F-containing species is more or less homogeneously distributed throughout the SEI, except for the region close to the electrode, where they are less abundant. With concentrations of 5–16 at.% and 5–8 at.% at the surface, C and O, respectively, are the third-most abundant elements in the as-prepared SEI. For both elements, the concentration changes significantly upon sputtering, decreasing drastically after two minutes. We assume that the higher surface concentrations on the as-prepared SEI at t=0 are due to residual solvent traces remaining on the sample after the cleaning procedure. During continued sputtering, the elemental concentrations of oxygen and carbon remain more or less constant. During the last 18 minutes of sputtering, however, the concentration of C increases for the samples cycled at 10 mV s^{-1}, whereas the amount of O remains about constant. The different trends of these two species in the later stages of the sputter procedure (12 to 30 min) on the samples cycled at the

fast scan rate indicate that there is no increase in the amount of species which contain both C and O, but that this is carbon-specific. This is tentatively attributed to growing contributions from the HOPG substrate, as the graphite bulk is probed by XPS after the SEI has largely been removed (see also below). This allows for an estimate of the SEI thickness, using the sputter rate of about ~1 nm min^{-1}. Therefore, we estimate that the SEI formed on the samples cycled in DMC-based electrolyte at 10 mV s^{-1} is around 30 nm thick. For the sample cycled at 10 mV s^{-1} in EC, the increase in C 1s intensity is even more pronounced, indicating a comparable thickness of the SEI layer. For the samples cycled at 0.1 mV s^{-1} we do not find such kind of C 1s intensity increase after t=12, regardless of the electrolyte. Accordingly, we assume the SEIs formed under these conditions to be thicker. These findings and possible problems arising from the simplified data evaluation will be discussed in more detail in section 3.3.4.2, when examining also the peak forms and BEs. P-containing species, finally, represent the smallest contribution to the SEI. Even on the as-prepared surface (t=0), the phosphorus concentration does not exceed 3 at.%. It further decreases upon sputtering, reaching values below 1 at.% after two minutes of sputtering irrespective of electrolyte and cycling speed.

As a last remark we would like to emphasize that all samples, regardless of electrolyte and scan rate employed during cycling, show a dominant contribution of compounds resulting from decomposition of the salt species, such as LiF. This will be discussed further in the next section.

3.3.4.2. SEI Compound Identification

In **Figure 3-5** and **Figure 3-6**, we show XP detail spectra measured in different spectral regions on the as-prepared (t=0) SEI on a HOPG surface cycled in EC- (DMC-)based electrolyte at 0.1 mV s^{-1} and on the SEI after six minutes of Ar^+ sputtering (t=6). Similar spectra recorded on the samples after cycling at 10 mV s^{-1} as well as the ones recorded after two, 12 and 30 minutes of sputtering for both slow and fast scan rate can be found in the SI, section 3.5.5, in **Figure S3-4** to **Figure S3-11**. We will start with the discussion of the spectra recorded after cycling and subsequent sample transfer (t=0). Because of the relatively small differences, the respective spectra of the EC-cycled and DMC-cycled samples will be discussed together. The contributions from different compounds were determined via a comprehensive peak fitting procedure, which is based on the following assumptions: 1) the binding energies (BEs) and the full width at half maximum (FWHM) of the elemental peaks of a given compound are fixed for all spectra, i.e., after cycling at different scan rates, in different

electrolytes and after sputtering for different times. 2) Except for the cases indicated, their intensities are determined by the stoichiometry of the compound and by the respective ASFs. **Table 3-1** lists the BE values used for peak fitting, a listing of reference values may be found in **Table S3-3**, Supporting Information / section 3.5.5, together with further details on the fits.

For the Li 1s spectra of the non-sputtered samples, we obtain three peaks. A major contribution at 55.8 eV is assigned to LiF,[147] which is supported also by a similar amount of F species (see below). Two minor signals at 55.5 and 57.3 eV we relate to Li alkoxides[85] and $LiPF_6$ decomposition products (Li_xPF_y/$Li_xPF_yO_z$).[197,198] In the P 2p binding energy region the spin-orbit-coupled doublet corresponding to the $LiPF_6$ decomposition products is located at 135.0 eV.[198]

In the C 1s spectral region, the largest contribution is found at 284.9 eV, which we assign to C-H and C-C species in the electrolyte and its decomposition products, as well as to adventitious carbon.[147] Two smaller peaks at higher binding energies, which have a higher relative intensity for the DMC-cycled samples than for the EC-cycled samples, are attributed to Li alkoxides (288.0 eV) and ether / polymer species (286.4 eV). The latter peak may also include polymer-type species like polyethylene oxide for EC-cycled samples,[60,71,77] while the peak at 288.0 eV includes Li alkoxides for DMC-cycled samples.[199] The related signals in the O 1s spectrum, whose intensities are adjusted such that they reflect the stoichiometry, are located at 533.3 eV (ether / polymer[60,71,77]) and 532.1 eV (alkoxide[199]). The residual peak area (530-532 eV) is tentatively attributed to $Li_xPF_yO_z$ moieties. The LiF signal in the F 1s spectrum at 685.0 eV, finally, fully agrees in its intensity with the stoichiometric 1 : 1 ratio of LiF when comparing it with the Li 1s signal at 55.8 eV. It is accompanied by two low-intensity signals at 686.6 and 688.3 eV, which are attributed to Li_xPF_y and $Li_xPF_yO_z$.[197,198]

Next, we move on to the changes in specific species induced during stepwise sputter removal of the SEI layer, which most simply reflect the varying composition of the SEI at increasing depths, but possibly also changes induced by the sputter process itself. The variations in the concentration of characteristic species with increasing sputter times are illustrated by the spectra recorded after six minutes of sputtering (**Figure 3-5** and **Figure 3-6**). The changes are summarized in **Figure 3-7**.

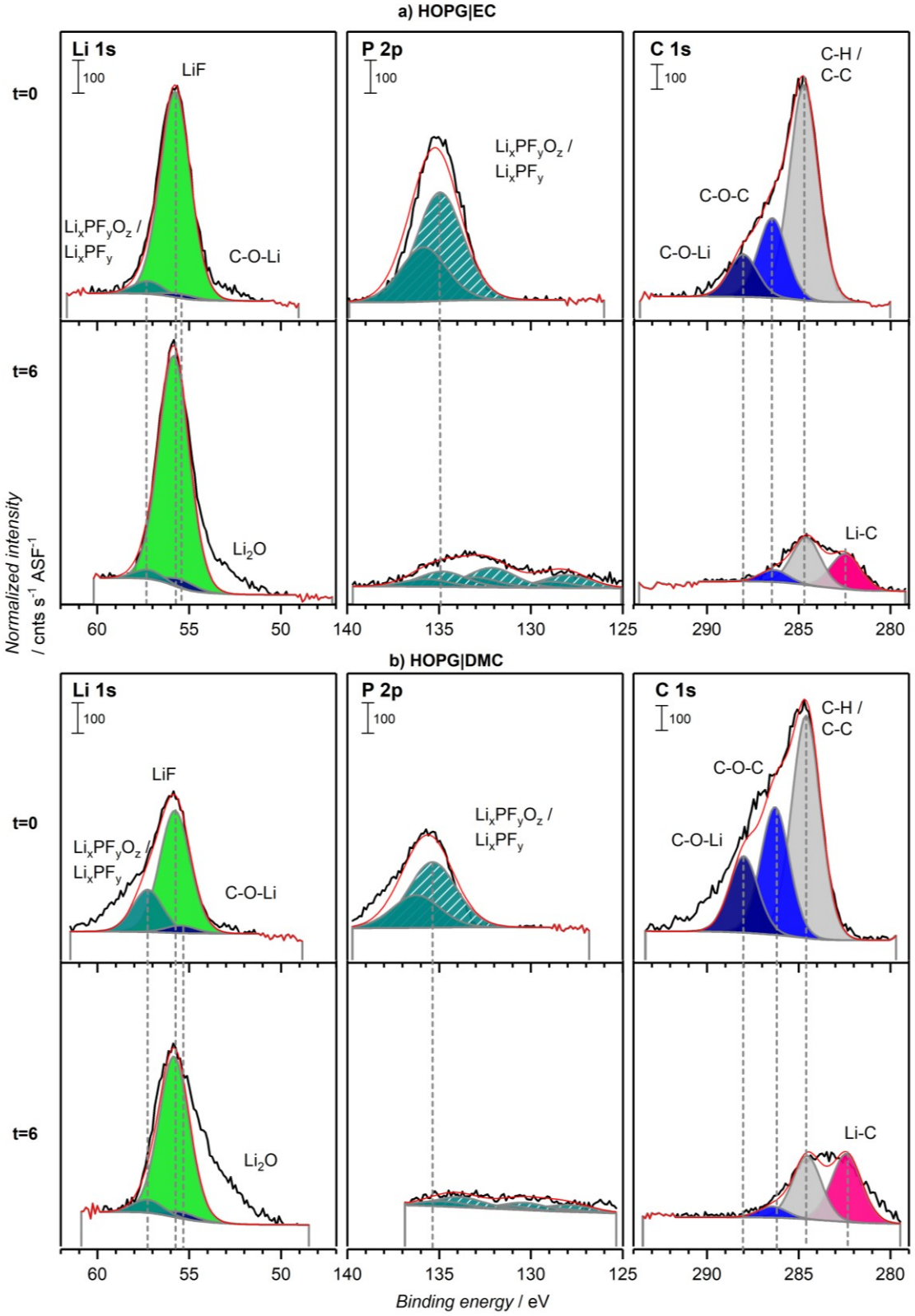

Figure 3-5. XP detail spectra of the Li 1s, P 2p and C 1s regions of the SEI formed on HOPG in a) EC- and b) DMC-based electrolyte cycled at 0.1 mV s^{-1}, measured on the as-prepared sample (t=0, top panel) and after six minutes of sputtering (t=6, bottom panel). Red lines indicate the sum of the individual peak intensities.

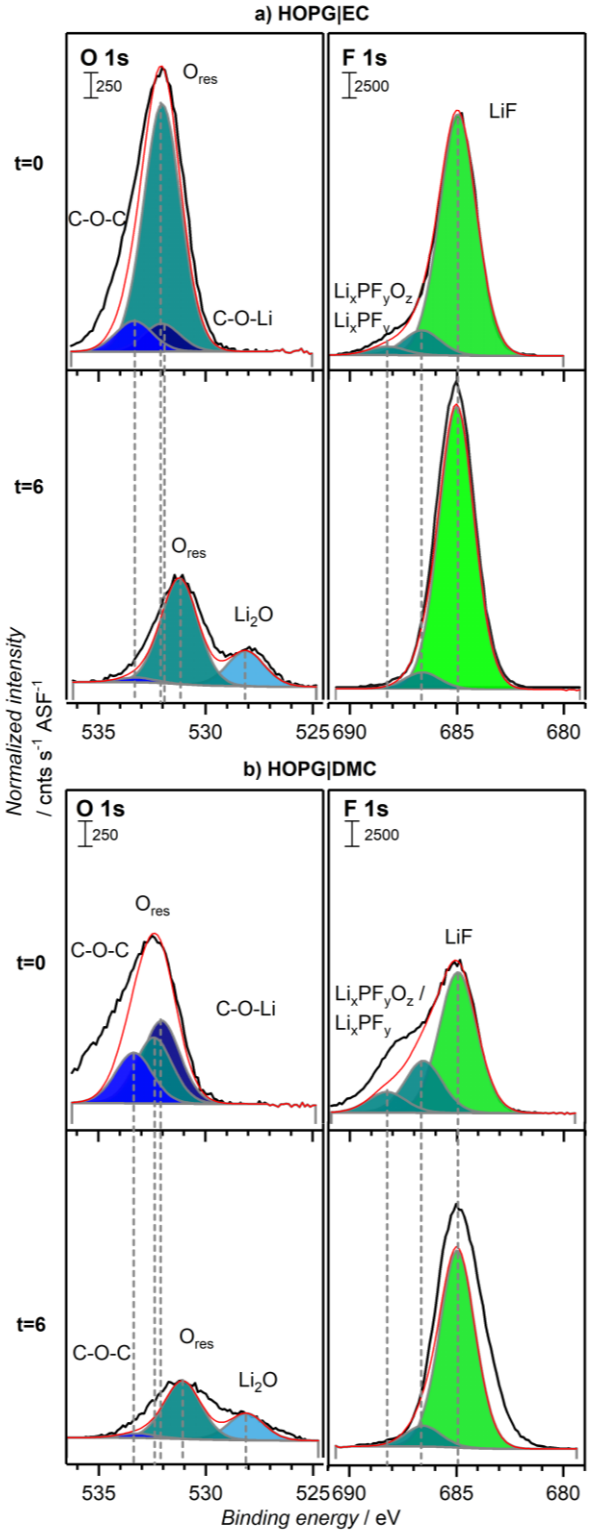

Figure 3-6. XP detail spectra of the O 1s and F 1s regions of the SEI formed on HOPG in a) EC- and b) DMC-based electrolyte cycled at 0.1 mV s^{-1}, measured on the as-prepared sample (t=0, top panel) and after six minutes of sputtering (t=6, bottom panel). Red lines indicate the sum of the individual peak intensities.

They show the development of the atomic concentrations (at.%) of selected SEI compounds, which are calculated from the sum of the individual elemental contributions, e.g., the Li 1s LiF and the F 1s LiF component, both for the different electrolytes and for different scan rates (0.1 and 10 mV s^{-1}). For the LiF concentration, we find an initial increase of LiF between t=0 and t=2 for all samples. It is followed by an approximately constant, high concentration for the samples cycled at the slow scan rate, while for the samples cycled at the fast scan rate, the concentration decreases again for the last 18 minutes of sputtering. The latter observation is in agreement with the appearance of the HOPG substrate after 30 min sputtering for the samples cycled at 10 mV s^{-1}, supporting our previous claim of a SEI thickness of about 30 nm in this case. In average, the LiF concentration was 75–85 at.%, both for the samples cycled in EC- and in DMC-based electrolyte, and it is more or less homogeneously distributed in the SEI. After six minutes of sputtering, the F 1s peak at 688.3 eV has disappeared and the signal at 686.6 eV has decreased significantly (see **Figure 3-6**). Most likely, this means that the related $Li_xPF_yO_z$ and Li_xPF_y species are present only at the initial surface of the SEI. Sputter-induced decomposition could explain this only if the resulting products were gaseous, since the intensity of the P 2p peak disappears almost completely rather than shifting in BE.

Table 3-1. Binding energies of the solvent / electrolyte salt decomposition products found within the SEI on basal HOPG cycled in EC- and DMC-based electrolyte.

	C 1s / eV	O 1s / eV	Li 1s / eV	F 1s / eV	P 2p / eV
C–O–C (polymer/ether)	286.4	533.3			
C–O–Li (alkoxide)	288.0	532.1	55.5		
LiF			55.8	685.0	
Li_xPF_y			57.3	686.6	135.0
$Li_xPF_yO_z$			57.3	688.3	135.0
Li_2O		528.0	55.5		
Li–C	282.4				
C–H/C–C	284.9				

The high amount of LiF in the SEI is in contrast to findings of Peled *et al.,* who determined organic components as dominant component in the SEI on the basal HOPG surface in a mixed

EC/DEC-based electrolyte, while the SEI on the cross-sectional surface was found to mostly consist of LiF.[56] Because of the very different experimental conditions in our three-electrode half-cell measurements and in their two-electrode setup, a more detailed discussion of possible reasons for these discrepancies is not possible.

As illustrated in **Figure S3-6** of the Supporting Information, section 3.5.5, sputtering induces the disappearance of the C–O–Li signal in the C 1s BE region after two minutes, as well as a pronounced loss of the ether / polymer and hydrocarbon species. Apparently, these organic species are mainly formed close to the SEI|electrolyte interface and are only present in low concentrations in deeper regions of the SEI, i.e., closer to the electrode. Focusing on the intensity of the C–H- / C-C-related C 1s signal, this remains constant at a lower value after its initial decrease (between t=0 and t=2), both for the EC-cycled and the DMC-cycled HOPG electrode (scan rate 0.1 mV s^{-1}). However, it increases again slightly after 12 minutes of sputtering (t=12) for the samples cycled at 10 mV s^{-1}, as, supposedly, the substrate is reached. Furthermore, a new C 1s signal emerges at 282.4 eV after two minutes of sputtering (t=2, **Figure S3-6** / **Figure S3-7** and **Figure S3-9** / **Figure S3-10**, section 3.5.5), both for the EC-cycled and the DMC-cycled electrodes, which has previously been attributed to lithiated graphite.[86,150] Considering that at this point the passivating SEI layer on top of the graphite is still sufficiently thick that the HOPG substrate is not yet accessible by the XPS measurement; we attribute this signal to Li–C species (Li carbides) that are created during sputtering. Similar signals had been observed also in other measurements on related materials in our group. This assignment is supported also by the fact that the CV measurements were stopped at a potential of 1.5 V, where Li^+ intercalation should be absent. In the last sputtering phase, the intensity of the Li–C species (C 1s at 282.4 eV) increases abruptly on the electrode cycled in DMC-based electrolyte at 10 mV s^{-1}, while the EC-cycled electrode shows a more steady increase in signal intensity. For the DMC-cycled sample, after 30 min sputtering, the C 1s intensity of the Li–C species is about four times as high as that of C-H species / adventitious carbon. This increase in intensity goes along with the above-mentioned decay in LiF concentration. We interpret the sudden increase of the Li–C signal in the final sputter sequence as an indication of the close proximity of the HOPG substrate. This is based on the assumption that on this sample, Li–C species are preferentially formed close to the HOPG|SEI interface, either by sputter-induced reaction of Li species with HOPG fragments, or during cycling, e.g., in the initial activation

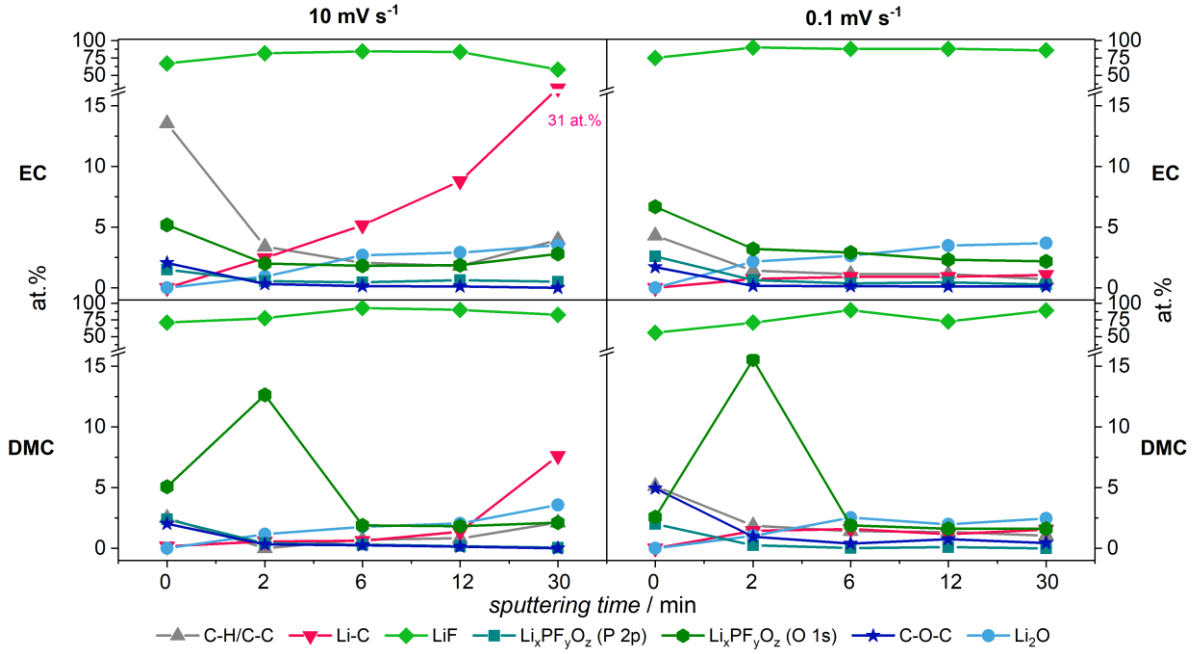

Figure 3-7. Depth profile of the concentration of selected components of the SEI formed in EC- (above) and DMC-based (below) electrolyte at different scan rates (concentration is given in at.%. For the calculation, the H-containing components were excluded).

phase (at 1 and 10 mV s^{-1}). In this case, sputtering for 30 min would be sufficient to remove most of the SEI, and we can estimate the thickness of the SEI layer to about 30 nm. This would be in line with the conclusion derived from the elemental composition, where we tentatively concluded from the increase in total C 1s intensity that XPS starts to detect the HOPG substrate after 30 minutes of sputtering the SEI formed at fast scan rate.

Nevertheless, we cannot rule out that the sudden increase in Li-C-related C 1s intensity arises from other effects, which would invalidate our thickness estimate of the SEI layer. In any case, the state-specific C 1s data in **Figure 3-7** also illustrate the potential problems that can arise when using the total intensities of the XPS signals (see **Figure 3-4**) rather than deconvoluting them to use state-specific intensities.

For the EC-cycled sample, the activity for sputter-induced formation of Li–C species in the SEI itself seems to be significantly higher, resulting in a steady increase of these species with increasing sputter time from the beginning on. In this case, an estimate of the SEI layer thickness is even harder.

Comparing the different scan rates, the amount of Li–C species detected by XPS increases much more for the samples cycled at 10 mV s^{-1} than for the samples cycled at slow scan rate

(see **Figure 3-7**), which is in line with a thicker SEI layer obtained after slow cycling. Increasing carbon contents after longer sputter times were reported also by Peled *et al.*[56] They explained this by an increasing concentration of C–C species stemming from the graphite substrate and concluded that most of the SEI is removed at the time when an unambiguous increase of the C–C signal is observed. This allows an estimation of the SEI thickness.

Moving on to the oxygen-containing compounds, we first of all find a new species appearing after two minutes which is indicated by an O 1s signal at 528.1 eV (**Figure 3-6**). We assign this peak to Li_2O,[85] with its counterpart in the Li 1s region at 55.5 eV. This compound has been reported before as part of the SEI formed on graphite compound electrodes in EC/DEC-based electrolytes in the presence of water traces and as a side product of Li_2CO_3 decomposition upon Ar^+ sputtering.[85] For the present experiments, we cannot distinguish between these possibilities. Although we do not find any (semi-)carbonate-related peaks in the C 1s spectrum on the SEI surface at t=0, they may have been part of the deeper regions of the SEI prior to sputtering, and were decomposed upon sputtering. On the other hand, the presence of trace impurities of water cannot be ruled out, either.

The evolution of the Li_2O concentration during sputtering is displayed in **Figure 3-7**. Except for the initial phase, its intensity is more or less constant throughout the depth profile. The overall intensity in the O 1s detail spectra, in contrast, decreases significantly during sputtering, and the alkoxide signal mostly disappears after two minutes of sputtering (see **Figure 3-7** and section 3.5.5, **Figure S3-8** and **Figure S3-11**). At the same time, the concentration of the $Li_xPF_yO_z$ species in the SEI increases considerably for the sample cycled in DMC-based electrolyte. It then decreases again, reaching 1–2 at.% after six minutes, and then remains constant. For the EC-cycled samples, the concentration decreases to about half during the first two minutes of sputtering, and then remains about constant. The initial maximum obtained on the DMC-cycled sample points to a higher amount of mixed salt- and solvent-based decomposition products formed close to the SEI surface. On the EC-cycled sample the maximum concentration of these species appears even directly at the SEI surface. The concentrations of the purely C- and O-containing compounds stay about constant throughout the SEI.

Based on the sputter profiles in **Figure 3-7**, the passivation layers formed at slow scan rates seem to be thicker than those formed at fast scan rates. In neither of the systems studied, though, surface passivation was completed in the number of cycles measured (0.1 mV s^{-1}:

DMC: three cycles in a wide potential window, EC: five cycles in a narrower potential window). We assume that this may be caused by two different effects. First, the sensitive competition between counteracting activation and passivation processes, which has been discussed before, will affect also the thicknesses of the SEIs generated upon cycling with different scan rates (see section 3.3.2). Second, it may foremost be affected by the time spent at reductive potentials below 1.5 V, which was about 30 times longer for the model electrodes cycled at 0.1 mV s^{-1} compared to those cycled at 10 mV s^{-1} (10 mV s^{-1}: five for EC-, ten cycles for DMC-cycled samples).

Furthermore, we found the SEI to mainly consist of fluoride-containing decomposition products (LiF: ~60–90 % of the elemental composition, using the average stoichiometry of the compounds given above) and small amounts of Li-containing, and possibly also Li-free, organic compounds. Furthermore, cycling in DMC-based electrolyte led to the formation of a higher concentration of Li salt decomposition products, such as $Li_xPF_yO_z$ and Li_xPF_y, than cycling in EC-based electrolyte. This differs significantly from the findings of Peled *et al*., who reported a high concentration of solvent-based (organic) decomposition products.[56,58] As mentioned earlier in this section, we first of all explain these differences by the significant discrepancies in the experimental procedures and set-up in both experiments. In addition to the divergent cycling procedures and cell configurations, organic compounds formed during solvent decomposition are more likely to be dissolved into the bulk electrolyte in our experiments due to the larger electrolyte volume (0.3/0.7 ml) compared to the electrolyte-soaked separators in typical battery cells.

3.4. Conclusion

Aiming at a better understanding of the SEI formation in carbonate-based electrolytes on carbon electrodes in LIBs, we have investigated this process in three-electrode half-cell model experiments by cyclic voltammetry and detailed chemical surface analysis via *ex situ* X-ray photoelectron spectroscopy, using a well-defined HOPG electrode and EC + $LiPF_6$ as well as DMC + $LiPF_6$ model electrolytes. In addition, the influence of the scan rate was explored. Based on the results presented above and comparison with previous findings, we arrive at the following conclusions:

1) On smooth, structurally well-defined HOPG model electrodes, passivation is slow and not completed after three (EC) or five (DMC) cycles, regardless of electrolyte and scan rate. On defective surfaces, in contrast, passivation is completed after one cycle. The low

passivation efficiency on the smooth electrodes is explained by their low defect density, indicating that defects which are not instantaneously poisoned by the decomposition products act as (more) active sites for reductive electrolyte decomposition in these electrolytes. This finally leads to the formation of a stable passivation layer, inhibiting further electrolyte decomposition.

2) The electrolyte sensitively affects the passivation process, since even large defect concentrations do not lead to complete surface passivation within five cycles in DMC-based electrolyte, pointing to a less efficient passivation process compared to EC-based electrolyte. Obviously, the products formed from DMC decomposition are less effective in forming a completely passivating SEI.
3) Depending on the scan rate we find an initial activation on the smooth HOPG surface, which we tentatively explain by an increase in surface area. We suggest that this is caused by exfoliation of the electrode due to solvent co-intercalation. This HOPG-specific activation effect is considerably stronger when cycling in DMC-based electrolyte than in EC-based electrolyte. The kinetics of this activation process differ from that of the counteracting, potential-dependent passivation process, which results in a scan rate-dependent activation / passivation behavior with the initial activation being most pronounced at 1 mV s^{-1}.
4) These processes are furthermore affected by the concentration of defect sites on the substrate surface. We did not find any activation effects on highly defective electrode surfaces, indicating that on these surfaces passivation is so efficient that the competing activation process are essentially inhibited.
5) Different from previous reports, we find the passivation layer to mainly consist of salt decomposition products on smooth basal HOPG, in particular LiF, which is almost homogeneously distributed in the SEI. After cycling in EC-based electrolyte, the SEI contains relatively more organophosphates, which are formed from both solvent and salt decomposition, while after cycling in DMC-based electrolyte it contains more decomposition products which either result from solvent or salt decomposition, such as C–O–C and/or Li_xPF_y species. The latter seem to be less efficient in passivating the electrode completely.
6) Depth-profile XP spectra and, specifically, the C 1s detail spectra, indicate that the passivation layer formed by five/ten cycles at 10 mV s^{-1} in EC-based / DMC-based electrolyte (thickness about 30 nm) is significantly thinner than that formed at 0.1 mV s^{-1},

which is concluded from the rapid increase of the C 1s intensity typical for Li–C species after 30 min of sputtering. At the same time, the depth profiles appear rather similar for the EC- and DMC-cycled substrates, respectively, with organophosphates and other organic species (C 1s) as well as $Li_xPF_yO_z$ and Li_xPF_y species being more present at the SEI|electrolyte interface and LiF distributed almost equally throughout the SEI.

Overall, the distinct effects of electrode surface quality (defect density) and of the experimental conditions / parameters (scan rate) on the SEI formation process and the properties and composition of the resulting SEI illustrate the important role of model studies performed under well-defined conditions and with well-defined model systems for the conceptual understanding of these processes. This is a basis for a systematic improvement of the SEI.

3.5. Supporting Information

3.5.1. Physical Characterization of the HOPG Substrate

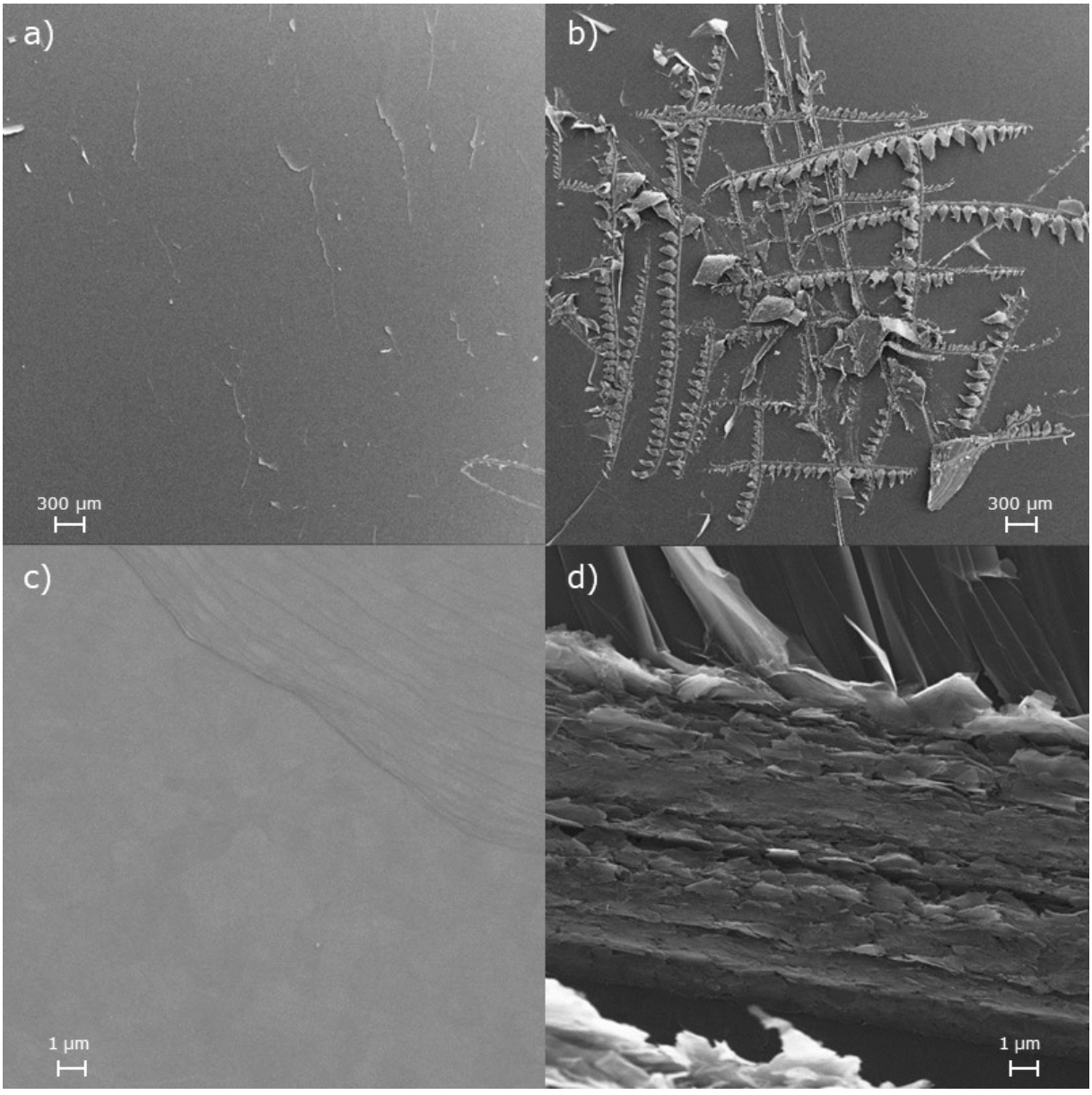

Figure S3-1. SEM micrographs of the optically smooth (a, c) and roughened (b, c) HOPG substrate at magnifications of 44x (above) and 10,000x (below). a,b) depict the as-prepared HOPG surface, c,d) show a close-up of the surface structure.

In **Figure S3-1**, scanning electron microscopy (SEM) micrographs of the optically smooth and of the roughened HOPG substrate are shown. Both samples were prepared as described in the Experimental section. The as-prepared, optically smooth HOPG surface (**Figure S3-1**a) features a number of small, irregular folds, which most likely relate to defects in the otherwise smooth graphite surface. The close-up in **Figure S3-1**c focuses on one of these folds. While it shows some more structure, the graphene layer below the surface is not exposed. On the

roughened HOPG surface (**Figure S3-1**b and d), we find deep trenches, which cut into the graphene layers and which are surrounded by graphite flakes. As shown in the higher magnification image in **Figure S3-1**d**,** the side walls of the trenches in d) expose cross-sectional HOPG sites. These structures increase both the active surface area as well as the substrate's capacity for Li^+ (de-)intercalation.

3.5.2. Reproducibility in DMC-Based Electrolytes

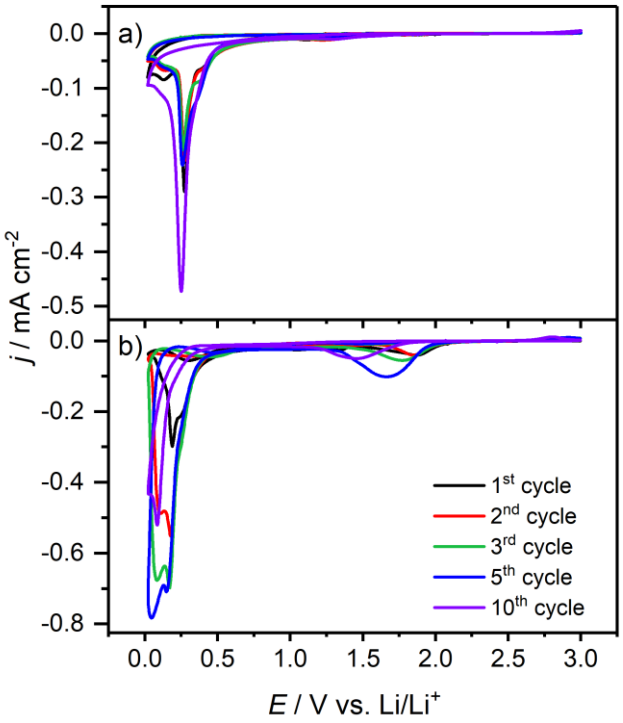

Figure S3-2. Cyclic voltammograms of basal HOPG in DMC + 1M $LiPF_6$, cycled at 10 mV s^{-1} in the potential range of 3.0–0.02 V. a) shows the surface passivation with continuing cycling. In b), activation is observed before formation of the passivating film sets in and new signals appear at 0.08 V and ~1.9 V.

Figure S3-2a compares the CV in DMC-based electrolyte at 10 mV s^{-1} (also shown in the lower right panel of **Figure 3-3**) with another one (**Figure S3-2**b) measured under allegedly identical conditions. One obvious difference is a cathodic peak at 1.9 V, which appears only in the CV shown below. A combined CV and electrochemical AFM study conducted by Chu *et al.* of HOPG in EC/DMC + $LiPF_6$ electrolyte obtained a reduction peak at ~2.0 V, which did not occur in EC/DMC + $LiClO_4$ electrolyte. Hence, it was attributed to the decomposition of $LiPF_6$ salt or of impurities, e.g., moisture from the solvent.[70] Considering that, in our case, the peak centered at 1.9 V appears only in certain measurements (and undergoes variations in the

peak maximum potential and intensity which seem to be connected to the presence and intensity of the electrolyte decomposition peak at 0.3 V with increasing cycling time), it is most likely not related to $LiPF_6$. In addition, another peak at 0.08 V was observed in part of the measurements, which appeared only if the peak at ~1.9 V was present as well and which starts to evolve in the second cycle of the CV. These two peaks also show a similar trend with respect to their current density evolution upon cycling, i.e., they grow initially before they decrease again eventually (tenth cycle).

3.5.3. First Cycles at Different Scan Rates

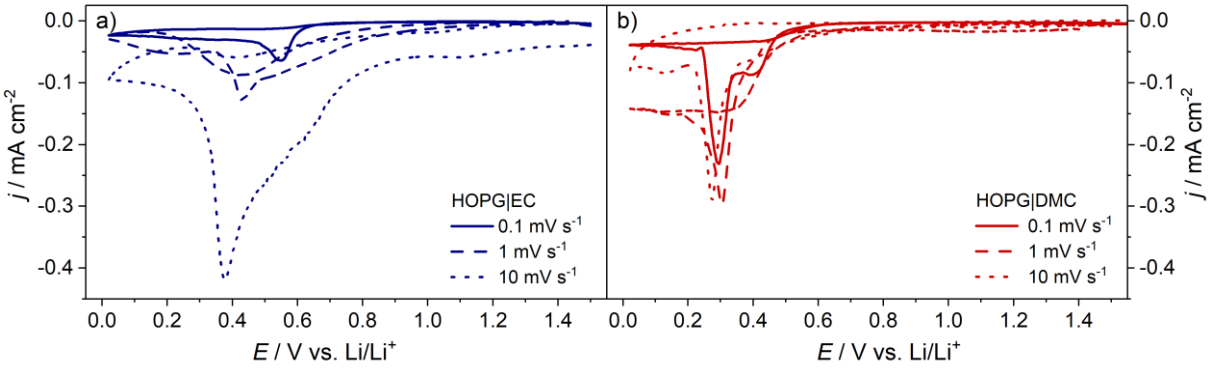

Figure S3-3. Cyclic voltammograms (initial cycle) of basal HOPG recorded in a) EC- and in b) DMC-based electrolytes at three different scan rates: 0.1 mV s^{-1} (straight line), 1 mV s^{-1} (dashed line) and 10 mV s^{-1} (dotted line).

Figure S3-3a displays the set of CVs recorded in EC-based electrolyte. Qualitatively, the CVs resemble each other with the following trends: The onset for electrolyte decomposition, which is located at 0.8 V at 0.1 mV s^{-1}, moves towards higher potentials with increasing scan rate. In contrast, the peak maxima shift to lower potentials. As expected, the current densities increase with increasing scan speed. However, the increase is not sufficient to compensate for the shorter time spent in the range of the reduction peaks, which results in a decrease of the integrated charge in the first cathodic cycle (1.5–0.02 V) with increasing scan rate (see **Table S3-1** herein). This agrees with a slow, ongoing reduction process which continues in the following cycles even at the lowest scan rate (**Figure 3-1**a). Only for the higher scan rates the reductive decomposition processes in the anodic scan, which were discussed before, lead to a clearly visible reduction peak at 0.4 V instead of the plateau observed at 0.1 mV s^{-1}. Overall, the similarities found for HOPG|EC + $LiPF_6$ at the different scan rates indicate that the main

processes are active in all cases, although their contributions are affected by the kinetics in the minute- to sub-minute range.

Analogous measurements performed for HOPG in DMC-based electrolyte (**Figure S3-3**b) show a roughly similar shape of the CVs, with the scan rate-induced changes being less pronounced than in EC-based electrolyte. In particular, the increase in current density with increasing scan rate is weaker, resulting in a larger decay of the decomposition charge in the first cycle with increasing scan rate. This points to a stronger effect of kinetic limitations in the SEI formation process.

3.5.4. Integrated Charges

Table S3-1. Integrated charges under the current traces in the first cathodic scan from 1.5-0.02 V at different scan rates.

Q / mC	**0.1 mV s^{-1}**	**1 mV s^{-1}**	**10 mV s^{-1}**
HOPG|EC + $LiPF_6$	42.36	11.16	2.21
HOPG|DMC + $LiPF_6$	643.35	15.77	1.13

3.5.5. XPS

The peak fitting procedure employed in the present study is based on the following assumptions: 1) The binding energies (BEs) and the full width at half maximum (FWHM) of the elemental peaks of a given compound are fixed for all spectra, i.e., after cycling at different scan rates, in different electrolytes and after sputtering for different times. 2) Except for the cases indicated, their intensities are determined by the stoichiometry of the compound and by the respective ASFs. The widths (FWHMs) of the individual peaks were adjusted to achieve the best fit for all data sets for P, O and C, which for O and C resulted in values close to those given in the literature.[147] For the P 2p signals, the fits resulted in a significantly larger FWHM value of 3 eV, which will be discussed below. The peak widths for Li and F, finally, were derived from a reference measurement with pure LiF. The following detailed discussion relates to **Figure 3-5** and **Figure 3-6** of the manuscript and Figures **S3-4** to **S3-11** of the Supporting Information (this section).

First of all, we calculated the amount of LiF by fitting the component at 55.8 eV into the Li 1s spectrum (FWHM 1.9 eV) and determining the corresponding F 1s peak (FWHM 2.0 eV) at

685.0 eV from the stoichiometric 1 : 1 ratio. This is illustrated for the Li 1s and F 1s peaks in the respective detail spectra at t=0. For the **F 1s** spectra, proper fitting requires the use of two further peaks at 686.6 and 688.3 eV, which are most probably related to F-containing $LiPF_6$ decomposition products such as $Li_xPF_yO_z$ and Li_xPF_y. The resulting BE values are close to those reported in the literature for Li_xPF_y (687-688 eV[197]) and for $Li_xPF_yO_z$ (688.5 eV[198]). For the sample cycled in EC these contributions are rather small, while for the electrode cycled in DMC they are somewhat more pronounced. In return, more LiF is formed on the electrodes cycled in EC at 0.1 mV s^{-1}. As illustrated in the spectra, the measured F 1s spectra can be fitted rather well with these contributions.

The **Li 1s** spectrum displays aforementioned dominant peak at 55.8 eV (FWHM 1.9 eV), which agrees well with the literature value for LiF.[147] The differences between the Li 1s signal expected for LiF (see above) and the measured peak can largely be fitted by the addition of another signal at 57.3 eV. This peak is associated with Li_xPF_y and/or $Li_xPF_yO_z$ moieties.[171] In this case, only the BE and the FWHM are fixed, as the exact stoichiometry of these moieties is unknown. In contrast to the F 1s spectrum, there seems to be only a single Li 1s signal for Li_xPF_y and $Li_xPF_yO_z$ species, indicating that the Li atom is essentially insensitive to the type and number of P, F and O ligands, while this is not the case for the F atoms. The intensities in these related Li 1s and F 1s signals (57.3 and 688.3/686.6 eV) at t=0 indicate a Li : F ratio of <1, as expected for situations with measurable contributions from Li_xPF_y/$Li_xPF_yO_z$ species. As indicated by the spectra, the contribution from these species at t = 0 is clearly larger for the DMC-cycled electrode than for the EC-cycled one. Furthermore, based on the presence of C 1s and O 1s peaks with BEs typical for Li (alk-)oxides (see below), there must be a Li 1s signal related to these species. In previous reports, a characteristic value of 55.5 eV was given.[200] The intensity of this peak contribution is calculated from the intensity of the C 1s signal of C–O–Li at 288.0 eV, assuming a C : Li ratio of 1 : 1. The contributions from these species to the Li 1s signal are, however, very low, both for the EC- and the DMC-cycled electrode. Next, we find a slight shoulder at the low-energy onset of the Li 1s peak, at around 53 eV. It appears with about similar relative intensity both for the EC-cycled and the DMC-cycled sample. Such kind of low-energy shoulder was also reported in the literature for LiF,[147] and we explain this as a satellite of the F 2s peak in this compound. It is therefore not included in the peak fitting. Finally, for the DMC-cycled sample, there is some intensity at the high BE side of the spectra, at around 59 eV, which has not been accounted for so far. Most likely, this is due to differential charging effects, which result in a shift of part of the peak intensity. A positive charging of part

of the surface will result in a lower kinetic energy, and hence in an apparently higher binding energy. This differential charging effect should equally affect all signals of this measurement, and we indeed find such kind of additional intensity also in the other spectra recorded on the DMC-cycled surface at t=0, supporting our explanation. In the simplest case, this could be described by adding a lower-intensity contribution of the entire peak at higher energies, where the relative intensity and the peak shift of/in this higher BE signal should be identical for all elements considered.

For the **P 2p** detail spectra, we identify a single doublet in both EC- and DMC-based electrolyte at t=0, with the P $2p_{3/2}$ maximum at 135.0 eV and the $2p_{1/2}$ peak up-shifted by 0.9 eV (in the following, BEs will always refer to that of the P $2p_{3/2}$ peak). Here, we used a broader peak shape with a FWHM of 3 eV for the peak fit, which is much wider than expected for a well-defined P compound (~1.0 eV).[147] This means that, in reality, we deal with a number of compounds whose P 2p BEs differ (by up to 2 eV), and which in total result in a broadened peak. Considering that the P 2p signal of non-decomposed, residual $LiPF_6$ was reported previously to appear at 138.0 eV,[72,200] the signal at 135.0 eV must result from PF_6^- decomposition products which may either be correlated with the F 1s peaks at 686.6 and 688.3 eV or which refer to F-free decomposition products. The former signals were assigned to $Li_xPF_yO_z$ and Li_xPF_y species (see above). Examples for the latter may be trimethyl phosphate, $OP(OCH_3)_3$, or phosphate-terminated PEO-oligomer species ($(R–(O–CH_2–CH_2)_n–OPO(OR)_2$, R=H or alkyl chain), which were suggested by Dedryvère *et al*. previously.[200] Due to the unknown stoichiometry, we cannot expect a well-defined P : F atomic ratio when using the intensity of the F 1s peaks at 686.6 and 688.3 eV. Hence, this ratio was chosen such that it fits best to the measured intensity of the P 2p peak. Experimentally, we obtained a P : F ratio of 1 : 3 for the electrode cycled in EC-based electrolyte at t=0 (after cycling at 0.1 mV s^{-1}), using again only the F 1s intensity in the related signals at 686.6 and 688.3 eV. Accordingly, in average these decomposition products lost about half of the original fluoride content in PF_6^- during decomposition. This would formally fit to POF_3 species, but as shown below, this assumption is too simple. F- and Li-free species, such as organophosphates, could contribute to the higher P content in the SEI formed after cycling in EC (see above). This would also fit in with the high O intensity in the O 1s spectrum of the EC-based SEI.

In DMC-based electrolyte, the P 2p signal (at t=0) is significantly smaller than for the EC-cycled sample, and we obtained a P : F ratio of 1 : 9 for the decomposition product(s). Hence,

the resulting SEI components contain in average less phosphorus than the SEI formed in EC-based electrolyte. Similar to the P-, F- and O-containing products of SEI formation in EC-based electrolyte, a combination of compounds with different P : F : O stoichiometries is more likely. The P : F ratio of 1 : 9 is actually lower than in the original compound PF_6^-, indicating that, in this case, some P-containing decomposition products were removed from the surface during cycling, while other F-containing products with a similar BE for F 1s remain. This points to the formation of soluble or gaseous P-containing decomposition products for this electrolyte. Finally, similar to the Li 1s peak, we find some additional intensity at the high BE side of the P 2p spectra for the DMC-cycled sample, which has not been accounted for so far and which, most likely, is due to differential charging effects (see above).

The **C 1s** region at t=0 is dominated by a main peak at 284.9 eV (FWHM 1.9 eV) in both electrolytes. Furthermore, two less intense signals appear at 286.4 and 288.0 eV. The first signal at 284.9 eV is generally assigned to C–C and C–H groups, i.e., to a combination of hydrocarbon components from SEI formation and/or contaminants on the sample surface (adventitious carbon).[147] The other two signals we assign to electrolyte decomposition products containing electronegative species, such as O or F. This includes C–O–C species (mainly polyethylene carbonate (PEO)) in EC-based electrolyte and alkoxides (C–O–Li) in DMC-based electrolyte, in agreement with suggestions by Andersson *et al.*[71,77] and by Rendek *et al.*,[199] respectively. Similar to our findings for the F 1s and the Li 1s peaks, the intensity of the (Li-containing) decomposition products is higher on the DMC-cycled sample than for the EC-cycled one, as indicated by the higher intensity of the peak at 288.0 eV. Interestingly, there is no indication of a (semi-)carbonate (H_3COCO_2Li (lithium methyl carbonate) / $(H_2COCO_2Li)_2$ (lithium ethylene dicarbonate)) signal, which should appear at about 290.1 eV.[68] This has previously been postulated as decomposition product in the SEI formed on graphite electrodes in carbonate-containing electrolytes based on *ex situ* XPS.[66,68,71,72,77,79] This discrepancy between our results and earlier findings can either be explained by structural effects, assuming that the basal HOPG plane leads to a passivation layer that contains less of the (semi-)carbonate species than obtained on structurally ill-defined graphite electrodes, and/or by rinsing effects: if the carbonates are sensitive to the rinsing procedure, the rinsing agent may dissolve them, leaving behind insoluble, inorganic salts such as LiF.[148,192] In preliminary measurements on (defect-rich) graphite powder electrodes and after a similar rinsing procedure, we indeed found (semi-)carbonate species in the SEI, pointing to structural effects. Furthermore, also in the C 1s signal we find some additional intensity at the high BE side of

the C 1s peak on the DMC-cycled sample, which has not been accounted for so far and which, as discussed before, we relate to differential charging effects.

Finally, we move to the **O 1s** region. Based on the C 1s spectrum, two O 1s signals, related to C–O–C (polymer / ether) and C–O–Li (alkoxide) species, must be used for the peak fit in this region (FWHM 2.0 eV). Assuming a C : O ratio of 2 : 1 and 1 : 1 for these species, respectively, we calculate the signal peak areas in the O 1s spectrum from the corresponding peaks in the C 1s spectrum and fit the signals at the literature BE values of 533.3 eV (C–O–C)[79] and 532.1 eV (C–O–Li).[199] As a result, there remains considerable O 1s intensity, which must de due to additional O-containing species that were not accounted for in the polymer / ether and alkoxide signals. This intensity is summarized by a peak around 530-532 eV (O_{res}). It may represent, e.g., organophosphate moieties, like the aforementioned $OP(OCH_3)_3$ and $R–(O–CH_2–CH_2)_n–OPO(OR)_2$ species. For HOPG|EC + $LiPF_6$ (at t=0) the O 1s signal is dominated by these species, while it only contributes about one third of the whole signal intensity for HOPG|DMC + $LiPF_6$ (see above). The C 1s intensity related to the organophosphate species would be expected in the range characteristic for adventitious carbon, and can thus not be distinguished from that species. The respective P 2p signal would be expected in the BE range of the $Li_xPF_yO_z$ species at 135.0 eV. Comparing the intensity in that peak with the O_{res} peak at 532 eV, we obtain stoichiometries of 3 : 1 and 1 : 1 for the O : P ratio in the samples cycled in EC- and DMC-based electrolyte at t=0, respectively. Comparing the samples cycled in different electrolytes, the relative amount of the ether and alkoxide species (at 533.3 and 532.1 eV) is higher in the DMC-cycled sample than on the EC-cycled electrode. It seems that electrolyte decomposition in EC-cycled HOPG substrates favors the formation of organophosphates, e.g., a combination of salt and solvent, while DMC-based SEIs are mainly composed of the ‘pure’ salt- and solvent-derived decomposition products.

Here it should be noted that the signals recorded on the DMC-cycled sample after six minutes of sputtering exhibit additional intensity at the low-energy side of the peaks, which has not been accounted for by the fitted peaks. Considering that this appears for all peaks, we attribute this to a differential charging of the sample. In contrast to the positive differential charging in the spectra recorded on the DMC-cycled electrodes at t=0, we now have a negative differential charging effect which results in a higher kinetic energy of the photoelectrons and hence in a contribution at lower BEs.

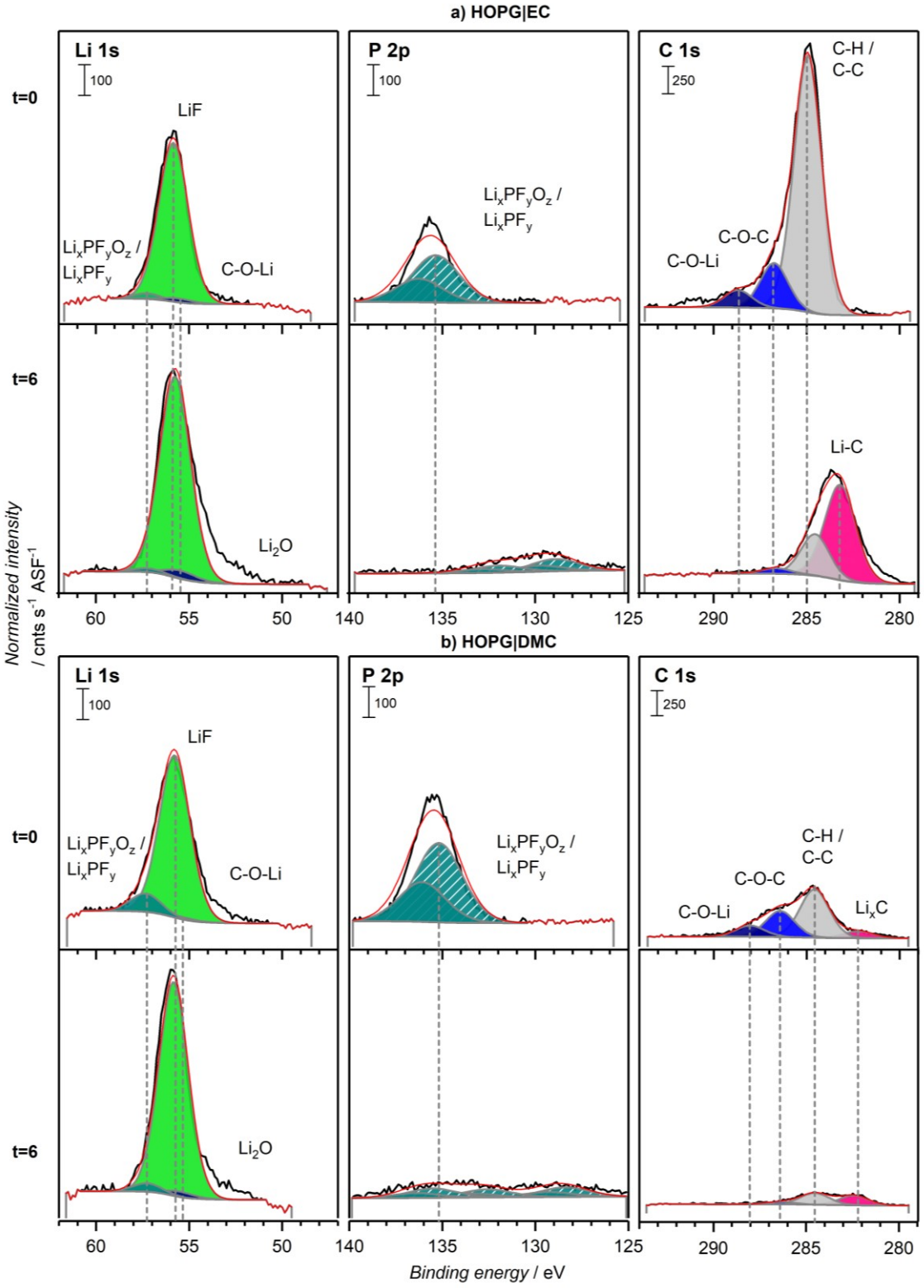

Figure S3-4. XP spectra (Li 1s, P 2p and C 1s binding energy regions) of the SEI formed on HOPG in a) EC- and b) DMC-based electrolyte upon cycling at 10 mV s^{-1}, measured on the as-prepared sample (t=0, top panel) and after six minutes of accumulated sputtering time (t=6, bottom panel).

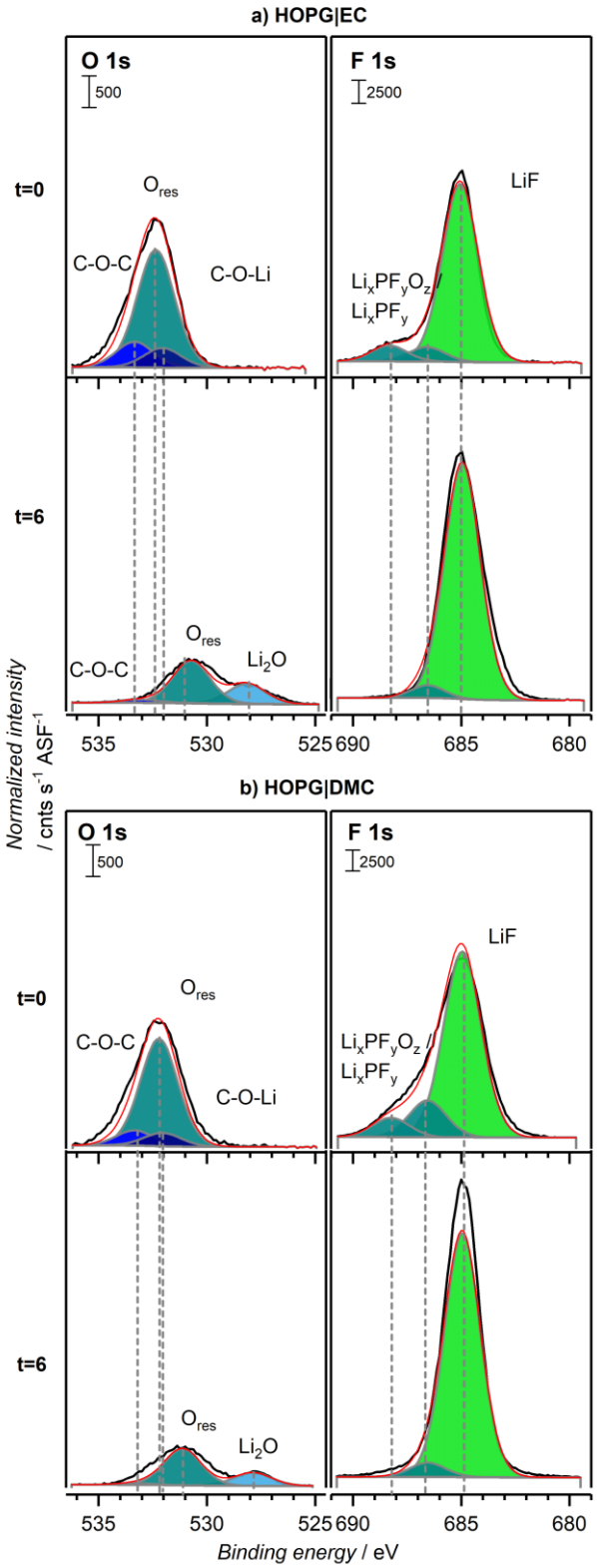

Figure S3-5. XP spectra (O 1s and F 1s binding energy regions) of the SEI formed on HOPG in a) EC- and b) DMC-based electrolyte upon cycling at 10 mV s^{-1}, measured on the as-prepared sample (t=0, top panel) and after six minutes of accumulated sputtering time (t=6, bottom panel).

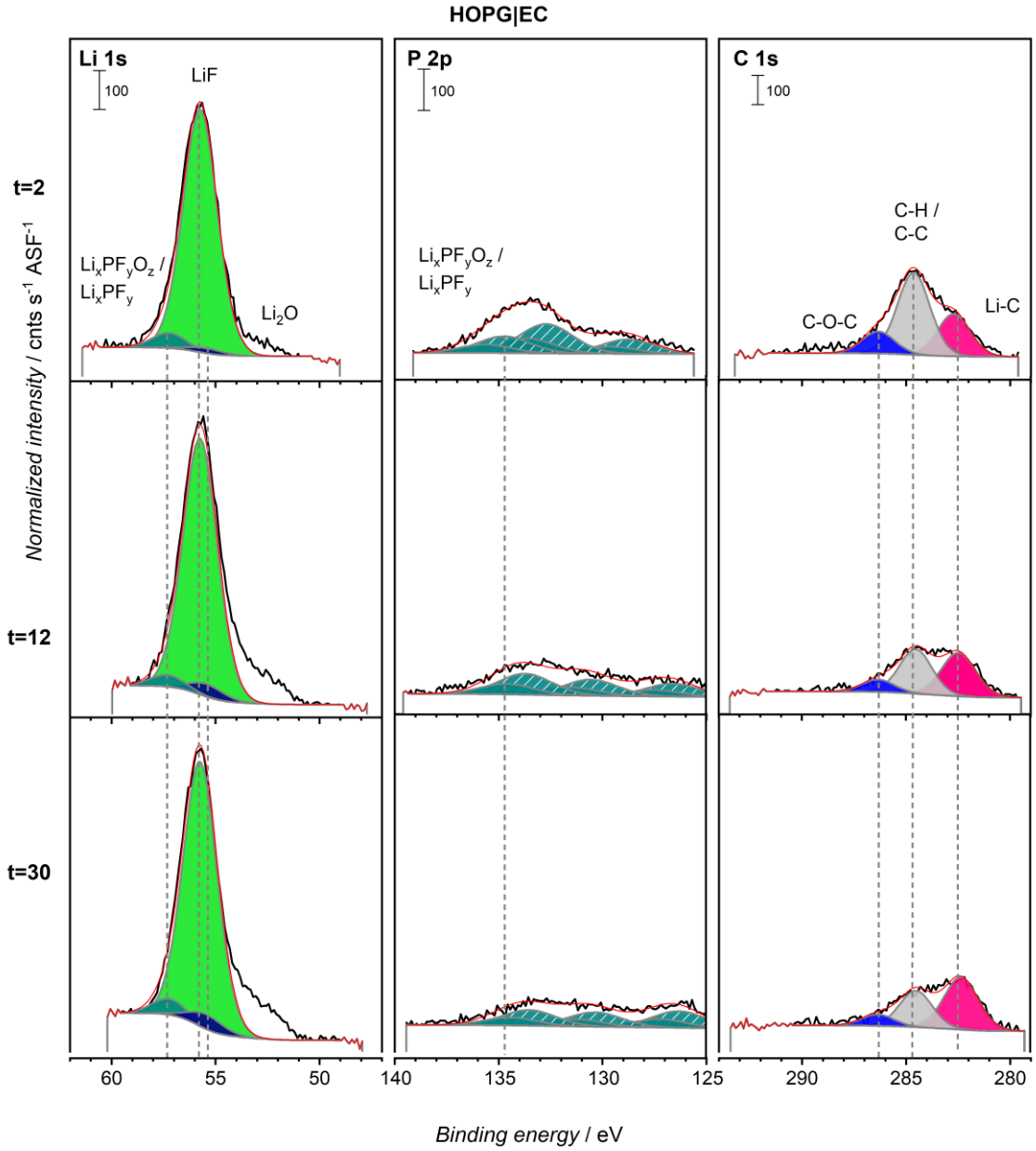

Figure S3-6. XP spectra (Li 1s, P 2p and C 1s binding energy regions) of the SEI formed on HOPG in EC-based electrolyte upon cycling at 0.1 mV s^{-1}, measured on the sample after two (t=2), 12 (t=12) and 30 (t=30) minutes of accumulated sputtering.

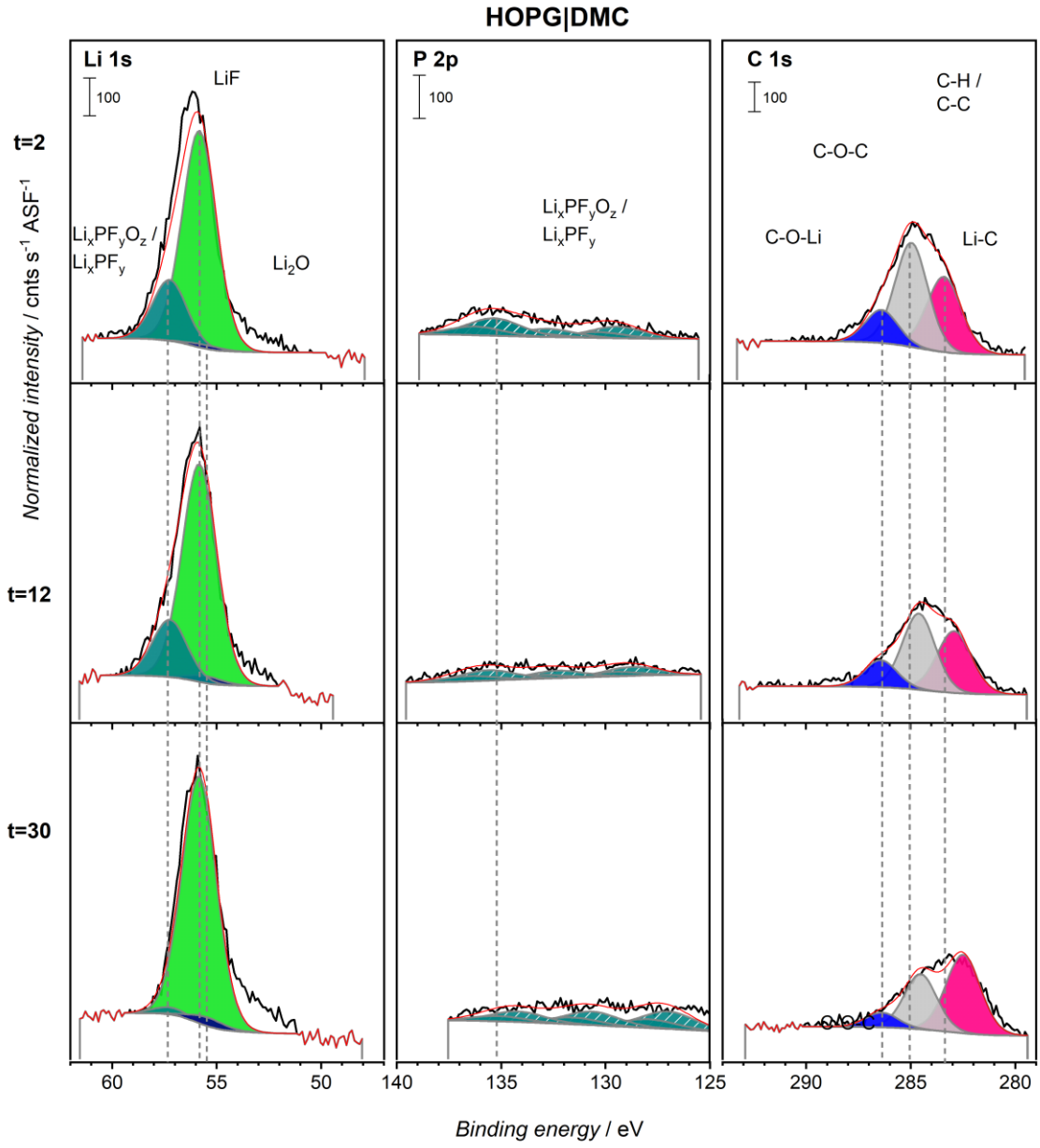

Figure S3-7. XP spectra (Li 1s, P 2p and C 1s binding energy regions) of the SEI formed on HOPG in DMC-based electrolyte upon cycling at 0.1 mV s^{-1}, measured on the sample after two (t=2), 12 (t=12) and 30 (t=30) minutes of accumulated sputtering.

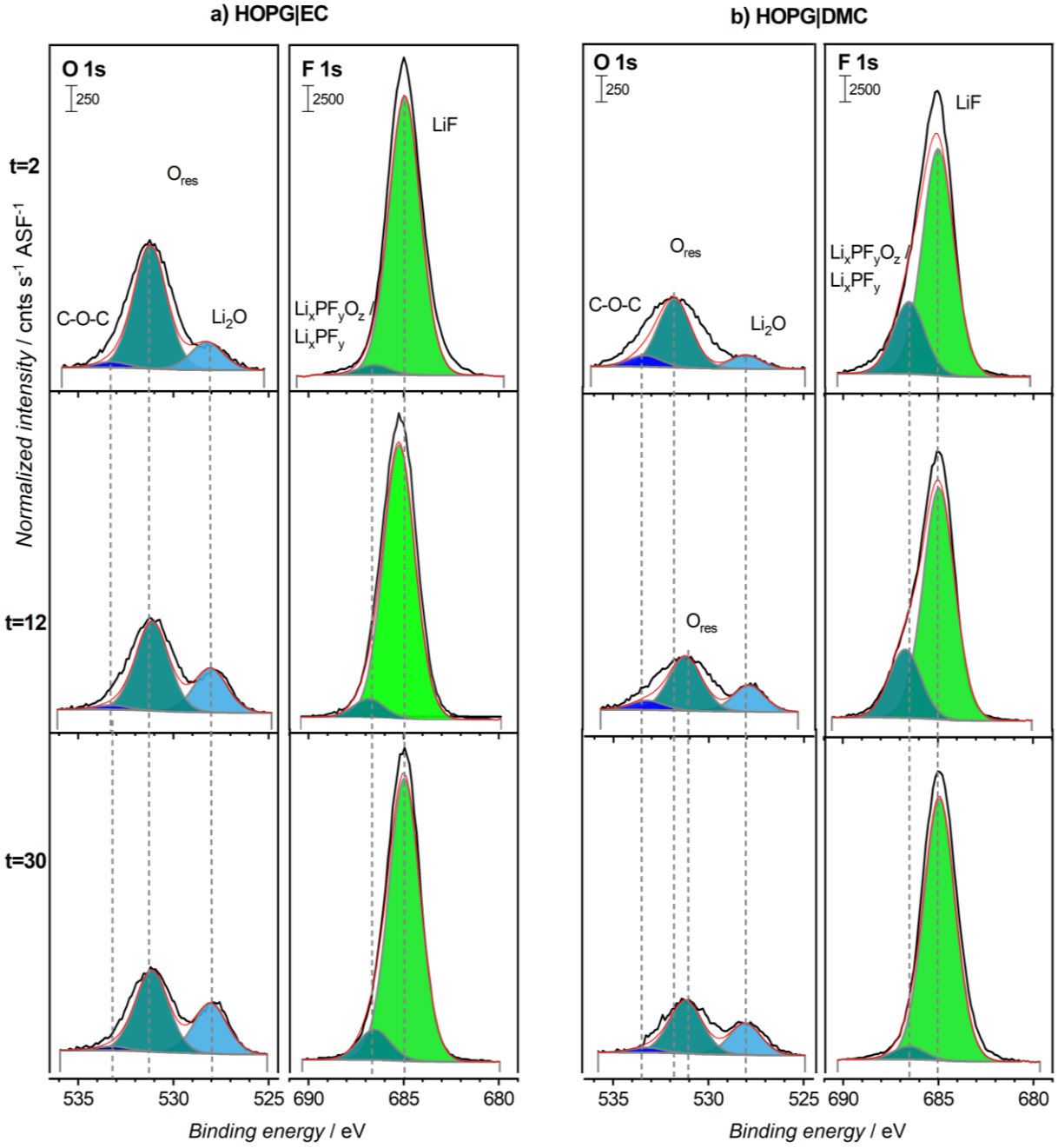

Figure S3-8. XP spectra (O 1s and F 1s binding energy regions) of the SEI formed on HOPG in a) EC- and b) DMC-based electrolyte upon cycling at 0.1 mV s^{-1}, measured on the sample after two (t=2), 12 (t=12) and 30 (t=30) minutes of accumulated sputtering.

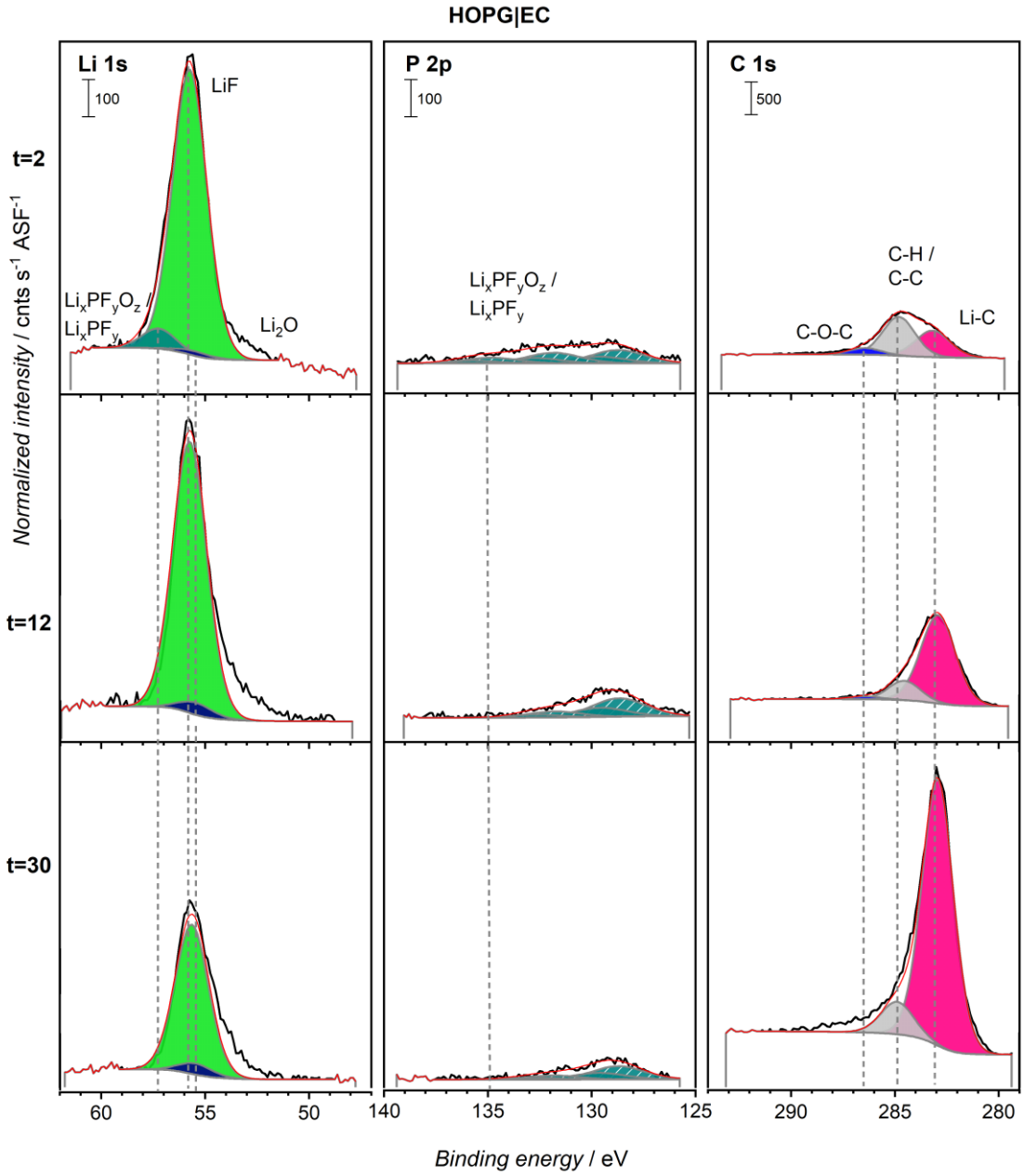

Figure S3-9. XP spectra (Li 1s, P 2p and C 1s binding energy regions) of the SEI formed on HOPG in EC-based electrolyte upon cycling at 10 mV s^{-1}, measured on the sample after two (t=2), 12 (t=12) and 30 (t=30) minutes of accumulated sputtering.

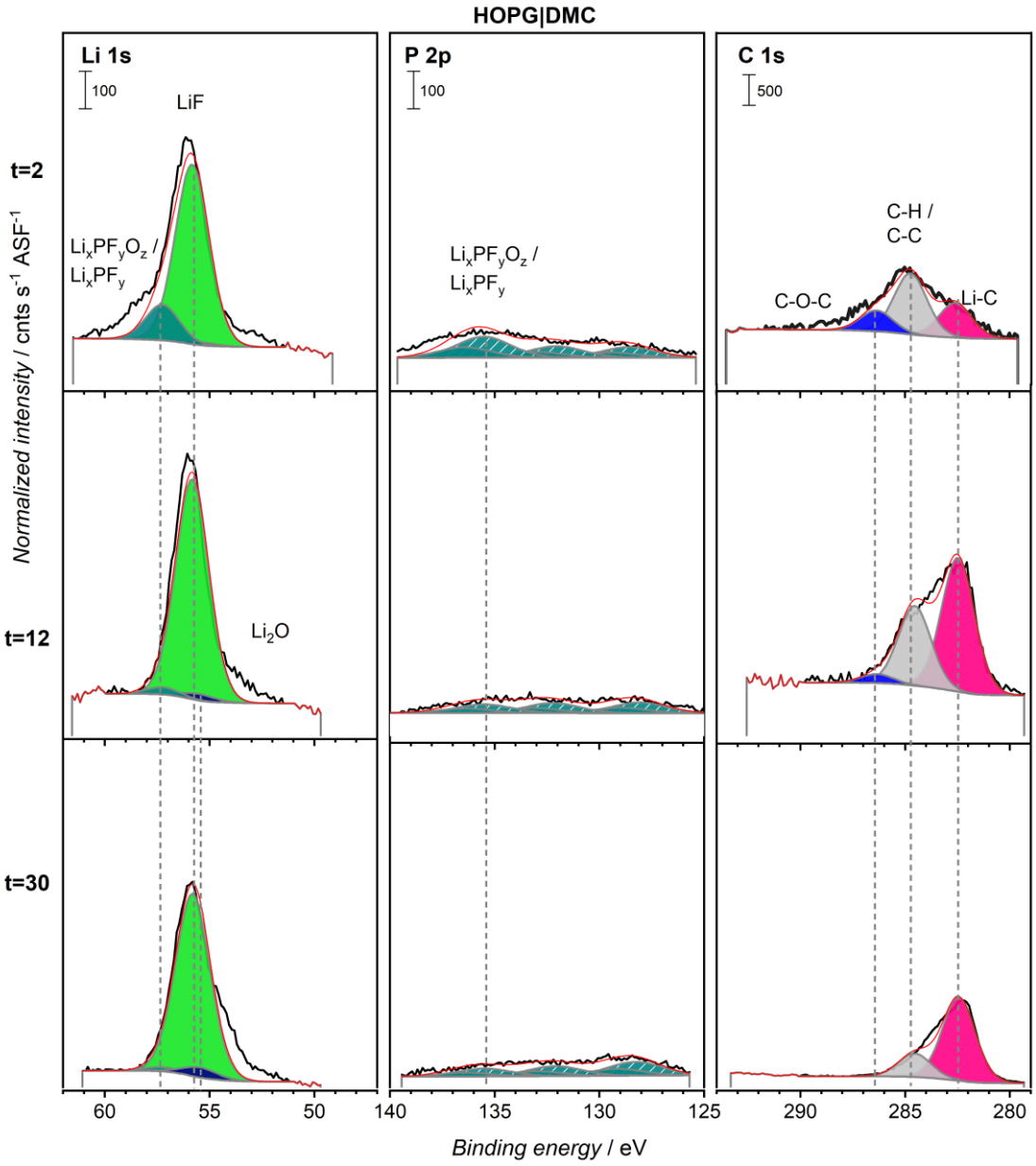

Figure S3-10. XP spectra (O 1s and F 1s binding energy regions) of the SEI formed on HOPG in DMC-based electrolyte upon cycling at 10 mV s^{-1}, measured on the sample after two (t=2), 12 (t=12) and 30 (t=30) minutes of accumulated sputtering.

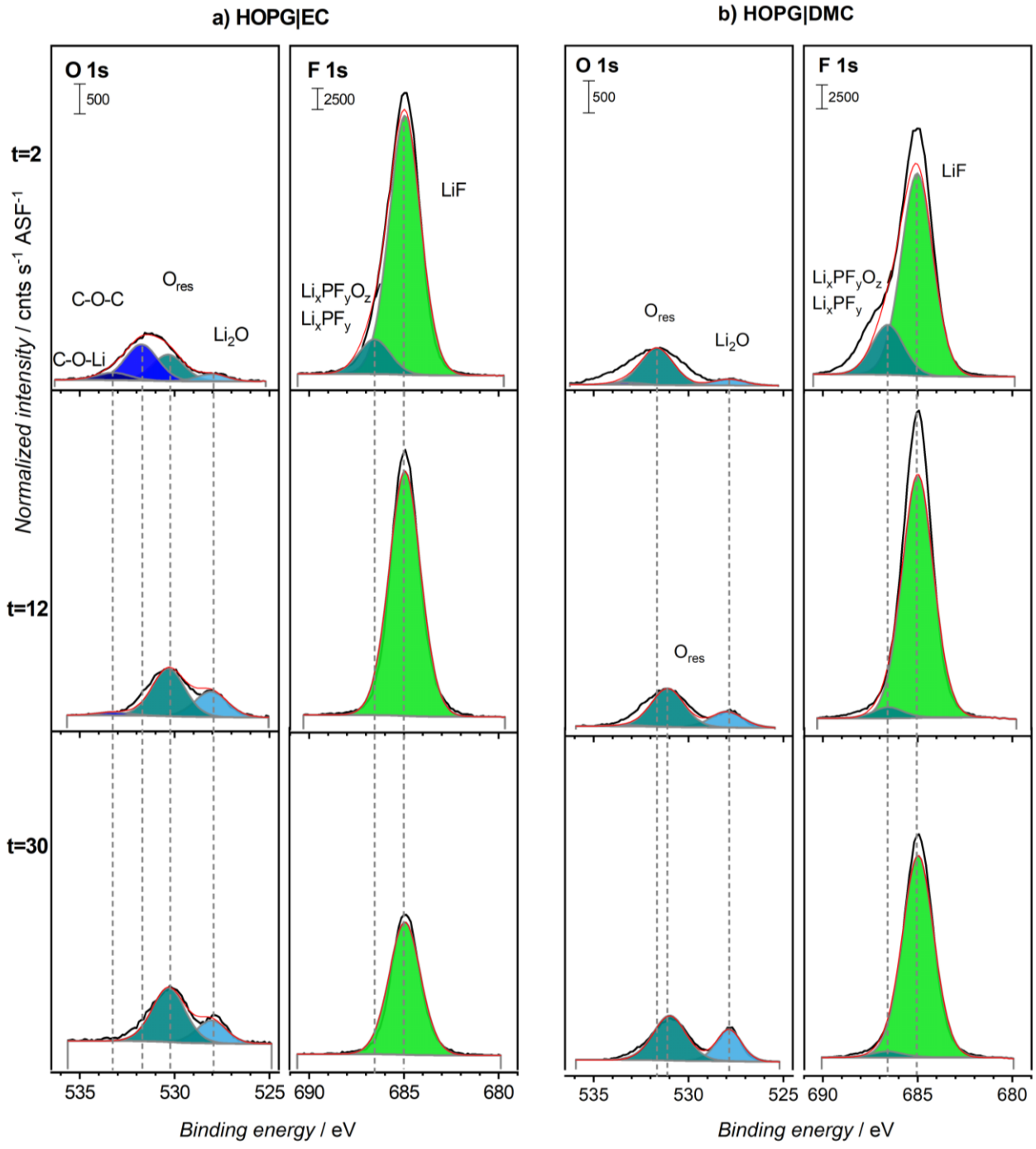

Figure S3-11. XP spectra (O 1s and F 1s binding energy regions) of the SEI formed on HOPG in a) EC- and b) DMC-based electrolyte upon cycling at 10 mV s^{-1}, measured on the sample after two (t=2), 12 (t=12) and 30 (t=30) minutes of accumulated sputtering.

Table S3-2. Atomic sensitivity factors for the individual elements detected in the SEI for the PHI 5800 Multi Technique ESCA System, Physical Electronics, as given by the manufacturer.

	Li 1s	P 2p	C 1s	O 1s	F 1s
Atomic sensitivity factors (ASF)	0.028	0.525	0.314	0.733	1.0

Table S3-3. Reference data used for the fitting of the XP spectra of HOPG in EC / DMC electrolyte.

	C 1s / eV	O 1s / eV	Li 1s / eV	F 1s / eV	P 2p / eV
C_{adv}	284.8 [147,159]				
EC ($C_2H_4OCO_2$)	**CO_3^{2-}:** 290.1 **C–C–O:** 287.1 [159]	**CO_3^{2-}:** 534.3 **C–O–C:** 532.6 [159]			
LiEDC ($CH_2OCO_2Li)_2$ [a]	**CO_3^{2-}:** 290.1 **CH_3:** 286.9 [79]	**C–O–C:** 533.5 **CO_3^{2-}:** 531.9 [79]			
Polymers (PEO)	285.5-286.5 [71,77]	532.5-533.5 [71,77]			
DMC ($C_2H_6OCO_2$) [b]	**CO_3^{2-}:** 294.3 **CH_3:** 290.0 [201]	**C–O–C:** 538.0 **CO_3^{2-}:** 533.5 [201]			
LiMC (CH_3OCO_2Li)	**CO_3^{2-}:** 290.1 **CH_3:** 286.7 [79]	**C–O–C:** 533.3 **CO_3^{2-}:** 531.8 [79]	55.5 [79]		
MeOLi (CH_3OLi)	287.4 [199]	532.1 [199]	55.0 [158]		
$LiPF_6$ (pure salt) [c]			58.2 [200]	687.9 [200]	138.2 [200]
LiF			56.0 [147]	685.0 [147]	
Li_xPF_y			56-57 [197]	687-688 [197]	136.5 [197]
$Li_xPF_yO_z$				688.5 [198]	134.8 [198]
Li_2CO_3	290.1 [79]	531.8 [79]	55.5 [79]		
Li_2O		528.3 [85]	53.7 [85]		
Li_xC	282.1 [150]				

[a] Values indistinguishable from H_3COCO_2Li

[b] Binding energies not corrected for sample charging, shift of ~Δ4 eV

[c] Values correspond to the maximum of the $2p_{3/2}$ signal.

4. Model Studies on the Solid Electrolyte Interphase Formation on Graphite Electrodes in Ethylene Carbonate and Dimethyl Carbonate II: Graphite Powder Electrodes

The content of the next chapter, including the graphical abstract (Figure 4-0), was published in ChemElectroChem 2020, volume 7 pp. 4794-4809, and is reprinted here with permission from John Wiley and Sons.[202]

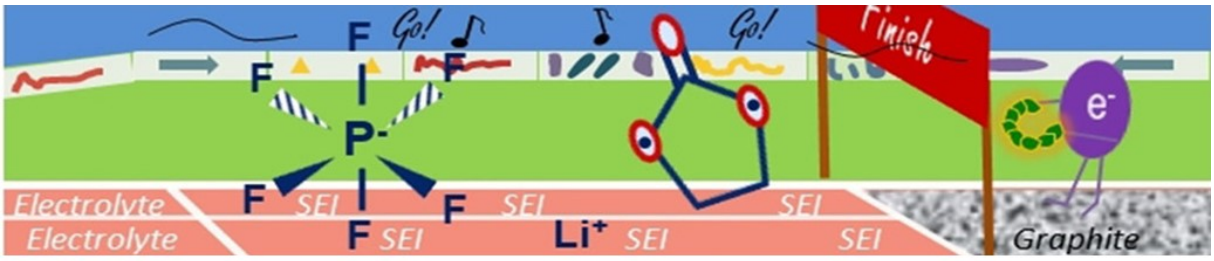

Need for speed:

Based on cyclic voltammetry and depth-profile XPS measurements of solid electrolyte interphase (SEI) formation in simplified, ethylene carbonate and $LiPF_6$-based electrolytes on binder-free graphite powder film electrodes at different potential scan rates, we propose that SEI formation occurs at the electrode surface and that the chemical composition of the SEI is governed by the chemistry of the electrode and by the diffusion rate of the solvent and the Li salt species through the growing SEI layer.

Figure 4–0. Graphical abstract.

The contents of the experimental part of the following manuscript are part of Chapter 2.2.3 of this thesis. The style, spelling, sections, enumeration, references and figures were adapted to fit the current layout, and the content of the supporting information was added at the end of the chapter.

Electrochemical measurements in this chapter were conducted by B. Wang (Institute of Surface Chemistry and Catalysis, Ulm University) and by M. Chakraborty (Institute of Surface Chemistry and Catalysis, Ulm University) in the course of their Master Theses, by C. Bodirsky (Institute of Surface Chemistry and Catalysis, Ulm University) in the course of her Bachelor Thesis and by myself. Dr. T. Diemant (Institute of Surface Chemistry and Catalysis, Ulm University) conducted the *ex situ* XPS experiments while Dr. M. Eckardt (Institute of Surface Chemistry and Catalysis, Ulm University) recorded the TEM micrographs. Our partners from Zentrum für Sonnenenergie- und Wasserstoff-Forschung (ZSW) Ulm, Dr. M. Wachtler,

Dr. M. Rapp and J. Martin, are to thank for providing the graphite materials, the binder-containing graphite powder electrodes and the helpful discussions. AMG Kropfmühl (Hauzenberg, Germany) provided the natural graphite raw material that was used for the synthesis of the SNG material. I evaluated the experimental data and was heavily involved in the creative process of the publication.

Financial supported was granted by the German Federal Ministry of Education and Research (BMBF) in the project 03X4636 C ("Li-EcoSafe – Entwicklung kostengünstiger und sicherer Lithium-Ionen-Batterien"). This work contributes to the research performed at CELEST (Center for Electrochemical Energy Storage Ulm-Karlsruhe).

4.1. Abstract

As part of a systematic study on the formation and composition of the solid electrolyte interphase (SEI) in lithium-ion batteries (LIBs), going stepwise from highly idealized electrodes such as highly oriented pyrolytic graphite and conditions such as ultrahigh vacuum conditions to more realistic materials and reaction conditions, we investigated the decomposition of simplified electrolytes (ethylene carbonate (EC) + 1 M $LiPF_6$ and dimethyl carbonate (DMC) + 1 M $LiPF_6$) at binder-free graphite powder model electrodes. The results obtained from cyclic voltammetry and *ex situ* X-ray photoelectron spectroscopy half-cell measurements – in particular on the effect of cycling rate, solvent and electrode – are explained in terms of a mechanistic model where electrolyte decomposition occurs at the SEI|electrode interface and where transport of solvent and salt species through the growing SEI plays an important role for explaining the observed change from preferential salt decomposition to solvent decomposition with increasing cycling rate.

4.2. Introduction

Lithium-ion batteries (LIBs) are by now well-established in portable communication devices[7,15] and also increasingly important as power sources for automotive applications.[17,19] Typically, they consist of electrode materials capable of inserting and de-inserting Li cations[11,13,186,203] and blends of Li salt-containing carbonate solvents[21,22,65] and additives[74] as electrolyte. During the first charge / discharge cycles, the thermodynamically unstable electrolyte decomposes at the anode, forming a passivating interphase. This is commonly denoted as solid electrolyte interphase (SEI),[49] which allows for continuous Li^+ diffusion and (de-)insertion while, at the same time, passivating the electrode surface against further electrolyte decomposition and thus protecting the battery from electrolyte depletion and

electrode corrosion. The SEI is composed of a mixture of salt and solvent decomposition products depending on the solvent,[64,68] salt[82,200] and possible additives,[74,204,205] but also on the nature of the electrode material.[59,61,63,66,69,191,206] It is known to decisively affect the battery performance,[51,54,55,189,207] which is why its formation and composition have been investigated for decades. Nevertheless, a detailed understanding of the SEI formation mechanisms is still missing, mainly due to the complex situation in realistic LIBs which include electrode materials, electrolyte and reaction conditions. We thus started an extensive study of the SEI formation process, employing materials with reduced complexity such as structurally well-defined highly-oriented pyrolytic graphite (HOPG) as model systems[159,185] and simplified reaction conditions such as ultrahigh vacuum conditions[159] or electrochemical measurements in single-solvent model electrolytes.[185] In the present work, we extended this to a more realistic situation, studying the SEI formation at two different binder-free graphite powder film electrodes in 1 M $LiPF_6$-containing single-solvent electrolytes, either ethylene carbonate (EC) or dimethyl carbonate (DMC), which are components of the commonly used battery electrolyte LP30 (1 M $LiPF_6$ + EC/DMC, 1 : 1 v/v). Two types of graphite were studied: the first one, MAGE, is an artificial graphite produced by Hitachi Chemical Co., Ltd. which is used as anode material in high-energy LIBs. The second anode material investigated in this work, SNG, is prepared from natural graphite flakes using a lab-type mechanical spheroidization process.[163,165] For comparison, we also characterized the SEI formation on the binder-free and binder-containing graphite powder film electrodes in LP30 electrolyte.

SEI formation was first characterized by cyclic voltammetry measurements, following the current evolution upon repeated potential cycling. Analysis of the chemical surface composition was conducted by X-ray photoelectron spectroscopy (XPS). In addition, depth profiling gained information also on the variation of the elemental SEI composition with increasing depth. Finally, we will compare the present results with our previous findings obtained on HOPG model electrodes in single-solvent electrolytes.[185]

Before presenting and discussing the results, we will briefly summarize previous studies and conclusions relevant for the understanding of our data. Numerous electrochemical studies employed HOPG as a model electrode with a low defect site density to investigate the formation and composition of the SEI under structurally well-defined conditions.[56,59,68,70,76,155,158,192,205,208,209] The results indicated a very low Li^+ intercalation capacity and the slow and inhomogeneous formation of a passivation film at the basal plane,

which was proposed to be dominated by solvent decomposition.[56,59,158] The edge plane, on the other hand, was shown to be active both for preferential salt decomposition[56,59,158] and for Li^+ (de-)intercalation.[209,210] Several studies reported exfoliation of the HOPG electrode, most likely induced by solvent co-intercalation (especially in DMC[64,185]). Individual, HOPG-supported graphite particles, which were studied by electrochemical atomic force microscopy, displayed an enhanced SEI formation activity and a better cell performance, which was attributed to the higher concentration of defect sites.[205] This is in line with our observations of the significant influence of the HOPG surface roughness on the SEI formation process.[185] Finally, the influence of the individual electrolyte components was investigated in further model studies using single-solvent electrolytes[64,185,190,192] instead of the typical carbonate solvent blends.

Moving on to more realistic, but still simplified, electrodes, Lucht and coworkers prepared binder-free graphite electrodes (SFG-6, TIMCAL) by electrophoretic deposition to investigate the composition of the SEI formed in $LiPF_6$-containing electrolyte[211] and in several other Li-salt-containing electrolyte blends.[198] Nie *et al.* studied the solvent – salt interactions in $LiPF_6$-based single-solvent electrolytes and observed a distinct influence of the salt concentration on the electrochemical performance of the binder-free graphite electrodes.[67] Employing different spectroscopic techniques, they identified the semicarbonate Li ethylene dicarbonate and Li alkoxides as the main products of ethylene carbonate reduction and LiF as the dominant reduction product of $LiPF_6$ decomposition.[66] Novák *et al.* investigated the influence of surface defects on the SEI formation by modifying the structural order of the graphite (TIMREX SLX50, TIMCAL) surface via (reactive) annealing in different gases (Ar, He, H_2).[212,213] Using binder-containing graphite electrodes without additional conductive carbon, they showed that the electrolyte decomposition and thus the formation of a passivating SEI is shifted to higher potential by a high concentration of surface defects and increasingly hinders exfoliation of the graphite.[212,213]

Overall, this work strives at a more detailed understanding of the various structural and chemical effects on the SEI formation process and the composition of the resulting passivation layer in Li-ion batteries.

4.3. Results and Discussion

Both graphite materials, the artificial graphite MAGE and the processed natural graphite SNG, consist of irregular particles (with rounded edges for SNG, a result of the spheroidization process) and a highly graphitized inner structure. MAGE has an average d_{50} particle size of 24.4 µm, a specific surface area of 3.5 $m^2\ g^{-1}$ and a reversible capacity of 365 mAh g^{-1}.[162] For SNG, the corresponding values are a d_{50} particle size of 12.8 µm, a specific surface area (via N_2 sorption) of 8.6 $m^2\ g^{-1}$ and a reversible capacity of 366 mAh g^{-1}.[163] Representative transmission electron microscopy (TEM) images are presented in **Figure S4-1** in the Supporting Information, section 4.5.1. Aside from the discrepancy in the average particle size, there are no significant differences in morphology of the graphite materials.

Thin films of these graphite powders were deposited on a glassy carbon (GC) electrode (see section 2.2.3 in this work).

4.3.1. Electrochemical Electrolyte Decomposition and SEI Formation

4.3.1.1. Influence of the Active Material and Solvent

Cyclic voltammograms (CVs) of the two graphite materials recorded in single-solvent EC- and DMC-based electrolytes at 0.1 mV s^{-1} are displayed in **Figure 4-1**. While the nature of the electrode material has only little effect on the current densities, these are tenfold lower in DMC- than in EC-based electrolyte. A reduction peak (c_e) appears at 0.7 V in the cathodic scan of the first cycle both for the MAGE and the SNG electrode in EC-based electrolyte. In accordance with previous findings,[64] and also with results of our own model studies on HOPG,[185] we assign this peak to reductive electrolyte decomposition and subsequent formation of a solid electrolyte interphase (SEI). Note that, at this point, we cannot distinguish between predominant solvent decomposition and predominant salt decomposition, which will be discussed in more detail later. In DMC-based electrolyte, the first peak in the negative-going scan (c_c) of the CVs is observed at 0.8 V on MAGE and at 1.4/1.0 V on SNG, while a second set of signals (c_e) appears at 0.3 and 0.4 V, respectively. The higher-potential peaks observed in the DMC-based CVs at 0.8 V (1.4/1.0 V) on MAGE (SNG) film electrodes are most likely due to reductive processes involving residual H_2O (EC: ≤50 ppm, DMC: ≤20 ppm, glove box: <1.0 ppm) or O_2 traces, but have also been attributed to $LiPF_6$ reduction previously.[68,70] We think that the presence of H_2O/O_2 trace contaminations is more likely than $LiPF_6$ reduction. It also explains the comparatively high cathodic current densities recorded between the upper potential limit and 0.5 V in DMC-based electrolyte. Next, electrolyte decomposition (c_e) takes

place at 0.3/0.4 V, in agreement with previous reports.[64,185] Note that the onset potentials for electrolyte reduction follow a similar trend as observed in our previous experiments on HOPG electrodes cycled under the same conditions, with higher onset potentials for EC-based electrolyte.[185]

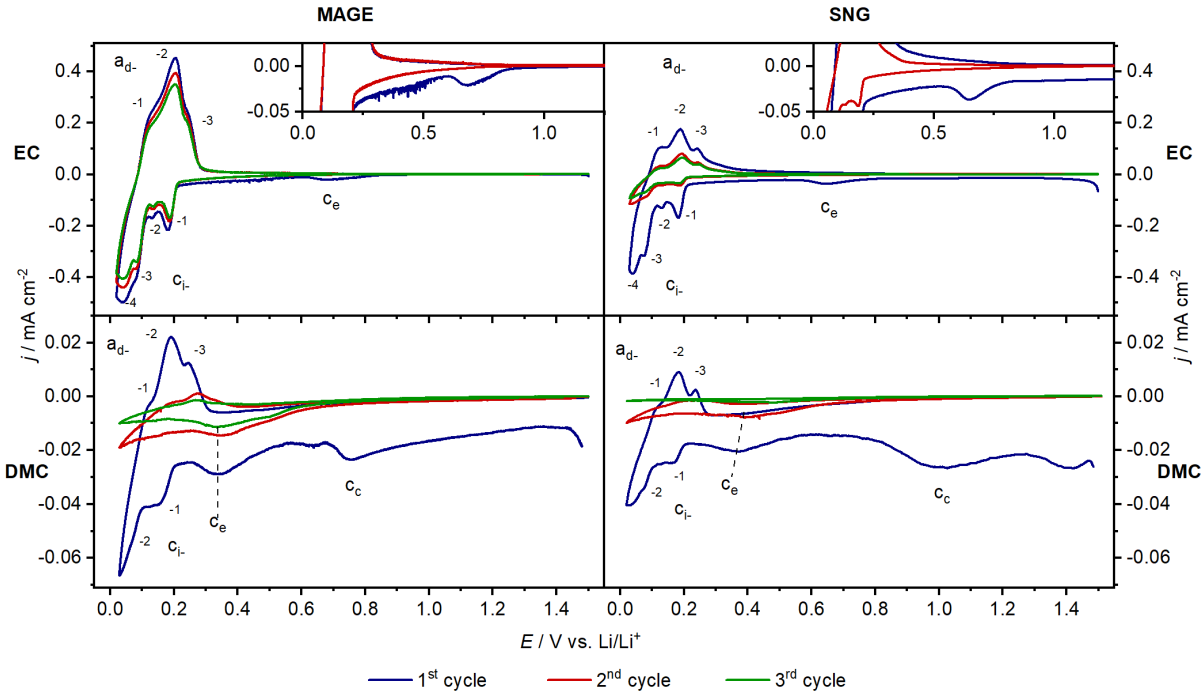

Figure 4-1. Cyclic voltammograms recorded on binder-free MAGE (left) and SNG (right) powder film electrodes in EC (top) and DMC (bottom) +1 M $LiPF_6$ at a scan rate of 0.1 mV s^{-1}. The insets display the current at tenfold magnified scale.

After electrolyte decomposition, stepwise Li^+ intercalation sets in at around 0.2 eV, in accordance with previous findings.[11] Three sharp peaks (c_{i1}, c_{i2}, c_{i4}) appear at 0.2, 0.1 and 0.05 V for both MAGE and SNG cycled in EC-based electrolyte, where the peak at 0.05 V (c_{i4}) is preceded by a small shoulder at 0.08 V (c_{i3}). Cycling in DMC-based electrolyte, however, we only observed two intercalation steps with lower and broader signals at 0.2 and 0.07 V (c_{i1} and c_{i2}, respectively) for both graphite electrodes. The lower resolution of the Li^+ intercalation peaks and the overall lower current densities observed for DMC-based electrolyte (as compared to the EC-based one) most likely indicate that the graphite material has been at least partially exfoliated as a result of solvent co-intercalation occurring between 0.6 and 0.2 mV.

In the anodic scan of the first cycle, Li^+ de-intercalation peaks (a_{d1}-a_{d3}) are observed at potentials of 0.1, 0.2 and 0.25 V, both for EC-based and for DMC-based electrolyte. Interestingly, the current traces in the (de-)intercalation potential range are similar for the two

electrode materials, but differ for the two solvents. Hence, the influence of the graphite material is less pronounced compared to the influence of the solvent. For both the MAGE and the SNG electrodes, there are no distinct peaks at higher potentials. When cycling in EC-based electrolyte, small anodic currents remain directly after Li^+ de-intercalation, while for DMC-based electrolyte, cathodic currents are observed in this potential range, indicating continuous reduction processes at the graphite|electrolyte interface. These are probably a result of exfoliation of the graphite, creating new surfaces which are overgrown by an SEI film. Net cathodic currents during Li^+ de-intercalation were reported also by Nie *et al.* on binder-free graphite electrodes in propylene carbonate (PC) + 2.4 M $LiPF_6$ (0.05 mV s^{-1}).[66] Interestingly, we obtained a similar behavior of the CVs recorded both for the MAGE and SNG electrodes in DMC-based electrolyte as reported by Nie *et al.* at faster scan rates (see **Figure S4-2** and discussion in the following section). In the study of Nie *et al.*, the overall currents observed during and after Li^+ de-intercalation were found to be cathodic at lower salt concentration, while at higher concentration, net anodic currents were reported.[66] In our measurements, we found net anodic currents in DMC-based electrolyte for much lower salt concentrations, indicating that SEI formation in DMC-based electrolyte is more efficient in inhibiting electrolyte decomposition than SEI-formation in PC-based electrolyte, despite the occurring graphite exfoliation in the former electrolyte.

In the second cathodic scan in EC-based electrolyte we did not observe the electrolyte decomposition peak c_e at 0.7 V anymore, neither for the MAGE nor for the SNG electrode. Hence, the electrodes are completely passivated for this process, as expected for successful SEI formation. In DMC-based electrolyte, in contrast, we still observe reductive electrolyte decomposition at 0.3–0.4 V in the second (and third) cycle for both graphite electrodes, retaining about half (one third) of the current density observed in the first cycle. These ongoing reductive processes are most likely also responsible for the negative currents observed in the anodic scan. While the loss of Li^+ (de-)intercalation currents is negligible in the first three cycles for MAGE|EC, this is different for SNG|EC, where half of the Li^+ (de-)intercalation current is lost in the second cycle. In the third cycle, the loss is less pronounced. In DMC-based electrolyte, the current density for Li^+ (de-)intercalation drops by two third from the first to the second cycle and again by about half in the third cycle. We suggest that the decreasing Li^+ (de-)insertion capacity is at least in part due to exfoliation, which disrupts the graphite lattice and reduces the number of Li^+ storage sites. In addition, this is caused by both SEI formation and irreversible Li^+ intercalation, where the latter increasingly blocks sites for

reversible Li^+ intercalation ('irreversible specific charge'[11]). Alternatively, it could also be due to increasing kinetic limitations for thicker SEI layers, assuming that the SEI grows at the interface between SEI and electrode rather than between SEI and electrolyte (see below), or due to a loss of active material from the model electrodes due to the lack of binder. This will be discussed in more detail at the end of the paper.

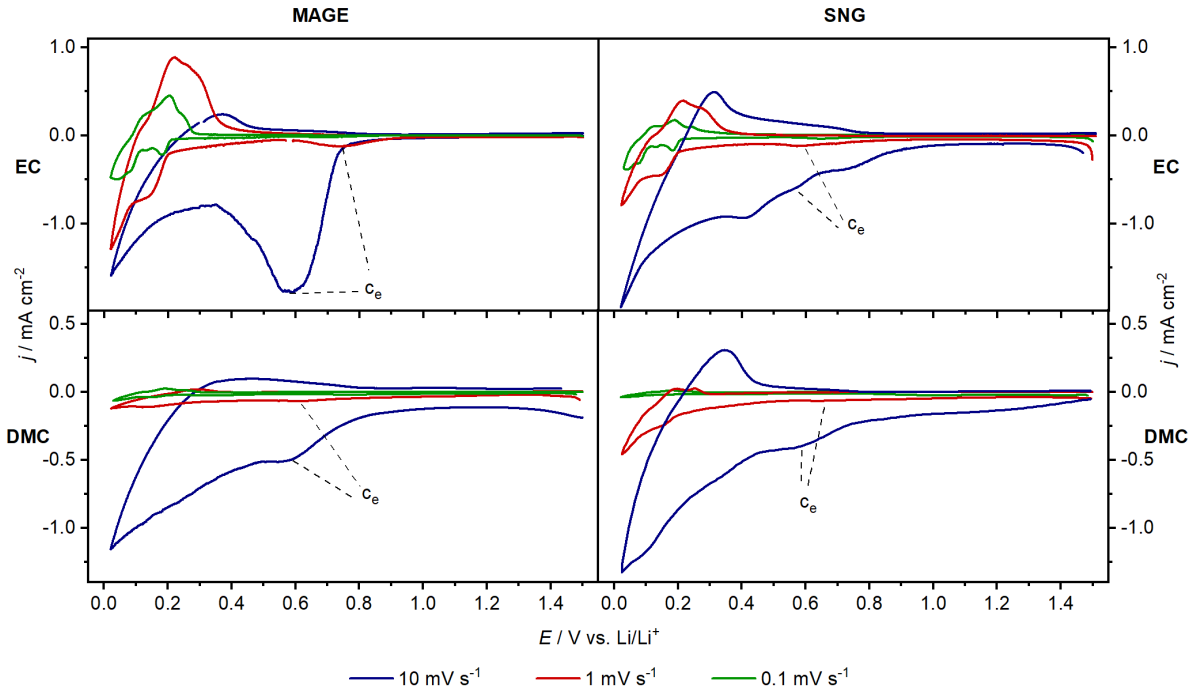

Figure 4-2: First cycle of the cyclic voltammograms of MAGE (left) and SNG (right) powder film electrodes cycled in EC- (top) and DMC-based (bottom) electrolyte at different scan rates (10, 1 and 0.1 mV s^{-1}).

Finally, for both electrodes, the individual peaks denoting stepwise intercalation disappear after the first cycle in DMC-based electrolyte and only a broad (de-)intercalation signal remains instead. Most simply, this can be explained by continued graphite exfoliation and by the formation of an inhomogeneous SEI with local differences in the Li^+ transport properties.

4.3.1.2. Influence of the Scan Rate

Figure 4-2 shows the influence of different scan rates (10, 1, and 0.1 mV s^{-1}), simulating different charge/discharge rates, on the characteristics of the first cycle recorded on MAGE and SNG in EC- and DMC-based electrolyte (for more cycles, see **Figure S4-2** in section 4.5.2). The CVs recorded at 0.1 mV s^{-1} were described above. The CVs cycled at 1 and 10 mV s^{-1} display essentially the same characteristics, albeit with shifted peak potentials and broadened peaks due to the increase in scan speed, both for electrolyte decomposition (c_e) and Li^+

(de-)intercalation. At the same time, the overall current densities increase with increasing cycling speed. This is especially pronounced for the graphite materials in DMC-based electrolyte cycled at 10 mV s^{-1}, where the current density in the Li^+ (de-)intercalation region is of the same order of magnitude as that recorded for the graphite materials during cycling in EC-based electrolyte (C|EC). Note that, as described above, the current density for the graphite powder electrodes in DMC-based electrolyte (C|DMC) is only about one tenth compared to that for C|EC when cycling at 0.1 mV s^{-1}. We suggest that this discrepancy is due to a rather slow passivating process in DMC-based electrolyte, where only at slow scan rates this has enough time for efficient passivation despite the graphite exfoliation, leading to lower current densities. For cycling at 10 mV s^{-1}, in contrast, the time is too short and the scan reaches the Li^+ intercalation region before the surface is significantly passivated against this process. It is also worth mentioning that, for cycling at 1 and 10 mV s^{-1}, the peak potentials for electrolyte decomposition (0.6 V) are very similar in both EC- and DMC-based electrolyte, whereas at 0.1 mV s^{-1}, the respective peaks appear at rather different potentials (0.7 V (EC) and 0.3–0.4 V (DMC), respectively). This is true for both MAGE and SNG electrodes. Obviously, with increasing scan rate, the peak at 0.3–0.4 V disappears, while a new one at 0.6 V grows in (**Figure 4-2**). This would be compatible with two different processes, where the low-potential process is slow, and hence only observed at lower scan rates, while the upper one is fast(er), but can proceed only on the surface area not yet modified by SEI formation. As will be discussed later when examining the SEI composition for EC-based electrolyte, the high-potential processes seem to be related to salt decomposition, while reductive solvent decomposition prevails at lower potentials. Considering the cycling stability, we find a significant loss of current density from the first to the second cycle for all electrode|electrolyte combinations and scan rates (**Figure S4-2**). This is both valid for the electrolyte decomposition peak and, to a lesser extent, also for the current density in the Li+ (de-)intercalation region. The relative loss in the (de-)intercalation region is, however, larger in the DMC-based than in the EC-based electrolyte, likely due to graphite exfoliation. For faster scan rates, we previously reported an activation effect for HOPG electrodes (increasing current densities with continued cycling before passivation sets in).[185] Based on the present data, this effect seems to be significant only for smooth, basal HOPG substrates where exfoliation may lead to surface roughening. It becomes less important or negligible with increasing defect density of the surface, or when going to powder graphite materials.

Aside from passivating the graphite surface against further electrolyte decomposition, the SEI increasingly modifies Li^+ (de-)intercalation: with continued cycling, the characteristic stepwise Li^+ (de-)intercalation peaks are less resolved. This trend is more pronounced for i) DMC-based than for EC-based electrolyte, and ii) for the samples cycled at fast scan rate (where the peaks are hardly visible even in the first cycle) than for the ones cycled at slow scan rate. The stronger effect in DMC-based single-solvent electrolyte is again attributed to partial graphite exfoliation. The loss in overall current density in the Li^+ (de-)intercalation region upon continued cycling may result either from decreasing Li^+ (de-)intercalation and/or from decreasing electrolyte decomposition, where Li^+ (de-)intercalation at this stage is demonstrated by the respective peak in the anodic scan. Also this loss in current density is more pronounced when cycling in DMC-based electrolyte, due to the partial exfoliation of the graphite materials; and at slow scan rates. In the latter case there is more time for both electrolyte decomposition and graphite exfoliation, leading to a more pronounced loss in current density.

4.3.1.3. Influence of the Binder

Finally, we also tested the influence of the binder on the electrochemical characteristics of the MAGE and SNG graphite powder film electrodes, using polyvinylidene difluoride (PVDF)-containing electrodes coated onto a Cu foil (see Chapter 2.2.3). Here, we compared the electrochemical characteristics of binder-free graphite powder film electrodes on GC and of PVDF-containing electrodes in commercial LP30 (EC/DMC 1 : 1 v/v + 1 M $LiPF_6$) electrolyte. The resulting voltammograms, as well as a detailed discussion of the results, are presented in the Supporting Information (section 4.5.2, **Figure S4-3** and **Figure S4-4**). Even when considering the different experimental parameters, they demonstrate that the electrochemical properties of graphite electrodes cycled in LP30 are dominated by the EC component, which leads to the formation of a cover layer that passivates against electrolyte decomposition and graphite exfoliation already in the first cycle, while Li^+ (de-)intercalation is still possible. Furthermore, the use of the PVDF binder in the graphite powder electrode has little effect on the formation of this SEI layer and on the Li^+ (de-)intercalation, except for an overall increase in current density.

4.3.2. Chemical Composition of the SEI – Ex Situ XPS Characterization

Next, we characterized the surface composition of the SEI by XPS to gain further information on the nature of the electrolyte decomposition products. We used depth profiling by Ar^+ ion sputtering to be sensitive not only to the decomposition products formed on the surface of the

SEI (sputter time t=0), i.e., at the SEI|electrolyte interface, but also to the SEI composition in deeper layers closer to the electrode. The SEI-covered electrode was sputtered for two, four, six and 18 minutes before recording XP spectra, resulting in total sputter times of two, six, 12 and 30 minutes (t=2, t=6, t=12 and t=30). Since the samples cycled in DMC-based electrolyte exhibited considerable differential charging effects – evident from broadened peak shapes and arbitrarily shifted binding energies – we will discuss only data obtained on MAGE and SNG electrodes cycled in EC-based electrolyte both at 0.1 and at 10 mV s^{-1}.

4.3.2.1. Depth-Dependent Elemental Composition of the SEI

Before discussing the spectra in detail, we will summarize the elemental composition (Li, C, O, F, and P) of the SEI layers formed on the MAGE and SNG electrodes at fast and slow scan rates (10 and 0.1 mV s^{-1}), which are derived from the respective signal intensities using the atomic sensitivity factors (ASFs, see section 4.5.3, **Table S4-1**) without any ambiguities arising from peak fitting and deconvolution processes. The evolution of the different elemental concentrations with increasing sputter times is illustrated schematically in **Figure 4-3**. Here, it should be noted that the electrolytes used in this study are the same as those employed in a previous study on HOPG electrodes,[185] which means that differences in SEI formation must be due to structural effects and cannot be caused by electrolyte impurity effects.

F shows concentrations of 8 and 14 at.% on the initial surface of the SEI formed at fast scan rate on the MAGE and SNG electrodes, respectively. Since the Li concentration (17 and 21 at.%) is significantly higher, this results in an excess of Li for these samples, as compared to the 1 : 1 ratio expected for LiF. The F content is significantly higher after slow cycling, with 30 (33) at.% for the MAGE (SNG) electrode, and the Li content is either slightly lower (MAGE) or identical (SNG) to the F content. For the SEI resulting upon slow cycling, the Li : F ratio already points to a large contribution of species with a 1 : 1 stoichiometric ratio of both elements, such as LiF (see below). After two minutes of sputtering, the atomic F concentration increases for both electrodes on the SEI obtained after fast cycling, followed by a continuous decrease for the remaining sputtering time. Finally, it reaches 6–8 at.% after 30 minutes sputtering for either of the two electrodes.

The atomic concentration of Li, albeit significantly higher than that of F, follows the trend of the F concentration, increasing between t=0 and t=2 and decreasing from there on. After 30 minutes, the concentration is around 14 at.% for both electrodes. At slow scan rates, the concentrations of Li and F remain more or less constant (around 30 at.%) for both the

electrodes throughout the entire sputtering time. The Li and F concentrations for the graphite powder electrodes cycled both at fast and at slow scan rate are lower than those obtained for the SEI formed on HOPG|EC,[185] where Li and F were the dominant elements also at fast scan rate, regardless of the electrolyte composition. At the same time, the depth variations for both elements and the close-to 1 : 1 ratio agree with the trends in the elemental composition of the SEI formed on basal HOPG.[185]

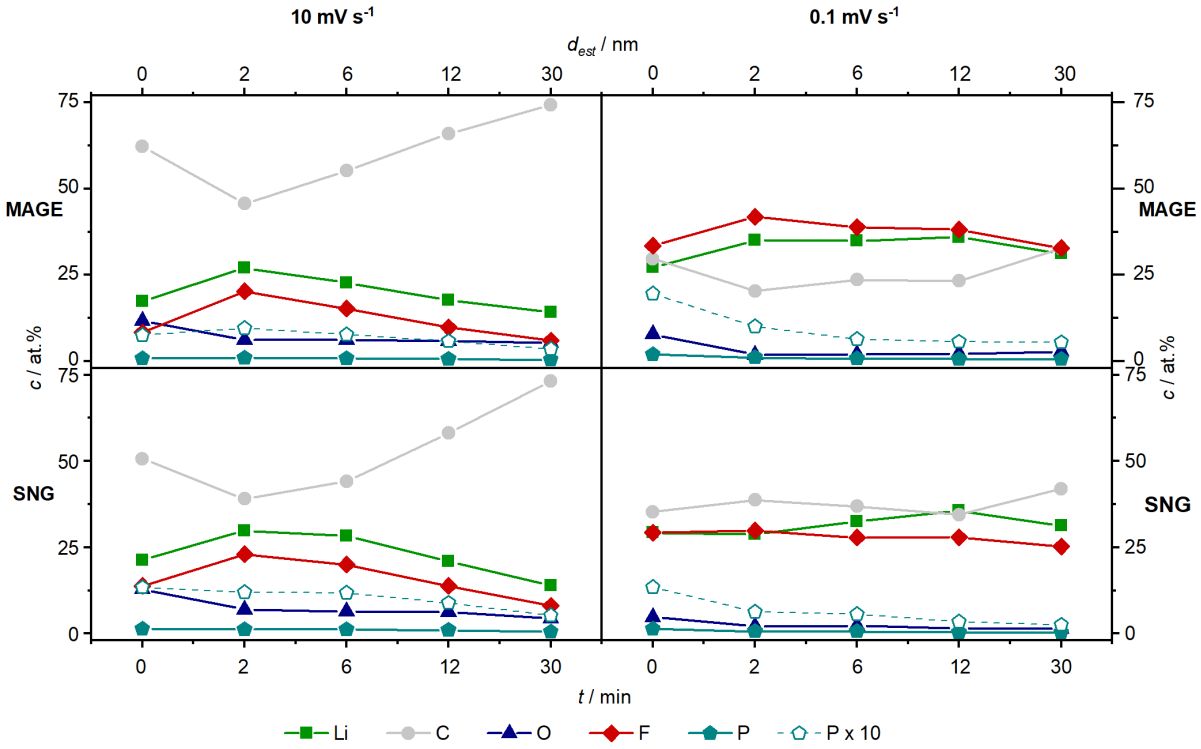

Figure 4-3: Depth profiles of the elemental composition of the SEI formed on MAGE (top) and SNG (bottom) film electrodes in EC-based electrolyte after cycling at scan rates of 10 (left) and 0.1 mV s^{-1} (right). An estimate of the thickness of the removed SEI layer (d_{est}), starting at the initial SEI surface, is given in the additional upper x-scale.

Focusing on the C concentration, the MAGE and SNG electrodes cycled at 10 mV s^{-1} exhibit high initial concentrations of 62 and 51 at.%, respectively, which is much more than on HOPG. Upon sputtering, the C content varies opposite to the trend observed for F and Li, with an initial decrease to 40–46 at.% after two minutes of sputtering, followed by an increase for longer sputtering times. The latter increase would be consistent with an SEI composition that is increasingly dominated by solvent decomposition products when going closer to the electrode surface. For the slow scan rate, the C concentration begins at 30–35 at.% for both electrodes, with a small (but still resolvable) initial decrease and subsequent increase for MAGE during sputtering and a more or less constant value for the SNG electrode. Again, this reflects the

trends in the Li and F concentrations on these electrodes. Hence, in this case salt decomposition products are dominant in the SEI range probed. A generally similar behavior, with an initial decrease in C concentration followed by an increase / constant value for longer sputter times, was reported for the SEI formed on HOPG electrodes during fast/slow cycling in EC-based electrolyte, albeit with significantly lower C concentrations.[185] The initial decrease in carbon concentration observed for all electrodes would be consistent with a thin, carbon-rich cover layer, which will be discussed in more detail later. Finally, we would like to note that the more or less pronounced increase in C concentration at the end of the sputtering phase may also indicate that the graphite substrate is reached, similar to our observations for SEI formation on HOPG.[185] We will demonstrate that this is not the case and that the increase in C concentration mainly results from a different carbon species in the following section.

O represents the second-smallest contribution to the elemental composition of the SEI, with an initial atomic concentration of about 12 at.% after fast cycling and a lower concentration of 5 and 8 at.% for SNG and MAGE, respectively after slow cycling. This mirrors the scan rate dependence observed for the C concentrations. After two minutes of sputtering, the O concentration decreases and then remains more or less constant for the remaining sputtering time for all electrode materials and scan rates. The lower concentration of O-containing species in the SEI for the samples cycled at lower scan rate, as compared to the values obtained for fast cycling, is in agreement with a preferential solvent decomposition process at fast scan rates, while salt decomposition is more dominant at slow scan rates. This will be discussed in more detail at the end of the next section. The initial decrease in O-content and its later about-constant value also agree with our previous observations for SEI formation on HOPG in the same electrolyte, though the initial oxygen concentration on the latter samples (7–8 at.% for both scan rates) was slightly lower (fast scan) or about equal (slow scan) than on the graphite powder electrodes.[185]

The smallest contribution, finally, comes from P-containing moieties, whose concentrations are in the range <2 at.% on both MAGE and SNG and at both scan rates. First of all, this reflects the low P concentration in the electrolyte (P : F in $LiPF_6$ 1 : 6). The observation of relative P concentrations well below the PF_6 stoichiometry points towards the formation of volatile or soluble P-containing moieties with lower F content during cycling, in addition to LiF formation, leaving P-richer species in the SEI. Based on the relative P 2p intensity, the overall concentration of P-containing moieties arising from salt decomposition is slightly higher on the

SEIs formed at 0.1 mV s^{-1} than on those generated at 10 mV s^{-1}, which agrees with the trends in the F- and O-/C-containing decomposition products. Upon sputtering, the P concentration decays further: for all samples, we find a continuous decrease upon sputtering, with a somewhat steeper initial decay at slow scan rates. For comparison, a steeper decay was observed for the SEI on HOPG electrodes for both scan rates.[185]

Our data seem to disagree with previous findings from the Peled group.[60,158] Similar to our observations for SEI formation on the present graphite electrodes cycled at fast scan rates, these authors determined C-containing, organic components from solvent decomposition as dominant species, but for the SEI formed on HOPG during charge / discharge in $LiAsF_6$-containing EC/DEC (diethyl carbonate) electrolyte. In addition, their result of dominant LiF formation on cross-sectional HOPG is rather similar to our previous findings on basal HOPG, where this prevailed independent of the scan rate.[158,185] As stated earlier, these discrepancies may well arise from the very different experimental conditions in our three-electrode half-cell, cyclic voltammetry measurements and in their charge / discharge two-electrode setup.[185] For instance, we also observe preferential LiF formation on the present graphite powder electrodes at slow scan rate, which would agree with their findings for cross-sectional graphite, i.e., for the more defective carbon materials. Furthermore, these authors also compared the SEI layer formed on so-called "soft" (graphite-like) and on "hard" (non-graphitized) carbon in $LiPF_6$-containing EC/DEC electrolyte during charge / discharge measurements. The elemental composition profiles reported by them on the graphite-like carbon are rather close to our present results on the graphite electrodes, except for slightly higher F and slightly lower Li concentrations.[60]

Overall, our data point to an SEI formation mechanism where salt decomposition is favored at slower scan rates, resulting in higher concentrations of F-containing species (e. g., LiF) within the SEI, while solvent decomposition with predominantly organic, C-containing products is the dominant process at fast scan rates (see also next section). This is different from SEI formation on HOPG in identical electrolytes, where the effect of the scan rate was much less pronounced and high Li and F contents prevailed at both scan rates.[185]

4.3.2.2. SEI Compound Identification

In **Figure 4-4** and **Figure 4-5**, we present XP detail spectra recorded on the as-prepared SEI layer (t=0) and after six minutes of sputtering (t=6) of the samples which were cycled at slow scan rate (0.1 mV s^{-1}) in EC (**Figure 4-5**: O 1s region and F 1s region, **Figure 4-4**: Li 1s, P 2p

and C 1s region). Similar spectra recorded after the other sputter times (t=2, t=12, t=30) or from the samples cycled at fast scan rate (10 mV s^{-1}) at all sputter times are presented in **Figure S4-5** to **Figure S4-8** and **Figure S4-9** to **Figure S4-14** in the Supporting Information (section 4.5.3 in this work), respectively. In the following, we will start with the discussion of the components contributing to the elemental peaks in the spectra recorded on the original SEI after subsequent electrode transfer (t=0), which were identified by a comprehensive peak fitting and deconvolution procedure. We will also discuss changes in the spectra observed upon sequential sputtering. Finally, we will summarize the evolution of the concentration of different compounds with increasing sputter time (**Figure 4-6**). This is closely related to the depth profiles in **Figure 4-3**, with the difference that **Figure 4-6** displays the concentration profiles of different compounds or moieties rather than elemental profiles. Finally, we will try to rationalize these results in a mechanistic picture, which can explain in particular the effects of scan rate, substrate and electrolyte. Here, we will include also transport effects, which have been discussed in previous experimental and theoretical studies.[191,214,215] For the identification of the different compounds contributing to the SEI and their relative contribution, we applied a comprehensive procedure for XPS peak fitting which has been recently employed for the analysis of similar SEI films on HOPG model electrodes[185] In short, it is based on the following assumptions: 1) the number of possible components is restricted to a minimum, 2) the binding energies (BEs) and the peak widths (full width at half maximum – FWHM) of the elemental peaks of a given component are fixed to ±0.2 eV for all spectra (different electrodes, different scan rates) at t=0, and 3) except for the cases indicated, the intensities of the elemental peaks related to a given compound reflect the stoichiometry of that compound, corrected by the atomic sensitivity factors (ASFs). The contribution of the respective compounds or moieties is calculated from the sum of the individual elemental contributions, which means that only contributions from C, F, Li, O and P are included. For moieties with unknown composition, such as the fluorophosphates Li_xPF_y or $Li_xPF_yO_z$, the compound concentration was calculated from the intensities of the respective peaks with appropriate BEs. The concentrations of these species were limited to the sevenfold of the P concentration at maximum, reflecting the stoichiometry of the undecomposed compound with the highest O and F content, e. g. $LiPF_6$, while lower concentrations, arising from lower O and F contents due to sputter-induced decomposition, were possible. The different components considered were mainly derived from previous studies, including our own.[60,71,158,185,199,216,217]

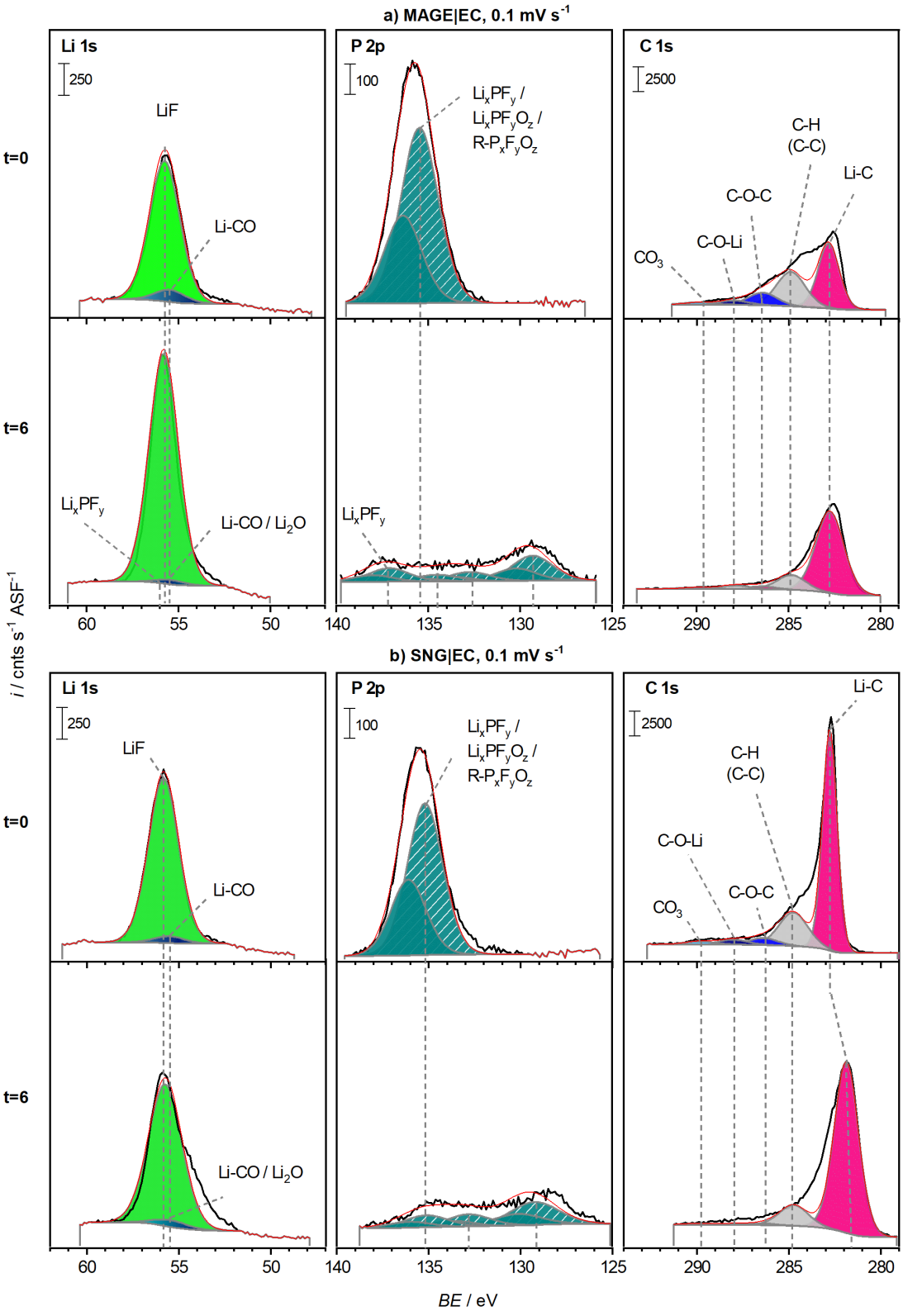

Figure 4-4. XP detail spectra of the Li 1s, P 2p and the C 1s regions of the SEI formed on a) MAGE and b) SNG powder film electrodes cycled at 0.1 mV s^{-1} on the as-prepared samples (t=0) and on the samples obtained after six minutes of sputtering (t=6). The red lines indicate the sum of the individual peak intensities.

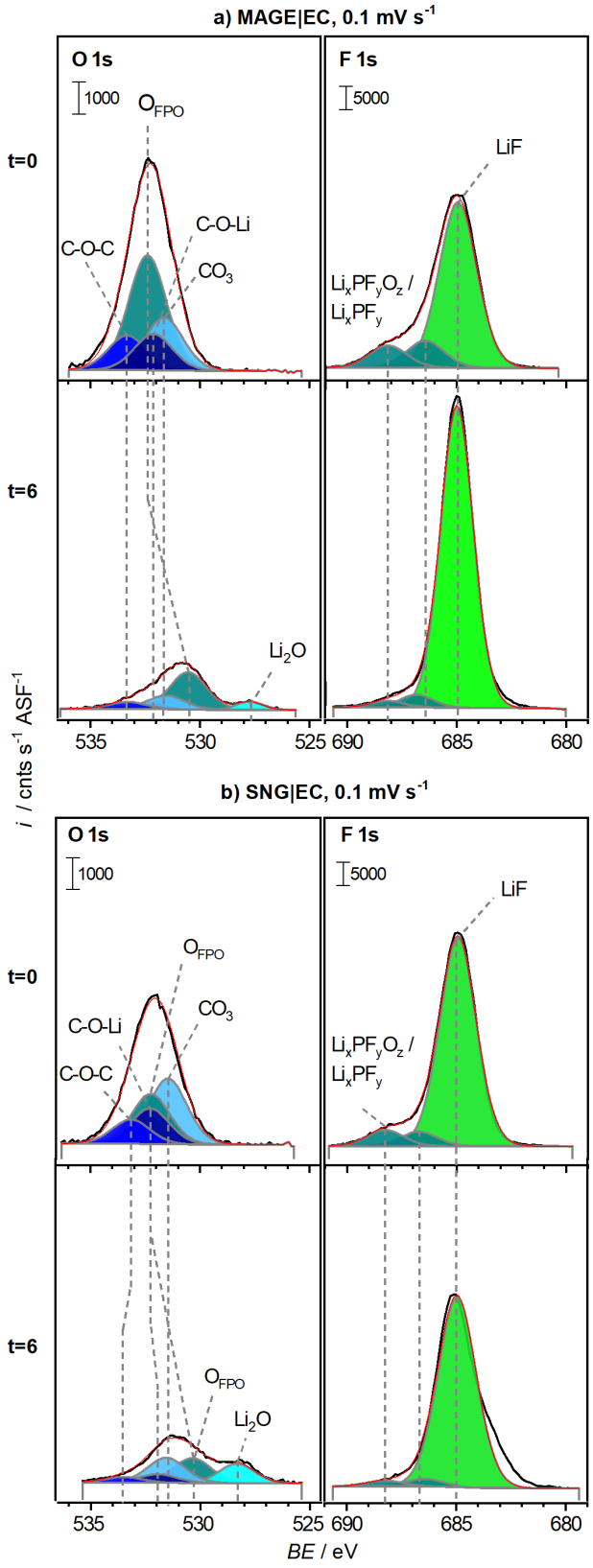

Figure 4-5. XP detail spectra of the O 1s and the F 1s regions of the SEI formed on a) MAGE and b) SNG powder film electrodes cycled at 0.1 mV s^{-1} on the as-prepared samples (t=0) and on the samples obtained after six minutes of sputtering (t=6). The red lines indicate the sum of the individual peak intensities.

Further details are given in the Supporting Information of Ref. 185. We believe that this is the most rational approach for a consistent fit of all elemental peaks, even though some of the individual fits may not be perfect. The BEs and stoichiometric ratios used for peak fitting and quantification are listed in **Table 4-1**. Note that a slight peak broadening and shift occurs upon sputtering.

Beginning with the F 1s region, we find a pronounced signal at 685.0 eV (**Figure 4-5** and **Figure S4-10** in section 4.5.3), which can be related to LiF (see discussion of the Li 1s peak),[147] and two smaller signals at higher binding energies (686.6 and 688.3 eV), which are assigned to $Li_xPF_yO_z$ and Li_xPF_y species (no fixed stoichiometries), respectively.[185,197,198] The amount of LiF is about 50 at.% after slow cycling and about 10–25 at.% for the samples cycled at fast scan rate (see **Figure 4-6**). The at.% values given for (stoichiometric) compounds are the sums of the contributing elemental values. This value of 50 at.% is significantly less than the 70 to 80 at.% which we had detected in the SEI formed on basal HOPG electrodes, independent of the scan rate.[185] Also, the concentration of the other F-containing species ($Li_xPF_yO_z$/Li_xPF_y) is higher after slow cycling (0.1 mV s^{-1}) than the one obtained after fast cycling (4–8 at.% vs. 2 at.%). This observation is in line with findings reported by Ryu *et al.*, who studied the SEI formation in EC/DEC-based Li^+-containing electrolyte with different anions on 'graphite bulk'.[216] Comparing the CVs in different electrolytes, they could distinguish between salt (anion) and solvent decomposition, where salt decomposition occurred at different potentials depending on the anion. For $LiPF_6$, these authors found a distinct peak at higher potentials than solvent decomposition, which was claimed to proceed with an exponentially increasing rate at lower potentials.

Based on these observations, the effect of the scan rate in our experiments can be explained by different potential dependencies of the two competing decomposition processes, in combination with kinetic limitations, e.g., in the formation of the passivation layer. In this case, cycling at slow scan rates would favor the build-up of a passivation layer via the process with the earlier onset in the negative-going scan (thermodynamically favored, salt decomposition) over the process with the steeper increase with increasing overpotential (kinetically favored, solvent decomposition). Cycling at higher scan rate, in contrast, would be more affected by kinetic limitations and thus emphasize the kinetically preferred solvent decomposition. Possible reasons for such behavior will be discussed at the end of this section.

Upon short sputtering (t=2), the LiF concentration increases for all electrodes and scan rates, except for the SNG|EC sample cycled at 0.1 mV s^{-1}, where it remains about constant. On the other hand, the combined contribution of the two signals related to $Li_xPF_yO_z$ and Li_xPF_y decreases continuously, also for longer sputtering times, and in some cases even disappears completely (see section 4.5.3, **Figure S4-10**, **Figure S4-12** and **Figure S4-14**). While this behavior is likely to reflect the concentration profile of these species, we cannot rule out that their decreasing concentration is due to increasing sputter decomposition of the $Li_xPF_yO_z$ and Li_xPF_y species, or a combination of both.

In the O 1s region, we identified peaks at 533.3, 532.1 and at 531.7 eV, which can be correlated to specific C 1s signals. These O 1s peaks have been assigned to polymer, ether or semicarbonate species (C–O–C or R–C–O–CO_2^-) at 533.3 eV,[71,77,80] to alkoxide species (C–O–Li)[199] at 532.1 eV, and finally to semicarbonate species (R–C–O–CO_2^-)[78] or Li_2CO_3[68] at 531.7 eV. (Note that the authors of a recent study claimed that the semicarbonate is actually lithium ethylene monocarbonate (LiEMC).[218]) As will be shown later, contributions from such semicarbonates seem to be negligible in our case. Interestingly, Li_2CO_3 was not observed in the SEI formed on HOPG.[185] This discrepancy may arise from the lower defect density of the basal HOPG substrate, which could affect the SEI formation. The combined amount of carbonates, alkoxides and polymer or ether species, which we consider as typical solvent decomposition products, is about similar on all electrodes, except for the MAGE anode cycled at 10 mV s^{-1}. The lower concentration of these species on the latter electrode agrees well with the absence of a C 1s peak in the range of 290 eV (see below), which is typical for carbonates, and the related O 1s component on that electrode. In addition to the aforementioned O-containing species, two further O 1s peaks are required for a reasonable fit. An O 1s signal at about 532 eV (t=0) is tentatively assigned to fluorophosphates, e. g., $Li_xPF_yO_z$ (labelled O_{PFO}), based on the fact that we also observe a P 2p signal with a BE typical for these species (see below).[197] For the MAGE samples, this component contributes most to the O 1s signal, both for the graphite electrodes cycled at 0.1 and 10 mV s^{-1}, while its contribution is smaller (second highest) for the SEI surface formed on SNG anodes. Note that the O 1s signal at ~532 eV may also contain contributions from simple inorganic components, such as Li hydroxides (~531.0 eV[147]), which may form by reaction with residual moisture in our solvents (<50 ppm). This may lead to a too-high content of these species in the calculations (see **Figure 4-6**), which is at least partly corrected by limiting the content of these species to the sevenfold of the P-concentration. The Li 1s signal would not be in disagreement with that possibility. Finally, we detected a small

signal at 528.4 eV in the O 1s spectrum of MAGE cycled at 10 mV s^{-1}, which, based on its BE, is most likely related to Li_2O.[85] This may result, e.g., from side reactions of Li_2CO_3 with trace impurities of water or from sputter decomposition of Li_2CO_3.[85] For the spectrum recorded before Ar^+ sputtering (t=0), however, the latter origin can be excluded. Since for this sample there was also no carbonate signal at 531.7 eV at t=0, this seems to indicate that the carbonate species on that surface reacted chemically to Li_2O, either via side reactions or during the cleaning process. It is important to note that a number of peaks seemed to shift in BE upon sputtering. Consequently, an unambiguous assignment is often hard to make. In these cases we tried to maximize the number of peaks with constant BE. For the other three samples (SNG|EC at fast and slow scan rate, MAGE|EC at slow scan rate), the Li_2O-related signal around 527–528 eV appeared only after two minutes of sputtering. In this case, it may also originate from sputter decay of Li_2CO_3 and semicarbonates or from solvent decomposition due to reaction with traces of water.[85,185] Among the three C- and O-containing species identified in the O 1s region (polymer / ethers, carbonates and alkoxides), carbonates have the highest concentration based on their O 1s intensity, except for the MAGE|EC sample cycled at 10 mV s^{-1}, where this species does not appear at all. This latter sample also suffers most upon sputtering. The $Li_xPF_yO_z$-related O 1s signal (O_{FPO}, ~532 eV) decreased during sputtering, simultaneously, a signal appeared at lower binding energies (~530 eV). The latter peak may reflect the presence of organophosphates with lower P oxidation states ($R–P_xF_yO_z$), which are observed in the P 2p signal (see also discussion below).[217] In contrast to the decreasing concentration of F species for higher scan rates, the overall concentration of O-containing species increases with faster scan rate. This can be explained in the same picture as before, with a dominant SEI formation from decomposition products of the Li salt (mainly LiF) at slow scan rates, while solvent decomposition products (i.e., C- and O-containing compounds) contribute more strongly to the SEI formation at fast scan rates.

In order to fit the experimental data in the C 1s region, we started with the components derived from the O 1s detail spectra, including polymer / ether (C–O–C, e.g., polyethylene oxide (PEO)[71,77] or (semi-)carbonate ($R–C–O–CO_2^-$)[80]) species at 286.4 eV, alkoxides (C-O-Li, 288.0 eV[199]) and (semi-)carbonate (CO_3^{2-} or $R–C–O–CO_2^-$, 290.0 eV[80]) species. Where unclear, the stoichiometries (C : O ratios) of the above components are listed in **Table 4-1**. Based on the rather low intensity in the O 1s region at 533.3 eV, the formation of significant amounts of semicarbonates with a $C_{286.4\ eV} : O_{533.3\ eV}$ ratio of 1 : 1 can be excluded. Therefore, the C 1s peak at 286.4 eV must be mainly due to polymer and ether species. Accordingly, the

C 1s peak at 290.0 eV is mainly assigned to Li_2CO_3. This is compatible also with the O 1s intensity at 531.7 eV, which fits to a C : O ratio of 1 : 3 for the related peaks. The absence of semicarbonates seems to be in contradiction with the findings of Cresce *et al.*, who observed a 1 : 1 ratio between the C 1s signals at ~290 eV and 286.8 eV, respectively, on their HOPG samples before rinsing, which is typical for semicarbonate.[192] After thorough rinsing, however, they obtained much higher carbonate concentrations compared to semicarbonates. Since our XPS measurements were performed after extensive rinsing, both experiments arrive at the same result of a low semicarbonate concentration on the well-rinsed SEI. Furthermore, we find significant contributions from a C 1s signal for adventitious carbon / hydrocarbon groups (C–H/C–C) at approximately 285 eV,[147] which appears for all electrode|electrolyte combinations and both scan rates. While these peaks lead to very reasonable fits for both electrodes directly after cycling at 10 mV s^{-1} (t=0), an additional signal is required at 282.7 eV (Li–C, FWHM 0.9–1.2 eV at t=0) for the SEI formed upon cycling at 0.1 mV s^{-1}. In our previous study on HOPG model electrodes, we observed a peak at approximately 283 eV after sputtering. We had attributed this signal to Li carbide species (Li_xC),[150] which were generated upon sputtering.[185] Since, in the present study, this signal appears already before sputtering, this carbide species must (also) be formed in the (electro-)chemical decomposition process during the slow CV measurements rather than only by sputter-induced decomposition. Apparently, this chemical process is enhanced on rough surfaces, since the peak did not appear in the equivalent measurements on HOPG.[185] For the present electrodes, this species contributes significantly to the SEI composition (see **Figure 4-6**), which will be discussed in more detail later. It is important to note that the increasing C 1s intensity in the last sputter cycle (see **Figure 4-3**) is mainly due to an increase of this Li carbide species and not caused by an upcoming signal of graphite electrode material, which should be at 284.6 eV. This assignment is further supported by the fact that the different C 1s signal intensities are still changing even at later stages. While it is reasonable to expect that SEI constituents are present in the inner pores of the electrode and thus can be observed also after removal of the surface SEI layer, one would not expect changes in the composition in that case. Hence, we can reasonably exclude that the graphite electrode is unburied during 30 minutes of sputtering, which also means that the SEIs formed on these graphite electrodes are significantly thicker than those formed on HOPG.[185] Finally, we would like to note that there is additional intensity in the range between the C–H/C–C signal at 284.8 eV and the Li_xC signal at 282.7 eV in the spectra of the samples cycled at slow scan rates. We think that this results from Li-containing

carbon species with lower Li content, which therefore appear at higher BEs. Because of the unknown nature of these species, however, we did not include an additional peak for them. In agreement with the trend in the O 1s intensities of the O- and C-containing species, the overall carbon concentration of C-containing species is higher after cycling at 10 than after cycling at 0.1 mV s^{-1}. This is again compatible with a mechanism favoring more pronounced solvent decomposition at faster scan rates, while salt decomposition prevails at slow scan rates.

For the P 2p signal, which consists of a doublet with a spin-orbit separation of Δ0.9 eV, we resolve a $p_{3/2}$ signal at 136.7 eV and another one at about 134.0–134.4 eV for t=0 after fast cycling (10 mV s^{-1}), which we assign to $LiPF_6$ and its decomposition products, e. g., Li_xPF_y and $Li_xPF_yO_z$.[197,198] After slow cycling (0.1 mV s^{-1}), the P 2p spectrum at t=0 consists of a single signal only at 134.5 eV for MAGE and at 135.2 eV for SNG, respectively. We attribute these BEs to different compositions of the Li_xPF_y and $Li_xPF_yO_z$ species. Accordingly, we did not assume a fixed stoichiometry and therefore the P : F or P : O intensity ratios were allowed to vary freely within certain limits: the concentrations of these species were limited to the sevenfold of the P concentration at maximum. The peak at 136.7 eV observed for the SEI formed at fast scan rate (t=0) is tentatively assigned to $LiPF_6$[200] which was not removed despite careful rinsing. Sputtering of the electrodes leads to a significant decrease of the P 2p intensities in the $Li_xPF_yO_z$- and Li_xPF_y-related signals at 134.4–136.7 eV which, in all cases, is accompanied by the appearance of new signals at 132.8 and 129.7 eV. This is particularly well visible in the spectra, e.g., in **Figure 4-4** or **Figure S4-9** (section 4.5.3). We explain this by sputter-induced decomposition of the $Li_xPF_yO_z$/Li_xPF_y components and the appearance of (organo-)phosphates ($R–P_xF_yO_z$, see also the O 1s discussion) and phosphides / elemental phosphorous. Interestingly, we observed a weak signal at about 137 eV on the sputtered MAGE electrode which, based on the BE, could be $LiPF_6$. Also note that the total amount of P decreases in the SEI with increasing sputter time, regardless of the graphite material and the scan rate (see discussion of **Figure 4-3**).

Finally, for the Li 1s region, peak fitting resulted in two main peaks at 55.5 eV and 55.8 eV for both anode materials and cycling times. We assign them to LiF (55.8 eV)[147] and to Li carbonates / alkoxides (55.5 eV), respectively.[85,147] The latter species, which result from solvent decomposition, are labelled as Li–CO in the spectra. The intensity of the LiF-related Li 1s peak is given by the intensity of the corresponding LiF component in the F 1s spectrum (Li : F ratio of 1 : 1). The intensity of the Li–CO signal is calculated from the overall amount

of Li- and O-containing species, assuming Li : O ratios of 2 : 3 (for the O 1s component at 531.7 eV) for Li_2CO_3 and of 1 : 1 (for the O 1s component of alkoxides at 532.1 eV), respectively. Assuming that the high-energy peak of the P 2p spectrum for the SEIs formed at 10 mV s^{-1} (t=0, **Figure S4-9**) results from residual, undecomposed $LiPF_6$, we calculated the intensity of the related Li 1s peak, which appears at 56.0 eV (note that due to the small contribution this is hardly visible). The lower overall amount of Li–CO (alkoxide, carbonate) species obtained for the samples cycled at 0.1 mV s^{-1} compared to those obtained after fast cycling (10 mV s^{-1}) at t=0 (see also **Figure 4-6**) reflects the behavior of the respective O and C signals, which were used to calculate the intensity of the respective Li 1s peak.

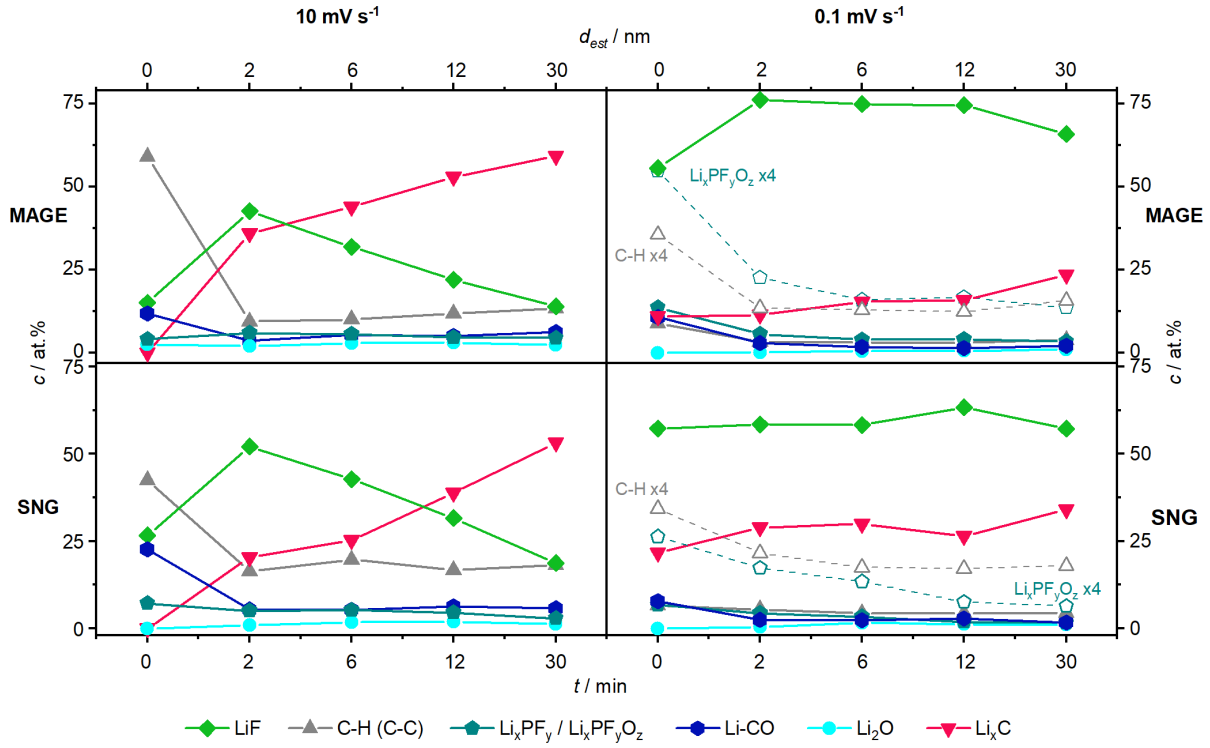

Figure 4-6. Depth profiles of the XPS-probed concentrations of selected species on MAGE (top) and SNG (bottom) graphite electrodes cycled at 10 (left) and 0.1 mV s^{-1} (right). The concentrations are given in at.%. For the calculations, we only used the elemental concentrations of C, F, Li, O, and P. The open symbols connected by broken lines represent up-scaled versions of the C-H and P-containing species, included for better comparison. An estimate of the thickness of the removed SEI layer (d_{est}), starting at the initial SEI surface, is given in the additional upper x-scale.

Figure 4-6, finally, depicts the evolution of the concentrations of the different SEI constituents (e. g., LiF, Li_2O, Li–CO, Li_xC) and moieties, which are based on the respective concentrations of C, F, Li, O, and P therein in at.%, with increasing sputtering for the respective samples. The term Li–CO is used to summarize contributions from different solvent decomposition products,

including carbonates, ethers or polymers and alkoxides. The line labelled C–H (C–C) reflects the contribution from the C 1s signal for hydrocarbon species at ~285 eV, which will also include adventitious carbon.

The atomic concentrations of these species for all four electrodes and at all sputter times are listed in **Table S4-2** in the Supporting Information (section 4.5.3 in this work). In addition to sensing the depth-dependent concentrations of the various compounds or moieties, these data may also reflect sputter-induced transformations of the original SEI components.

For both graphite materials, LiF represents the highest contribution to the SEI surface formed at slow scan rate and the second-highest contribution at fast scan rate. After two minutes of sputtering, all samples show a significant increase in the LiF concentration, except for SNG|EC (0.1 mV s^{-1}), where the concentration remains more or less constant. Similar to our observations on SEI formation on HOPG in these electrolytes, LiF is one of the two main components within the SEIs. For the samples cycled at slow scan rate, its concentration remains approximately constant after the initial increase throughout the remaining sputtering time, while for those cycled at 10 mV s^{-1} it passes through a maximum concentration after two minutes of sputtering (t=2) and then decreases steadily from thereon (**Figure 4-6**). Hence, except for SNG|EC (0.1 mV s^{-1}), the LiF concentration is lower directly at the SEI surface, and then either increases in the near-surface regions or remains constant, depending on the cycling rate.

These results can be compared with previous findings on related systems. For the SEI generated on basal HOPG electrodes under similar conditions we observed a high and approximately constant LiF concentration upon sputtering.[185] Niehoff *et al.* reported an increase of the LiF concentration upon sputtering, with a maximum after 1-3 minutes, and a subsequent decay for a comparable system (composite electrode, EC/DEC + LiPF6).[150] Furthermore, these authors could demonstrate that the increase of the LiF concentration (in at.%) during the first 30 seconds of sputtering correlates quantitatively with the decrease in the Li_xPF_y/$Li_xPF_yO_z$ concentration.[150] This is different from our present findings, where sputter-induced decomposition of Li_xPF_y and $Li_xPF_yO_z$ species is likely to occur as well, but, due to their low concentration at t=0, cannot explain the pronounced increase in the LiF concentration observed between t=0 and t=2.

Table 4-1. Binding energies (BEs) of the peaks related to solvent and/or electrolyte salt decomposition products detected in the SEI on graphite model electrodes after cycling in EC-based electrolyte. Stoichiometric ratios employed for the peak intensity calculations are given in brackets where unclear.

	C 1s / eV	O 1s / eV	Li 1s / eV	F 1s / eV	P 2p / eV	Ref.
C–O–C (polymer / ether)	286.4 (2)	533.3 (1)				71, 77, 80
C-O–Li (alkoxide)	288.0 (1)	532.1 (1)	55.5 (1)			85, 199
Li_2CO_3 (carbonate)	290.0	531.7	55.5			68, 147
LiF			55.8	685.0		147
$Li_xPF_yO_z$ / $R\text{-}P_xF_yO_z$		~532 Slow upon sputtering ~530		686.6/ 688.3	Fast 134.0, 136.7 Slow 134.5/ 135.2 upon sputtering 132.8/ 129.4	198, 217
$LiPF_6$			56.0	687.5	137.6	197, 200
Li_2O		~528	55.5			85
LiOH		~531				147
C–H (C–C)	~285					147
Li_xC	~283[c]		55.5			150

Peled and coworkers, in contrast, reported an initial increase of the LiF concentration upon sputtering an SEI that was generated during galvanostatic charge / discharge experiments on cross-sectional HOPG in EC/DEC + $LiAsF_6$ electrolyte, followed by a constant concentration.

For the basal plane, in contrast, they observed a maximum after eight minutes of sputtering and a decay for longer sputter times.[60,158] We find it most likely that the initial increase in LiF concentration is due to the removal of a thin surface layer of carbon-rich deposits, which may have resulted, e.g., from the after-treatment of the electrode (see the following discussion).

The C-H moieties, which contribute most to the SEI formed on these graphite materials upon cycling at 10 mV s^{-1}, start with an initial contribution of 58 (42) at.% on the MAGE (SNG) sample, which then decreases considerably for both electrodes upon sputtering. After longer sputtering times their contribution passes through a minimum and then increases again for the MAGE electrode (final concentration ~30 at.%). For the SNG electrode, their concentration is about constant (~20 at.%) at longer sputtering times. Upon cycling at 0.1 mV s^{-1}, the initial concentrations are significantly lower (~6 at.% for both MAGE and SNG). They, too, decrease during the initial two-minute-sputtering phase and then remain more or less constant. These results are consistent with a model that involves the presence of a C–H-rich deposit layer on the SEI surface (SEI|electrolyte interface). This will be discussed at the end of this section. The initial intensities of the combined Li–CO solvent decomposition species are about 12 at.% for the MAGE samples, both after fast and slow cycling, and about 25 (6) at.% for the SNG samples cycled at fast (slow) scan rate. After two minutes of sputtering, the concentration decreases considerably, regardless of the substrate and the cycling rate, and then remains about constant upon longer sputtering. Both this and the similar trend of the C–H species upon sputtering point to an approximately constant concentration of solvent decomposition products throughout the probed SEI, underneath a surface region where these species appear in higher concentrations. The initial decrease agrees with reports by Peled *et al.*[56,60,158] and Edström *et al.*,[71,77] who proposed that organic (solvent decomposition) products are enriched at the SEI surface (electrolyte|SEI interface). Upon sputtering, these organic species are quickly removed.

The $Li_xPF_yO_z/Li_xPF_y$ signal with its contributions from related P 2p, Li 1s and F 1s signals is the second-lowest contribution to the SEI composition at t=0. It is slightly higher on the MAGE electrodes (13 at.%) than on the SNG electrodes (6–7 at.%), regardless of the scan rate. Sputtering initially causes the concentration of these species to decrease to ~5 at.%, independent of electrode material and scan rates. From thereon, the concentration remains about constant (MAGE) or continues to decrease (SNG). The initial decrease in concentration of this species is attributed to a sputter-induced decomposition to LiF, reflected by the initial increase in LiF concentration. The higher original concentration of $Li_xPF_yO_z/Li_xPF_y$ on the

slowly cycled MAGE electrode would fit to the higher overall amount of Li salts after slow cycling. The Li_xC C 1s signal at about 283 eV appears first after two minutes of sputtering for the samples cycled at fast scan rates, while it is present already before sputtering after slow cycling (see our earlier discussion of the C 1s deconvolution). For the latter samples, the concentration of Li_xC remains about constant during sputtering, while it increases continuously for the fast cycled electrodes, reaching more than 50 at.% for both the MAGE and the SNG electrode. As discussed before, the BE clearly indicates that this signal is not due to contributions from the graphite substrate, as it was observed for HOPG.[185] This also means that the SEI formed on the graphite powder film electrodes is significantly thicker than that created under identical conditions on HOPG, which is in full agreement with expectations.

Finally, we also observed the formation of Li_2O, which is indicated by the O 1s signal at 528.4 eV and a Li 1s signal at 55.5 eV. In most cases, this species appeared only after sputtering. The only exception was the MAGE electrode cycled at 10 mV s^{-1}, where it was detected also at t=0. During sputtering, its concentration remained below 3 at.% in all cases. We assume that this species results mainly from decomposition of carbonates, either by chemical interaction or upon sputtering.[85]

Overall, our results are consistent with an SEI formation process where solvent decomposition prevails at fast scan rates, resulting in dominant contributions from solvent decomposition products (Li–CO species). At slow scan rates, salt decomposition is the dominant process, with LiF and $Li_xPF_yO_z$ species as typical decomposition products. This is clearly evident already from the total amount of C or F in the SEI, and thus does not depend on the deconvolution procedure. The more or less pronounced initial increase in LiF concentration upon sputtering, which is also indicated by the total F and Li concentrations, is tentatively explained by effects of the after-treatment (rinsing, sample transport). This can involve both removal of Li salts from the surface region and deposition of a carbon-rich surface layer. The general decrease of the Li salt content with increasing sputtering time, i.e., in deeper layers of the SEI, can be explained by transport effects, which have been reported both in experimental and theoretical studies on SEI formation in LIBs.[191,215] In the case of a porous SEI which grows at the electrode surface, the SEI surface reflects the initial SEI at the onset of SEI formation. If the ongoing SEI formation takes place at the electrode surface and is dominated by transport effects, and if transport of Li salts through the growing SEI is more hindered compared to solvent transport, SEI formation at later times would more and more be governed by solvent

decomposition. Note that, in this case, differences in the efficiency of SEI formation are also due to differences in the chemical interaction between graphite electrode and solvent molecules. The effect of the scan rate during cycling can be rationalized in the same way, since transport effects should be less pronounced during slow cycling. Hence, one would expect higher salt concentrations at the electrode surface for slow cycling, and the decay of the salt components with increasing thickness of the SEI should be less pronounced. As expected, the effects explained here by hindered transport in the growing SEI are much less pronounced in the thinner SEI layers observed on HOPG. These effects should depend also on the transport properties of the solvent molecules, which are not so different in the present case, and the pore structure of the SEI. Focusing on the $Li_xPF_yO_z$ species, which can be considered as intermediates in the formation of LiF, their low concentration compared to LiF indicates that these rapidly decompose to LiF during cycling. In addition, their decomposition seems to be induced also by Ar^+ sputtering, which results in a distinct decay after the first sputter cycle. The amount of carbon-containing solvent decomposition products increases when approaching the electrode surface, mirroring the decreasing amount of salt decomposition products. This trend is more pronounced for the SEI created by fast cycling. Similar to $LiPF_6$ decomposition to $Li_xPF_yO_z$ and LiF, we find two groups of decomposition products, C–C/C–H and Li_xC species. Sputter-induced decomposition processes play a role in this case, as well: the increasing concentration of Li_xC species, relative to the total amount of carbon, reflects the increasing decomposition of C–C/C–H species by Ar^+ sputtering. Nevertheless, there must be a pathway for purely electrochemical formation of the carbide species from solvent decomposition products during cycling as well, since these species are observed also on the initial surface of the SEI formed after slow cycling.

Finally, we would like to note that in the present case we concentrated on the transport of solvent molecules and salt species. Transport of Li^+ ions, which must be active to allow Li^+ (de-)intercalation and cell currents under conditions where further SEI formation is negligible, was not considered. Nevertheless, this simple model can explain our findings on the SEI composition and its variation rather well on a qualitative scale.

4.4. Conclusion

Extending our previous study on SEI formation in $LiPF_6$-containing single-solvent carbonate electrolytes on structurally well-defined HOPG electrodes, we have investigated this process on more realistic binder-free and binder-containing graphite powder film electrodes by cyclic voltammetry and chemical analysis of the SEI by depth profile XPS. Binder-free electrodes were prepared using two different types of graphite, an artificial commercial graphite powder (MAGE) and a spheroidised natural graphite (SNG). For comparison, also binder-containing electrodes prepared from these graphite materials were studied. Employing different potential scan rates and two different $LiPF_6$-containing single-solvent (EC and DMC) electrolytes, as well as the commonly used LP30 electrolyte (EC + DMC), we arrive at the following main results and conclusions:

1) Despite of their different nature and particle size, the two graphite materials are rather similar in their electrochemical properties in the single-solvent electrolytes, both with respect to electrolyte decomposition and Li^+ (de-)intercalation. Compared to the HOPG model electrodes, the LiF content in the SEI is generally lower and the SEI formed during cycling is thicker. The addition of a binder has some effect on the electrochemical properties in LP30: most prominently, it shifts the electrolyte decomposition to more negative potentials compared to binder-free electrodes. The pronounced peak-broadening observed on these electrodes is mainly attributed to transport effects and inhomogeneities in these thicker electrode layers.
2) In contrast to the limited influence of the nature of the graphite powder, the nature of the electrolyte and the scan rate during potential cycling have a (more) pronounced effect on the SEI formation and its composition on these electrodes. For DMC-based electrolyte, the SEI formation is less efficient and probably results in – at least partial – graphite exfoliation, allowing further electrolyte decomposition even in the third cycle. When cycling in EC-based electrolyte, in comparison, electrolyte decomposition and thus further SEI formation are negligible after the first cycle. This is attributed to differences in the chemical interaction between graphite electrode and solvent molecules. The characteristic features for electrolyte decomposition and Li^+ (de-)intercalation are, however, comparable in both cases, except for a slight difference in the peak positions. In LP30, the more efficient EC decomposition seems to dominate the solvent decomposition process.
3) The effect of the scan rate is most pronounced. It severely affects the composition of the resulting SEI and causes variations in the composition when going towards the

SEI|electrode interface. Fast cycling results in a generally lower concentration of salt decomposition products and a continued distinct decrease of their contribution with increasing depth, while the content of salt decomposition products is much higher and changes with increasing depth are much less pronounced for the SEI formed at slow cycling. The concentration of carbon-containing salt decomposition products mirrors these trends. These distinct variations and trends are explained in terms of transport limitations, where SEI formation takes place directly at the electrode surface and transport of salt species through the growing SEI layer is more hindered than transport of solvent molecules. This effect increases with increasing thickness of the SEI. The competition between salt transport and ion transport through the growing SEI is likely to be affected also by the transport properties of the solvent molecules and by the pore structure of the SEI.

Overall, these results and their comparison with previous findings on SEI formation under similar conditions and in similar electrolyte, but on structurally well-defined HOPG electrodes, provided detailed insights into the SEI formation process and the underlying mechanisms, including transport effects, which will be useful for further systematic studies and the improvement of the SEI.

4.5. Supporting Information

4.5.1. Structural Characterization

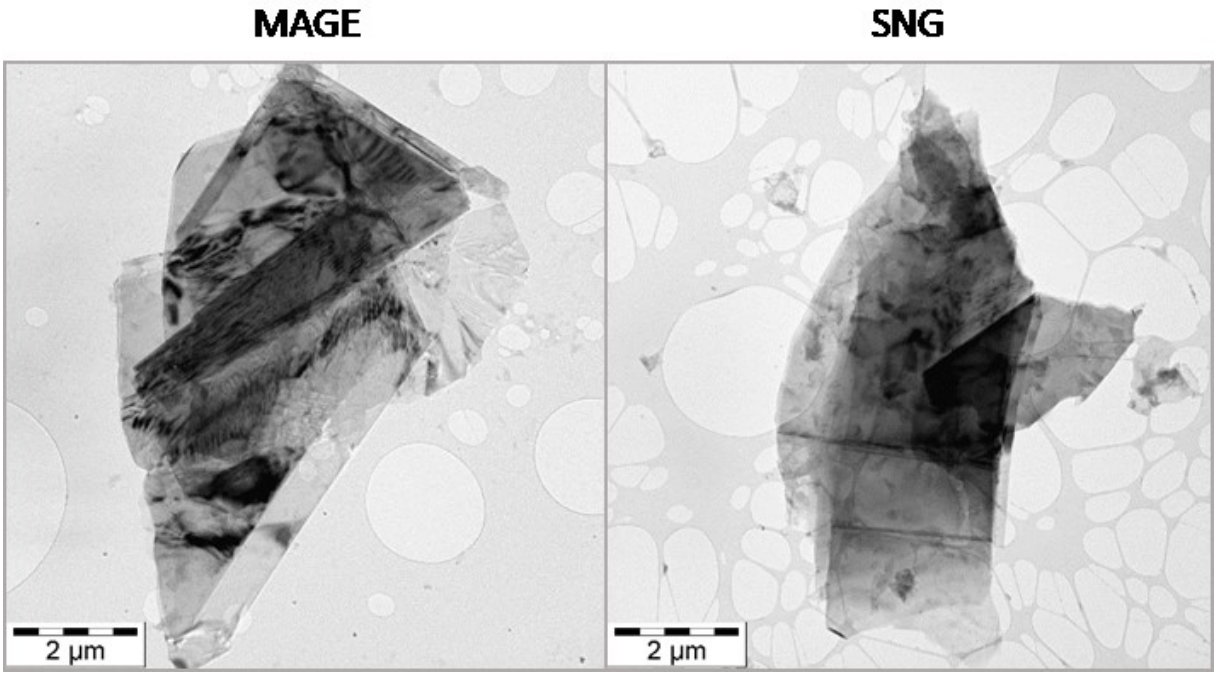

Figure S4-1. Transmission electron micrographs of the graphite powders employed as active material: MAGE (left) and SNG (right).

4.5.2. Electrochemical Characterization

4.5.2.1. Scan-Rate Dependence of MAGE and SNG Graphite Powder Electrodes

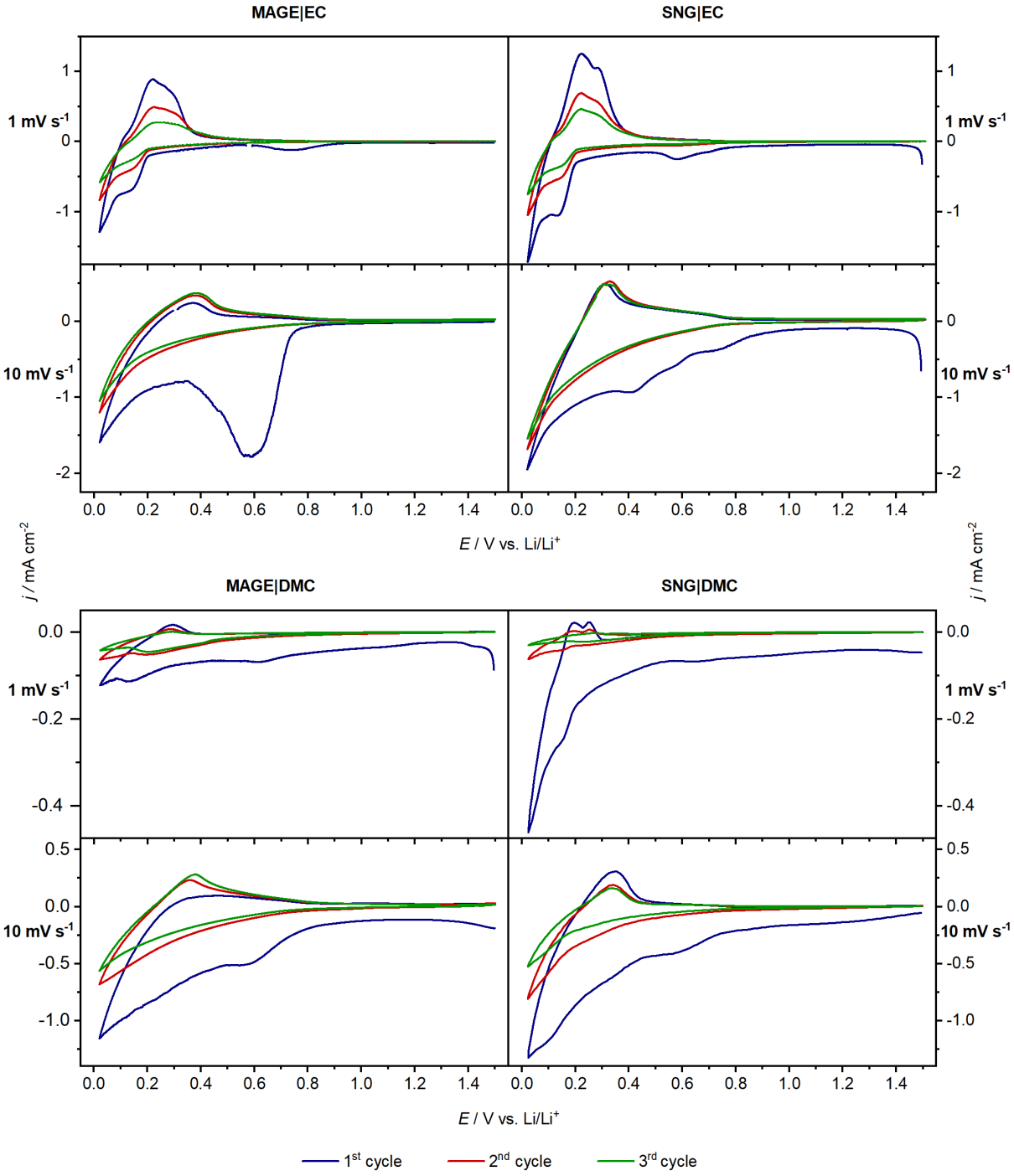

Figure S4-2. First three cycles of the CVs recorded on MAGE and SNG electrodes cycled in EC- and DMC-based electrolyte at 1 (top) and 10 mV s^{-1} (bottom).

4.5.2.2. Influence of the PVDF Binder

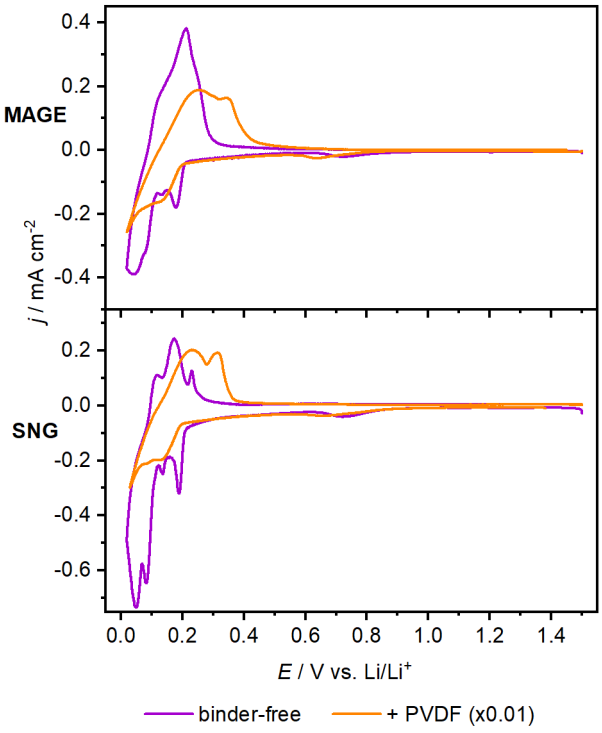

Figure S4-3. Comparison of the first cycle recorded on the binder-free MAGE (top) and SNG (bottom) film electrodes on glassy carbon and the respective graphite materials mixed with PVDF on Cu foil at 0.1 mV s^{-1} in LP30 electrolyte.

Cyclic voltammograms comparing the electrochemical characteristics of binder-free graphite powder film electrodes on GC and of PVDF-containing electrodes in commercial LP30 (EC/DMC 1 : 1 v/v + 1 M $LiPF_6$) electrolyte, recorded at 0.1 mV s^{-1}, are displayed in **Figure S4-3** and **Figure S4-4**.

First, we compare the CVs (first cycle) of both binder-free electrodes in LP30 (**Figure 4-3**, section 4.3.1) with those recorded in single-solvent electrolytes. In LP30, we find nearly identical features as observed for the same graphite powder film electrodes in EC-based electrolyte. Electrolyte reduction takes place at 0.7 V both for MAGE and SNG graphite materials; stepwise Li^+ intercalation signals are observed at 0.2, 0.1, 0.08 and 0.05 V, and the respective de-intercalation peaks appear at 0.1, 0.2 and 0.25 V. The potentials closely resemble those observed for Li^+ (de-)intercalation on MAGE and SNG in EC single-solvent electrolyte. Despite the mixed EC/DMC solvent, the individual Li^+ intercalation peaks are as sharp as the ones in single-solvent EC electrolyte. Overall, it seems that EC dominates the electrochemistry of these electrodes in LP30 electrolyte. This is true also for the stability of the currents in the

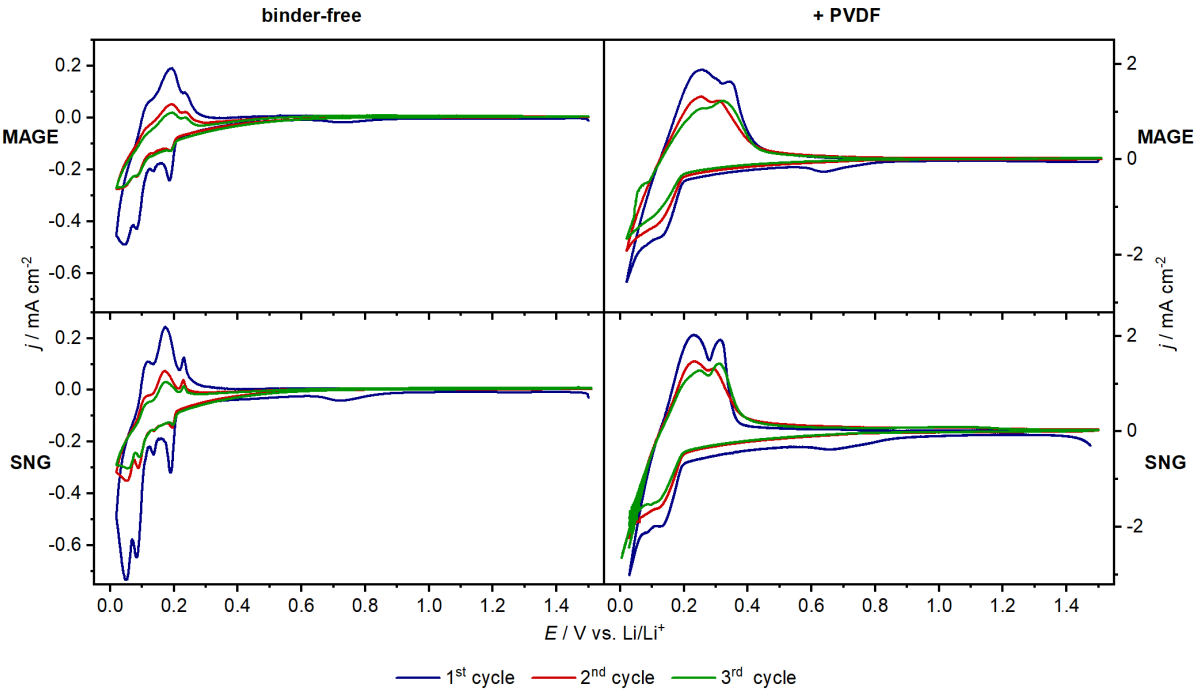

Figure S4-4. Comparison of the first cycle recorded on the binder-free MAGE (top) and SNG (bottom) film electrodes on glassy carbon and the respective graphite materials mixed with PVDF on Cu foil at 0.1 mV s^{-1} in LP30 electrolyte.

Li^+ (de-)intercalation regime, where only one third of the current is lost during the first three cycles (see **Figure S4-3**) both for the binder-free MAGE and SNG film electrodes, while the loss for DMC-based electrolyte was between 90 and 100 %. Obviously, the much more pronounced inhibition of the processes in the Li^+ (de-)intercalation regime in DMC-based electrolyte, as compared to EC-based electrolyte, and the partial graphite exfoliation, play only a lesser role in LP30.

In the current traces of the respective binder-containing electrodes, where the materials are mixed with PVDF binder and coated onto a Cu foil, the current densities are by about two orders of magnitude higher than on the binder–free film electrodes.

This is mainly due to a significantly higher loading of graphite in the latter electrodes (see Experimental, i.e., section 2.2.3 in this work). Most importantly, broad features are observed both for intercalation and de-intercalation, rather than the characteristic peaks reflecting stepwise Li^+ intercalation. Furthermore, the CVs recorded on PVDF-containing graphite display a more pronounced Ohmic drop, which we similarly attribute to the higher loading and, subsequently, much higher currents. This results in down-shifted potentials for the reductive electrolyte decomposition (about 0.6 instead of 0.7 V) and Li^+ intercalation (e.g., 0.1 V instead

of 0.2 V for the most anodic peak) and corresponding up-shifts for the Li^+ de-intercalation peaks. Most likely, the distinct peak broadening is due to inhomogeneities in the electrode caused by the presence of the binder, and possibly also affected by the much higher graphite loading. In the second cycle, LP30 decomposition (at about 0.6 V) is completely inhibited both on the binder-free and on the PVDF-containing graphite electrodes (**Figure S4-3**). Focusing on the Li^+ (de-)intercalation potential range, the current densities decrease by about one half (two thirds) between the first and the second cycle for the binder-free electrodes (both MAGE and SNG), while the current loss in the third cycle compared to the second cycle is negligible. For the binder-containing electrodes in LP30, both the current losses between the first and the second cycle and between the second and third cycle are less pronounced than observed for the binder-free electrodes. We speculate that the lower losses in current density for the binder-containing electrodes are most likely due to a better adhesion of the active material to the Cu substrate, which reduces the loss of active material during cycling compared to the binder-free, GC-supported electrodes.

In total, the results show that the electrochemical properties of graphite electrodes cycled in LP30 are dominated by the EC component, which leads to the formation of a cover layer that passivates against electrolyte decomposition and graphite exfoliation already in the first cycle, while Li^+ (de-)intercalation is still possible. The use of the PVDF binder in the graphite powder electrode has little effect on the formation of this SEI layer and on the Li^+ (de-)intercalation, except for an overall increase in current density. Finally, the differences in peak shape (slightly tilted and less sharp) of the CVs compared to the ones recorded on binder-free electrodes are attributed to Ohmic drop effects.

4.5.3. Chemical Composition of the SEI

Table S4-1. Peak width (full width at half maximum, FWHM) and atomic sensitivity factors (ASF) used for the peak fitting and deconvolution procedure.

	C 1s	**O 1s**	**Li 1s**	**F 1s**	**P 2p**
$FWHM_{t=0}$ / eV	1.8	2.0	1.9[a]	2.0[a]	2.4
ASF	0.314[b]	0.733[b]	0.027[a]	1.000	0.252[b]

[a] Calculated from reference measurements on LiF

[b] Moulder, J. F.; Stickle, W. F.; Sobol, P. E.; Bomben, K. D.: *Handbook of X-ray Photoelectron Spectroscopy*, Perkin Elmer Corp., Eden Prairie/USA, **1992**.

Table S4-2. Depth profiles obtained by Ar sputtering with increasing sputter time of the concentration (in at.%) of species containing the given compounds in the SEI formed on the MAGE and SNG electrodes during cycling at 10 and 0.1 mV s^{-1} in 1 M $LiPF_6$-containing EC.

	t	C-H (C-C)	Li_xC	LiF	Li_xPF_y $Li_xPF_yO_z$	Li-CO	Li_2O
MAGE|EC 10 mV s^{-1}	0	59	0	15	11	12	3
	2	10	36	43	6	4	2
	6	10	44	32	6	5	3
	12	12	53	22	5	5	3
	30	14	59	14	5	6	2
MAGE|EC 0.1 mV s^{-1}	0	8	11	56	14	11	0
	2	3	12	76	6	3	0
	6	3	15	75	4	2	0
	12	3	16	75	4	2	1
	30	4	23	66	3	2	1
SNG|EC 10 mV s^{-1}	0	43	0	27	7	23	0
	2	16	20	52	5	5	1
	6	20	25	43	5	5	2
	12	17	39	32	5	6	2
	30	18	53	19	3	6	1
SNG|EC 0.1 mV s^{-1}	0	7	22	57	7	8	0
	2	5	29	58	4	2	0
	6	4	30	58	3	2	2
	12	4	26	63	2	3	1
	30	4	34	57	2	2	1

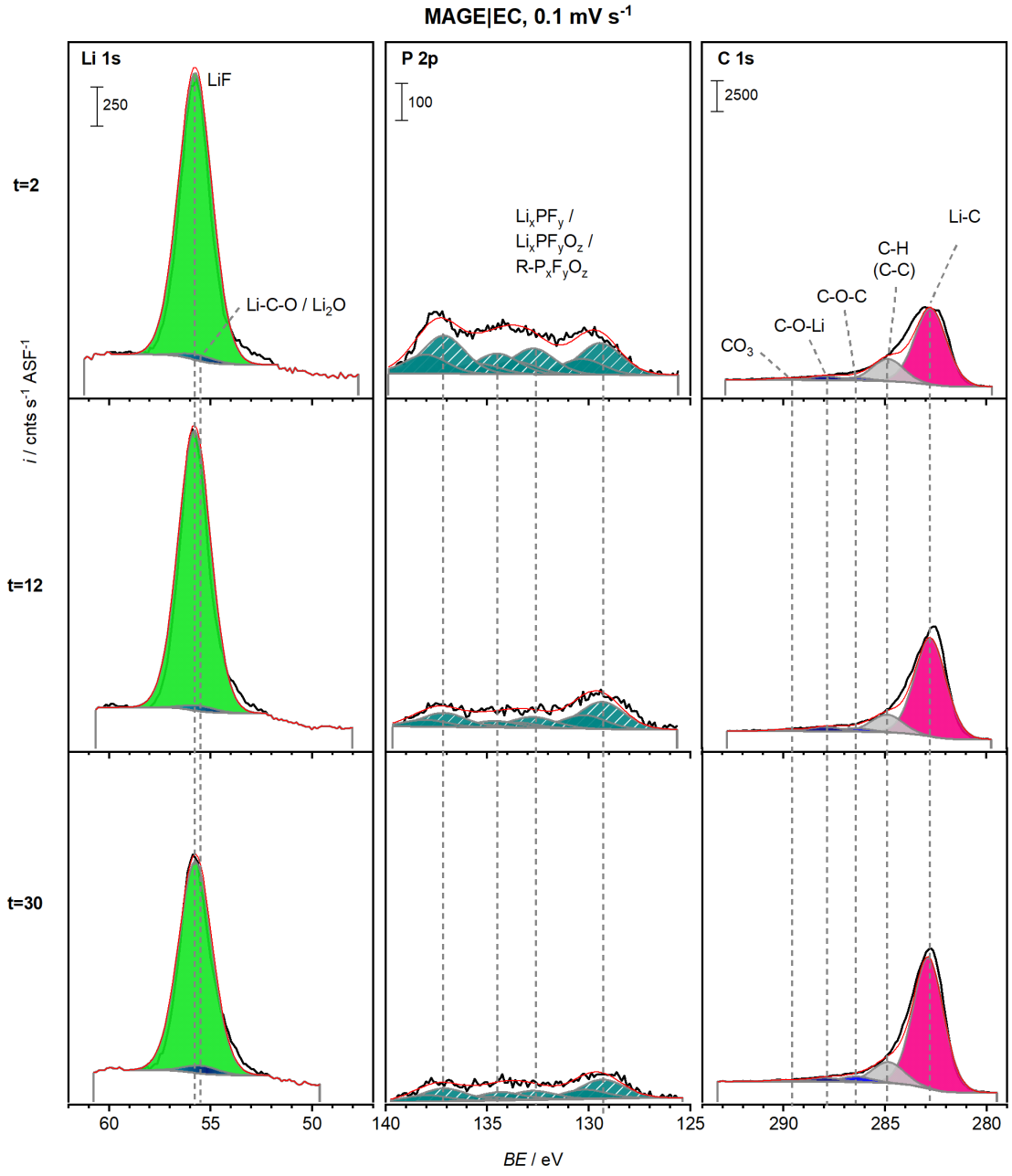

Figure S4-5. Li 1s, P 2p and C 1s spectra of the SEI formed on MAGE cycled in EC-based electrolyte at 0.1 mV s^{-1} after 2 (t=2), 12 (t=12) and 30 minutes (t=30) of consecutive sputtering.

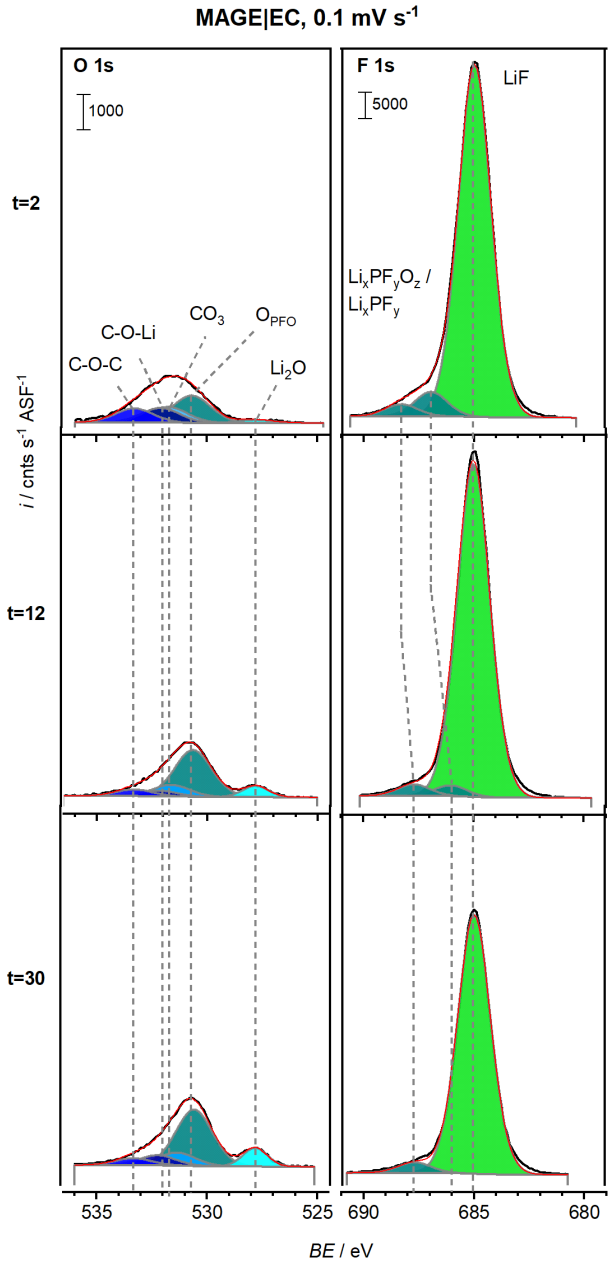

Figure S4-6. O 1s and F 1s spectra of the SEI formed on MAGE cycled in EC-based electrolyte at 0.1 mV s^{-1} after 2 (t=2), 12 (t=12) and 30 minutes (t=30) of consecutive sputtering.

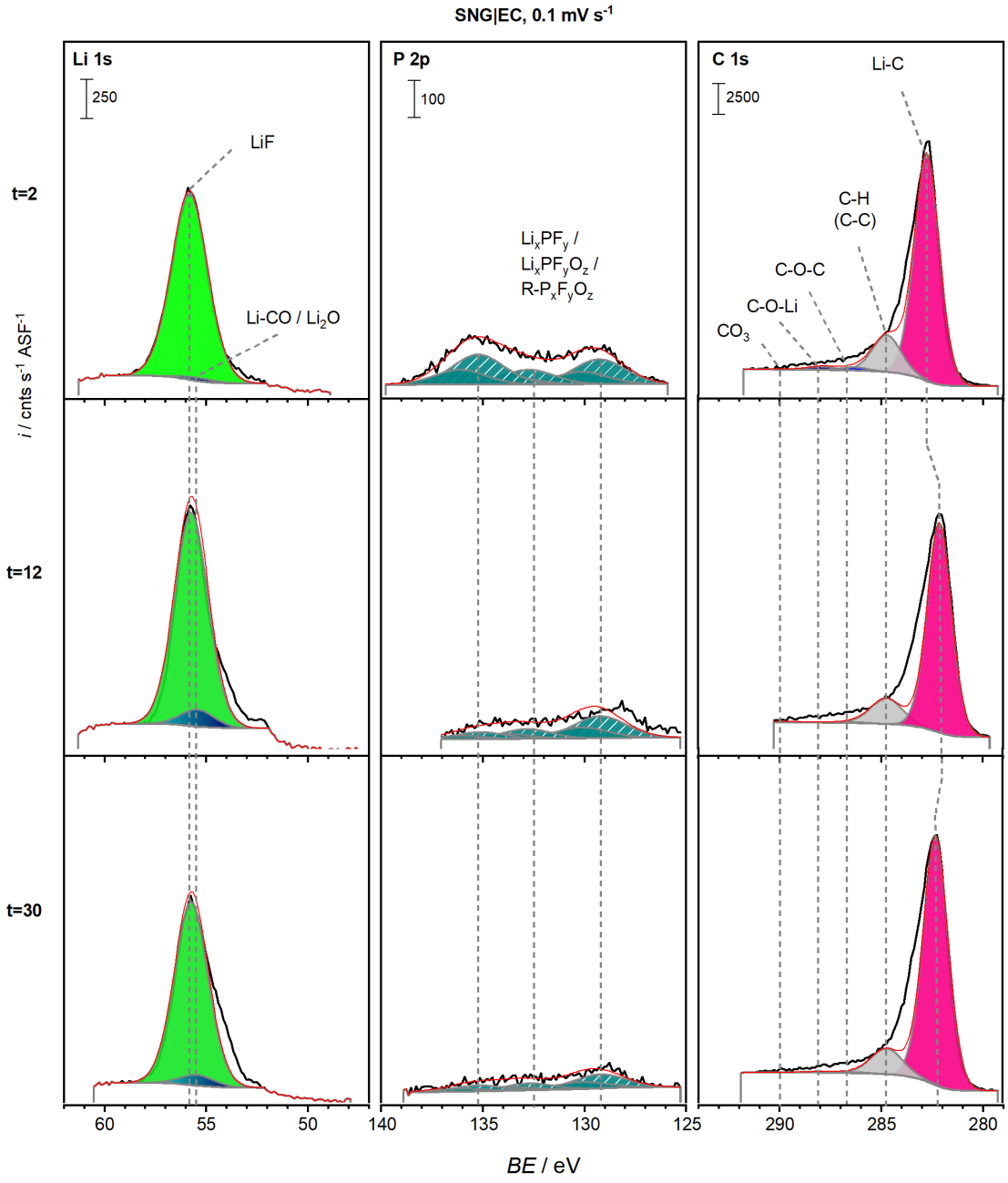

Figure S4-7. Li 1s, P 2p and C 1s spectra of the SEI formed on SNG cycled in EC-based electrolyte at 0.1 mV s^{-1} after 2 (t=2), 12 (t=12) and 30 minutes (t=30) of consecutive sputtering.

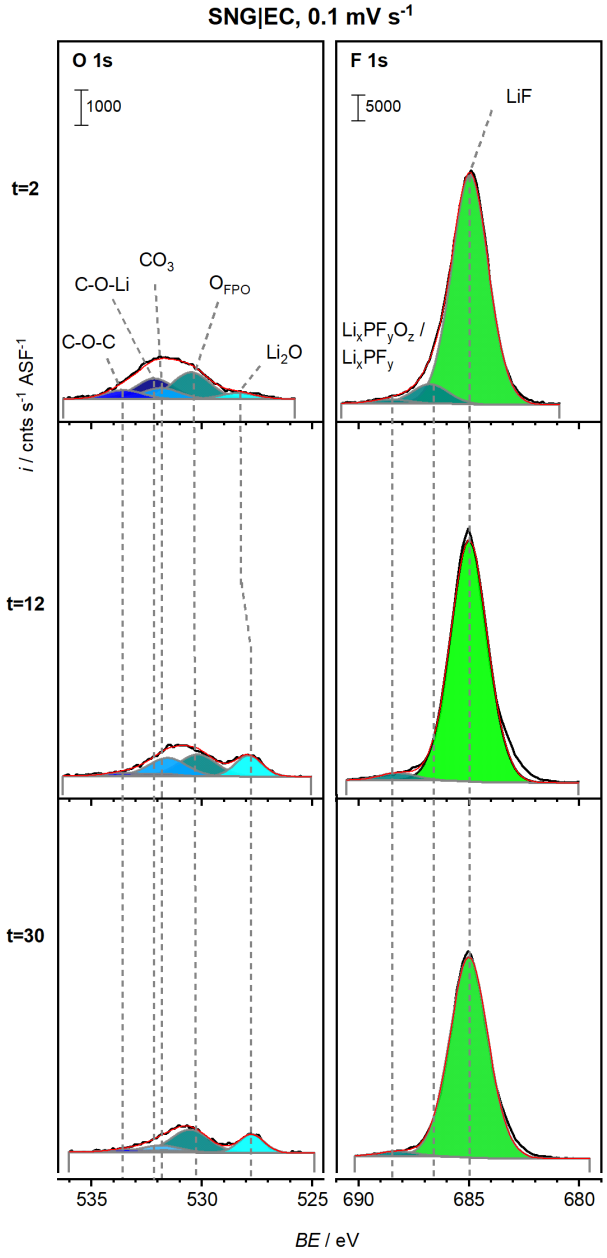

Figure S4-8. O 1s and F 1s spectra of the SEI formed on SNG cycled in EC-based electrolyte at 0.1 mV s^{-1} after 2 (t=2), 12 (t=12) and 30 minutes (t=30) of consecutive sputtering.

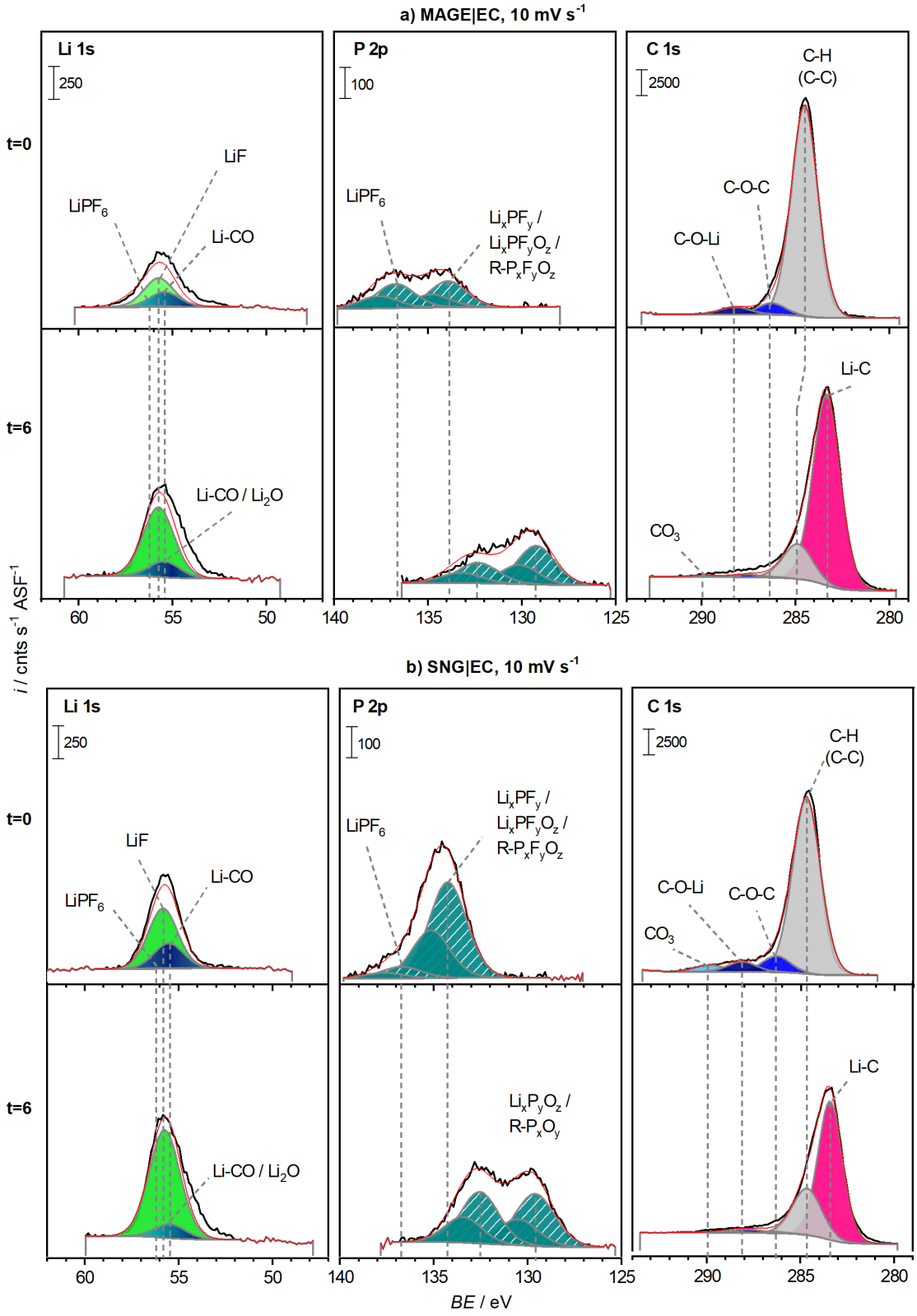

Figure S4-9. Li 1s, P 2p and C 1s spectra of the SEI formed on a) MAGE and b) SNG graphite electrodes cycled in EC-based electrolyte at 10 mV s^{-1} before (t=0) and after 6 (t=6) minutes of consecutive sputtering.

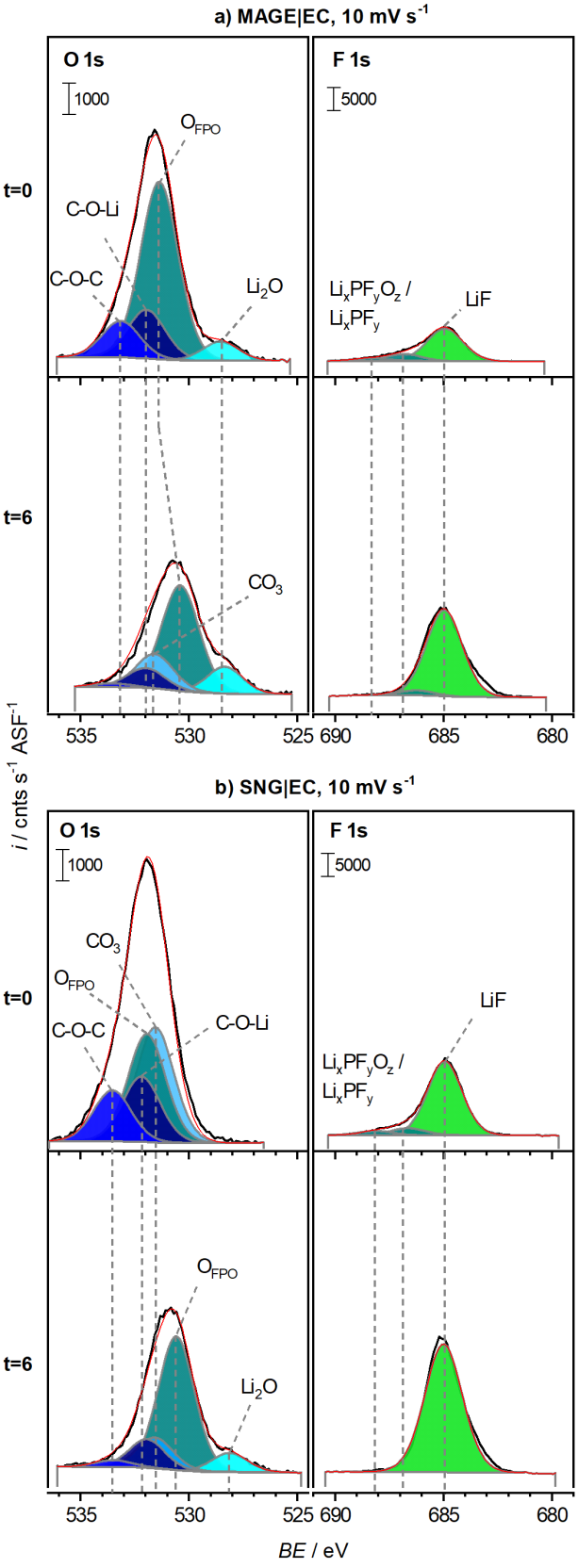

Figure S4-10. O 1s and F 1s spectra of the SEI formed on a) MAGE and b) SNG graphite electrodes cycled in EC-based electrolyte at 10 mV s^{-1} before (t=0) and after 6 minutes (t=6) of consecutive sputtering.

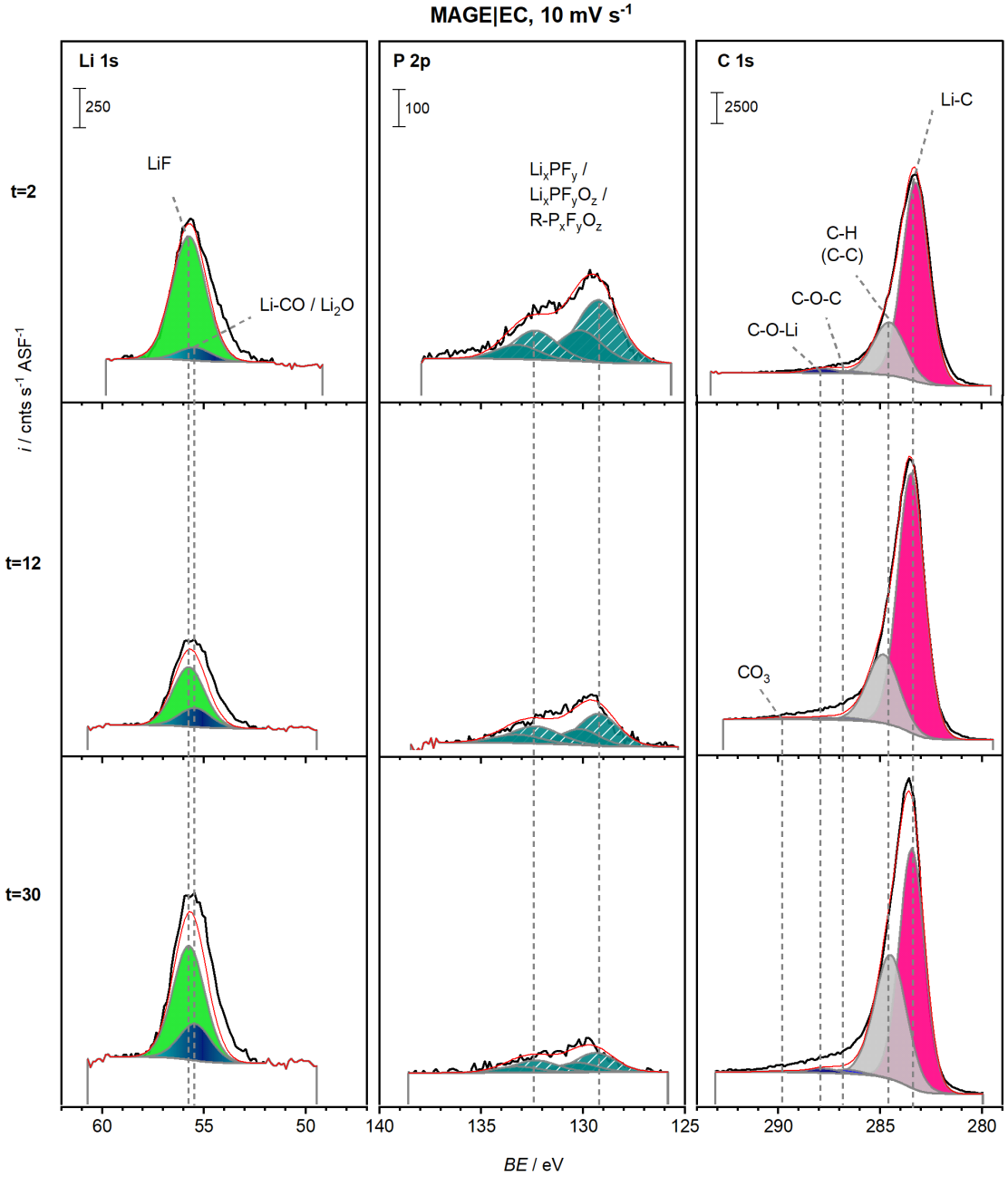

Figure S4-11. Li 1s, P 2p and C 1s spectra of the SEI formed on MAGE cycled in EC-based electrolyte at 10 mV s^{-1} after 2 (t=2), 12 (t=12) and 30 minutes (t=30) of consecutive sputtering.

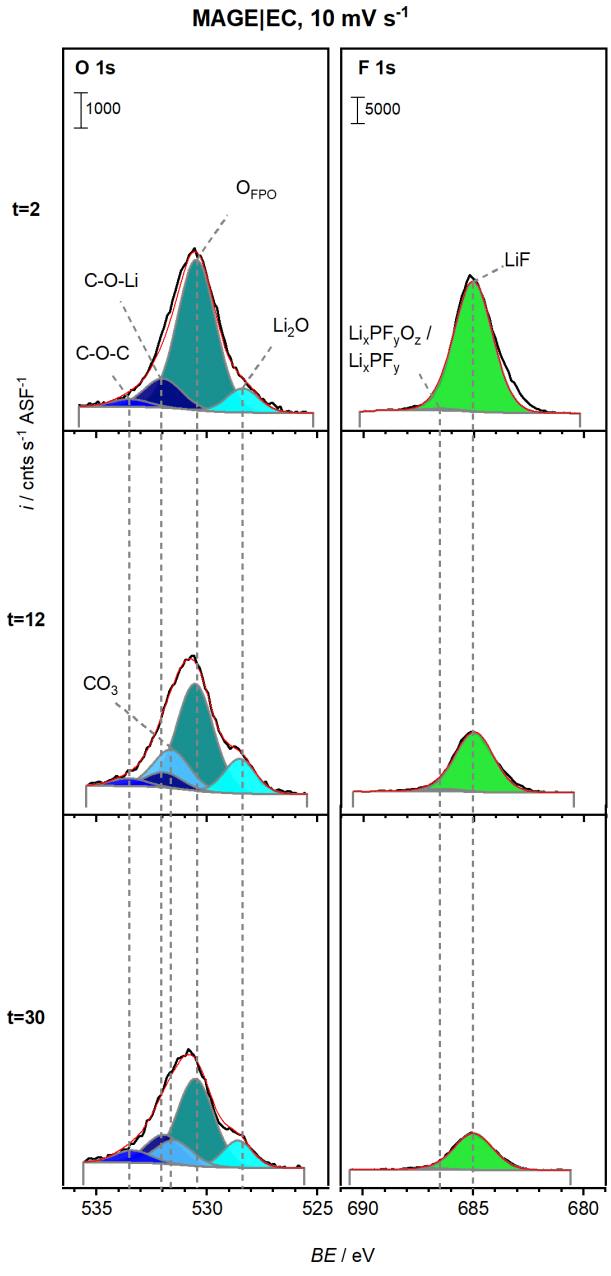

Figure S4-12. O 1s and F 1s spectra of the SEI formed on MAGE cycled in EC-based electrolyte at 10 mV s^{-1} after 2 (t=2), 12 (t=12) and 30 minutes (t=30) of consecutive sputtering.

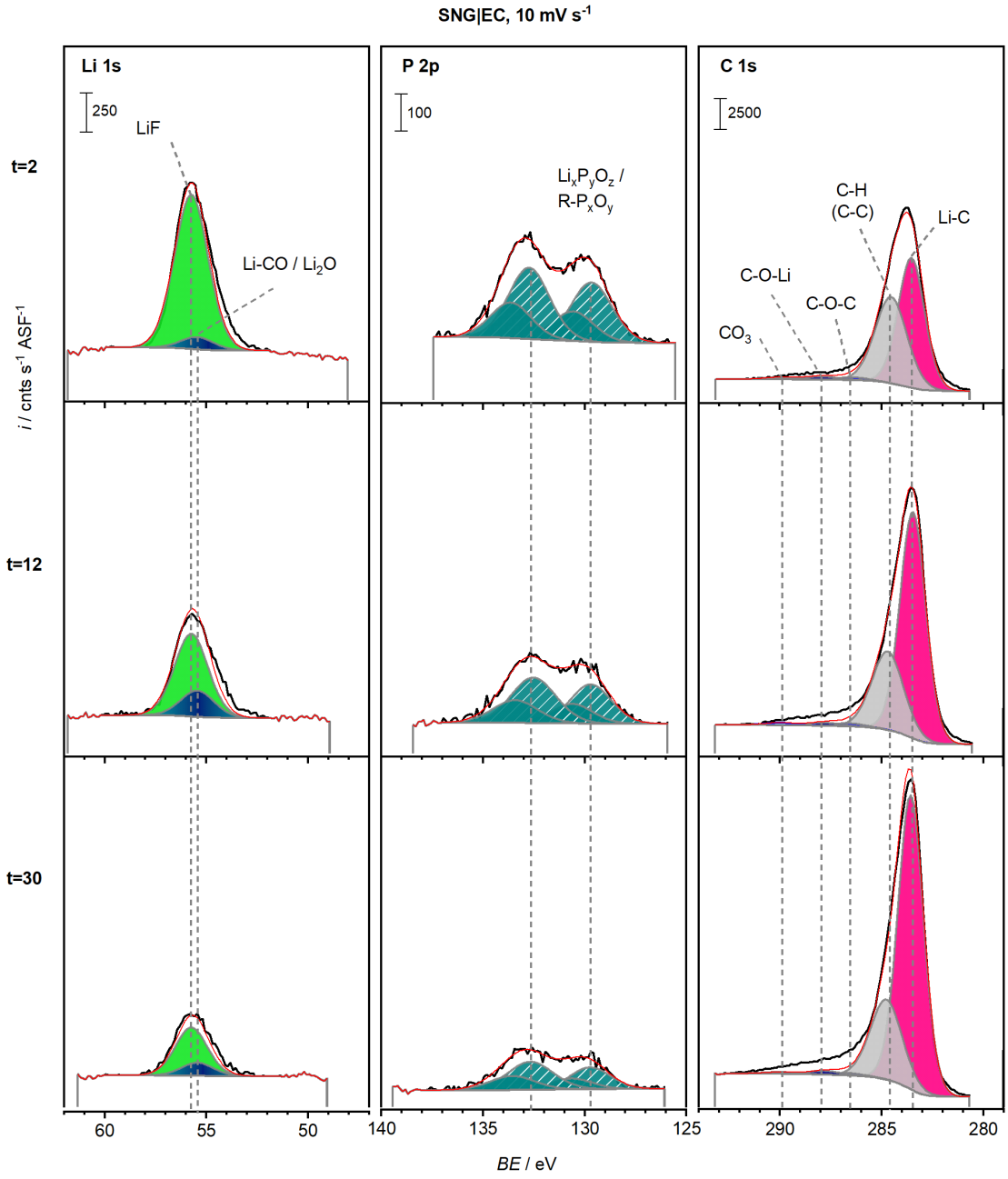

Figure S4-13. Li 1s, P 2p and C 1s spectra of the SEI formed on SNG cycled in EC-based electrolyte at 10 mV s^{-1} after 2 (t=2), 12 (t=12) and 30 minutes (t=30) of consecutive sputtering.

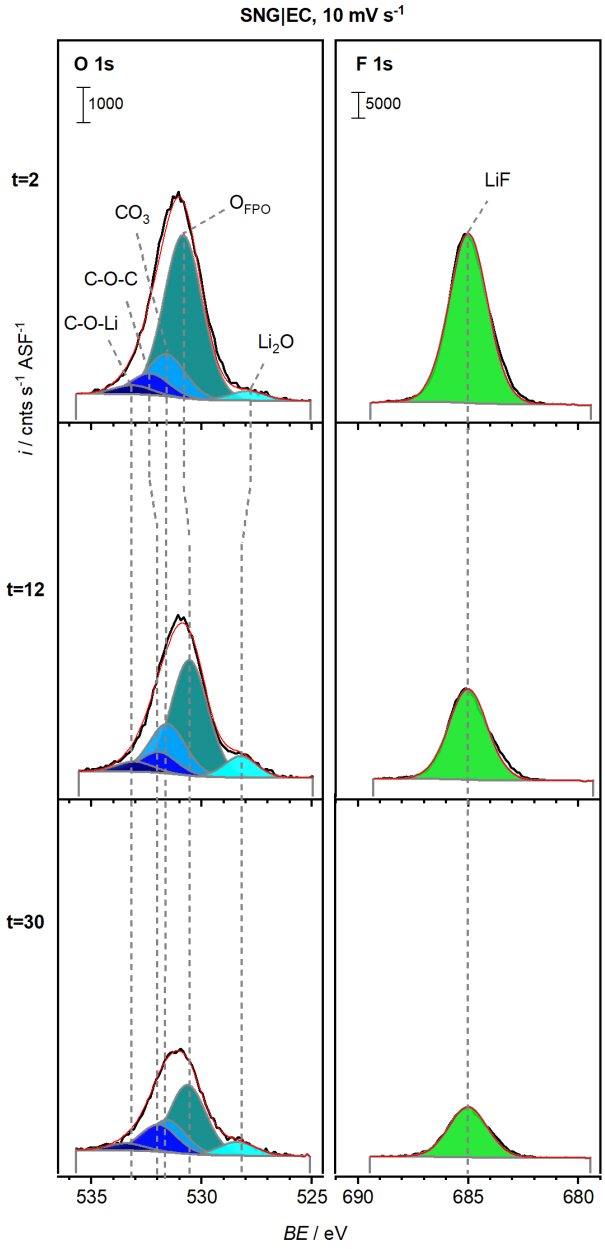

Figure S4-14. O 1s and F 1s spectra of the SEI formed on SNG cycled in EC-based electrolyte at 10 mV s^{-1} after 2 (t=2), 12 (t=12) and 30 minutes (t=30) of consecutive sputtering.

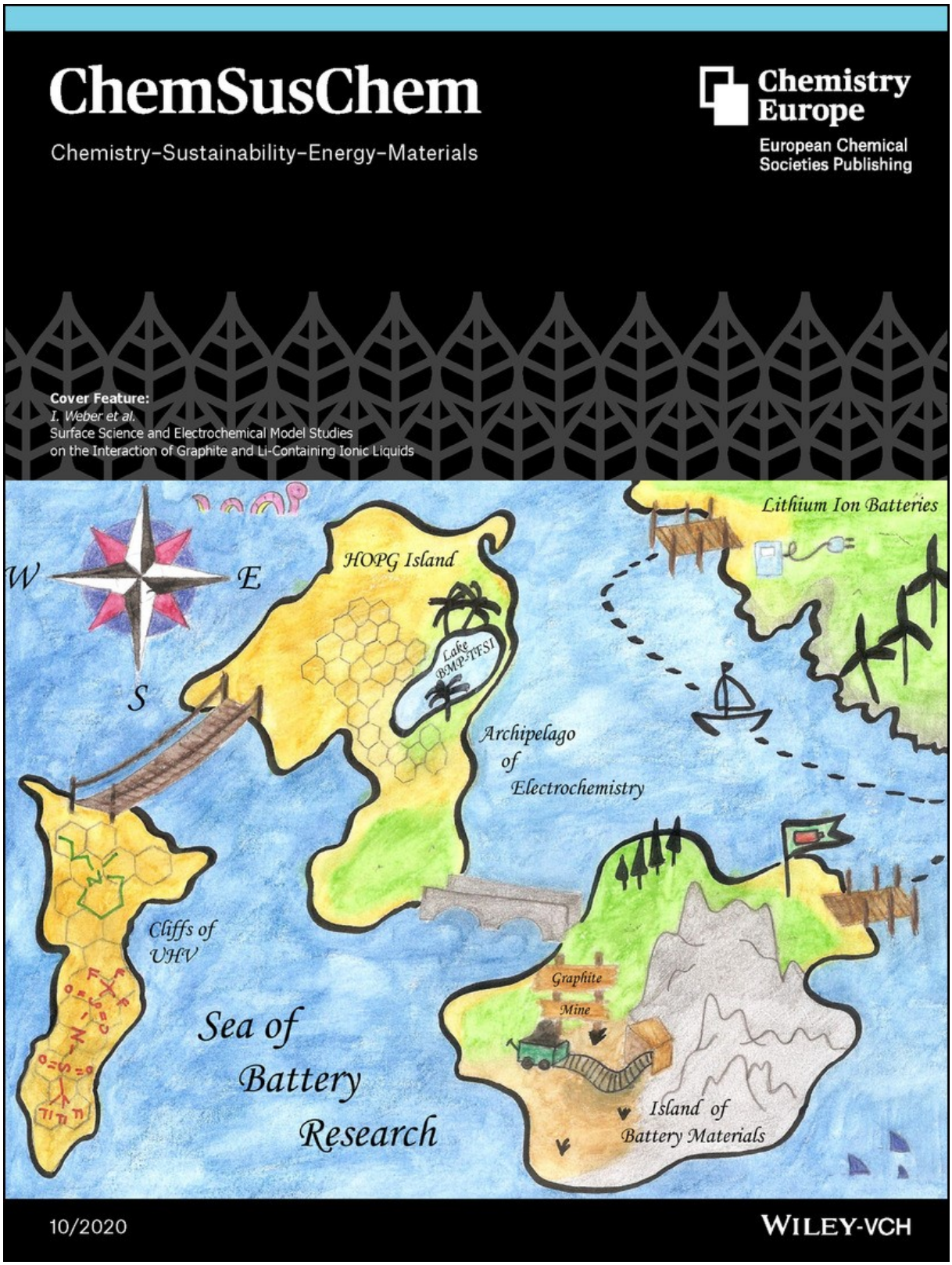

Reprinted with permission from John Wiley and Sons.

5. Surface Science and Electrochemical Model Studies on the Interaction of Graphite and Li-Containing Ionic Liquid

The content of the following chapter, including the graphical abstract (Figure 5-0), was published in ChemSusChem 2020, volume 13 pp. 2589-2601, and is reprinted with permission from John Wiley and Sons.[219]

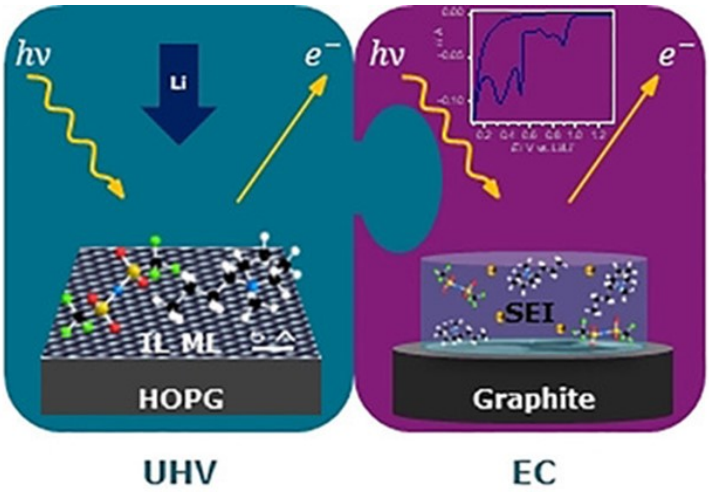

Interphase formation during Li post-deposition on multilayers of the ionic liquid (IL) 1-butyl-1-methylpyrrolidinium bis(trifluoromethylsulfonyl) imide (BMP-TFSI) on highly oriented pyrolytic graphite is studied under vacuum and during electrochemical cycling of graphite electrodes in Li^+-containing BMP-TFSI by using X-ray photoelectron spectroscopy. BMP^+ decomposition occurs preferentially during Li^0-induced IL decomposition, whereas electrochemical cycling leads to $TFSI^-$ reduction.

Figure 5–0. Graphical Abstract.

For the following chapter, the Experimental section of the original publication was removed in order to avoid duplication; its contents can be found in Chapter 2.2 of this thesis. The style, spelling, sections, enumeration, references and figures were adapted to fit the current layout. The figures and tables published in the Supporting Information were added at the end of the chapter.

I contributed the electrochemical experiments to this manuscript, while Dr. J. Kim (Institute of Surface Chemistry and Analysis, Ulm University) and Dr. F. Buchner (Institute of Surface Chemistry and Analysis, Ulm University) provided the XPS data. I evaluated the experimental data – with great help from Dr. J. Kim for the XPS plotting and analysis – and was heavily involved in the creative process of the publication.

Financial support was granted by the German Federal Ministry of Education and Research (BMBF) in the project 03X4636C ('Li-EcoSafe – Entwicklung kostengünstiger und sicherer Lithium-Ionen-Batterien'), and by the Deutsche Forschungsgemeinschaft via project ID 422053626 (Cluster of Excellence 'Post-Li Storage') and project BE 1201/22-1 ('Zn-Air Batteries'). This work contributes to the research performed at CELEST (Center for Electrochemical Energy Storage Ulm-Karlsruhe).

5.1. Abstract

We have systematically investigated the process of solid electrolyte interphase (SEI) formation and its chemical composition on carbon electrodes in an ionic liquid-based, Li-containing electrolyte in a combined surface science and electrochemical model study using highly oriented pyrolytic graphite (HOPG) and binder-free graphite powder electrodes (MAGE) as model systems. The chemical decomposition process was explored by deposition of Li on a pre-deposited multilayer film of 1-butyl-1-methylpyrrolidinium bis (trifluoromethylsulfonyl) imide (BMP-TFSI) under ultrahigh vacuum conditions. Electrochemical SEI formation was induced by and monitored during potential cycling in BMP-TFSI + 0.1 M LiTFSI. The chemical composition of the resulting layers was characterized by X-ray photoelectron spectroscopy (XPS), both at the surface and also in deeper layers, closer to the electrode|SEI interface, after partial removal of the film by Ar^+ ion sputtering. Clear differences between chemical and electrochemical SEI formation, and also between SEI formation on HOPG and MAGE electrodes, are observed and discussed.

5.2. Introduction

Lithium ion batteries (LIBs) are heavily used in portable communication devices and in the transportation sector due to their low self-discharge and memory effect, high specific energy and long cycle lives.[7,15] Typically, they consist of Li^+-hosting electrode materials[13,28,186] and blends of carbonate solvents mixed with Li^+-containing salts as electrolyte.[21,22,65] Despite considerable progress, however, LIBs still suffer – at least in part – from the use of flammable and/or poisonous electrolytes. Certain ionic liquids (ILs) have been shown to exhibit very low vapor pressures and, consequently, low flammability, while at the same time possessing the high electrochemical stability window which is required for the use of high-voltage cathodes.[106,108,110,136,220,221] Drawbacks, on the other hand, are their high viscosity, low conductivity and currently high costs. Nevertheless, they have been carefully studied for potential battery applications.[103,104,111,135,222-226]

Key factor for the stability of a LIB is the so-called solid electrolyte interphase (SEI), which is formed by decomposition of the electrolyte during charge and discharge.[51,54,55,189] It passivates the anode surface towards further electrolyte decomposition and thus prevents electrolyte depletion, while at the same time protecting the electrode from corrosion. Despite of numerous studies, a microscopic understanding of the SEI formation process is still lacking; mainly because of the complex composition of electrodes and electrolyte in realistic systems. Here, model studies using simplified components and often also simplified preparation conditions come into play, allowing a better identification of the significant processes and interactions. Disadvantage of these model studies is however, that they may be of limited relevance for realistic systems / conditions.

This is background of the present paper, where we report on the results of a combined electrochemical and surface science-type model study on the formation of such passivation layers on the well-defined basal surface of highly oriented, pyrolytic graphite (HOPG) electrodes and on binder-free graphite powder model electrodes, where the latter are closer to realistic systems, upon interaction with the IL 1-butyl-1-methylpyrrolidinium bis (trifluoromethylsulfonyl) imide (BMP-TFSI) and Li^0/0.1 M LiTFSI. This approach allows us to stepwise bridge the gap between idealized model studies performed under ultrahigh vacuum (UHV) conditions, and more realistic electrode material / SEI formation conditions.

The passivation layers were prepared either by vacuum deposition of BMP-TFSI and Li^0 on HOPG in UHV, or by potentiodynamic cycling of graphite electrodes in BMP-TFSI + 0.1 M LiTFSI electrolyte. By comparing the composition of the adlayer / passivation layer created by these processes, as characterized by *ex situ* X-ray photoelectron spectroscopy (XPS), we want to i) learn about the role of the electrochemical conditions on the formation and composition of the resulting layer and ii) elucidate the effect of the graphite structure on the IL decomposition / SEI formation. The process of electrochemical SEI formation was monitored by cyclic voltammetry (CV). Furthermore, depth profiling of the SEI was performed by Ar^+ sputtering; as well as sputtering of pure LiTFSI and BMP-TFSI to verify the influence of the Ar^+ beam.

This work is part of a comprehensive effort to better understand the electrochemistry and decomposition behavior of ILs, specifically of BMP-TFSI, and typical salts such as LiTFSI. Due to its high decomposition temperature, very low vapor pressure and a large stability window ranging from -2.5 to 3.0 V vs. Ag/AgCl (about 0–5 V vs. Li/Li^+),[135] BMP-TFSI is a very promising candidate for LIBs. Special interest was placed on the interactions at the

substrate|IL interface under UHV conditions using several model substrates,[129] e.g., single-crystalline metal surfaces,[122,123,137,227] oxide surfaces,[124,228,229] and highly oriented pyrolytic graphite.[127,128] The above studies, which were conducted in the absence of an applied potential and which focused on the structure formation and the decomposition of the ionic liquid, clearly demonstrated that the chemical interaction with the substrate surface and/or with the added lithium is sufficient to cause decomposition of the IL. On the other hand, there is a large number of electrochemical model studies investigating the interaction of BMP-TFSI with a variety of different electrodes under electrochemical conditions. Examples include Li (Li-coated Cu),[153,230] Pt,[231-233] Au[231,233] and glassy carbon[231] as well as HOPG[234] and graphite composite electrodes.[235] These studies revealed that the comparatively large stability window of BMP-TFSI is greatly influenced and diminished by the presence of traces of moisture and other contaminants.[132,232,233,236,237] Electrolyte degradation has been reported to progress via reductive $TFSI^-$ decomposition[153,226,230,234] and subsequent SEI formation / surface passivation.[234] In addition, the presence of 0.12 M of LiTFSI has been shown to enhance $TFSI^-$ decomposition on Pt in 1-ethyl-3-methylimidazolium (EMIm)-TFSI.[238] Furthermore, employing *in situ* scanning tunneling microscopy (STM), Hu *et al.* observed that reductive cation decomposition takes place in the first cathodic scan when cycling a HOPG electrode in 0.5 M LiTFSI-containing 1-methyl-3-propyl-pyrrolidinium (MPP)-TFSI.[239] The authors claimed that MPP^+ decomposition is related to reversible cation co-intercalation into the anode substrate, which was concluded from an increase of the step height on the HOPG surface.[239] Employing *in situ* atomic force microscopy (AFM), Shi *et al.* similarly suggested reversible cation co-intercalation into step edges of HOPG.[234] For more realistic battery materials such as graphite composite electrodes consisting of KS6 graphite, Carbon SuperP and polyvinyliden difluoride binder it was found that $TFSI^-$ is too stable, hindering the formation of a SEI which can support continuous cycling.[240] However, the formation of a passivation layer with SEI-like features was observed when cycling composite electrodes consisting of various graphite materials and binder in LiTFSI-containing 1-methyl-1-propylpiperidinium (MPPp)-TFSI.[235]

In the following, we first give a brief account of the experiments conducted at the graphite|BMP-TFSI + 0.1 M LiTFSI interphase during electrochemical cycling at different scan rates on i) well-defined, basal HOPG electrodes and ii) on binder-free graphite powder model electrodes, which are closer to realistic systems. By comparing the two model electrodes, we want to study the effect of the graphite structure on the IL decomposition / SEI formation. *Ex situ* X-ray photoelectron spectroscopy (XPS) was employed in order to compare

the 'chemical' SEI formed via vapor-deposition of multilayers of IL and subsequent Li post-deposition on the well-defined substrate in UHV to the 'electrochemical' SEI formed during cyclic voltammetry (CV). Furthermore, depth profiling of the SEI was performed by Ar^+ sputtering; as well as sputtering of pure LiTFSI and BMP-TFSI to verify the influence of the Ar^+ beam.

5.3. Results and Discussion

5.3.1. Electrochemical Characterization

First, we recorded cyclic voltammograms (CVs) on HOPG and on binder-free MAGE graphite in LiTFSI-containing IL, which will be denoted as HOPG(Mage)|IL + LiTFSI, at different scan rates (potential range 1.5-0.02 V). **Figure 5-1** depicts the first three cycles of the CVs recorded at 0.1 mV s^{-1} (top) and the first cycle recorded on the same materials at 0.1, 1 and 10 mV s^{-1} (bottom). Further cycles recorded at intermediate and fast scan rates are presented in the Supporting Information in **Figure S5-2** and **Figure S5-3** (section 5.5.2). In the following, we will first discuss the potential range positive of 0.3 V and then the range 0.3–0.02 V.

5.3.1.1. Potential Region from 1.5 to 0.3 V

Starting with CVs recorded on the basal HOPG substrate at slow scan rate (0.1 mV s^{-1}), the first cathodic scan shows a pre-peak at 0.7 V ($^{0.1}H_1$) and a maximum at 0.6 V ($^{0.1}H_2$) (**Figure 5-1**a). For the CVs recorded at intermediate and fast scan rate, respectively (1 and 10 mV s^{-1}, **Figure 5-1**c and **Figure S5-2** in section 5.5.2), the peaks shift to lower potentials, namely to 0.6 ($^{1}H_1$) and finally to 0.4 V ($^{10}H_1$). No corresponding signals appear in the anodic scan above 0.3 V. These cathodic peaks disappear after the first cycle, regardless of the scan rate. Such behavior is typical for systems showing an irreversible surface passivation, as it was also observed for HOPG electrodes in organic electrolytes.[64,68] Accordingly, we assign the peaks to electrolyte decomposition, which results in self-poisoning for this process. Interestingly, a very similar peak is also observed in the CV of neat BMP-TFSI on HOPG, as shown in **Figure 5-2**, which indicates that the reductive decomposition process does not directly involve the Li^+ ion. However, the Li^+ cations (or possibly water) appear to enhance the electrolyte decomposition, as the current density is much higher when LiTFSI is added to the IL (which may also increase the resulting water content).

Previous results reported for HOPG-based systems are contradictory. Gasparotto *et al.* reported a rather featureless CV in the first cycle for HOPG in 0.5 M LiTFSI-containing BMP-TFSI in the potential window of 1.0 to -2.0 V vs. Pt[241] (about -1.5 to -4.5 V vs. Li/Li^+). Exploring the

electrochemical properties of a HOPG electrode in BMP-TFSI + 0.5 M LiTFSI, Shi *et al.* observed a very small reduction peak at around 1.0 V in the cathodic scan, which, based on comparison with BMP-FSI (bis (fluorosulfonyl) imide), they assigned to reductive decomposition of $TFSI^-$.[234] Finally, also for a HOPG electrode but in MPP-TFSI + 0.5 M LiTFSI, Hu and coworkers reported a basically featureless CV (first scan) in the potential region between 1.5-0.3 V, with a minor reduction signal around 0.6 V. They, too, assigned the signal to reductive anion decomposition.[239]

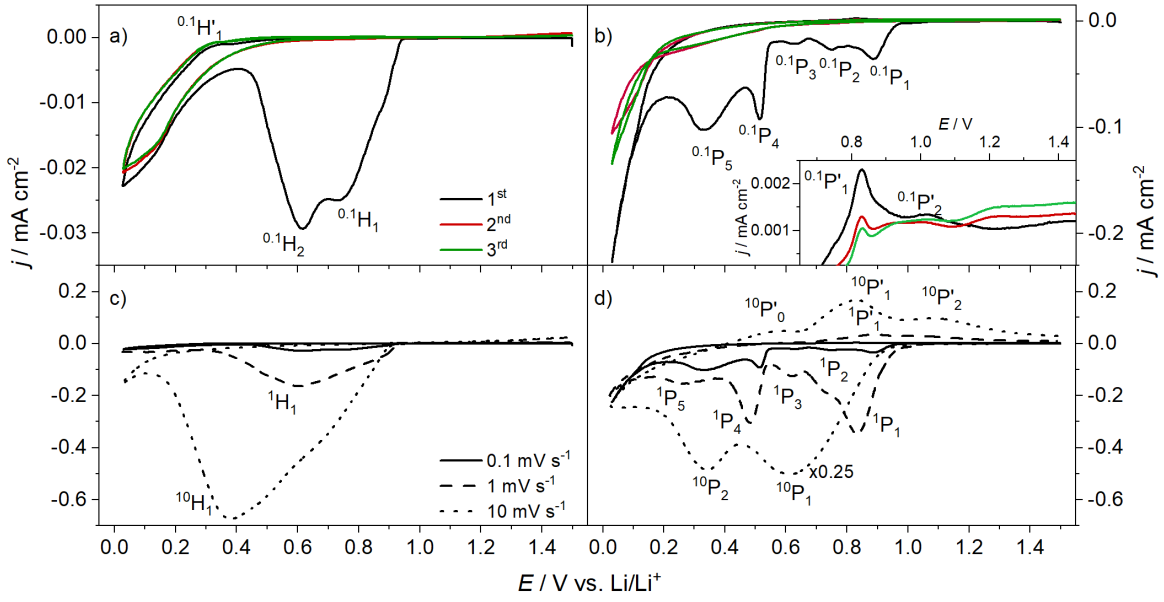

Figure 5-1. Cyclic voltammograms recorded on a) HOPG and b) MAGE in BMP-TFSI + 0.1 M LiTFSI at 0.1 mV s 1 for three cycles, and the influence of the scan rate (10, 1 and 0.1 mV s 1) during the first cycle on c) HOPG and d) MAGE. The inset in b) shows an enlarged part of the anodic scan(s). Peaks are marked H for HOPG and P for powder (MAGE) electrodes, with indices for the scan speed (0.1, 1, 10) and the peak number (in the order of their appearance). Anodic peaks are marked by an asterisk.

The CVs recorded on the MAGE powder electrodes appear more complex. When cycling at slow scan rate, we observe a cathodic peak already at 0.9 V ($^{0.1}P_1$). It behaves akin to the H_1 peak, shifting towards more negative potentials with increasing scan rate. Furthermore, it only appears in the first cycle. Therefore, we similarly assign it to a reductive, self-poisoning anion decomposition process leading to surface passivation for this process. The more positive reduction potential (peak maximum) compared to the HOPG substrate reflects the presence of more active sites on the graphite powder electrode compared to the HOPG substrate. Previous studies on binder-containing graphite compound electrodes reported that the reductive processes begin at 0.8 V in the cathodic scan, which was assigned to partly reversible BMP^+

intercalation.[235,242,243] Appetecchi *et al.* and Nádherná *et al.* both reported several irreversible reduction peaks between 0.8 and 0.3 V for graphite composite electrodes in BMP-TFSI in the first cathodic scan and more or less complete passivation of the surface towards further reductive reactions, while Li (de-)intercalation was still possible.

They, too, assigned these peaks to cation co-intercalation, arguing that a) $TFSI^-$, as compared to FSI^-, is too stable and hence does not decompose,[240] and that b) FSI^- decomposition starts above 1.0 V and thus SEI formation takes place above the BMP^+ intercalation potential range.[244] However, these studies were conducted in dried electrolyte systems. It is therefore possible that the as-received electrolytes used by us undergo surface passivation due to residual moisture / oxygen contamination. Moving on in the cathodic scan on our MAGE powder electrode, a second peak (P_2) appears at about 0.7 V, i.e., at the same potential as the $^{0.1}H_1$ peak, and a third peak (P_3) at about 0.6 V. Neither of them shifts when changing to an intermediate scan rate, indicating that they are due to (reversible) site-specific surface processes such as BMP^+ adsorption. At present, however, this cannot be specified further. Finally, two peaks appear at 0.5 (P_4) and 0.3 V (P_5) at slow and intermediate scan rates, which were not resolved on the HOPG electrode and thus seem to be characteristic for the graphite powder electrode. Changing to the fast scan rate, we find a P_1 peak at 0.6 V, which we assume corresponds to the down-shifted P_1 peak at slower scan rates, possibly together with the not or only slightly shifted P_2 and P_3 peaks. The next peak appearing at 0.3 V, we assume to correspond to the down-shifted P_4 at the slower scan rates, and we therefore denote it as $^{10}P_4$. There is no detectable analogue to the P_5 peak at 10 mV s^{-1}.

Interestingly, during intermediate scan rate, the peak $^1P_4$ was detected over twenty cycles (see Supporting Information, **Figure S5-3**). The cathodic signals at lower potentials seem to be correlated with the anodic peaks at around 0.8–0.9 V (P'_1) and 1.0 V (P'_2) in the anodic scan at all scan rates, whose current densities decrease in parallel to the current density of the signals P_4 and P_5. Thus, we suggest that these signals are due to (partly) reversible BMP^+ co-intercalation, in agreement with previous assignments.[240,244] It takes place in addition to increasing surface passivation, at least with respect to electrolyte decomposition (H_1/P_1). Our suggestion also agrees with the conclusions of an *in situ* Raman study by Markevich *et al.*, in which they assigned reduction signals between 0.7 and 0.5 V and around 0.3 V to cation co-intercalation and other ones around 0.8 and 0.2 V to irreversible $TFSI^-$ decomposition.[242]

5.3.1.2. Potential Region from 0.3 to 0.02 V

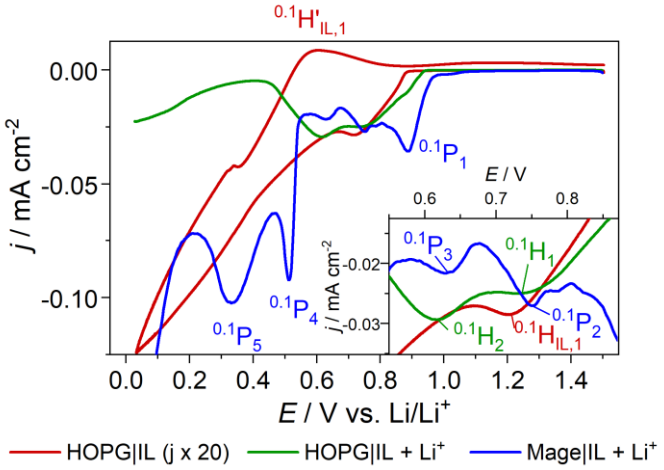

Figure 5-2. Comparison of the CVs (1st cycle) of HOPG in BMP-TFSI (red), HOPG in BMP-TFSI + 0.1 M LiTFSI (green) and MAGE in BMP-TFSI + 0.1 M LiTFSI (blue) cycled at 0.1 mV s^{-1}. The inset shows the enlarged current traces in the reduction region between 0.9 – 0.5 V.

Below ~0.3 V in the CV recorded on HOPG|IL + LiTFSI (**Figure 5-1**a and c), the reductive currents grow exponentially until the lower potential limit. The same applies for the CVs recorded on MAGE in Li^+-containing ionic liquid (**Figure 5-1**b and d) and on HOPG in neat ionic liquid (**Figure 5-2**). Such an increase in reductive currents in Li^+ containing electrolyte at potentials below 0.2 V is usually attributed to Li^+ intercalation into graphite.[11] While the intercalation of Li^+ into the basal plane of HOPG substrates is very slow,[160,161] it still may take place, e.g., via step and edge defects on the surface.[130,185,228,242] In addition to Li^+ intercalation, the currents observed around 0.2 V have also been attributed both to $TFSI^-$ decomposition[242] and to BMP^+ intercalation as competing processes.[240,244] Furthermore, a subtle shoulder is present at ~0.3 V in the anodic scan on HOPG|IL + LiTFSI (peak H'_1, see Supporting Information, **Figure S5-2** and **Figure S5-3**) in the CVs, independent of the scan rate. At certain conditions (scan rate, cycle number), the net current at that peak is negative due to the superposition with cathodic decomposition processes. While a typical process in this potential region in the anodic scan would be Li^+ de-intercalation, we favor an explanation where this peak arises from the re-oxidation of adsorbed decomposition products. This, we conclude from the appearance of a similar feature at 0.3 V in the CV recorded in Li-free electrolyte ($^{0.1}H'_{IL,1}$). The absence of Li^+ de-intercalation seems to indicate that the concentration of defect sites on the HOPG electrodes is too low for significant contributions from Li^+ inter- and de-intercalation.

As the concentration of defect sites on the MAGE powder electrode is much higher than on the HOPG substrate, the currents starting at 0.2 V are more than ten times higher than the ones observed on HOPG. However, like on HOPG, no corresponding Li^+ de-intercalation features appear in the anodic scan up to 0.3 V, where they have been observed in organic carbonate-based electrolytes on similar graphite compound electrodes.[235] It is worth noting that, studying the Li^+ intercalation behavior on composite KS6L graphite electrodes in different IL compositions, among them BMP-TFSI + 0.7 M LiTFSI, Nádherná *et al.* found Li^+ de-intercalation peaks between 0.0 and 0.4 V in all of these electrolytes.[244] On the other hand, Appetecchi *et al.,* using composite KS6 graphite electrodes and BMP-TFSI + 0.3 M LiTFSI, observed only little and varying Li^+ (de-)intercalation currents.[240] They attributed these variations to the inherent stability of $TFSI^-$ and the subsequently slower formation of a stable SEI. The latter was considered to be essential for reversible Li^+ intercalation, as it is observed for the less stable FSI^-.[240] Zheng *et al.* cycled natural graphite composite electrodes in trimethyl-n-hexylammonium (TMHA)-TFSI + 1 M LiTFSI.[245] They, too, observed only minor Li^+ (de-)intercalation. However, both the cathodic and the anodic current densities around 0 V increased with increasing cycling time, while the (supposed) IL cation co-intercalation currents at higher potentials decreased. This is particularly the case after the addition of SEI-forming additives, such as vinylene carbonate.[245]

We agree with the above authors that the processes taking place in BMP-TFSI (+ LiTFSI) on our model substrates do not lead to the formation of a functional SEI layer. We suggest that two catalytic electrolyte decomposition processes are at play: one at potentials above 0.3 V, which is rapidly inhibited, and another one occurring at potentials below 0.3 V, which is not necessarily affected by this self-poisoning process and continues for several cycles. It is not clear if, especially on the graphite powder electrode, the latter process is also accompanied by Li^+ or BMP^+ intercalation and whether it results in the formation of a surface layer that passivates against further insertion processes. In recent DEMS studies, we found indirect evidence for the formation of adsorbed decomposition products in Li^+-containing BMP-TFSI.[132] This was concluded from the lack of volatile decomposition products during the reduction in Li^+-containing electrolyte, while BMP^+ and $TFSI^-$ fragments were found in neat and Mg^{2+}-containing IL.[132].

5.3.2. XPS Characterization

In order to gain a more detailed understanding of the formation and composition of this passivation layer, we employed X-ray photoelectron spectroscopy for the characterization of

additional model systems. Beginning with a well-defined, UHV-prepared model system, we first studied the effect of Li post-deposition on a multilayer film of BMP-TFSI, which was pre-deposited under UHV conditions on a HOPG substrate. In addition, we also recorded detail spectra from a LiTFSI powder sample as reference. Next, we characterized a HOPG working electrode which was exposed to BMP-TFSI + 0.1 M LiTFSI at open circuit potential (OCP) for 68 h. In a third step, we studied a similar electrode and a MAGE powder electrode after the potential cycling discussed in the previous section. Finally, sputtering of LiTFSI salt as well as depth profiling experiments of the HOPG sample after immersion into the IL at the OCP and of the electrochemically cycled graphite electrodes (both HOPG and MAGE) were conducted using Ar^+ sputtering.

5.3.2.1. Comparison: A Chemically and an Electrochemically Formed SEI

In **Figure 5-3**, we compare XP core level spectra of the F 1s, Li 1s, O 1s, N 1s, C 1s and S 2p regions of the SEI formed on the HOPG substrate after vapor deposition of a BMP-TFSI multilayer film (10 ML) (**Figure 5-3**a), after subsequent Li deposition (**Figure 5-3**b) under UHV conditions, and of the SEI formed electrochemically on the HOPG and MAGE substrates by potential cycling in a 0.1 M LiTFSI-containing BMP-TFSI electrolyte (**Figure 5-3**e and f). XP reference spectra of LiTFSI (Li salt) and of the 0.1 M LiTFSI in BMP-TFSI electrolyte are also displayed (**Figure 5-3**c and d).

We begin by briefly describing the characteristic XP spectra of the BMP-TFSI multilayer film deposited on HOPG under UHV conditions (**Figure 5-3**a), which will be used as reference spectra for the following experiments. In the detail spectra of the different regions, all $TFSI^-$-related peaks are colored blue and all BMP^+-related ones red. In the F 1s spectrum, a single peak appears at 689.5 eV, originating from the F atoms of the $-CF_3$ group in the $TFSI^-$ anion (F_{TFSI}). The O 1s spectrum shows a peak at 533.3 eV, which is related to the $TFSI^-$ sulfonyl groups (O_{TFSI}). Two well-separated peaks in the N 1s spectrum at 403.3 and 400.0 eV represent the nitrogen atoms within the pyrrolidinium cation (N_{BMP}) and the imide anion (N_{TFSI}), respectively. Their intensities show a 1 : 1 ratio of $N_{BMP} : N_{TFSI}$, as expected for molecularly adsorbed BMP-TFSI species. In the C 1s region, the signal at 293.5 eV is assigned to the $-CF_3$ group (C_{TFSI}) of the $TFSI^-$ anion, while the ones at 287.3 eV and 286.0 eV, respectively, represent the carbon bonded to nitrogen (C_{hetero}) and the alkyl-type carbon atoms (C_{alkyl}) of the BMP^+ cation. Similar to the N 1s region, the C 1s spectrum reflects molecularly adsorbed BMP-TFSI with a peak area ratio $C_{TFSI} : C_{hetero} : C_{alkyl}$ of 1.8 : 4.3 : 5, in agreement with the nominal atomic ratio of 2 : 4 : 5 in BMP-TFSI. A low-intensity shoulder at 284.6 eV is due to

the underlying graphite substrate (C_{sub}, filled grey),[147] which is strongly damped by the IL multilayer film. In the S 2p region, finally, a doublet for the $–SO_2CF_3$ species (S_{TFSI}) appears at 169.6 (S $2p_{3/2}$) and 170.8 eV (S $2p_{1/2}$). Our assignment is in agreement with the those reported previously for BMP-TFSI on metal (oxide)[122-124,129,153,227] and HOPG substrates,[127,129] as well as for similar ionic liquids containing $TFSI^-$ anions on Au(111).[246]

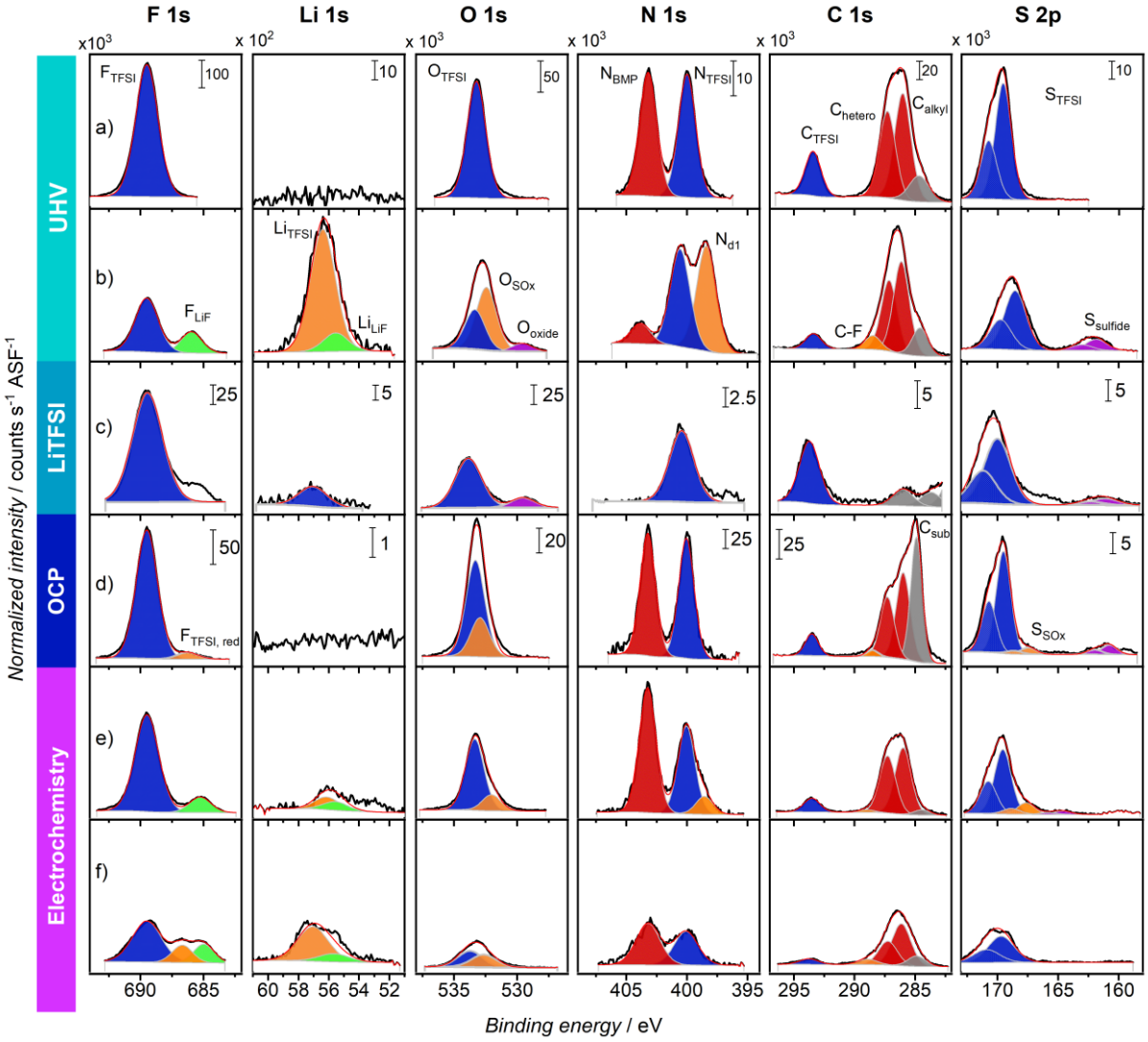

Figure 5-3. Core level spectra of the SEI formed on HOPG by vapor deposition under UHV conditions (a, b), of neat LiTFSI (c), of the surface layer formed on HOPG in LiTFSI-containing BMP-TFSI held at OCP (d), and of the SEI formed electrochemically on HOPG and MAGE (e, f). In detail: XP spectra of a) a 10 ML film of BMP-TFSI on HOPG prepared by vapor deposition, b) the same film after subsequent deposition of Li, c) LiTFSI salt for reference, d) a HOPG electrode held at OCP in BMP-TFSI + 0.1 M LiTFSI, and the SEI formed on HOPG (e) and on MAGE (f) by potential cycling in BMP-TFSI + 0.1 M LiTFSI. The intensity scales given in d) apply to e) and f), as well. A larger version of these spectra is given in the Supporting Information.

In the next step (**Figure 5-3**b), Li (~3 MLE) was post-deposited on the substrate covered by 10 ML of IL at r.t. The BMP^+- and $TFSI^-$-related peaks ($F_{TFSI,}$ O_{TFSI}, N_{BMP}, C_{TFSI}, S_{TFSI}, C_{hetero}, C_{alkyl}) decreased in intensity after the Li deposition step, indicating both partial cation and anion decomposition and/or desorption. At the same time, new peaks arise (filled orange) in the Li 1s, N 1s, C 1s and S 2p spectral ranges, which must be due to the formation of decomposition products. However, the losses in intensity differ not only between cation- and anion-related peaks, but also between different signals assigned to either anion (or cation) decomposition. Two exemplary cases are i) the N_{BMP} and corresponding N_{TFSI} peaks, which show a pronounced difference in intensity loss, and ii) the difference between N_{TFSI} and F_{TFSI} or C_{TFSI} peaks, where the decrease in the first one is much smaller than that in the latter ones. A quantitative discussion of the rather different trends in peak intensities will be given in the following.

Firstly, after Li deposition, the $F_{TFSI,}$ O_{TFSI} and C_{TFSI} peaks all decrease by about 60-65 %. The F_{TFSI} : C_{TFSI} ratio, which is 3 : 1 for $TFSI^-$, changes to 3.3 : 1, indicating a loss of the C component compared to the F component, even though they both originate from the $–CF_3$ groups of the anion. This discrepancy may be explained by the formation of new, fluorine-containing moieties, such as C-F species (C 1s: 290-287 eV[147]). This would be plausible, as they appear at an almost identical BE in the F 1s range as $–CF_3$, but at a significantly lower BE in the C 1s range. The transformation from $–CF_3$ to C-F is supported by the appearance of a new C 1s peak with low intensity at 288.5 eV (C-F, filled orange). The sum of the F 1s intensities in the C-F and $–CF_3$ peaks indeed accounts for the intensity of the F_{TFSI} peak in the F 1s region (within the error margins given by the atomic sensitivity factors (ASFs)). At the same time, a new peak appears at 685.8 eV in the F 1s spectrum (F_{LiF}, filled green), which we attribute to LiF.[147,227] Such a peak was recently obtained also upon stepwise deposition of Li onto an adsorbed IL (sub-) monolayer on HOPG under UHV conditions, where details about the decomposition mechanism were revealed by a combined computational analysis.[228] The formation of LiF decomposition products is also in excellent agreement with *ab initio* molecular dynamic simulations by Ando *et al.,*[247] which included electric field effects. These authors predicted that $TFSI^-$ is reduced on a lithium electrode independently of the applied potential. Briefly, $TFSI^-$ interaction with the Li electrode results in cleavage of the S-C and C-F bonds and the subsequent formation of LiF. Furthermore, XP spectra recorded after electrochemical measurements of an IL containing $TFSI^-$ anions and a Li salt also obtained LiF.[238] Its appearance in our measurement is also confirmed by a corresponding signal at 55.9 eV (filled green) in the Li 1s spectrum,[147] whose intensity corresponds to a 1 : 1 atomic

ratio of Li : F. The remaining peak area of the Li 1s signal is filled by an additional peak at 56.4 eV (filled orange), which is most likely due to other, Li-containing decomposition products or LiTFSI. All in all, we observe a loss of about 45 % of the total intensity in the F 1s spectrum, which probably is due to the formation and desorption of volatile decomposition products. The O 1s spectrum obtained after Li post-deposition is characterized by three peaks, which are obtained by fixing the BE position of the O_{TFSI} peak at 533.3 eV and leaving the rest of the spectrum to be filled by two further peaks. The nominal O_{TFSI} : F_{TFSI} ratio of the first peak is approximately 3.7 : 6, indicating a decrease of the O_{TFSI} species by 63 % compared to before Li deposition. This agrees well with the similar intensity decrease in the F_{TFSI} and C_{TFSI} peaks, respectively, after Li deposition. On the other hand, the new O 1s peaks appearing at 532.4 eV (filled orange) and at 529.6 eV (filled violet) are characteristic for sulfite and oxide species (O_{SOx} and O_{oxide}, respectively).[147] Howlett *et al.*, too, reported on the formation of sulfite species (e.g., Li_2SO_3) in the SEI formed on a Li metal electrode after galvanostatic cycling in $TFSI^-$-based electrolyte and subsequent XPS characterization.[153] Differently than the F 1s region, the total sum of the intensity in the O 1s spectrum does not decrease upon Li post-deposition, indicating that the volatile decomposition products are essentially free of oxygen. The N 1s spectrum after Li post-deposition features a shift of the two main peaks by 0.6 eV towards higher BEs, and a new signal appears at the lower BE side (N_{d1}, filled orange). The N_{TFSI} peak shows a very low intensity decrease of only 10 %, which is in contrast to the considerable intensity loss of all other anion-related peaks in the other spectral ranges by around 60 %. Hence, we assume that the decline of the N_{TFSI} signal is compensated by the formation of (Li-bound) decomposition products of $TFSI^-$, such as $LiNSO_2CF_3$,[228] which have a rather similar N 1s BE as $TFSI^-$. Interestingly, the cation peak intensity loss is much more pronounced than that of the N_{TFSI} peak (about 80 %), indicating that also most of the cations are decomposed and that the extent of BMP^+ decomposition even exceeds that of $TFSI^-$ decomposition. The new peak at 398.4 eV has been ascribed to Li_3N[63,153,227,248,249] although other nitrogen-containing Li-bound fragments, e.g., linear LiC_xH_yN species resulting from a ring-opening of the pyrrolidinium molecule,[228,250] might be possible as well. Despite the strong changes in the individual peak intensities, however, the total peak intensity of the N 1s spectrum remains almost constant, similar to that in the O 1s region, but different from the F 1s signal. In the C 1s range, the shape of the spectrum changes significantly after Li deposition, now showing a much more pronounced maximum between 284.0 and 287.0 eV indicative for changes of the C_{TFSI} : C_{alkyl} : C_{hetero} ratio. As discussed above, the C_{TFSI} peak decreases by 64 %, which is plausible considering the similar decrease of the F_{TFSI} and O_{TFSI} peak intensities

observed in the respective BE regions. However, the loss indicated in the N 1s spectrum for the BMP^+ species (about 80 %) is not reflected in the loss of the peak intensities of the C_{hetero} and C_{alkyl} peaks at 287.3 eV and 286.0 eV, respectively, of 20 to 30 %. We suggest that the apparent 'excess' of C-H species in the C 1s region is due to the formation of BMP^+ decomposition products with similar functional groups and thus similar BEs, resulting in a total loss of 21 % in the ASF-normalized intensity for the C 1s region after Li post-deposition. Next, in the S 2p BE region, the doublet for S_{TFSI} decreases in intensity by ~28 % and the shape of the signals broadens towards lower BEs, implying the presence of anion decomposition products with very similar BEs. Simultaneously, the $C_{TFSI} : S_{TFSI}$ ratio of 1 : 1 for intact $TFSI^-$ changes to around 1 : 2 after Li post-deposition. Again, judging from the F_{TFSI}, O_{TFSI} and C_{TFSI} signals, the intensity of the S 2p S_{TFSI} doublet should decrease by about 60-65 %. However, the loss caused by Li post-deposition in the S 2p spectral range is only about 27 %. We attribute this discrepancy to the formation of S-containing $TFSI^-$ decomposition products with similar BEs as the anion. Buchner *et al.* have discussed the possibility of the formation of sulfite species, e.g., Li_xSO_x, upon the post-deposition of Li on pre-adsorbed BMP-TFSI adlayers on Cu, which resulted in the appearance of a S $2p_{3/2}$ doublet at around 166.2 eV.[227] This is in agreement with the doublet observed at around 167.5 / 168.7 eV in our work, and with the results obtained by Howlett *et al.*[153] We are, however, unable to distinguish between different sulfite species such as $Li_2S_2O_4^-$, Li_2SO_3, $LiSO_2CF_3$, etc. from the present XP spectra. The sulfite contribution also agrees with the presence of the O_{SOx} signal in the O 1s spectrum, as the ratio of $(O_{SOx} + O_{TFSI})$ to S_{TFSI} is around 2.6, which would be in agreement with a mixture of $TFSI^-$ and SO_x species. In addition, a new doublet is observed at 161.8 / 163.0 eV (filled violet). This, we tentatively attribute to polysulfides[248] or Li_2S species.[227] The overall loss of intensity upon Li post-deposition on IL adlayers in the S 2p spectrum is only 13 %, indicating both the loss of $TFSI^-$ and the formation of S-containing product species. Finally, for the Li 1s region, we see a pronounced peak upon Li post-deposition, resulting in a concentration of almost 25 %. Furthermore, we can cross-check the consistency of the above signal assignments. Assuming the formation of LiF (F 1s peak at 686.0eV), Li_2O (O 1s peak at 529.6 eV), Li_3N (N 1s peak at 398.0 eV), $LiCF_x$ (C 1s peak at 288.5 eV), Li_2S (S 2p peak at 161.8 eV) and LiTFSI (or Li-bound $TFSI^-$ fragments, e.g., $LiNSO_2CF_3$, whose contribution is calculated as the difference between the N_{BMP} and the N_{TFSI} peak intensities at 403.3 and 400.0 eV) as the Li-containing species, these can account for 88 % of the total Li 1s peak intensity, underlining the credibility of our peak assignments.

In the following, we briefly discuss the XP spectra recorded on the LiTFSI powder. In the spectra shown in **Figure 5-3**c, we find all peaks (F_{LiTFSI}, O_{LiTFSI}, N_{LiTFSI}, C_{LiTFSI}, S_{LiTFSI}, Li_{LiTFSI}) expected for $TFSI^-$-containing species. Interestingly, all BEs of the LiTFSI related peaks are up-shifted by around 3 eV compared to those in BMP-TFSI. The massive up-shift points toward a positive charging of the sample surface, indicative of a rather low electrical conductivity. Even after that correction there are slight variations in the BE compared to the BMP-TFSI multilayer film, which we tentatively attribute to the influence of the different cation (Li^+ instead of BMP^+).[227] In addition, all peaks are slightly broadened in comparison to the peaks shown in **Figure 5-3**a and b, which we assign to differential and non-uniform charging effects. Finally, the O 1s spectrum reveals an additional peak at 529.4 eV (O_{oxide}, filled violet), which we assign to oxygen-containing contaminations of the LiTFSI salt.

Next, we move on to the XP spectra of the HOPG sample kept in the IL + 0.1 M LiTFSI electrolyte in the electrochemical cell at open circuit conditions (OCP) for 68 h (HOPG|IL@OCP). This way, we wanted to test for the influence of the Li counter and reference electrodes on the SEI formation. XP spectra recorded subsequently, after rinsing the sample with DMC and subsequent transfer into the UHV chamber without contact to air, are depicted in **Figure 5-3**d. The spectra are rather similar to those obtained for BMP-TFSI multilayer films deposited under UHV conditions, with their F_{TFSI}, O_{TFSI}, N_{TFSI}, C_{TFSI}, C_{hetero}, C_{alkyl} and S_{TFSI} peaks, respectively (see **Figure 5-3**a). Obviously, small amounts of IL remained on the HOPG surface after rinsing. Only the C 1s spectrum contains a slightly higher contribution of the graphitic substrate (C_{sub}) than in **Figure 5-3**a, indicative of a thinner or inhomogeneous IL layer remaining on the HOPG substrate as compared to the 10 ML film in **Figure 5-3**a (1 ML ~0.3 nm). The quantitative evaluation reveals a $N_{BMP} : N_{TFSI}$ ratio of 1 : 1, as expected for molecularly adsorbed BMP-TFSI species. However, the C 1s intensity ratio of $C_{TFSI} : C_{hetero} : C_{alkyl}$ of 1 : 3 : 5 instead of 2 : 4 : 5 suggests that some cation decomposition has taken place where the C-N- and C-H-containing decomposition products are superimposed with the C_{hetero} and the C_{alkyl} signals. A slight C 1s deficiency is observed also for the anions based on a number of peak intensitiy ratios, including the $F_{TFSI} : C_{TFSI}$ ratio (4 : 1 instead of 3 : 1), the $S_{TFSI} : C_{TFSI}$ ratio (1.1 : 1), the $O_{TFSI} : C_{TFSI}$ ratio (2.55 : 1) and the $N_{TFSI} : C_{TFSI}$ ratio (0.64 : 1). The low-intensity C-F peak at 288.5 eV in the C 1s spectrum also points towards $TFSI^-$ decomposition, possibly caused by the metallic Li counter and reference electrodes. Interestingly, we obtained no signal in the Li 1s spectrum, although we used LiTFSI-containing electrolyte. However, considering that there are about 30 BMP^+ ($TFSI^-$) ions for every single Li^+ ion, and thus 180 F atoms for each Li^+ in the electrolyte, and taking into account also the

low ASF of the Li 1s peak, this would not be expected. As an example, if there is no enrichment of Li on the surface, the F peak must be approximately 15,000 times higher than the Li peak. With a total of about 440,000 counts (normalized intensity), the Li signal would be about 29 counts and thus is entirely lost in the noise.

Finally, we discuss the XP core-level spectra of the electrochemical SEI which is formed by potential cycling on HOPG (HOPG|SEI) and on MAGE (MAGE|SEI) electrodes. The resulting spectra are presented in **Figure 5-3**e and f.

The spectra of the SEI formed on HOPG during potential cycling largely show intact, adsorbed IL species which remained on the surface after rinsing, together with small amounts of decomposition products (filled orange): decomposed $TFSI^-$ species at ~688 eV (F 1s) and ~398 eV (N 1s), SO_x at ~533 eV (O 1s) and ~167 eV (S 2p), and $C_{C\text{-}F}$ at 288.5 eV (C 1s). In the F 1s BE region, specifically, we find a LiF peak at 685.0 eV (filled green and down-shifted by 0.8 eV from the position observed for sample b)). The corresponding Li_{LiF} peak appears at 55.6 eV in the Li 1s spectrum. As observed and discussed with the sample characterized after Li post-deposition on a UHV-prepared IL film (sample b), we find a higher relative intensity loss of the C_{TFSI} peak compared to the F_{TFSI} and N_{TFSI} peaks. Both in the N 1s and the C 1s spectrum, the ratio of the intensities of the $TFSI^-$ peaks and the BMP^+ peaks decreases in comparison to the pristine IL, i.e., the intensity of the $TFSI^-$ peak has decreased. It appears that $TFSI^-$ decomposition takes place preferentially during electrochemical SEI formation. These results agree well with our CV experiments reported in chapter 3.1; as well as with numerous studies claiming reductive $TFSI^-$ decomposition.[153,230,233,234,236-239,251,252] In contrast, BMP^+ is predominantly decomposed under surface science conditions, i.e., upon post-deposition of Li on a ML film of the IL. Preferential cation (BMP^+ and 1-octyl-3-methylimidazolium ($OMIm^+$), respectively) decomposition on Li layers and after Li post-deposition has also been reported previously.[227,250] However, of all BE regions, the C 1s range is the one least suited for the (quantitative) interpretation of possible products, as it – except for the C-F peak – only features the characteristic IL and substrate peaks. Any possible decomposition products would be superimposed by the original signals, as was discussed above. In addition, the graphite C_{sub} peak is comparatively low, demonstrating that a film with a thickness of > 6 – 9 nm must cover the HOPG surface. The MAGE|SEI sample displays most of the features characteristic for the HOPG|SEI sample. In addition, a third F 1s signal for reductively decomposed $TFSI^-$ species with about similar intensity as the LiF peak appears in between the F_{TFSI} and the F_{LiF} signal (286.7 eV). In the Li 1s spectrum, there is a pronounced

intensity at BE higher than LiF. This could either be due to LiTFSI or related decomposition products. Furthermore, the peaks observed for the SEI formed on the MAGE substrate are strongly broadened due to differential charging. However, the wide peak shape could also be related to the presence of products with different oxidation states.

5.3.2.2. Effect of Ar^+ Sputtering on the SEI

To gain deeper insight into the possibly varying composition during electrochemical SEI growth we recorded depth profiles, characterizing the surface composition of the SEI after different times of Ar^+ sputtering. Here it is important to note, however, that sputtering will in any case result in a roughening of the surface. Furthermore, the composition detected by XPS after certain sputter times will not be exactly identical to that of the original SEI at the corresponding level due to the selective element removal caused by different sputter yield, and sputter-induced decomposition of the molecules present in the film may lead to additional changes. To test for such effects, we first carried out Ar^+ sputtering of pure LiTFSI salt (**Figure 5-4**). Here we minimized the measurement time by recording only F 1s and Li 1s detail spectra, which showed the largest changes in the other sputter experiments described below. The results will be used as basis for the interpretation of the XP spectra obtained from a SEI layer formed on HOPG under OCP conditions (**Figure 5-4**) and of a SEI formed by potentiodynamic cycling on HOPG and MAGE electrodes (**Figure 5-5**).

Starting with the reference spectra recorded upon LiTFSI sputtering, the F 1s and Li 1s regions show a decay in intensity of the F_{TFSI} (blue line) and Li_{TFSI} (yellow line) peaks at 689.5 and 57.0 eV, respectively, after two minutes of sputtering compared to the situation before sputtering (see **Figure 5-3**c. Furthermore, two new peaks arise at 686.7 and 685.7 eV, pointing to sputter-induced $TFSI^-$ decomposition. The new peaks are assigned to decomposition products such as $LiNSO_2CF_3$ or other C–F species ($F_{TFSI,\,red}$, see discussion above) and LiF (F_{LiF}), respectively. This trend continues for increasing sputtering time. Correspondingly, the signals in the Li 1s range are associated with $TFSI^-$ and reduced $TFSI^-$, as well as LiF. Note that the Li 1s peaks for Li_{TFSI} and $Li_{TFSI,\,red}$ cannot be distinguished in the fit and are assigned to the signal at 57.0 eV, while the Li_{LiF} signal appears at ~56 eV. Overall, Ar^+-sputtering of pristine LiTFSI clearly demonstrates decomposition of $TFSI^-$ to sputter-induced $TFSI^-_{red}$ moieties and other decomposition products, as well as LiF.

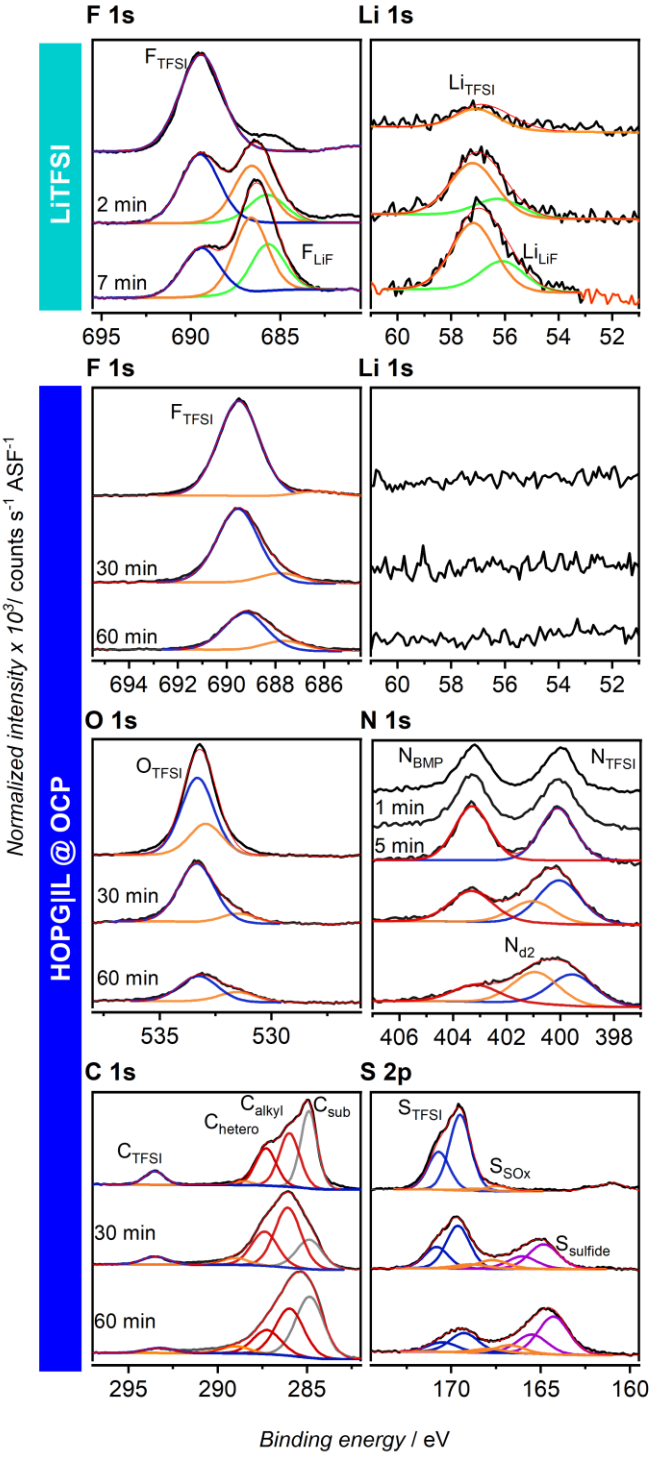

Figure 5-4. Above: F 1s and Li 1s core level spectra of LiTFSI before and after stepwise Ar^+ sputtering (after two and seven minutes of successive sputtering). Below: F 1s, O 1s, N 1s and S 2p core level spectra of sample c) (see above): HOPG|BMP-TFSI + 0.1 M LiTFSI@OCP after 30 and 60 minutes of successive sputtering.

Similar XPS measurements were performed on the sample HOPG|IL@OCP. The XP spectra of the F 1s, O 1s, N 1s, C 1s and S 2p region recorded before sputtering are dominated by the BMP^+- and $TFSI^-$-characteristic peaks discussed with **Figure 5-3**d.

Interestingly, the N 1s region reveals no sputtering-induced changes after one and five minutes of sputtering, except for an increase in total N 1s intensity. The latter may be due to sputter-removal of other species. Most important, the intensity ratio of the N_{TFSI} and N_{BMP} peaks in the N 1s spectrum is essentially constant during this time, indicating that the adlayer is still dominated by molecular BMP-TFSI species (**Figure 5-4**, panel at the bottom, left) after five minutes of sputtering. Upon increasing the sputtering time to 30 and then to 60 minutes in total, we observed changes in the F 1s, O 1s, N 1s, C 1s and S 2p regions. Now, the F 1s peak area decreased stepwise in intensity, and a low-intensity peak appears at the lower BE side (yellow line, 687.5 eV), which we assign to a small amount of sputter-induced $TFSI^-$ decomposition products. If sputtering results in the removal of fluorine atoms, this would result in volatile $C–F_2$ and C–F species, which may be bound to N or SO_x moieties (see discussion below). However, the changes observed in the F 1s region of the HOPG|IL@OCP sample after 30 minutes of sputtering are minor compared to the ones occurring after already two minutes of sputtering of the LiTFSI sample. Obviously, LiTFSI undergoes a more pronounced sputter-induced decomposition than BMP-TFSI itself.

Furthermore, the presence of Li strongly affects the sputter decomposition of $TFSI^-$, leading mainly to LiF formation. Based on force–distance atomic force[226] and quartz microbalance measurements,[238] it has been concluded that Li^+ cations result in a destabilization of $TFSI^-$ by influencing the electrochemical double layer formed on the substrate. According to these authors, Li^+ leads to formation of $[Li(TFSI)_2]^-$ complexes, which increases the concentration of $TFSI^-$ moieties at the anode and enhances anion decomposition. Overall, the concentration of LiTFSI is crucial for the coordination process,[253] and for $TFSI^-$ decomposition. No signal was observed in the Li 1s region, as expected from the low cross-section of Li 1s and the low concentration (as discussed with **Figure 5-3**). Moving on, the O 1s range is dominated by the O_{TFSI} peak at around 533.3 eV (blue line), which decreases in intensity upon increasing sputtering time. After 30 and 60 minutes of sputtering, a second peak appears at 531.6 eV, indicative of the formation of sputter-induced $TFSI^-$ decomposition products (O_{SOx}, yellow line). The main change in the spectra is, however, the decrease in the total peak area of both the F 1s and the O 1s peaks, pointing to a loss of fluoride- and oxygen-containing species in the accessible film region. In the N 1s range, 60 minutes of sputtering finally resulted in a decrease of the BMP^+ and the $TFSI^-$ peaks appearing at 403.3 and 400.0 eV in the original SEI layer. The loss is particularly pronounced for the N_{BMP} peak. This points to the onset of sputter-induced IL decomposition, which mainly affects the BMP^+ cation and less the $TFSI^-$ anion. Among the decomposition products is a nitrogen-containing species with an N 1s BE of around

401 eV (N_{d2}, yellow line), which appears after 30 minutes of sputtering and increases with continued sputtering. As the BE of this signal is located between those of the negative $TFSI^-$ and the positive BMP^+ N 1s signals, we assign it to a covalently bound nitrogen atom in an uncharged moiety. Based on the BE, N,N-dibutyl-N-methylamine or methylpyrrolidine (N–C) would be possible candidates. For the C 1s region, we observed a distinct increase in intensity for longer sputter times, dominated by a broad peak around 285 eV (C_{hetero}, C_{alkyl}, C_{sub}). At the same time, the C_{TFSI^-} signal decreased, in agreement with the decrease of the anion-related signals in all other BE regions. Finally, in the S 2p region, two new doublets emerge with BEs of 164.3 and 166.7 eV for the S $2p_{3/2}$ peaks (yellow lines), respectively. The intensity of these doublets is, however, very low. The latter doublet (S $2p_{3/2}$: 166.7 eV) may be related to sulfur-containing decomposition products like Li_xSO_x, as discussed above, while the former one (S $2p_{3/2}$: 164.3 eV) is assigned to sulfide species (Li_2S). Quantitatively, the S_{SOx} : $O_{TFSI, red}$ ratio is between 1 : 2 and 1 : 3, which would be in good agreement with Li_2SO_2 or Li_2SO_3 species. Moreover, the total intensity for the S 2p peaks is about constant during sputtering. Overall, the XP spectra during stepwise sputtering of BMP-TFSI indicate the selective desorption of F- and O-containing fragments or atoms, while the Li-, N- and S-containing decomposition products of BMP^+ and $TFSI^-$, such as $Li_xC_yH_zN$, N,N-dibutyl-N-methylamine or methylpyrrolidine, Li_xSO_x or Li_2S, remain on the surface. Both in LiTFSI and in BMP-TFSI, however, the $TFSI^-$ anions undergo decomposition upon Ar^+ sputtering, with the decomposition products closely similar to those obtained in the SEI upon electrochemical reduction products. In that sense, the results of depth profiling measurements of the SEI have to be taken with care.

The same XPS measurement was now performed on the HOPG|BMP-TFSI + LiTFSI sample held at OCP for 68 hrs (HOPG|IL@OCP). The XP spectra of the F 1s, O 1s, N 1s and S 2p region before sputtering (**Figure 5-4**, lower part) display the BMP^+- and $TFSI^-$-characteristic peaks discussed in section 5.3.2.1. Interestingly, the N 1s region reveals no sputtering-induced changes after one and five minutes of sputtering. That is, the N_{TFSI} and N_{BMP} peaks in the N 1s spectrum exhibit almost unchanged intensities due to the presence of molecular BMP-TFSI species (**Figure 5-4**, panel at the bottom, left), while LiTFSI (**Figure 5-4**, top of each panel) already displays major changes of the spectra already after two minutes. Obviously, Li^+-containing species undergo a more pronounced sputter-induced decomposition / recombination than BMP-TFSI itself. Upon increasing the sputtering time to 30 and 60 minutes in total, we observed changes in the F 1s, O 1s, N 1s and S 2p regions. Now, the F 1s peak area decreases stepwise in intensity, and a peak with negligible intensity appears at the low BE side (yellow

line), which we assign to a small amount of sputter-decomposed $TFSI^-$. For example, the main process might be the removal of fluorine atoms, which would result in volatile C–F_2 and C–F species possibly bound to N or SO_x (see discussion below). Similarly, the O 1s range features the O_{TFSI} peak at around 533.3 eV (blue line) which decreases in intensity upon increasing sputtering time. After 30 and 60 minutes of sputtering, a second peak appears at 531.6 eV, also resulting from sputter-induced $TFSI^-$ decomposition products (O_{SOx}, yellow line). The main observation, however, is the decrease in the total peak area of both the F 1s and the O 1s peaks due to a loss of fluoride- and oxygen-containing species. In the N 1s range, the BMP^+ and the $TFSI^-$ peaks appear at 403.3 and 400.0 eV, respectively. After increasing the sputtering time to 30 and 60 minutes, respectively (no change after one and five minutes), particularly the N_{BMP} peak decreases in intensity, which points towards the onset of a sputter-induced IL decomposition largely affecting the BMP^+ cation, but also the $TFSI^-$ anion. It probably includes transformation into another nitrogen-containing species, which appears around 401 eV (N_{d2}, yellow line) after 30 minutes of sputtering and increases upon increasing the sputtering time up to 60 min. As its BE is located between the one for the negative $TFSI^-$ and the positive BMP^+-nitrogen, we assign the signal to a most likely neutral N species, e.g., N,N-dibutyl-N-methylamine or methylpyrrolidine. During sputtering, the total peak area drops significantly in the F 1s and O 1s region, while in the other regions it remains almost constant. This means that S–O and C–S (or C–F) bonds are broken and volatile oxygen and fluoride species released. Furthermore, in the S 2p region, two new doublets emerge at 164.3 and 166.7 eV (S $2p_{3/2}$ peak, yellow solid lines), respectively. The intensity of the latter doublet is, however, negligible and might be related to sulfur-containing products like Li_xSO_x (discussed above), while the former is assigned to sulfide species (Li_2S). Quantitatively, the S_{SOx} : $O_{TFSI,\,red}$ ratio is between 1 : 2 and 1 : 3, which is in good agreement with Li_2SO_2 or Li_2SO_3 species. Overall, the XP spectra during stepwise sputtering of BMP-TFSI indicate the selective desorption of fluorine and oxygen atoms, while N_{BMP} and S_{TFSI} are transformed into decomposition products like $Li_xC_yH_zN$, N,N-dibutyl-N-methylamine or methylpyrrolidine, Li_xSO_x or Li_2S on the surface.

At this point, we would like to point out that sputtering decomposition of pure LiTFSI decomposed to LiF after two minutes already, while no F_{LiF} signal is observed in the F 1s and Li 1s spectra even after 60 minutes of consecutive Ar^+ bombardment. These results indicate that the influence of the cation goes beyond a simple BE upshift, as observed for LiTFSI salt. In addition, $TFSI^-$ sputtering decomposition only results in LiF if the cation is Li^+, not BMP^+. It has been shown that the Li^+ cation possesses a certain catalytic influence that leads to the destabilization of $TFSI^-$ as it influences the electrochemical double layer (EDL) formed by the

IL on the substrate.[238,254] In short, it causes the coordination of the $TFSI^-$ anions in $[Li(TFSI)_2]^-$ complexes and a subsequent increase of $TFSI^-$ at the anode, which facilitates anion decomposition. Thus, the concentration of LiTFSI is crucial to the coordination process,[253] and to $TFSI^-$ decomposition. Both LiTFSI and BMP-TFSI, however, undergo decomposition and desorption upon Ar^+ sputtering whose products, except for certain cases, cannot be distinguished from the electrochemical reduction products likely found within the SEI. The use of Ar^+ sputtering for depth profiling of surface cover layers, thus, is to be taken with a grain of salt.

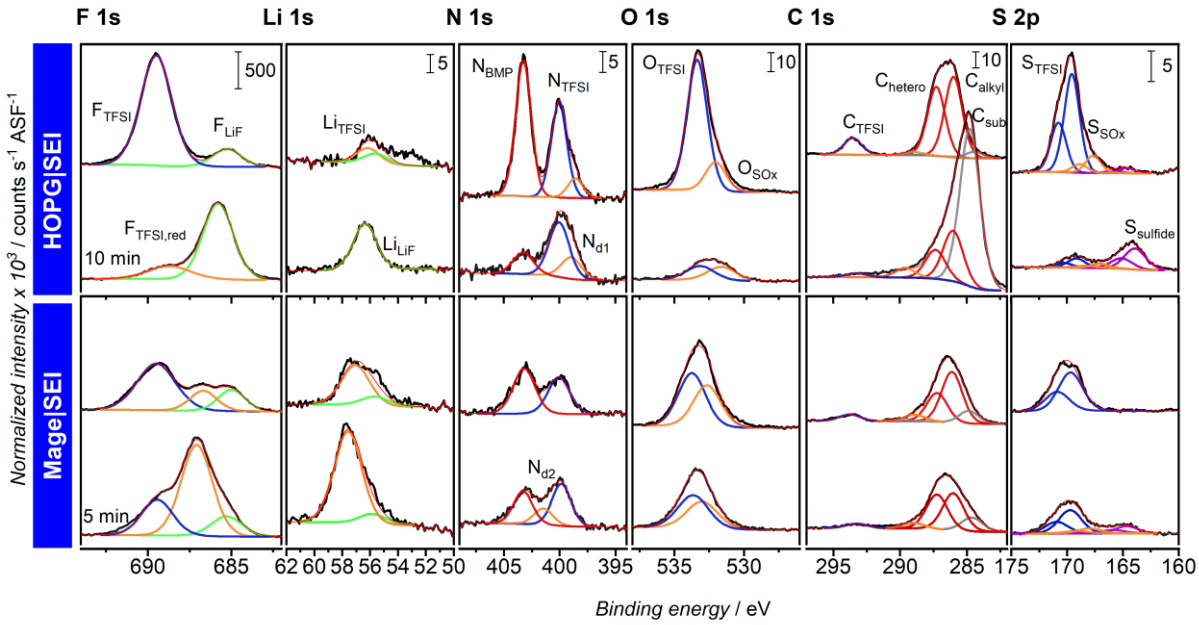

Figure 5-5. Core level spectra of the SEI formed electrochemically on HOPG (sample e) and MAGE (sample f) before and after 10 (five) minutes of Ar^+ sputtering. Note that the spectra recorded before sputtering are identical with those shown in **Figure 5-3**.

Next, we performed depth profiling of the SEIs formed after the electrochemical measurements. The XP core level spectra recorded before and after 10 (five) minutes of sputtering on the HOPG and MAGE electrodes, respectively, are shown in **Figure 5-5**. To begin with, the HOPG|SEI surface before sputtering (top of each panel) features F_{TFSI}, O_{TFSI}, N_{BMP} and N_{TFSI}, C_{TFSI}, C_{hetero}, C_{alkyl} and S_{TFSI} peaks, as well as peaks related to decomposition products which were already discussed together with the data in **Figure 5-3**. They include, e.g., $TFSI^-$ decomposition products like $LiNSO_2CF_3$ and C–F moieties (yellow lines) in the F 1s region, Li_3N in the N 1s region (yellow lines), Li_xSO_x (yellow lines) and Li_2S (violet line of almost negligible intensity) in the S 2p region, as well as LiF (green line) in the F 1s and Li 1s region.

After 10 minutes of Ar^+ sputtering, the F_{TFSI} peak in the F 1s range has disappeared almost completely. At the same time a new, dominant signal arises at the low BE side which, based on its BE, is attributed to LiF (green line). The related Li 1s peak appears at around 56 eV. Interestingly, the characteristics observed for the sputtered SEI on HOPG are almost identical to those of pristine LiTFSI after sputtering (**Figure 5-4**, top panels), but are in contrast to the traits observed after sputtering of the HOPG|IL@OCP sample (**Figure 5-4**, lower panels). This discrepancy seems to indicate that LiTFSI is enriched in the SEI formed upon potential cycling and that LiF formation is subsequently induced by the Ar^+ beam. However, we cannot rule out that LiF results directly from electrochemical $TFSI^-$ decomposition, and thus is a natural part of the SEI in regions closer to the electrode|electrolyte interface. For the HOPG|SEI sample, the N_{d1} peak (Li_3N, etc.) at 398.0 eV increases upon sputtering, while, for the MAGE|SEI sample, a new peak (N_{d2}) appears at about 401.1 eV (N–C, etc.). This peak was observed already for HOPG|IL@OCP after 30 minutes of sputtering and was assigned to neutral, N-containing $TFSI^-$ decomposition products. We tentatively suggest that the N_{d2} peak-related decomposition product arises from sputtering of the IL, since it is only observed after sputtering. The O 1s spectra resemble the sequence of spectra obtained upon sputtering of the HOPG|IL@OCP sample, revealing desorption of oxygen-containing species. In the C 1s region, the anion-related C_{TFSI} peak also disappears almost completely, while the BMP^+-related C 1s peaks decrease in intensity but do not disappear completely. On the other hand, the C_{sub} peak strongly increases, as expected upon sputter removal of part of the SEI layer. We suggest that most likely the BMP^+ species is partly transformed into other nitrogen- and carbon-containing species (N–C species, see N 1s region). Finally, the S_{TFSI} related peak disappeared almost completely. Since the O_{TFSI} and C_{TFSI} peaks decrease, as well, we conclude that the $TFSI^-$ species are either desorbed and/or sputter-transformed to Li_xSO_x or Li_2S.

Going to the Mage|SEI surface, the XP spectra recorded after sputtering appear rather different compared to those obtained for HOPG. In the F 1s range, the $TFSI^-$ anion (F_{TFSI}) is now partly transformed to reduced $TFSI^-$ species ($F_{TFSI,\,red}$) (yellow line), which only appeared in very low concentrations on HOPG. Another part is transformed to LiF, which was the dominant product upon sputtering of the HOPG substrate. The increase of the total peak area in both the F 1s and the Li 1s spectra after five minutes, where the former is much more pronounced, indicates that Li-containing species like $LiNSO_2CF_3$, LiC_xH_yN and Li_xSO_x within the SEI are either exposed or formed upon sputtering. In contrast to the system HOPG|SEI, where LiF was formed as main product during sputtering, sputtering of the SEI formed on the MAGE substrate (for five minutes) results mainly in reduced $TFSI^-$ decomposition products, as concluded from the lower

F 1s BE of these species. We cannot exclude, however, that longer sputter times may also lead to LiF formation. In the N 1s, O 1s and S 2p spectral ranges, we did not observe any pronounced changes upon sputtering. The C_{sub} peak in the C 1s range still appears with rather low intensity, which means that the surface is still covered with an at least >6-9 nm thick SEI layer after five minutes of sputtering. This is distinctly different from the HOPG|SEI surface, where the C_{sub} peak strongly increased after 10 minutes of sputtering. It seems that the SEI layers remaining after DMC rinsing were quite different in thickness on HOPG and on MAGE, respectively. This fits well to the much higher currents and, most likely, more effective SEI formation during electrochemical cycling of the MAGE powder electrode compared to the basal HOPG plane.

5.4. Conclusion

Aiming at a better understanding of the formation and composition of the SEI layer on carbon electrodes in an ionic liquid electrolyte (BMP-TFSI + 0.1 M LiTFSI), we have investigated these aspects on two very different carbon electrodes (HOPG and realistic MAGE powder electrodes) by half-cell measurements and subsequent *ex situ* XPS characterization, including also measurements after partial removal of the SEI by sputtering. Comparing these results with data obtained on films created by i) chemical reaction between BMP-TFSI multilayer films and post-deposited Li under UHV conditions on HOPG, ii) long-term exposure of HOPG to a BMP-TFSI + 0.1 M LiTFSI electrolyte under open circuit conditions, and iii) electrochemically cycled HOPG and MAGE model electrodes in BMP-TFSI + 0.1 M LiTFSI, we arrive at the following conclusions:

1) Self-poisoning, reductive $TFSI^-$ decomposition takes place on both HOPG and MAGE electrodes in the first cycle. The CV recorded on MAGE furthermore features several (reversible) peaks in the cathodic cycle which we assign to co-intercalation and decomposition of BMP^+. This also leads to surface passivation, inhibiting this process after a few cycles.
2) The addition of Li to multilayers of BMP-TFSI on the HOPG substrate in UHV leads mainly to the chemical decomposition of BMP^+, resulting in products like Li_3N and LiC_xH_yN. Electrochemical cycling, on the other hand, results predominantly in $TFSI^-$ decomposition to, e.g., LiF, $LiNSO_2CF_3$ and $–CF_3$ species.
3) $TFSI^-$ decomposes mainly to LiF on HOPG. An additional, unidentified F-containing species is observed for the MAGE surface, which we assign to reduced $TFSI^-$ species.

4) Depth profiling by Ar^+ sputtering may lead to the formation of new decomposition products which have not been present in the SEI layer originally. For example, sputtering of LiTFSI produces a large amount of reduced $TFSI^-$ decomposition products and LiF already after a short time. Similar products are observed also for the electrochemically formed SEI layer, both before and after sputtering. The fact that these products are present already before sputtering indicates that they are formed by electrochemical cycling, while after sputtering they can result from either sputter decomposition or electrochemical decomposition.

We believe that such kinds of model studies are crucial for a detailed, fundamental understanding of battery interfaces and interphases. As such, they constitute the first step towards a systematic further improvement of LIB safety and stability.

5.5. Supporting Information

5.5.1. Influence of the Li Salt Concentration

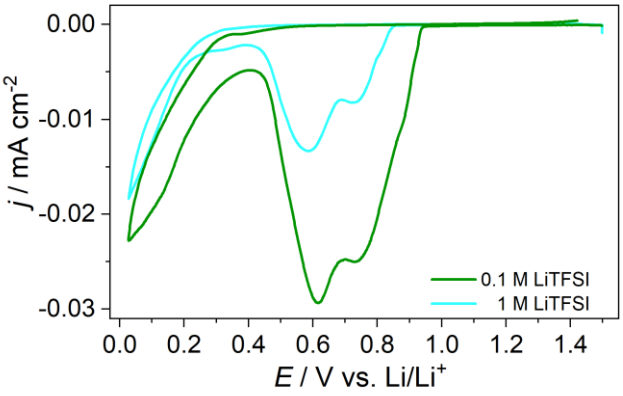

Figure S5-1. First cycle of the CVs of HOPG in BMP-TFSI + 1 (turquoise) and 0.1 M (green) LiTFSI recorded at 0.1 mV s^{-1} between 1.5–0.02 V.

5.5.2. Influence of the Scan Rate and Cycling Time

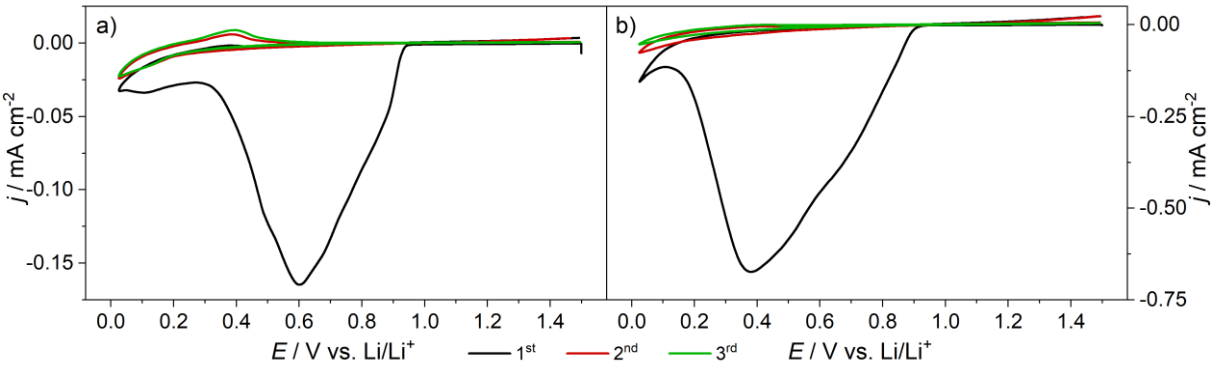

Figure S5-2. First three cycles of a HOPG substrate cycled in BMP-TFSI + 0.1 M LiTFSI at a) 1 and b) 10 mV s^{-1}.

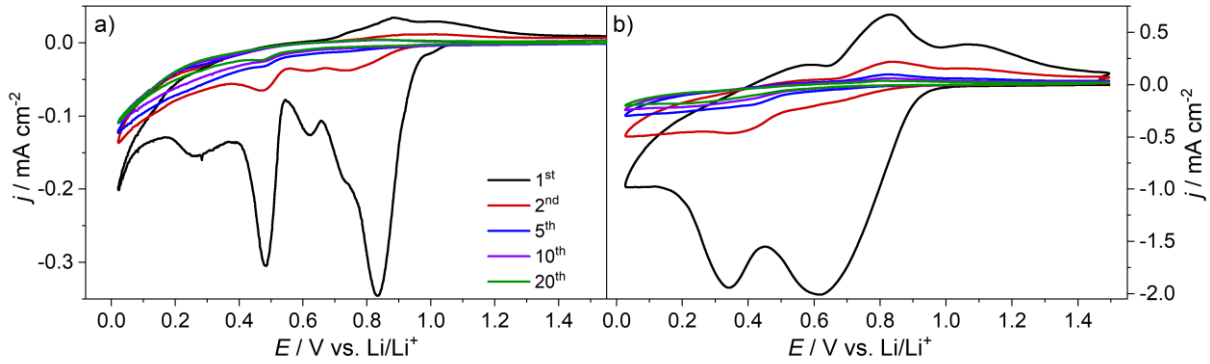

Figure S5-3. First, second, fifth, tenth and twentieth cycle of a MAGE powder substrate cycled in BMP-TFSI + 0.1 M LiTFSI at a) 1 and b) 10 mV s^{-1}.

5.5.3. Atomic Sensitivity Factors (ASF)

Table S5-1. Comparison of the ASF values for the components of the ionic liquid BMP-TFSI, both from literature and from four independent, identical measurements conducted in our group (sample A-D). Dev. / % is the deviation from the reference values (Ref.), as given by the manufacturer.

	Ref.	**A**	**Dev / %**	**B**	**Dev / %**	**C**	**Dev / %**	**D**	**Dev / %**
F	1.000	1.0	0.0	1.0	0.0	1.0	0.0	1.0	0.0
Li	0.012	-	-	-	-	-	-	-	
O	0.630	0.524	20.3	0.522	20.6	0.491	28.3	0.461	36.6
N	0.380	0.353	7.5	0.344	10.5	0.297	27.9	0.309	23.0
C	0.205	0.232	-11.7	0.189	8.5	0.234	-12.4	0.226	-9.3
S	0.350	0.463	-24.5	0.406	-13.8	0.351	-0.3	0.339	3.2

5.5.4. *XP Spectra – Enlarged*

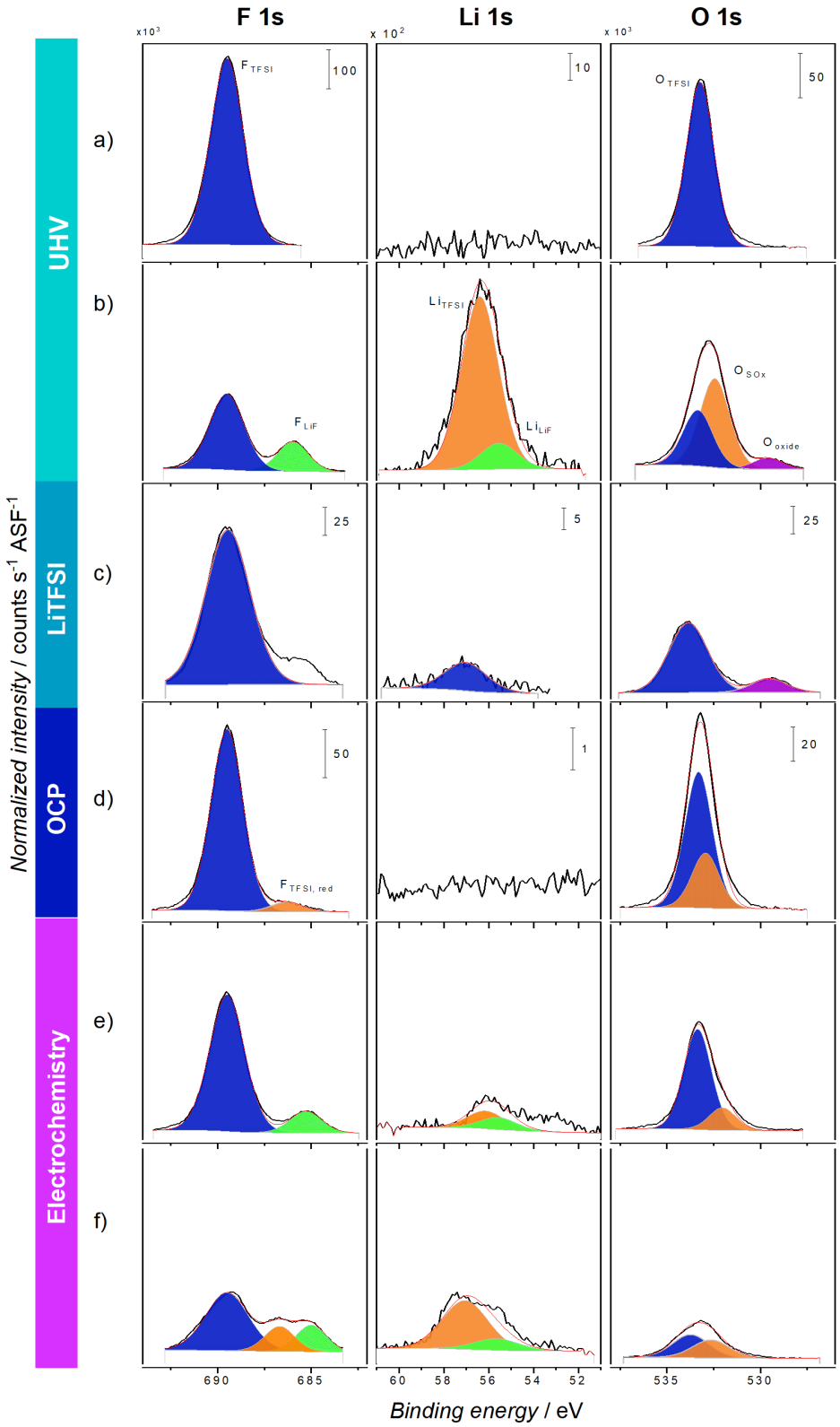

Figure S5-4. Core level spectra of the SEI formed chemically on HOPG in UHV and at OCP (a-d) and of the SEI formed electrochemically on HOPG and MAGE (e-f) for the F 1s, Li 1s and O 1s region. In detail: XP spectra of a) 10 ML of adsorbed BMP-TFSI on HOPG prepared by vapor deposition, b) subsequent post-deposition of Li, c) LiTFSI salt for reference, d) HOPG electrode held at OCP in BMP-TFSI + 0.1 M LiTFSI, e) SEI formed on MAGE and f) SEI formed on HOPG, both in BMP-TFSI + 0.1 M LiTFSI.

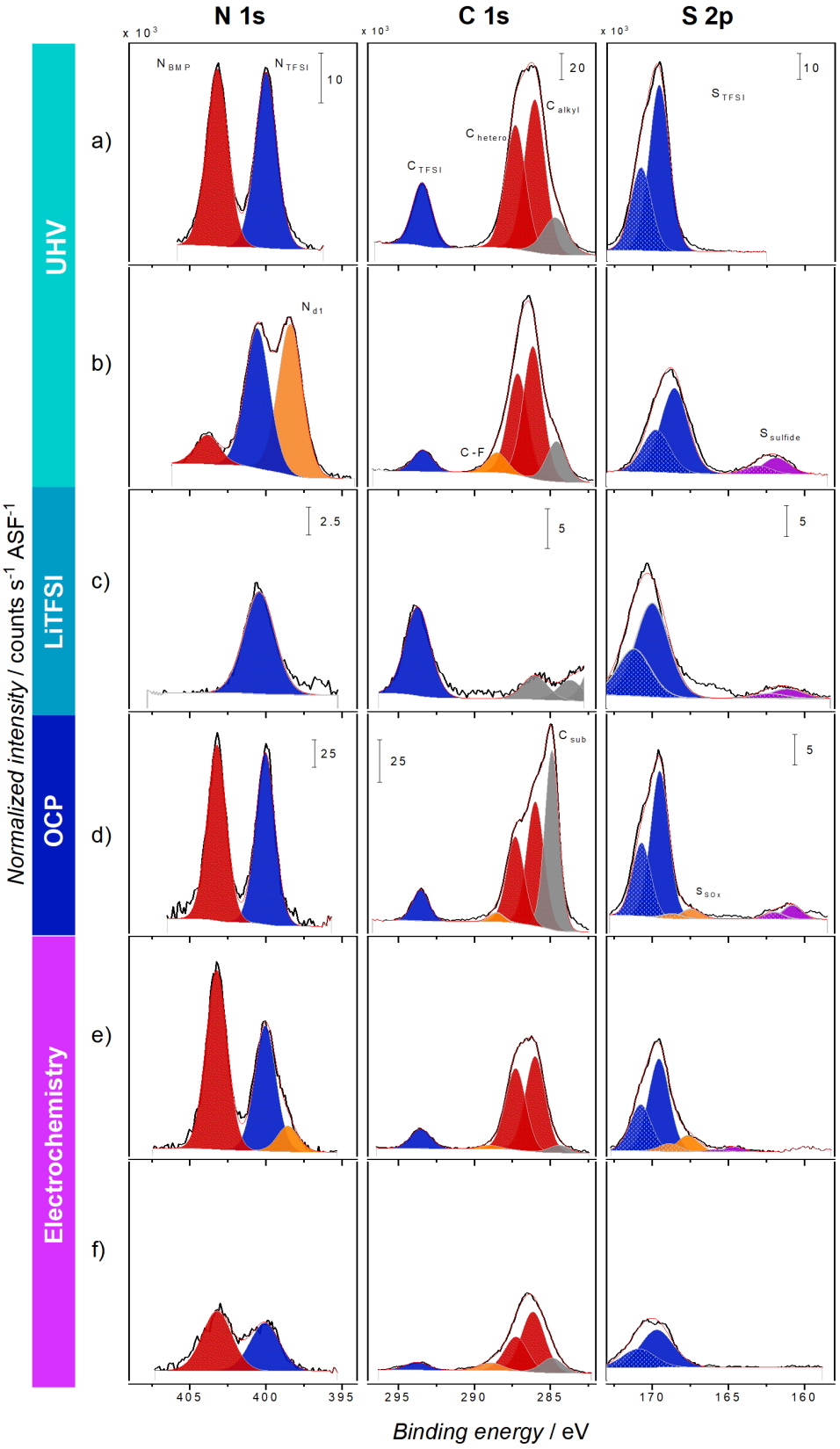

Figure S5-5. Core level spectra of the SEI formed chemically on HOPG in UHV and at OCP (a-d) and of the SEI formed electrochemically on HOPG and MAGE (e-f) for the N 1s, C 1s and S 2p region. In detail: XP spectra of a) 10 ML of adsorbed BMP-TFSI on HOPG prepared by vapor deposition, b) subsequent post-deposition of Li, c) LiTFSI salt for reference, d) HOPG electrode held at OCP in BMP-TFSI + 0.1 M LiTFSI, e) SEI formed on MAGE and f) SEI formed on HOPG, both in BMP-TFSI + 0.1 M LiTFSI.

6. Influence of Complexing Additives on the Reversible Deposition / Dissolution of Magnesium in an Ionic Liquid

The data and results presented in the following chapter, including the graphical abstract (Figure 6-0), was published in ChemElectroChem 2021 volume 8 pp. 390-402, and is reprinted with permission from John Wiley and Sons.[166]

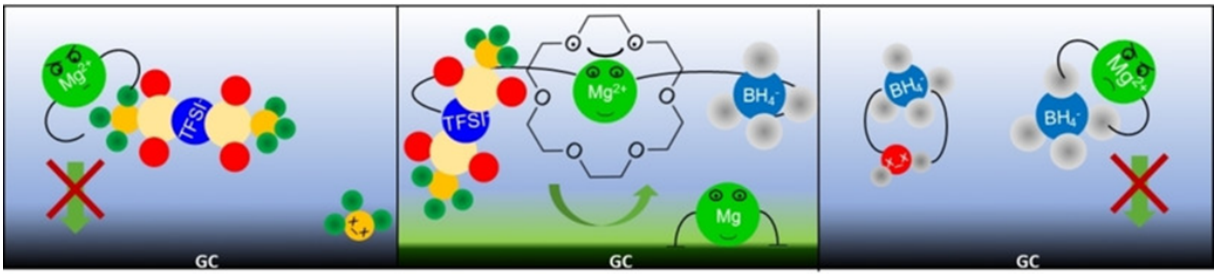

Better together:

Electrochemical measurements and quantum chemical calculations are presented, which show that addition of crown ether enhances the reversibility of Mg deposition/dissolution from a $MgTFSI_2$-containing ionic liquid by strongly coordinating to Mg^{2+}, weakening the $[Mg^{2+}–TFSI^-]$ interaction and $TFSI^-$ decomposition. BH_4^- is assumed to support this by acting both as coordinating ligand and as water scavenger.

Figure 6–0. Graphical abstract.

The initial screening of the ethereal additives and the IL with $Mg(BH_4)_2$ was performed by Dr. M. Eckardt (Institute of Surface Chemistry and Catalysis, Ulm University). I contributed the electrochemical measurements presented in the paper as well as the data evaluation, with invaluable help from Dr. J. Schnaidt (Institute of Surface Chemistry and Catalysis, Ulm University), and was heavily involved in the creative process of the publication. J. Ingenmey conducted, evaluated and presented the theoretical calculations, with assistance from S. Gehrke (both from Mulliken Center for Theoretical Chemistry, Bonn University).

Financial support was granted by the German Federal Ministry of Education and Research (BMBF) in the project 03EK3051C (‘LuCaMag: Wege zu sekundären Mg/Ca-Luftbatterien’) and by the Deutsche Forschungsgemeinschaft under project BE 1201/22-1 (‘Zn-Air Batteries’) and ID 390874152 (POLiS Cluster of Excellence). This work contributes to the research performed at CELEST (Center for Electrochemical Energy Storage Ulm-Karlsruhe).

6.1. Abstract

Aiming at a fundamental understanding of the synergistic effects of different additives on the electrochemical Mg deposition / dissolution in an ionic liquid, we have systematically investigated these processes in a combined electrochemical and theoretical study, using 1-butyl-1-methylpyrrolidinium bis (trifluoromethylsulfonyl) imide (BMP-TFSI) as the solvent and a cyclic ether (18-crown-6) and magnesium borohydride as additives. Both crown ether and BH_4^- improve Mg deposition, its reversibility, and cycling stability. The combined presence of both additives and their concentration relative to that of Mg^{2+} are decisive for more facile and reversible Mg deposition / dissolution. These results and those of quantum chemical calculations indicate that 18-crown-6 can partly displace $TFSI^-$ from its direct coordination to Mg^{2+}. Furthermore, the interaction between Mg^{2+} and directly coordinated $TFSI^-$ is weakened by coordination with 18-crown-6, preventing its Mg^+-induced decomposition. Finally, Mg deposition is improved by the weaker overall coordination upon Mg^{2+} reduction to Mg^+.

6.2. Introduction

Despite of the advantages of rechargeable Mg batteries in comparison to conventional lithium-ion batteries (LIBs), such as their generally higher energy density, the possibility of using elemental Mg anodes, the global availability and non-toxicity of Mg, and their recyclability and low costs,[35,37-40,42,193,255] their technical verification and commercial introduction is still far away. This is mainly due to problems in the reversible deposition and dissolution of Mg, which are – at least in part – related to complications arising from reductive electrolyte decomposition at the anode|electrolyte interface. In contrast to LIBs, where Li^+ transport is possible through the so-called solid electrolyte interphase (SEI) formed at the anode during charge/discharge, these layers often inhibit the Mg deposition / dissolution process.[37,193,256] Only recently, studies reported on a functional SEI formed upon Mg deposition, e.g., from $Mg(BH_4)_2/LiBH_4$-containing monoglyme,[257] in Mg/S systems,[258] or on Sn-modified anodes.[259] In general, most investigations so far have focused on salt / solvent combinations that allow reversible Mg deposition / dissolution without the formation of a protective surface layer. Among those, a limited number of electrolytes consisting of commercially available magnesium salts such as $Mg(BH_4)_2$[98,119,121,260-264] or $Mg((CF_3SO_2)_2N)_2$ (Mg bis (trifluoromethylsulfonyl) imide, $MgTFSI_2$)[264-271] have been found to support largely reversible Mg plating and stripping without negative impact on the cell components (such as corrosion, which poses a problem in Cl-containing electrolytes).[38] However, even for these electrolytes, the oxidative instability of the borohydride,[40] as well as the Mg^{2+}-[121,272] and moisture-induced[262,269,273,274] decomposition of $TFSI^-$, severely limit their application. Hence, the development of suitable electrolytes allowing

for reversible Mg plating / stripping is still of utmost importance for the introduction of rechargeable Mg-based batteries.[37,89,90,93,105,205]

Ionic liquids (ILs) are a promising alternative to electrolytes based on organic solvents due to their generally low flammability, high electrochemical stability, and low vapor pressure.[106,120,262] Specifically, $TFSI^-$-based ILs have attracted interest due to their relatively high conductivity, their commercial availability, and the simplicity of the system when adding $MgTFSI_2$ as Mg salt. This approach, however, has turned out to be little successful so far, as the reductive decomposition of $TFSI^-$, which is promoted by the interaction with the Mg^{2+} species,[46,115,117,132] leads to the formation of passivating films (in particular on Mg metal electrodes[105]). The successful use of IL-based electrolytes thus requires either ionic liquids that are stable in the entire potential range also upon interaction with Mg^{2+}, or the development of additives that could lower any detrimental interaction between Mg^{2+} and the IL – while still allowing reversible Mg deposition / dissolution.

This is the topic of the present paper, where we report results of a combined experimental and theoretical study on the effect of two different additives, the crown ether 18-crown-6 and borohydride (BH_4^-), on the deposition / dissolution of Mg from the IL 1-butyl-1-methylpyrrolidinium bis (trifluoromethylsulfonyl) imide (BMP-TFSI) using $MgTFSI_2$ and, where present, $Mg(BH_4)_2$ as Mg^{2+} source. Glassy carbon (GC) and, for comparison with realistic battery systems, Mg, were used as working electrodes. In this work, we are especially interested in a basic mechanistic understanding of the interplay between Mg^{2+}, the anion $TFSI^-$ and the additives $Mg(BH_4)_2$ and 18-crown-6, and particularly in synergistic effects. A semiquantitative understanding shall be derived by systematically varying the composition of the electrolyte, both in experiment and in simulations. Here, it is important that stabilization of the electrolyte does not inhibit Mg deposition. Furthermore, the role of the electrode shall be elucidated by comparing results obtained for the rather inert GC model electrodes and the more reactive, realistic Mg electrodes.

While there is a considerable number of studies investigating the Mg–TFSI interaction in organic solvents such as DME, THF or polyethers / glymes,[118,121,263,272,274-279] the number of studies performed in electrolytes using a $TFSI^-$-containing IL as main component is much less, and such kind of insights as aimed at in the present study have not been reported so far.[115,117,119,132,262] Finally, the idea of adding a complexing additive was followed also in a study by Watkins *et al.*, who prepared chelating ILs by adding a polyether chain to the cation.[119] Compared to that approach, ours seems to be experimentally simpler and more

feasible. On the other hand, combining chelating solvents such as glymes with an IL-based Mg source such as $MgTFSI_2$ (see above) may lose the advantages of a mainly IL-based electrolyte. The crown ether is a typical complexing agent[280] and has previously been employed to, e.g., enhance Mg plating / stripping in an ionic liquid.[46,117] $Mg(BH_4)_2$ has been repeatedly used as water scavenger in IL-containing electrolytes.[118,119,262,263,274,275,281] It was reported to prevent the formation of a passivating surface layer in $TFSI^-$-based electrolytes[101] and also serves as Mg source.[98] Furthermore, BH_4^- has been proposed to act as Mg^{2+}-complexing agent[261,262] and/or interact with the anode surface; either by adsorption (similar to chloride-containing electrolytes[282]) or by dissolving passivation layers either during formation or pre-existing ones (native passivation layers) due to its highly reductive character.

In the following, we will first present cyclic voltammetry data on the Mg deposition / dissolution behavior on glassy carbon from a BMP-TFSI-based electrolyte containing either $Mg(BH_4)_2$ or a combination of $Mg(BH_4)_2$ and crown ether. Next, we show results of similar experiments using electrolytes containing also $MgTFSI_2$, where, for a better understanding of possible synergistic effects, the concentrations of the different components were varied systematically. For comparison, we also show data obtained for Mg deposition / dissolution from similar electrolytes on a Mg electrode. Subsequently, we present results of a DFT-based quantum chemical analysis of the stability of clusters derived from classical molecular dynamics (MD) simulations, which contain Mg^{2+} in different coordination states and up to two BMP-TFSI ion pairs with or without 18-crown-6 as additional ligand. Finally, we discuss the implications of both the experimental and theoretical data and summarize the main conclusions derived from these data.

6.3. Results and Discussion

6.3.1. Electrochemical Characterization

In previous experiments, we had already shown that deposition and dissolution of Mg on a glassy carbon (GC) electrode is essentially inhibited in $MgTFSI_2$-containing BMP-TFSI electrolyte.[132] This was reproduced also in the present experiments, though some improvement is achieved for $Mg(BH_4)_2$-containing BMP-TFSI electrolytes. The first and later cycles of the CVs recorded at 10 mV s^{-1} on the GC substrate, without any additional additives, largely resemble previous findings.[119] They are displayed and discussed in detail with **Figure S6-1**a and b. In brief, the negative current increases towards the lower potential limit. A small anodic peak appears at around 1 V in the anodic scan. Within the first few cycles, both peaks decrease significantly. The overall reversibility of the cathodic and anodic processes, as indicated by the

overall charge ratio in these potential regimes (Coulombic efficiency), is about 18 % in the first cycle (inset in **Figure S6-1**a) and increases to around 35 % in subsequent cycles (see **Figure S6-4** and **Table S6-1**). Overall, however, the reversibility is very low and Mg deposition / dissolution is (at most) a minor process.

In the following, we will briefly summarize the different effects and influences of borohydride on the Mg deposition / dissolution process that have been reported in the past. First, the addition of reductive, contamination-scavenging additives such as di-butyl Mg (in our case: $Mg(BH_4)_2$), which can react with traces of water, oxygen and other protic species, was found to improve the Mg plating / stripping efficiency by forming Mg oxides and hydroxides in the bulk, which, in return, reduces / avoids surface passivation.[101,274] Second, reversible Mg plating / stripping was found to require a minimum amount of such additives, which approximately corresponded to a slight excess relative to the estimated water content of the electrolyte.[274] Third, reversible Mg plating / stripping was possible also from $MgTFSI_2$-containing solutions when using complexing solvents such as glymes upon addition of $Mg(BH_4)_2$[274] or once the electrolyte was carefully dried.[269] Finally, high deposition reversibilities were obtained even without additional drying when using $Mg(BH_4)_2$ as Mg source rather than $MgTFSI_2$.[98] Overall, these studies support the idea that borohydride acts as efficient water scavenger.[98,274] As stated above, our results of a very low reversibility for Mg plating / stripping fully agree with previous findings for cycling a Pt electrode in a similar electrolyte.[119,121] They seem to disagree, however, with the previous findings summarized above, considering that, in our experiments, the amount of $Mg(BH_4)_2$ added to the electrolytes should always be sufficient to fully remove the water impurities of BMP-TFSI, $MgTFSI_2$ and crown ether, based both on our estimations and on the suppliers' specifications (see Chapter 2.3) and assuming that each BH_4^- can react with one water molecule. The discrepancy is most likely caused by the different solvents, with only small amounts of $TFSI^-$ in the above cases, together with complexing solvents, while in our case the $TFSI^-$ is part of the solvent and thus present in large excess and no other complexing species are present. Electrolyte decomposition in $Mg(BH_4)_2$-containing BMP-TFSI was explained by the decomposition of $TFSI^-$, which is coordinated with the metal ions in such IL mixtures. This kind of complex formation, where $TFSI^-$ anions can coordinate to a single metal cation (contact ion pairs, CIPs) or to multiple metal cations in aggregate networks (where the Mg^{2+} cation is in direct contact with the $TFSI^-$ anion), has been identified previously by both Infrared[262] and Raman spectroscopy.[119,121,253,283] Theoretical studies have shown that partial reduction of the Mg center, which is expected to happen at the interface at potentials in the Mg deposition regime,

leads to a weakening of the C–S bond in the $TFSI^-$ anion, which in turn results in $TFSI^-$ decomposition rather than in Mg deposition.[121,272] In contrast, BH_4^- was found to be stable under these conditions. In electrolytes containing both borohydride and $TFSI^-$, $TFSI^-$ decomposition has been observed in experimental studies.[101,118,119,121,276,284]

Next, we investigated the influence of 18-crown-6 upon cycling in $Mg(BH_4)_2$-containing BMP-TFSI. CVs recorded in BMP-TFSI + 0.1 M $Mg(BH_4)_2$ + 0.1 M 18-crown-6 electrolyte are depicted in **Figure 6-1**. The additive leads to increased currents, both in the cathodic and in the anodic scan, as compared to the borohydride-containing IL in the absence of the crown ether (**Figure S6-1**). The cathodic current densities are at least four times higher and the increase of the anodic currents is even more drastic.

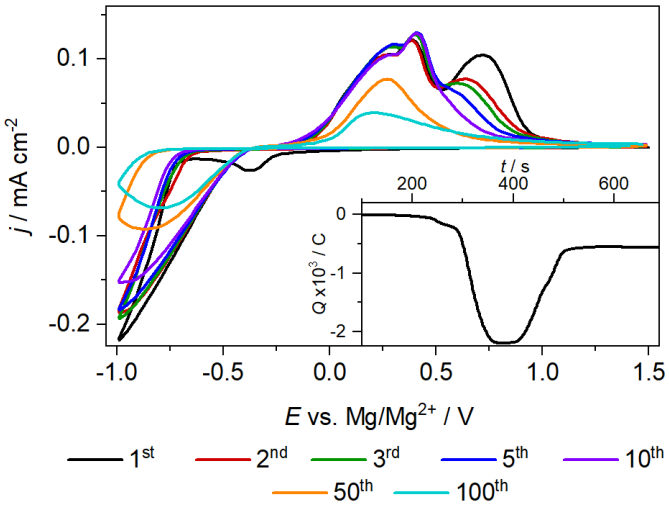

Figure 6-1. First and additional relevant potentiodynamic cycles recorded on a GC electrode in BMP-TFSI + 0.1 M $Mg(BH_4)_2$ + 0.1 M 18-crown-6 cycled at 10 mV s^{-1}. The inset shows the accumulated charge (i.e., the charge balance of Mg plating / stripping) during the first scan.

These changes may originate from reversible processes, such as Mg plating and stripping, although the present data do not provide definite proof for the latter assignment. A weak peak is observed at -0.4 V in the first cathodic scan, which does not appear anymore in the subsequent cycles. Interestingly, in a crown ether-free, borohydride-containing IL, a similar signal appeared at -0.3 V in the first cathodic cycle (**Figure S6-1**a). We tentatively assign these peaks to the reductive removal of a surface contamination on the GC substrate, considering that this peak was only observed on the GC electrode, independent of the electrolyte composition. At potentials below -0.7 V, the characteristic current increase for Mg deposition appears. Here, Mg plating takes place with a nucleation overpotential that is by 0.1 V lower than the one

observed for 0.1 M $Mg(BH_4)_2$-containing IL without any crown ether additive (see discussion with **Figure S6-1**). In the subsequent anodic scan, we find the corresponding signal for Mg dissolution at 0.3 V, down-shifted by 0.4 V from the Mg dissolution peak observed in crown ether-free IL. This is followed by two additional peaks at 0.4 V and 0.7 V, which seem to indicate that, next to Mg stripping, oxidation of species formed in cathodic side processes can take place under these conditions. It is worth noting that the position of the peak at 0.7 V observed in the crown ether-containing system coincides with the position of the anodic peak recorded in the first cycles of the crown ether-free system (**Figure S6-1**). Therefore, it is also possible that the anodic signal at 0.7 V is due to Mg dissolution from a similar Mg species – as obtained for deposition from $Mg(BH_4)_2$-containing electrolyte – while the peaks at 0.3/0.4 V are due to dissolution of Mg deposits created in crown ether-containing electrolyte.

In the following cathodic scan, the process taking place at -0.4 V is inhibited, like the analogous process in the ether-free system. The decreasing currents in the Mg deposition region and, subsequently, in the Mg dissolution region (anodic scan), also indicate an increasing inhibition of the related processes and/or the depletion of oxidizable components with increasing cycling. This current loss is most pronounced for the high-potential peak at 0.7 V. During the next ten cycles, it decreases and disappears completely, while the anodic signals at 0.3 and 0.4 V do not change significantly. The peak at 0.4 V starts to decrease only after ten cycles and has disappeared after about 35 cycles (not shown). The signal at 0.3 V also decreases, but much slower, becoming the main anodic peak. It is still visible even after 100 cycles. The reversibility is about 70 % in the first cycle (for comparison, the reversibility of the processes taking place in solely borohydride-containing IL was ~18 % in the first cycle) and increases to 78 % within the first ten cycles, as compared to 35 % reached in ether-free electrolyte after the same number of cycles. Upon further cycling, however, the reversibility in the $Mg(BH_4)_2$- and 18-crown-6-containing IL decreases, as well, dropping to 25 % after 20 cycles. This remains about constant for the rest of the cycling time (100 cycles in total), indicating that the continuing passivation process not only reduces the current densities both in the cathodic and anodic scan but also affects them in the same way, keeping the charge ratio between them constant (see **Figure S6-5** and **Table S6-2**).

The results in **Figure 6-1** can be compared with previous data and conclusions, which had already identified positive effects on the reversibility of the Mg plating / stripping process when modifying the IL cation[119,121,263] or varying the solvents and/or adding complexing additives.[45,46,261,263,285] Our results are in agreement with reports on an improved Mg

deposition / dissolution reversibility in the presence of ethers such as glymes, etc.[265,274,278,286] As one example, Mandai *et al.* reported an improved Mg deposition / dissolution activity for tetraglyme-coordinated $MgTFSI_2$ in BMP-TFSI in the presence of dialkylsulfones as compared to electrolytes with less efficiently coordinating additives, such as DMSO.[278] Increased current densities for Mg deposition in $MgTFSI_2$-containing electrolytes were reported also by Sagane *et al.* upon addition of 18-crown-6 ether, both in THF[45] and in N-methyl-N-propylpiperidinium (MPPp)-TFSI.[46] Similarly, Ma *et al.* have shown reversible and stable (for more than 280 cycles) Mg plating and stripping from 0.3 M $MgTFSI_2$-containing BMP-TFSI / tetraglyme mixtures (1 : 2) after treatment with 0.019 M $Mg(BH_4)_2$.[263]

Employing *ex situ* scanning electron microscopy (SEM) characterization, Sagane *et al.* also observed the formation of Mg dendrites in the Mg deposits formed from 0.5 M crown ether- and 0.5 M $MgTFSI_2$-containing THF, which could hardly be dissolved subsequently.[45] Going to much higher concentrations of both ether additive and $TFSI^-$ salt in an IL electrolyte ($MgTFSI_2$, 18-crown-6 and MPPp-TFSI, with molar ratios of 1 : 1 : 5 and 1 : 5 : 5), the Mg deposits were significantly smoother than the dendritic morphologies obtained in THF-based electrolyte, but still exhibited a 'mossy' structure, which the authors attributed to the high viscosity of the ionic liquid as well as to accelerated $TFSI^-$ decomposition.[46] We assume that this is also the reason for the poor reversibility of about 3 % obtained in that study. This deposition / dissolution behavior is very different from the uniform Mg deposits obtained in Grignard-based electrolytes, which also allowed reversible dissolution.[287] Watkins *et al.* had proposed that the addition of a chelating agent (in their case, oligoether glymes or 18-crown-6) separates the direct coordination of Mg^{2+} by $TFSI^-$ and results in the formation of $[(Mg(glyme)_x)^{2+}(TFSI^-)]^+$ complexes, which they referred to as solvent-separated ion pairs (SSIPs).[283] This was concluded from the disappearance of the Raman band typical for Mg^{2+}-coordinated $TFSI^-$ and the appearance of a new band that was associated with Mg^{2+}-coordinated glyme. Such a separation of $TFSI^-$ from the Mg^{2+} cations could explain the more facile Mg deposition in the measurements in **Figure 6-1**, but similar results could also be obtained from a weakening of the Mg^{2+}-$TFSI^-$ coordination. Finally, DFT calculations comparing the different abilities to coordinate cations in chloride-containing Mg complexes in monoglyme-, diglyme-, triglyme- and tetraglyme-based electrolytes indicated that the longer and more flexible glymes were increasingly able to adjust their conformation and thus enhance the interaction between Mg and solvent. This was proposed to allow for the formation of larger Mg^{2+}-, Cl^-- and solvent-containing aggregates, which, in turn, improves the reversibility of Mg deposition / dissolution, though at higher overpotentials.[288] Focusing on BH_4^--containing

electrolytes, both experimental studies[261,281] and calculations[289,290] for several electrolytes have concluded that the dissociation of the Mg^{2+}–BH_4^- coordination is a key aspect for Mg deposition, which, in ether-type solvents, is influenced by the number of coordinating oxygen atoms or possibly also by coordinating $TFSI^-$ ions. The Mg^{2+} coordination in BH_4^-- and $TFSI^-$-containing diglyme was investigated by Hu *et al.* in a combined experimental and theoretical study.[291] Using the electrolyte components without further purification or drying, they found an improved electrochemical performance in the mixed electrolyte as compared to a $TFSI^-$-free electrolyte. They explained this by a formation of mixed ion pair clusters containing Mg^{2+} as central ion, which is coordinated by BH_4^- and $TFSI^-$ anions as well as by O-atoms of the glyme molecules. The latter are expected to reduce the strong interaction between Mg^{2+} and BH_4^- anions, which was claimed to allow for reversible Mg plating and stripping.[291] Using a special $TFSI^-$-based IL with an oligoether group in the cation and $Mg(BH_4)_2$ as Mg source, Watkins *et al.* found that Mg deposition / dissolution reversibility are significantly improved compared to that from BMP-TFSI.[119] They attributed this to the complexation of the Mg^{2+} cation by the polyether groups, which prevents the direct $TFSI^-$ coordination and weakens the Mg^{2+}–BH_4^- coordination. Comparable results were reported by Gao *et al.*,[121] who, furthermore, observed that the above effects increase with increasing ether functionalization of the cation. Based on aforementioned results, the crown ether may either displace the $TFSI^-$ anions from the Mg^{2+} coordination sphere and thus prevent the decomposition of the $TFSI^-$; or it may weaken the interaction with Mg^{2+} and thus stabilize the $TFSI^-$ against decomposition. In both cases, one would expect an improved reversibility of the Mg deposition / dissolution process and, in particular, a better stability / slower inhibition of these processes in the presence of the crown ether. Still open, however, is the role of the borohydride in this process. It may either solely act as water scavenger, removing trace impurities of water in the different chemicals (see Chapter 2.3) from the electrolyte, or it may also coordinate to Mg^{2+}. BH_4^- coordination to Mg^{2+} has indeed been reported to be stronger than that of $TFSI^-$,[121,291] which will be important also for the present case. Finally, also the ratio between the different components seems to be important; as indicated by the results of Hu *et al.*, who observed significant differences in the Mg deposition / dissolution current when varying the ratio of the $TFSI^-$ and BH_4^- concentration in Mg^{2+}-containing diglyme.[291]

In order to investigate the role of the $TFSI^-$ and BH_4^- anions and of the crown ether and, in particular, their relative concentrations, in more detail, we prepared electrolytes with different concentrations of these species. In all cases, the Mg^{2+} concentration was kept at 0.1 mol L^{-1}. We would expect that, if borohydride acts only as water scavenger and is necessary for that, a

certain minimum concentration of borohydride is required for reversible Mg deposition / dissolution. In that case, crown ether would be furthermore required to coordinate to Mg^{2+} and displace $TFSI^-$. Alternatively, both borohydride and crown ether contribute to the displacement of $TFSI^-$ from the Mg^{2+} coordination sphere. In this case, the total amount of borohydride plus crown ether relative to the amount of Mg^{2+} would be decisive for reversible and reasonably stable Mg deposition / dissolution.

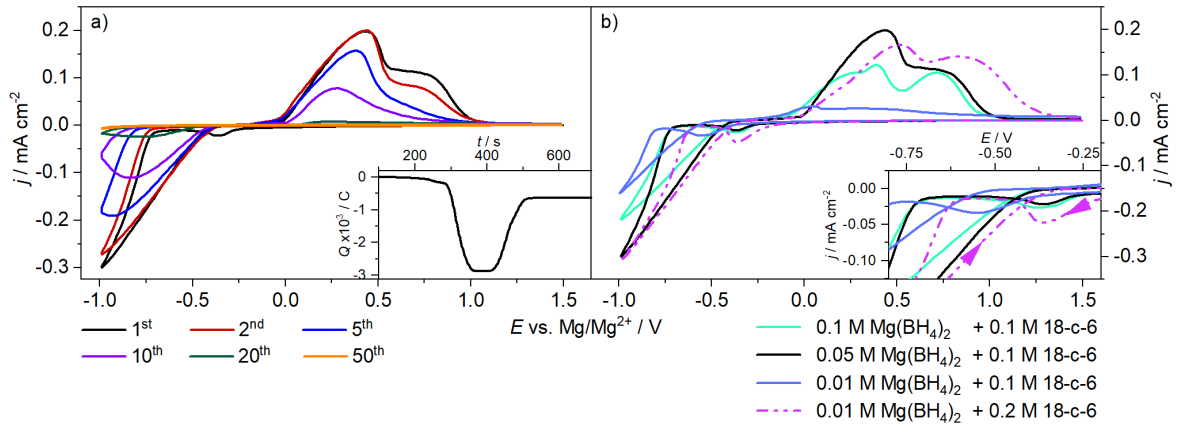

Figure 6-2. Sets of CVs recorded on GC in BMP-TFSI + 0.05 M $Mg(BH_4)_2$ + 0.05 M $MgTFSI_2$ + 0.1 M 18-crown-6 (a) and in BMP-TFSI with different concentrations of $Mg(BH_4)_2$, $MgTFSI_2$ and 18-crown-6 (b, first cycle). The concentration of $MgTFSI_2$ is 0.1 M – concentration of $Mg(BH_4)_2$. The inset in a) shows the accumulated charge during the first scan, in b) an enlarged section of the lower potential region between -0.2 and -0.8 V. All scan rates are 10 mV s^{-1}.

In **Figure 6-2**a, we present a set of CVs recorded with a GC substrate in $Mg(BH_4)_2$-, $MgTFSI_2$-, and 18-crown-6-containing BMP-TFSI, with a 1 : 1 molar ratio of crown ether to Mg^{2+} and a 1 : 1 mixture of $Mg(BH_4)_2$ and $MgTFSI_2$ (0.05 M $Mg(BH_4)_2$ + 0.05 M $MgTFSI_2$ + 0.1 M 18-crown-6). The characteristic features in these CVs are essentially identical to those obtained and discussed before for GC in a solution of 0.1 M $Mg(BH_4)_2$ and 0.1 M 18-crown-6 in IL (**Figure 6-1**). The reversibility is about 80 % in the first ten cycles, which is comparable to the results obtained for the $MgTFSI_2$-free electrolyte (**Figure 6-1**). However, with increasing cycling times, the reversibility decreases to about 12 % after 20 cycles (see **Figure S6-6** and **Table S6-3**) and the electrode is completely inert after 50 cycles (**Figure 6-2**a). For comparison, the GC electrode cycled in BMP-TFSI + 0.1 M $Mg(BH_4)_2$ + 0.1 M 18-crown-6 (discussed with **Figure 6-1**) still displayed more than half of the initial current densities after 50 scans. Considering that the relative increase in $TFSI^-$ concentration is marginal and the concentrations of Mg^{2+} and 18-crown-6 are identical to those in **Figure 6-1**, these changes in reversibility must be related to the lower amount of BH_4^- in the measurement to **Figure 6-2**a.

Upon further increasing the amount of $MgTFSI_2$ at the expense of $Mg(BH_4)_2$ (**Figure 6-2**, 0.09 M $MgTFSI_2$ + 0.01 M $Mg(BH_4)_2$ + 0.1 M 18-crown-6), we observe a pronounced decay of the current density and a down-shift of the Mg deposition potential (blue curve). Obviously, the increasing lack of BH_4^- is detrimental for the Mg^{2+} deposition process. The current trace in the anodic scan is affected even more and shows only a very weak and broad Mg dissolution feature. Hence, both Mg plating and Mg stripping are reduced when replacing BH_4^- by $TFSI^-$, or the other way around, when reducing the amount of BH_4^-, while keeping the concentration of crown ether constant. Interestingly, when doubling the amount of crown ether added to this $Mg(BH_4)_2$/$MgTFSI_2$ mixture (**Figure 6-2**b, violet dashed curve, 0.09 M $MgTFSI_2$ + 0.01 M $Mg(BH_4)_2$ + 0.2 M 18-crown-6, for more cycles see **Figure S6-7** and **Table S6-4**), the high current densities are restored again and the reversibility is significantly improved. The latter increases from 75 % in the first cycle to 82 % in the second cycle, then decreases again continuously to 75 % in the 10th cycle. This trend in the reversibility, with an initial increase and a later decrease, is very similar to that obtained for the sample cycled in IL containing 0.05 M $Mg(BH_4)_2$ + 0.05 M $MgTFSI_2$ + 0.1 M 18-crown-6 (**Figure 6-2**a). We assume that the similar trends reflect that, in both cases, an increasing excess of BH_4^- plus crown ether relative to the Mg concentration is beneficial for the Mg deposition / dissolution reaction. Also, the onset potential for Mg deposition (-0.6 V) is slightly more anodic than that obtained in pure borohydride and crown ether-containing IL with no $MgTFSI_2$ (-0.7 V, equivalent to an up-shift of the onset potential for Mg deposition by 0.1 V), supporting the above conclusion of more facile Mg deposition in this electrolyte. In combination, these results indicate that the sole coordination of $TFSI^-$ with Mg^{2+} is detrimental for the Mg deposition / dissolution processes. However, when either the crown ether or BH_4^- – or both in combination – are present in the electrolyte in sufficient amounts, $TFSI^-$ can either at least partly be displaced from the inner Mg^{2+} coordination sphere, or the Mg^{2+}–$TFSI^-$ interaction can be weakened to an extent that Mg^+-induced $TFSI^-$ decomposition is inhibited during reaction. Both could enable improved plating and stripping. On the other hand, Hu *et al.* had demonstrated that an increase of the $MgTFSI_2$ content, from zero content to fourfold excess at constant $Mg(BH_4)_2$ concentration (0.01 M), leads to a continuous increase in reversible Mg deposition / dissolution from diglyme.[291] Based on quantum chemical calculations, they proposed that $TFSI^-$ displaces one of the BH_4^- ligands in the inner coordination shell, which was seen as origin for the improved Mg deposition / dissolution. The apparent discrepancy to our findings – an improved Mg deposition / dissolution upon addition of $TFSI^-$ to $Mg(BH_4)_2$-containing electrolyte in their case versus an improved Mg deposition performance upon addition of $Mg(BH_4)_2$ to $TFSI^-$-based

electrolyte in our experiments – is most likely due to the very different situations in both cases. While in our experiments $TFSI^-$ is present also as solvent and thus in strong excess, they use $TFSI^-$ in rather low concentrations, comparable to that of BH_4^-, together with an excess of the Mg-coordinating glyme as solvent. These results point to an equilibrium of Mg^{2+} coordination with the various ligands, where coordination of $TFSI^-$ to Mg^{2+} and, thus, also Mg^+-induced decomposition of $TFSI^-$, are still possible as long as BH_4^- and/or crown ether (or a combination of them) are not present in over-stoichiometric amounts (for crown ether: 1 : 1). This conclusion also fits well to the results reported by Shao *et al.*, who observed a significant enhancement of the Coulombic efficiency with increasing BH_4^- concentration, as well as when changing from a monodentate solvent molecule (THF) to bidentate (DME) and finally tridentate (diglyme) molecules.[261] They explained this behavior by synergistic effects, without, however, explaining in more detail how this would affect Mg deposition. As mentioned before, we found that, also in the presence of crown ether, a certain amount of BH_4^- is required, as indicated by the experiment with 0.09 M $MgTFSI_2$ + 0.01 M $Mg(BH_4)_2$ + 0.1 M crown ether, where Mg deposition was strongly hindered. Finally, additional measurements with other concentrations of crown ether (**Figure S6-3**) further confirmed that a certain minimum amount of BH_4^- is required for Mg deposition from $MgTFSI_2$. Even a tenfold excess of crown ether did not support Mg deposition from $MgTFSI_2$ if no BH_4^- was added. This is most easily explained in a picture where some BH_4^- is necessary for removal of trace impurities of water, and, additionally may coordinate with Mg^{2+}. Here it should be mentioned that Sagane *et al.* observed that the addition of stoichiometric (1 : 1) amounts of 18-crown-6 to $MgTFSI_2$ in MPPp-TFSI is required and sufficient for a complete displacement of $TFSI^-$ from the coordination sphere of the Mg^{2+}, resulting in the formation of "free" $TFSI^-$ anions. The CV of that mixture shows Mg plating and stripping, but with a very low reversibility.[46] Furthermore, there may be an influence of the IL cation on the complexation process, as these authors used 1-methyl-1-propylpiperidinium ($MPPp^+$) as cation rather than the 1-butyl-1-methyl-pyrrolidinium (BMP^+) employed in the present work. Finally, we want to briefly test for possible effects induced by the nature of the electrode by changing to a Mg electrode.

Figure 6-3 displays a CV recorded in 0.1 M $Mg(BH_4)_2$-containing BMP-TFSI with 0.1 M 18-crown-6 on a magnesium substrate. Different from the current traces recorded on the glassy carbon substrates in 0.1 M $Mg(BH_4)_2$ and 0.1 M 18-crown-6-containing IL, the first cathodic scan (after a potential step from the OCV to the upper potential limit) already exhibits oxidative currents in the potential range 1.5–0 V, which we assume are due to Mg dissolution

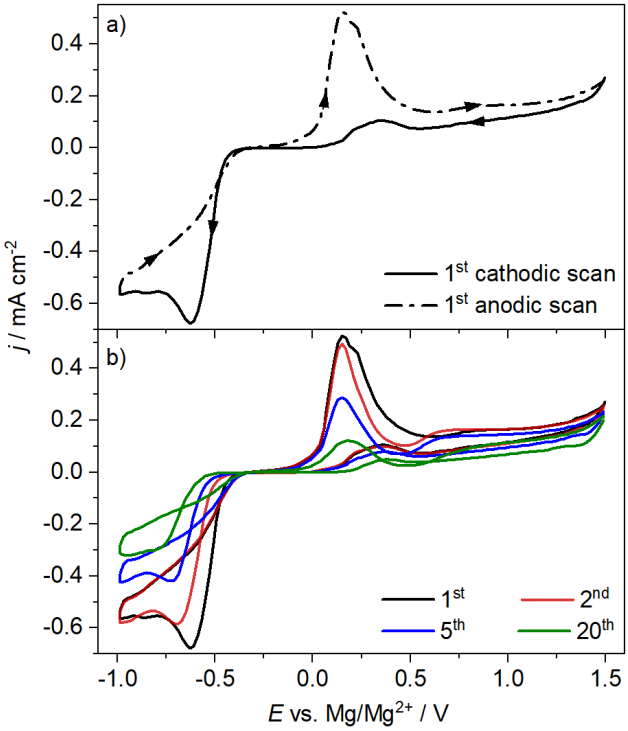

Figure 6-3. First (a) and additional relevant (b) cycles of the potentiodynamic scan of a Mg electrode in 0.1 M $Mg(BH_4)_2$ + 0.1 M 18-crown-6-containing BMP-TFSI at 10 mV s^{-1}.

from the roughened electrode (see Chapter 2.2). This is different from results reported by Ma *et al.*, who only observed dissolution of freshly deposited Mg, but not of the Mg substrate, in 0.5 M $MgTFSI_2$/tetraglyme electrolyte containing 6 mM $Mg(BH_4)_2$, at least when cycling below 1.0 V. They concluded that, most likely, the underlying Mg surface is passivated completely despite the roughening pretreatment.[274] Mg deposition starts already at a potential below 0.5 V, i.e., at a lower overpotential compared to that obtained on a glassy carbon electrode in the same electrolyte (**Figure 6-1**, around 0.7 V).

This indicates a lower nucleation overpotential for the roughened Mg electrode compared to the GC substrate, most likely due to the presence of efficient sites for heterogeneous nucleation on the surface. The corresponding Mg dissolution peak appears at 0.2 V, also down-shifted by 0.1 V compared to the Mg dissolution peak observed on GC. Initially, the current density is almost three times higher than the corresponding current traces on glassy carbon. With increasing cycle number it decreases rapidly, having lost about half the initial current density by the fifth cycle. This loss is far more pronounced than on glassy carbon. We tentatively explain this by the generally higher reactivity of the Mg surface, which reacts more efficiently both with trace impurities in the electrolyte and/or with the solvent during cycling. This

reaction may hinder further Mg deposition and thus result in the distinct peak between -0.6 and -0.7 V in the Mg deposition range, rather than the expected exponential current increase when approaching the lower potential limit. The peak in the anodic scan at about 0.2 V is most likely related to dissolution of the freshly plated Mg, whereas oxidation of the underlying Mg substrate proceeds only in the anodic currents above 0.5 V. Interestingly, while the onset and peak maximum for Mg dissolution remain the same, the onset for Mg deposition shifts to more negative potentials with continued cycling. Overall, compared to Mg plating / stripping on GC, both these and also the passivation processes are faster on Mg.

It is also worth mentioning that, aside of its role as water scavenger, borohydride may also dissolve the (native) passivation layer present on the Mg surface due to its strongly reducing nature.[98] However, we observed both Mg deposition / dissolution and electrolyte decomposition currents only on *in situ* roughened Mg electrodes. Hence, the sole presence of borohydride is not enough to dissolve the native passivation layer and allow for reversible Mg plating and stripping. To learn more about the question in how far these effects are specific for Mg deposition, we studied the plating / stripping behavior on GC in analogous electrolyte systems, employing Ca^{2+} instead of Mg^{2+}. No Ca^{2+} deposition was observed from $Ca(BH_4)_2$-containing BMP-TFSI, neither in the absence nor presence of 18-crown-6 (**Figure S6-2** and **Figure S6-3**). We speculate that this difference is related to the different mismatch[280] between the cavity size of the crown ether (2.9 Å for 18-crown-6) and the ion diameters of the two ions (Ca^{2+} 2.0 Å, Mg^{2+} 1.44 Å). The better fit would result in a stronger binding of Ca^{2+} than of Mg^{2+}. In that case, Mg^{2+} deposition could still be possible when it is coordinated to 18-crown-6, while Ca^{2+} is too tightly bound for deposition. This hypothesis is also in agreement with the fact that we found neither Ca nor Mg deposition from BMP-TFSI-containing 15-crown-5 (cavity size 2.0 Å), as, as we assume, both cations are too strongly bound for metal deposition.

Finally, we would like to note that the proposed mechanism of a displacement of the anion of the IL solvent / Mg source by the additives requires that the additives coordinate more strongly to the Mg^{2+} cation than the weakly coordinating $TFSI^-$ anions and also weaken the Mg^{2+}–$TFSI^-$ interaction, but still are sufficiently weakly coordinated to allow facile Mg deposition. The partial displacement of the Mg^{2+}-coordinated $TFSI^-$ species and the weakening of the Mg^{2+}–$TFSI^-$ interaction of the remaining $TFSI^-$ ligands inhibits the decomposition of the $TFSI^-$, which is induced by interaction with the Mg^+ upon partial reduction of the Mg^{2+} ion.[272] Hence, we propose that in such cases the optimum additive is one that is i) stable against

decomposition itself and that has ii) an optimum interaction with the metal cation; i.e., sufficiently strong that it can partly displace the instable component (here $TFSI^-$) and/or weaken its interaction with the central Mg^{2+} ion, but sufficiently weak that it does not inhibit metal deposition by formation of a stable coordination shell. This also requires that the coordination of the unstable component be sufficiently weak that it can still be displaced by the additive under the conditions described in ii).

These questions were investigated theoretically, as detailed in the next section.

6.3.2. Simulation

To test the above interpretation, we conducted MD simulations and quantum chemical calculations at the density functional level of theory (DFT), comparing the stability of the coordination sphere of the Mg^{2+} cation in the presence and absence of 18-crown-6 (for details, see Chapter 2.2.6 and Supporting Information, Chapter 6.5.3). Note that in our classical MD simulations, which are used as starting point, the interactions between Mg^{2+} and the solvent molecules are limited to solely electrostatic forces and will not include contributions from covalent interactions between Mg^{2+} and oxygen. However, such interactions are fully captured in the subsequent DFT calculations. In these calculations, the reference level for the energy of the respective clusters was defined by the energy of an isolated $MgTFSI_2$ cluster plus that of the separate additional ligands (BMP-TFSI ion pairs, 18-crown-6), where the energies were calculated using the frozen geometry of the most stable complete cluster. Accordingly, the coordination energies E_c refer to the energy gained upon coordinating one or more additional ligands to the $MgTFSI_2$ cluster, while the binding energy E_b of a specific ligand in that cluster refers to the energy required for removing that ligand in a frozen configuration. For selected configurations obtained during the MD simulations, we cut clusters containing the $MgTFSI_2$ as well as up to two BMP-TFSI ion pairs in the absence and presence of 18-crown-6, which were further optimized geometrically (see Experimental section, Chapter 2.2.6). For the determination of the coordination and binding energies presented in **Figure 6-4** and **Figure 6-6** and in **Table 6-1**, we used the cluster configurations with the most stable final geometry. Note that the structure of the $MgTFSI_2$ complex included therein may not be the most stable configuration of the isolated $MgTFSI_2$ cluster.

In **Figure 6-4**, we show a selection of clusters cut from the MD simulations consisting of $MgTFSI_2$ in the presence of up to two BMP-TFSI ion pairs and up to one 18-crown-6 molecule. The Mg^{2+} cation is displayed in different coordination states and geometries, along

with the respective (additional) coordination energies. The clusters are portrayed in the most stable configurations observed for the respective coordination. Note that these are not necessarily the configurations with the highest coordination energies. Visualizations of some other clusters considered in this work are provided in the Supporting Information (Chapter 6.5.3, **Figure S6-8**).

Table 6-1. Electron affinity E_A and equilibrium potential E_{red} for molecule / cluster reduction vs. Mg/Mg^{2+} for different molecule / cluster types.

Cluster / molecule	E_A / eV	E_{red} / V
$TFSI^-$	2.16	-1.19
18c6	-0.49	-3.84
Mg^{2+} + 18c6	1.68	-1.67
$MgTFSI_2$	3.75	0.40
$MgTFSI_2$ + BMP-TFSI	3.49	0.14
$MgTFSI_2$ + 2 BMP-TFSI	3.10	-0.25
$MgTFSI_2$ + 18c6	2.97	-0.38
$MgTFSI_2$ + 18c6 + BMP-TFSI	2.91	-0.44

A main characteristic for all clusters is the bond between the Mg^{2+} cation and the oxygen atoms of the $TFSI^-$ anions or of the 18-crown-6 molecule. The different configurations in **Figure 6-4** involve coordination geometries of the Mg^{2+} cation with different numbers of directly coordinating oxygen atoms, as illustrated in **Figure 6-5**. The Mg^{2+} cation prefers a seven-fold coordination by oxygen atoms in the presence of 18-crown-6, while a five- or six-fold oxygen coordination, arranged in a pyramidal or octahedral configuration, respectively, is preferred in its absence.

As expected, the increasing coordination of the Mg^{2+} ion in the $MgTFSI_2$ cluster increases the stability of the cluster. Coordination with an additional BMP-TFSI ion pair leads to a stabilization by -132 kJ/mol (**Figure 6-4**a). Note that this denotes the overall energy gain of the system, which may also contain contributions from a change in bonding within the original $MgTFSI_2$ cluster and within the ion pair. Hence, it is not necessarily the strength of the bond between Mg^{2+} and the ion pair, but it would properly describe the energy needed to detach the ion pair. Adding a second BMP-TFSI ion pair to the $MgTFSI_2$ + BMP-TFSI cluster does not lead to a further stabilization of the cluster; the coordination energy of -130 kJ/mol for two BMP-TFSI ion pairs is almost equal to that of a single ion pair (**Figure 6-4**b). Qualitatively,

this can be understood from the fact that, for coordination with a single BMP-TFSI ion pair, the $TFSI^-$ anion can coordinate via two oxygen atoms, while for coordination by

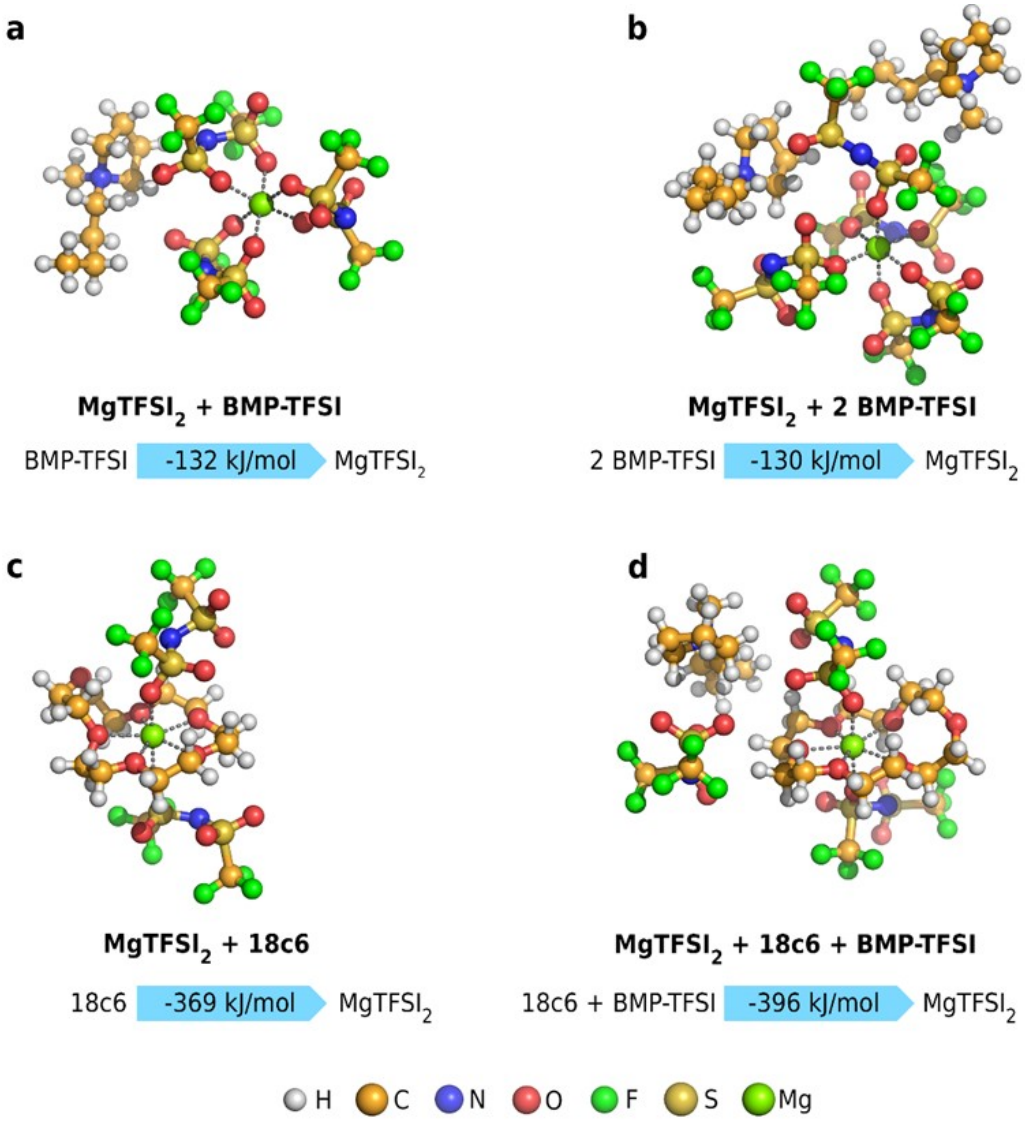

Figure 6-4. Representation of the most stable clusters at different compositions, cut from MD simulations, and the respective coordination energies *E*c.

two BMP-TFSI ion pairs each of them coordinates only by a single oxygen atom of the $TFSI^-$ species to the Mg^{2+} cation (see **Figure 6-4**). Hence, coordination by the second ion pair weakens the bond to the first ion pair, and this effect is quite significant. Therefore, one would expect an equilibrium between both states at room temperature, which also means that thermal detachment of the second ion pair is easily achieved at room temperature. This weakening of the bond to the first BMP-TFSI ion pair is illustrated also in the energy scheme in **Figure 6-6**. It represents the binding energies for different ligands in the frozen geometry of the final cluster, which were calculated by comparing the cluster energies before and after removal of the respective ligand in that geometry. In this case, the binding energies of the two different

BMP-TFSI ion pairs are almost identical (**Figure 6-6**c), and they are much smaller than that of the BMP-TFSI ion pair in **Figure 6-4**a. Also, it does not seem to matter which of the two ion pairs is added first. Hence, synergistic effects between the two ion pairs are absent.

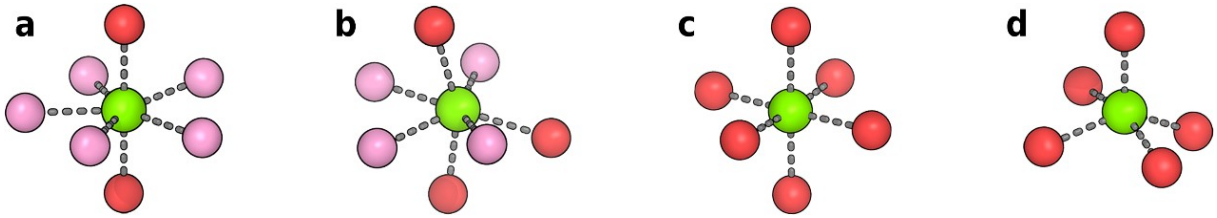

Figure 6-5. Different coordination states of Mg^{2+}, colored in green, in the presence (a, b) and absence (c, d) of 18-crown-6. Oxygen atoms belonging to the 18-crown-6 ring are colored in pink; those belonging to $TFSI^-$ in red.

In a similar way, we explored the additional coordination of an 18-crown-6 molecule to either the $MgTFSI_2$ (**Figure 6-4**c) or the $MgTFSI_2$ + BMP-TFSI (**Figure 6-4**d) cluster. In the first case, this results in a stabilization by -369 kJ/mol. Hence, the coordination of the $MgTFSI_2$ cluster by the crown ether is significantly stronger than that by a BMP-TFSI ion pair. Also, the addition of a single 18-crown-6 molecule to a $MgTFSI_2$ + BMP-TFSI cluster results in a drastic increase in cluster stability by -264 kJ/mol. Qualitatively, this is evident already from the structure of the most stable cluster in **Figure 6-4**d. This shows a significant weakening of the coordination to the two original $TFSI^-$ anions, which are coordinated now only via one oxygen atom, and to the third $TFSI^-$ anion (that of the BMP-TFSI ion pair), which is no longer part of the inner coordination sphere. Here, we identify the $TFSI^-$ anion of the ion pair by its stronger interaction to the BMP^+ cation compared to the other two $TFSI^-$ species. On a more quantitative scale, this is illustrated in the energy scheme in **Figure 6-6**d. Addition of a crown ether molecule to the $MgTFSI_2$ cluster, in the frozen geometry of the stable configuration of the $MgTFSI_2$ + BMP-TFSI + 18-crown-6, results in a binding energy stabilization by -353 kJ/mol; further addition of a BMP-TFSI ion pair stabilizes this by another -43 kJ/mol (total coordination energy -396 kJ/mol), which is even less than the binding energy per BMP-TFSI ion pair in the $MgTFSI_2$ + BMP-TFSI cluster. Also in this case, it almost does not matter whether the crown ether or the ion pair is added first and synergies are very small. Overall, the strong coordination by the crown ether molecule leads to a significant weakening of the bond between Mg^{2+} and the two $TFSI^-$ anions, and essentially a displacement of the BMP-TFSI ion pair. Also considering these effects in the overall energy balance, one expects that the bond between crown ether and Mg^{2+} cation is even significantly stronger than -353 kJ/mol.

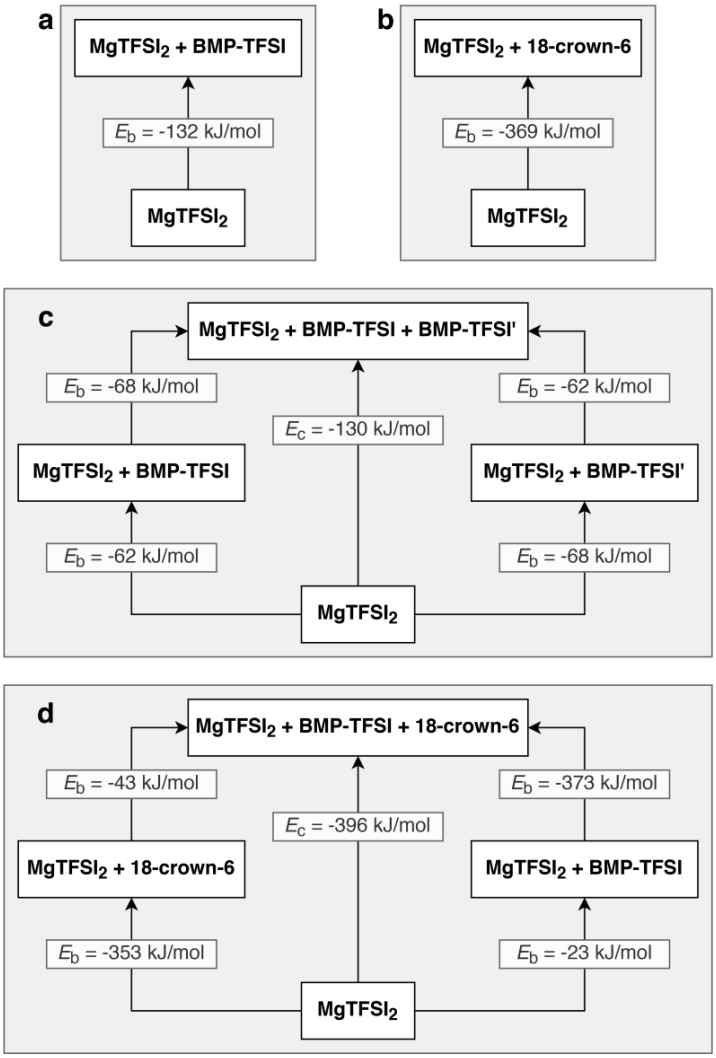

Figure 6-6. Scheme of the coordination energies E_c and binding energies E_b for different cluster compositions.

In addition to the above calculations, we also explored whether coordination of two 18-crown-6 molecules to the $MgTFSI_2$ cluster would be strong enough to additionally displace the original $TFSI^-$ anions from their direct coordination to the Mg^{2+} cation. For this purpose, we built and optimized a cluster in which the Mg^{2+} cation is surrounded by two 18-crown-6 molecules and the two $TFSI^-$ anions are displaced to the second coordination layer (**Figure S6-9**). Here, we find that the total binding energy in that cluster is stronger by -70 kJ/mol, as compared to the coordination states in the absence of 18-crown-6. However, it is less stable by -27 kJ/mol as compared to the coordination by just one 18-crown-6 and two directly coordinating $TFSI^-$ anions.

Overall, these calculations indicate that i) the coordination with the 18-crown-6 molecule is much stronger than that with $TFSI^-$ anions, that ii) the interaction with the 18-crown-6 molecule leads to a significant destabilization of the remaining coordination to the two $TFSI^-$

anions, as indicated by the change from two-fold to one-fold coordination, and, finally, that iii) a complete screening of the Mg^{2+} cation by two 18-crown-6 molecules is energetically unfavorable. In the absence of 18-crown-6, the coordination of $MgTFSI_2$ with one or two BMP-TFSI ion pairs always results in either a six-fold or five-fold coordination of the Mg^{2+} cation, i.e., in an octahedral or trigonal bipyramidal structure, respectively. In contrast, in the presence of 18-crown-6, the Mg^{2+} cation is coordinated by four to five oxygen atoms of the ether and two to three anions coordinated by a single oxygen atom each.

Next, we considered that Mg deposition requires the cation to be able to (stepwise) strip its coordination shell when attaching to the electrode surface. As evident from the numbers in **Figure 6-4** and **Figure 6-5**, the binding energies with the $TFSI^-$ anions in the BMP-TFSI ion pairs calculated are of an order of magnitude that allows their thermal detachment at room temperature. This is true both for coordination of one or two ions pairs – actually, removing the second BMP-TFSI ion pair does not cost any energy – and especially in the presence of a crown ether molecule acting as a second ligand. On the other hand, it would be very hard for the Mg^{2+} cation to escape coordination with 18-crown-6. Previous studies have suggested that the partial reduction of Mg^{2+} to Mg^+ via an outer sphere electron transfer reaction will weaken the interaction with $TFSI^-$.[121,272] Similar effects may also be expected for the coordination to an 18-crown-6 molecule.

Figure 6-7 compares the coordination energies of different 18-crown-6 and/or BMP-TFSI-containing clusters before and after partial reduction of the cation from Mg^{2+} to Mg^+. Indeed, the coordination energies decrease significantly (strictly speaking, the absolute values of the coordination energies decrease). Most importantly, the coordination energy of the 18-crown-6-containing cluster decreases by -130 kJ/mol, falling to -212 kJ/mol. This moves it significantly closer to the range where Mg deposition seems feasible. On the other hand, while the addition of a second BMP-TFSI ion pair to the coordination sphere of Mg^{2+} does not result in a further stabilization of the cluster (see above), this is different for the reduced Mg^+ ion. Here, the addition of a second BMP-TFSI ion pair to the coordination sphere of $[MgTFSI_2]^-$ reduces the cluster stability, which, in turn, would improve Mg deposition on the electrode due to its reduced coordination. Overall, the data in **Figure 6-7** demonstrate that partial reduction of the Mg^{2+} to Mg^+, e.g., via an outer sphere charge-transfer step, destabilizes the coordination not only to solvent ion pairs, but also to 18-crown-6 molecules to an extent that detachment of these species becomes feasible at room temperature, which is a precondition for Mg deposition.

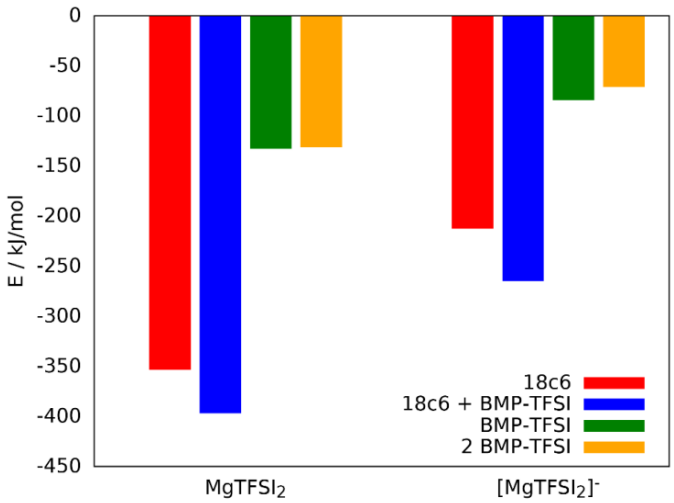

Figure 6-7. Coordination energies of different 18-crown-6 and BMP-TFSI-containing clusters ($MgTFSI_2$ + X, X see Figure) with $[Mg^{2+}–TFSI_2]$ or $[Mg^{+}–TFSI_2]^{-}$ as central unit. Coordination energies are referenced to the energies of the respective $MgTFSI_2$ clusters.

Finally, we investigated the reductive stability of the $TFSI^-$ anions in different clusters. Recently, several groups have proposed to derive trends in the electrochemical stability window calculating reduction and oxidation potentials, rather than using the strongly simplified previous scheme which relates the stability window to the HOMO and LUMO of the solvent molecules.[181-184] The main difference in this approach is the proper accounting of solvation effects and of contributions from reduction- / oxidation-induced reactions.[184] Here, we employed a method which is closely related to the general ideas of the thermodynamic cycle method, but proceeds in a different way: namely, by calculating the electron affinities E_A of the solvated clusters based on the adiabatic energy difference between a cluster and its reduced form. As described in the Experimental section (Chapter 2.2.6), both clusters were geometry-relaxed to the nearest local minimum. **Table 6-1** lists the values of E_A for a number of different clusters. For comparison, we also included the isolated $TFSI^-$ anion, the 18-crown-6 molecule, and the $MgTFSI_2$ cluster. Based on the electron affinities, trends in the equilibrium potential for reduction of the respective molecules / cluster E_{red} can be estimated (see Chapter 2.2.6), which are listed in **Table 6-1** as well. First of all, we find that the uncoordinated $TFSI^-$ anion shows a significantly higher electron affinity compared to its coordinated state in the $MgTFSI_2$ cluster. Considering the magnitude of the difference in electron affinities, this trend is significant, even though for these latter two species solvation effects are included only implicitly. A similar trend can be observed for 18-crown-6, which becomes more susceptible to reduction when coordinated to Mg^{2+}. However, both in its free and its coordinated state, 18-crown-6 ether shows significantly lower electron affinities than $TFSI^-$. Furthermore, we found that, during geometric relaxation, all $TFSI^-$-containing clusters

exhibit the dissociation of a $–CF_3$ group upon reduction. Therefore, the electron affinity of the $TFSI^-$-containing clusters is a measure also for the stability against reductive decomposition of the $TFSI^-$ group. In contrast, no bond breaking was observed in the 18-crown-6 ether, neither in the free molecule nor when coordinated to Mg^{2+} or $MgTFSI_2$. Spin density plots (**Figure S6-15**) reveal that, in $TFSI^-$- containing clusters, the unpaired electron is entirely located on the dissociated $–CF_3$ group after reduction, whereas in the case of the isolated $TFSI^-$ the unpaired electron is shared between both fragments. In the absence of $TFSI^-$ and presence of 18-crown-6, the additional, unpaired electron will be entirely located at the Mg^{2+} cation, reducing it to Mg^+. Hence, the coordination to Mg^{2+} strongly enhances the known tendency of $TFSI^-$ to decompose upon reduction via dissociation of a $–CF_3$ group.[121,272,292] Similar findings were recently described by Tuerxun *et al.* for $MgTFSI_2$ in different organic solvents (THF, diglyme), based on the comparison of the calculated HOMO / LUMO energy levels of the free $TFSI^-$ and of the $MgTFSI_2$ cluster, respectively.[264] In this case, implicit solvation effects were included, while explicit solvent effects by coordination of solvent molecules were not considered. Furthermore, we found that the addition of one BMP-TFSI ion pair slightly reduces the electron affinity E_A. On the other hand, the reductive stability of the coordinated $TFSI^-$ anion is significantly increased by the addition of an 18-crown-6 ligand. Hence, even though there are still two $TFSI^-$ anions weakly coordinated to the Mg^{2+} cation also in the presence of the 18-crown-6 molecule, these are less susceptible to reductive decomposition than the strongly coordinated $TFSI^-$ species present in the absence of the crown ether. The same trend is indicated by the spin density distribution plots. A high electron affinity correlates with a pronounced localization of the unpaired electron, whereas the clusters with lower electron affinity show a more diffuse spin distribution. In isolated 18-crown-6, the electron is delocalized over the whole ring upon reduction, while the additional electron is localized on the cation upon attachment to Mg^{2+}, reducing it to Mg^+ and increasing the electron affinity. The reduction of isolated $TFSI^-$ leads to the dissociation of a $–CF_3$ group, but the spin density plot shows that the unpaired electron is still shared between both fragments in the stable configuration. Again, the interaction with Mg^{2+} leads to a pronounced localization of the electron, which is then entirely located on the dissociated $–CF_3$ group. This leaves the other fragment with a twofold negative charge, which is stabilized by the cation. In the presence of 18-crown-6, the spin density distribution becomes more diffuse again, which goes along with a lower electron affinity.

Overall, on a qualitative scale these calculations can well explain the experimental observation that i) the addition of 18-crown-6 results in a pronounced suppression of the reductive

decomposition of $TFSI^-$ species, even though these are present at large excess, and that ii) Mg^{2+} deposition is still possible despite the rather strong coordination of the 18-crown-6 molecule to the Mg^{2+} cation. In the first case, this is due to the fact that coordination to 18-crown-6 prohibits the two-fold coordination to the $TFSI^-$ anions and, thus, decreases their binding energy to the Mg^{2+} cation. On the other hand, for the partly reduced Mg^+, the interaction of the 18-crown-6 additive with the Mg^+ cation is sufficiently weak that direct interaction with the electrode as a first step for Mg deposition seems to be feasible at room temperature.

6.4. Conclusion

Based on the results of a systematic electrochemical and theoretical study on the influence of additives, in our case 18-crown-6 and $Mg(BH_4)_2$, on the reversible deposition / dissolution of Mg on a glassy carbon model electrode in the ionic liquid BMP-TFSI, we could show that these can significantly improve the extent and reversibility of Mg plating / stripping. While Mg^{2+} deposition is inhibited in purely $MgTFSI_2$-containing BMP-TFSI, it is improved upon addition of the crown ether and/or of $Mg(BH_4)_2$. Varying the amount of the additives while keeping the Mg^{2+} concentration constant reveals i) that either of them can improve the deposition characteristics. However, ii) a certain excess of these species together relative to the Mg^{2+} concentration is required for more facile and reversible Mg deposition, and iii) regardless of the presence of the crown ether, a minimum amount of BH_4^- is required as well, most likely to act as water scavenger. These trends can be convincingly explained by the results of our quantum chemical calculations. Including implicit and explicit solvent effects, they reveal that i) the interaction between Mg^{2+} and the surrounding $TFSI^-$ anions is significantly weakened upon coordination of an 18-crown-6 molecule to $MgTFSI_2$ or to $MgTFSI_2$ + BMP-TFSI, which severely reduces the tendency for Mg^+-induced $TFSI^-$ decomposition during Mg^{2+} reduction, that ii) increasing coordination stabilizes the resulting cluster, but with a nonlinear effect, that iii) partial reduction of Mg^{2+} to Mg^+, possibly via an outer sphere reduction process, weakens the $[Mg^+–TFSI_2]^-$ interaction, which allows for coordination of the Mg cation to the electrode at room temperature, and that iv) the changes in Mg–TFSI interaction are reflected also by changes in the electron affinity and in the equilibrium potential for reduction of the respective clusters. When using a Mg substrate, as common in realistic battery systems, instead of the model GC electrode, the passivation process is far more efficient, but otherwise the data appear to be in agreement with our interpretation.

In combination, experiment and calculations result in a detailed mechanistic picture of the role of additives on Mg deposition / dissolution in an ionic liquid electrolyte, including also

synergistic effects. The observation of similar trends for reversible Mg plating / stripping on GC model electrodes and realistic Mg electrodes, only with higher currents, indicates that the above picture is not electrode-specific, but of more general validity.

6.5. Supporting Information

6.5.1. Cyclic Voltammograms – Mg/Ca Deposition / Dissolution

6.5.1.1. Electrochemical Characterization of GC in $Mg(BH_4)_2$-Containing BMP-TFSI

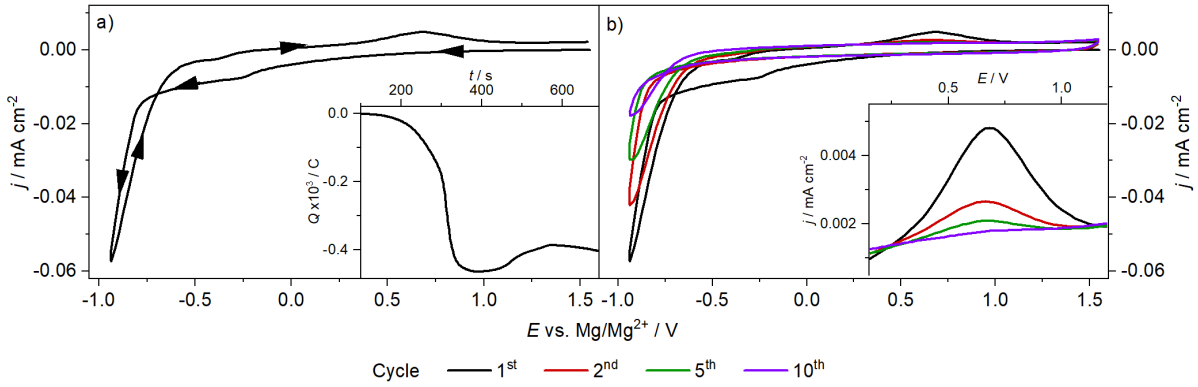

Figure S6-1. First (a) and additional relevant (b) potentiodynamic cycles recorded on a GC electrode in BMP-TFSI + 0.1 M $Mg(BH_4)_2$ The inset in a) shows the accumulated charge (i.e., the charge balance of Mg plating / stripping) during the first scan, the one in b) is a close-up on the anodic peak.

Figure S6-1a and b present the first and later cycles of the CVs recorded in 0.1 M $Mg(BH_4)_2$-containing BMP-TFSI at 10 mV s^{-1} on a glassy carbon (GC) substrate, without any additional additives. The first cycle (**Figure 6-1**a, section 6.3.1 in this work) shows that the reductive processes start at about 0.3 V in the cathodic scan. These, we attribute to side processes; such as electrolyte reduction or the decomposition of traces of water and other contaminants. This current signal is overlaid by a small peak at -0.3 V, whose origin is unclear so far. However, it also appears in the CV recorded in the presence of crown ether (see discussion with **Figure 6-1**, section 6.3.1). At -0.8 V, the reduction current increases steeply until reaching the lower potential limit. While this may, at least in part, be attributed to Mg deposition,[45,98,119,262,274,293] it more likely results from electrolyte decomposition. In the subsequent anodic scan, we find the typical hysteresis up to -0.7 V, with more pronounced negative currents than in the cathodic scan in this potential regime. Continuing to more positive potentials in the anodic scan, the small plateau around -0.5 V is likely due to ongoing reduction processes, similar to those described above for the cathodic cycle. Next, a small oxidative current peak appears at 0.7 V, which may be due to either Mg dissolution or to the oxidation of side products formed upon reduction at more cathodic potentials (see above). The overall reversibility of the cathodic and anodic processes, as indicated by the overall charge ratio in these potential regimes (Coulombic efficiency), is only about 18 % in the first cycle (inset in **Figure S6-1**a) This low reversibility

further indicates that the reductive currents observed in the cathodic scan are not due to Mg deposition, at least not as a major contribution.

In the second cycle (**Figure S6-1**b), the initial reductive processes between 0.3 and -0.8 V are not observed anymore, i.e., the source of the reductive (side) reactions occurring in the first cathodic cycle has either been depleted or the surface has been passivated for these processes. This is in agreement with the loss of both reductive and oxidative currents in the Mg deposition region. Due to the stronger relative loss of the cathodic currents, the Coulombic efficiency increases to 23 % in the second cycle and continues to rise up to the fifth cycle, where it stabilizes at around 35 % (see **Figure S6-4** and **Table S6-1**). At the same time, the cathodic and anodic current contributions decrease continuously.

As evident from the rapidly decreasing plating currents observed in the CVs in **Figure S6-1**b, the electrode surface is increasingly passivated as a result of $TFSI^-$ decomposition, also in the presence of $Mg(BH_4)_2$. This, and also the high contribution from irreversible processes in the Mg deposition region, agrees well with previous findings for Pt electrodes in 1 M $Mg(BH_4)_2$-containing BMP-TFSI by Watkins *et al.*[119] and by Gao *et al.*,[121] who also observed largely irreversible Mg deposition and dissolution in this electrolyte. Furthermore, Vardar *et al.* reported the absence of Mg plating / stripping both from $Mg(BH_4)_2$- and $MgTFSI_2$-containing 1-methyl-1-propylpyrrolidinium (MPP)-TFSI and suggested that $TFSI^-$ plays a dominant role in the surface passivation, either via anion adsorption or via anion decomposition / side reactions with contaminants.[118] Finally, Shterenberg *et al.* had proposed that the formation of an initial Mg layer via Mg deposition in the first cycle on the anode in $TFSI^-$-containing, DME-based electrolyte is immediately followed by subsequent surface passivation, most likely due to instantaneous adsorption and decomposition of $TFSI^-$.[101] Their results are in agreement with those reported by Tutusaus *et al.* in a comparable electrolyte.[284] The latter authors, however, suggested that Mg passivation occurs via the adsorption of products of the side reaction between Mg and $TFSI^-$.

Compared to the Mg deposition characteristics reported by Ma *et al.*,[274] who observed only very small losses even up to 500 cycles, the cycling stability in our experiments was much less, as indicated by a low reversibility and a rapid fading of the deposition currents. We assume that this difference is mainly caused by the different electrolyte compositions and chemistries, in particular the different Mg^{2+} coordination in tetraglyme or BMP-TFSI-based electrolyte, respectively, rather than by the water contents.

6.5.1.2. *Influence of Potentiodynamic Cycling for Different Mg^{2+}/Ca^{2+}-Containing Electrolytes*

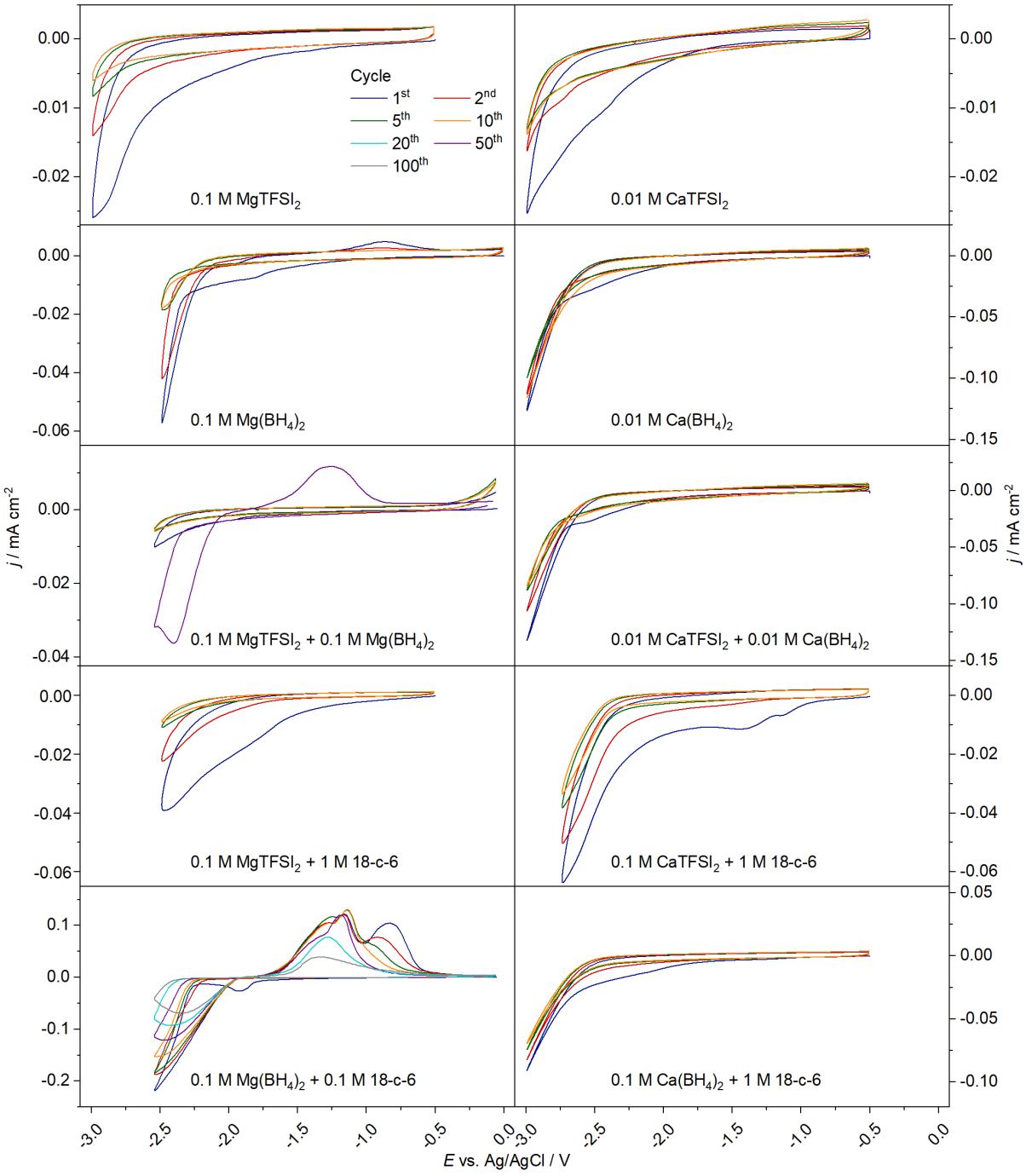

Figure S6-2. Relevant cycles of the CVs recorded on GC in Mg^{2+}- (Ca^{2+}-) containing BMP-TFSI at 10 mV s^{-1} in a beaker-type half-cell setup. Reference electrodes were a Mg rod (polished in the glove box) and an Ag/AgCl wire for the Mg^{2+}-/Ca^{2+}-containing electrolytes, respectively. All potentials were converted to Ag/AgCl (-1.55 V vs. Mg/Mg^{2+}). As counter electrode, an Au wire was used. The salts employed for each electrolyte are indicated in each panel of the figure.

6.5.1.3. Influence of the Crown Ether Concentration for Different Mg^{2+}/Ca^{2+}-Containing Electrolytes

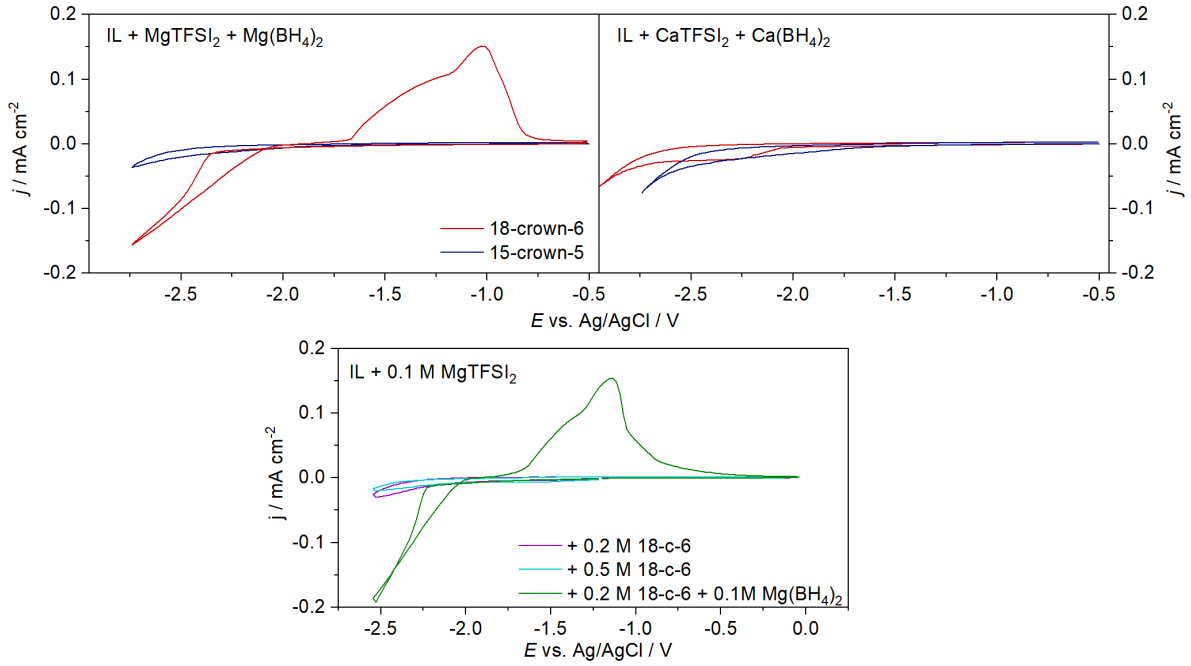

Figure S6-3. First cycle of the CVs recorded on GC in Mg^{2+}- and Ca^{2+}-containing BMP-TFSI at 10 mV s^{-1}. The concentration for the Mg salts is 0.1 M, for the Ca salts 0.01 M due to its lower solubility in the IL. Reference electrodes were a Mg rod (polished in the glove box) and an Ag/AgCl wire for the Mg^{2+}-/Ca^{2+}-containing electrolytes, respectively. All potentials were converted to Ag/AgCl (-1.55 V vs. Mg/Mg^{2+}). As counter electrode, an Au wire was used. The salts employed for each electrolyte are indicated in each panel of the figure. The lower panel shows the first cycle of 0.1 M $MgTFSI_2$-containing BMP-TFSI with different 18-crown-6 ether concentrations.

6.5.2. Coulombic Efficiency of the Mg Deposition / Dissolution

6.5.2.1. GC in BMP-TFSI + 0.1 M $Mg(BH_4)_2$

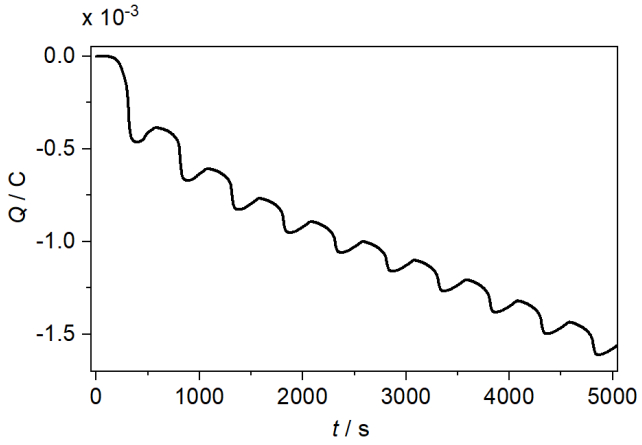

Figure S6-4. Charge accumulated in the first ten cycles (5000 seconds) of the GC substrate cycled in BMP-TFSI + 0.1 M $Mg(BH_4)_2$ at 10 mV s^{-1}.

Table S6-1. Coulombic efficiencies reached per cycle in the first ten cycles of the GC substrate cycled in BMP-TFSI + 0.1 M $Mg(BH_4)_2$ at 10 mV s^{-1}.

Cycle #	**1**	**2**	**3**	**4**	**5**	**6**	**7**	**8**	**9**	**10**
CE / %	17.9	23.4	29.6	34.6	39.6	36.6	41.2	33.3	38.9	36.8

6.5.2.2. GC in BMP-TFSI + 0.1 M $Mg(BH_4)_2$ + 0.1 M 18-crown-6

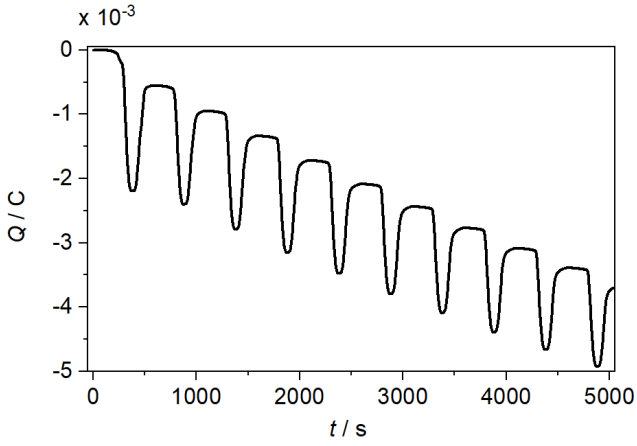

Figure S6-5. Charge accumulated in the first ten cycles (5000 seconds) of the GC substrate cycled in BMP-TFSI + 0.1 M $Mg(BH_4)_2$ + 0.1 M 18-crown-6 at 10 mV s^{-1}.

Table S6-2. Coulombic efficiencies reached per cycle in the first ten cycles of the GC substrate cycled in BMP-TFSI + 0.1 M $Mg(BH_4)_2$ + 0.1 M 18-crown-6 at 10 mV s^{-1}.

Cycle #	1	2	3	4	5	6	7	8	9	10
CE / %	69.1	78.5	80.7	79.5	80.3	80.9	78.3	78.6	79.5	76.2

Cycle #	20	30	40	50	60	70	80	90	100
CE / %	26.7	23.4	25.1	23.9	26.4	26.3	25.7	25.0	23.5

6.5.2.3. GC in BMP-TFSI + 0.05 M $Mg(BH_4)_2$ + 0.05 M $MgTFSI_2$ + 0.1 M 18-crown-6

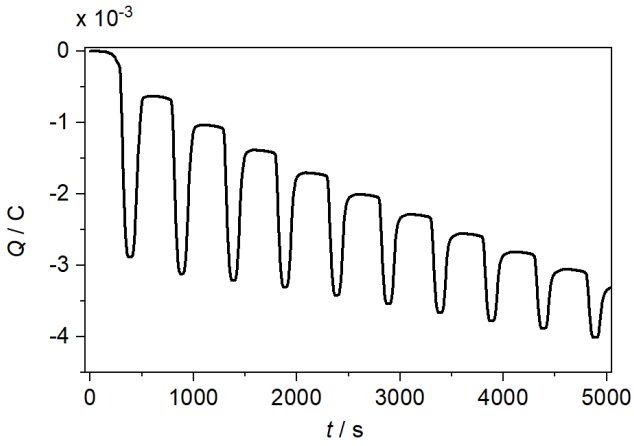

Figure S6-6. Charge accumulated in the first ten cycles (5000 seconds) of the GC substrate cycled in BMP-TFSI + 0.05 M $Mg(BH_4)_2$ + 0.05 M $MgTFSI_2$ + 0.1 M 18-crown-6 at 10 mV s^{-1}.

Table S6-3. Coulombic efficiencies reached per cycle in the first ten cycles of the GC substrate cycled in BMP-TFSI + 0.1 M $Mg(BH_4)_2$ + 0.1 M 18-crown-6 at 10 mV s^{-1}.

Cycle #	1	2	3	4	5	6	7	8	9	10
CE / %	78.1	84.4	83.9	83.5	82.0	81.1	80.9	80.4	76.9	75.5

Cycle #	20	30	40	50	60	70	80	90	100
CE / %	7.6	7.2	8.8	10.6	13.5	14.6	15.4	16.1	15.6

6.5.2.4. GC in BMP-TFSI + 0.01 M $Mg(BH_4)_2$ + 0.09 M $MgTFSI_2$ + 0.2 M 18-crown-6

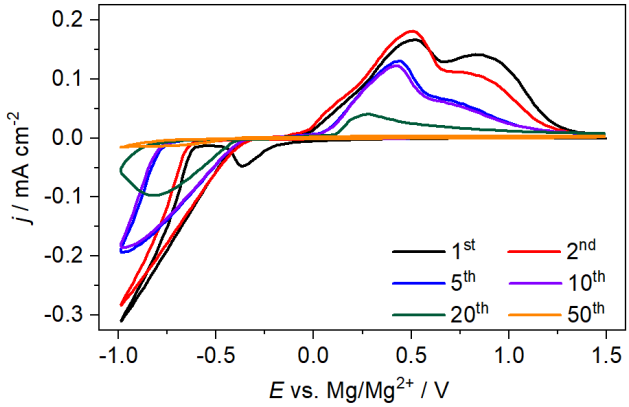

Figure S6-7. CV recorded on GC in 0.01 M $Mg(BH_4)_2$ + 0.09 M $MgTFSI_2$ + 0.2 M 18-crown-6 at 10 mV s^{-1} in a beaker-type half-cell setup. Reference electrode is a Mg rod (polished in glove box), counter electrode an Au wire.

Table S6-4. Coulombic efficiencies reached per cycle in the first ten cycles of the GC substrate cycled in BMP-TFSI + 0.01 M $Mg(BH_4)_2$ + 0.09 M $MgTFSI_2$ + 0.2 M 18-crown-6 at 10 mV s^{-1}.

Cycle #	**1**	**2**	**3**	**4**	**5**	**6**	**7**	**8**	**9**	**10**
CE / %	74.9	81.5	80.9	80.3	79.7	78.9	78.7	78.2	77.1	75.5

Cycle #	**20**	**30**	**40**	**50**	**60**	**70**	**80**	**90**	**100**
CE / %	11.7	6.6	7.1	5.4	5.9	6.2	6.8	8.0	6.8

6.5.3. Calculations

6.5.3.1. Further Cluster Configurations

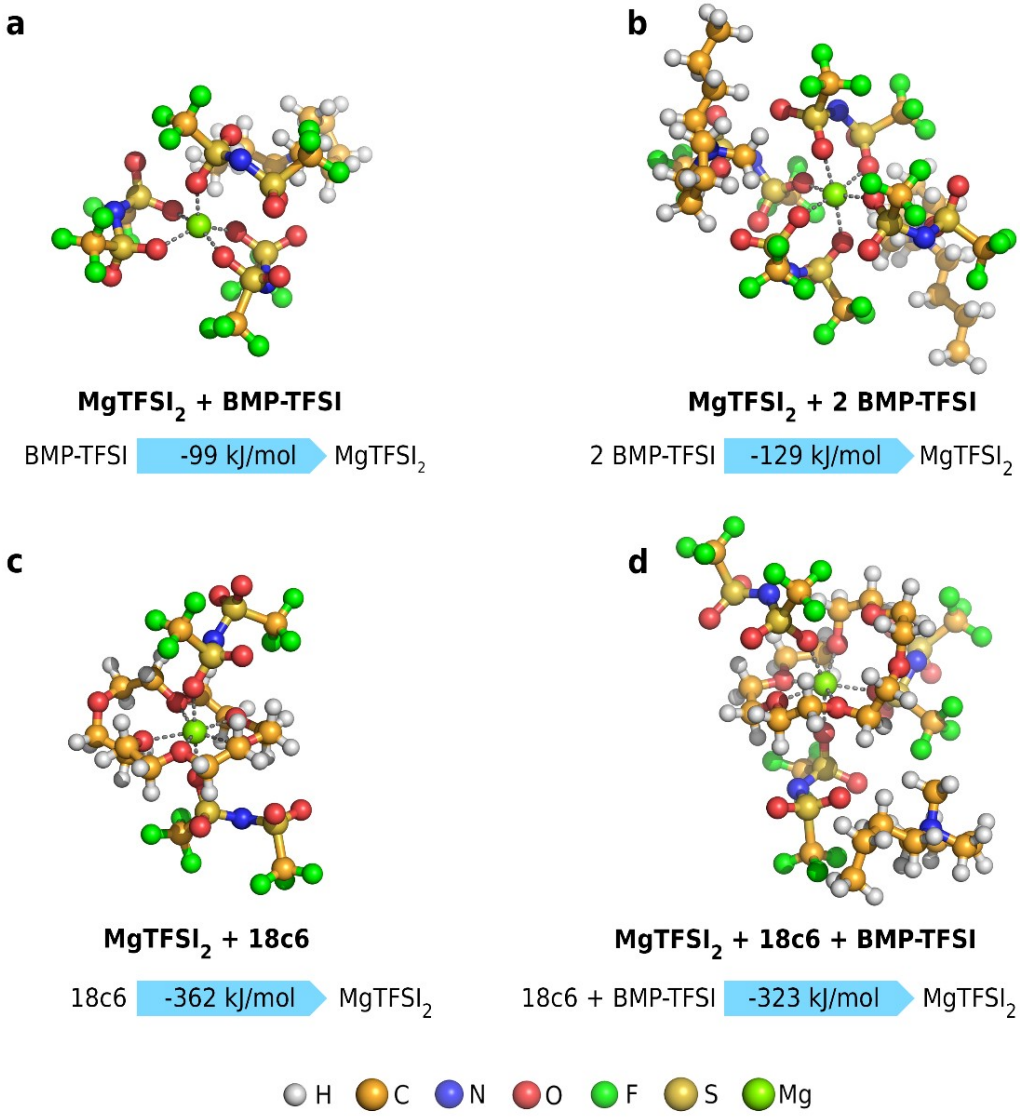

Figure S6-8. Representation of a selection of clusters at different compositions cut from MD simulations and their respective coordination energies. The depicted clusters differ from the most stable configurations at their respective composition, which are shown in **Figure 6-4**, and present the Mg^{2+} cation in different coordination states.

Table S6-5. Electron affinity E_A and equilibrium potential E_{red} for molecule / cluster reduction vs. Mg/Mg^{2+} for BH_4^- and $Mg(BH_4)_2$.

	E_A / eV	E_{red} / V
BH_4^-	-0.36	-3.71
$Mg(BH_4)_2$	1.48	-1.87

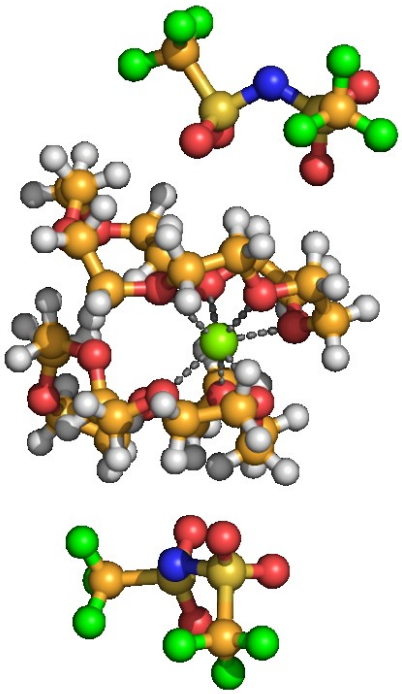

Figure S6-9. Representation of the $MgTFSI_2$ + 2 18-crown-6 cluster, in which the Mg^{2+} cation is completely surrounded by two 18-crown-6 molecules.

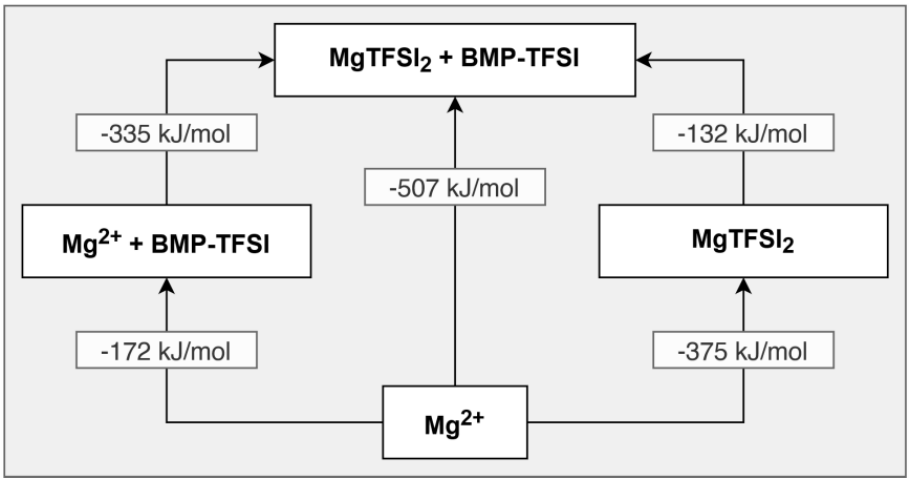

Figure S6-10. Detailed scheme of the coordination energies E_c and binding energies E_b of the $MgTFSI_2$ + BMP-TFSI cluster depicted in **Figure 6-4**.

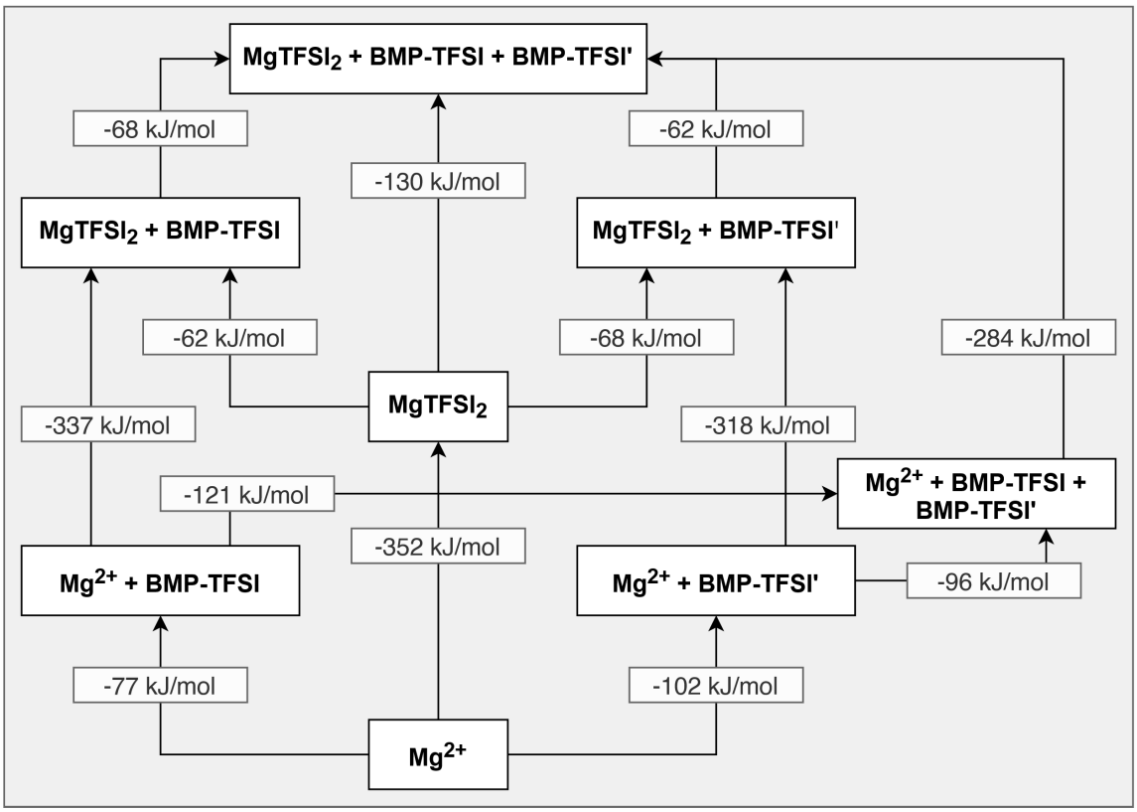

Figure S6-11. Detailed scheme of the coordination energies E_c and binding energies E_b of the $MgTFSI_2$ + 2 BMP-TFSI cluster depicted in **Figure 6-4**, referenced to the energy of the Mg^{2+} cation and that of the different ligands.

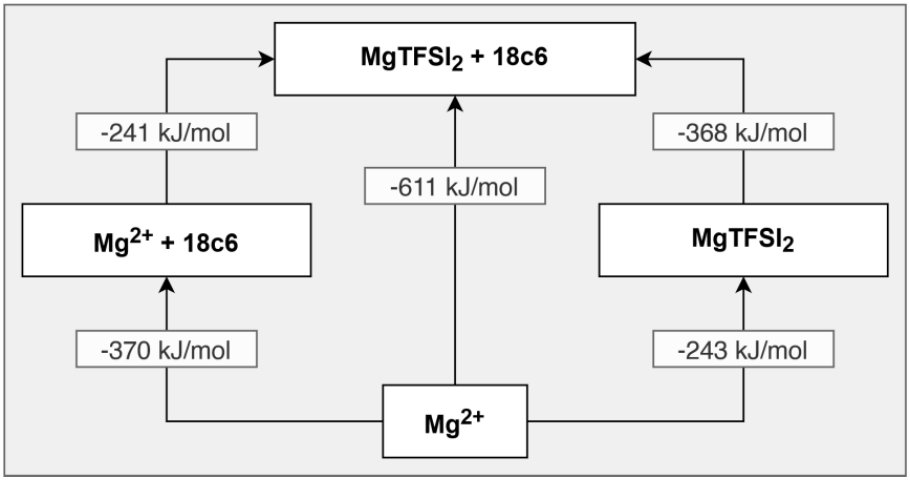

Figure S6-12. Detailed scheme of the coordination energies E_c and binding energies E_b of the $MgTFSI_2$ + 18c6 cluster depicted in Figure 4 referenced to the energy of the Mg^{2+} cation and that of the different ligands.

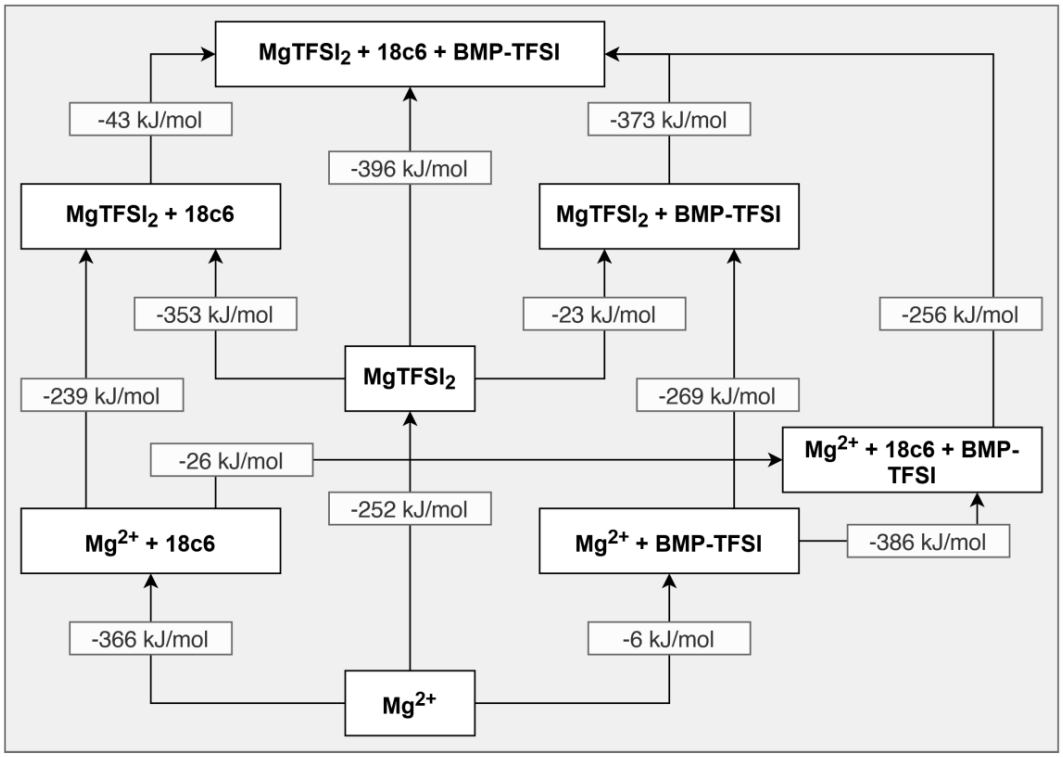

Figure S6-13. Detailed scheme of the coordination energies E_c and binding energies E_b of the $MgTFSI_2$ + 18-crown-6 + BMP-TFSI cluster depicted in **Figure 6-4**, referenced to the energy of the Mg^{2+} cation and that of the different ligands.

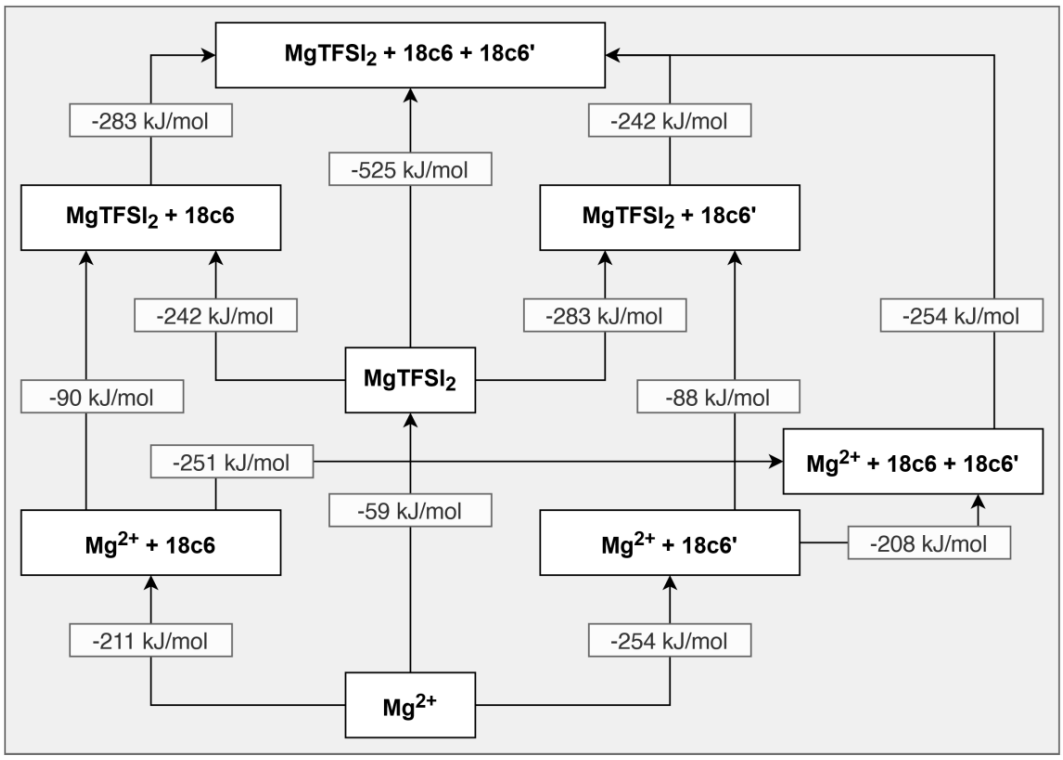

Figure S6-14. Detailed scheme of the coordination energies E_c and binding energies E_b of the $MgTFSI_2$ + 2 18-crown-6 cluster depicted in **Figure S6-9**, referenced to the energy of the Mg^{2+} cation and that of the different ligands.

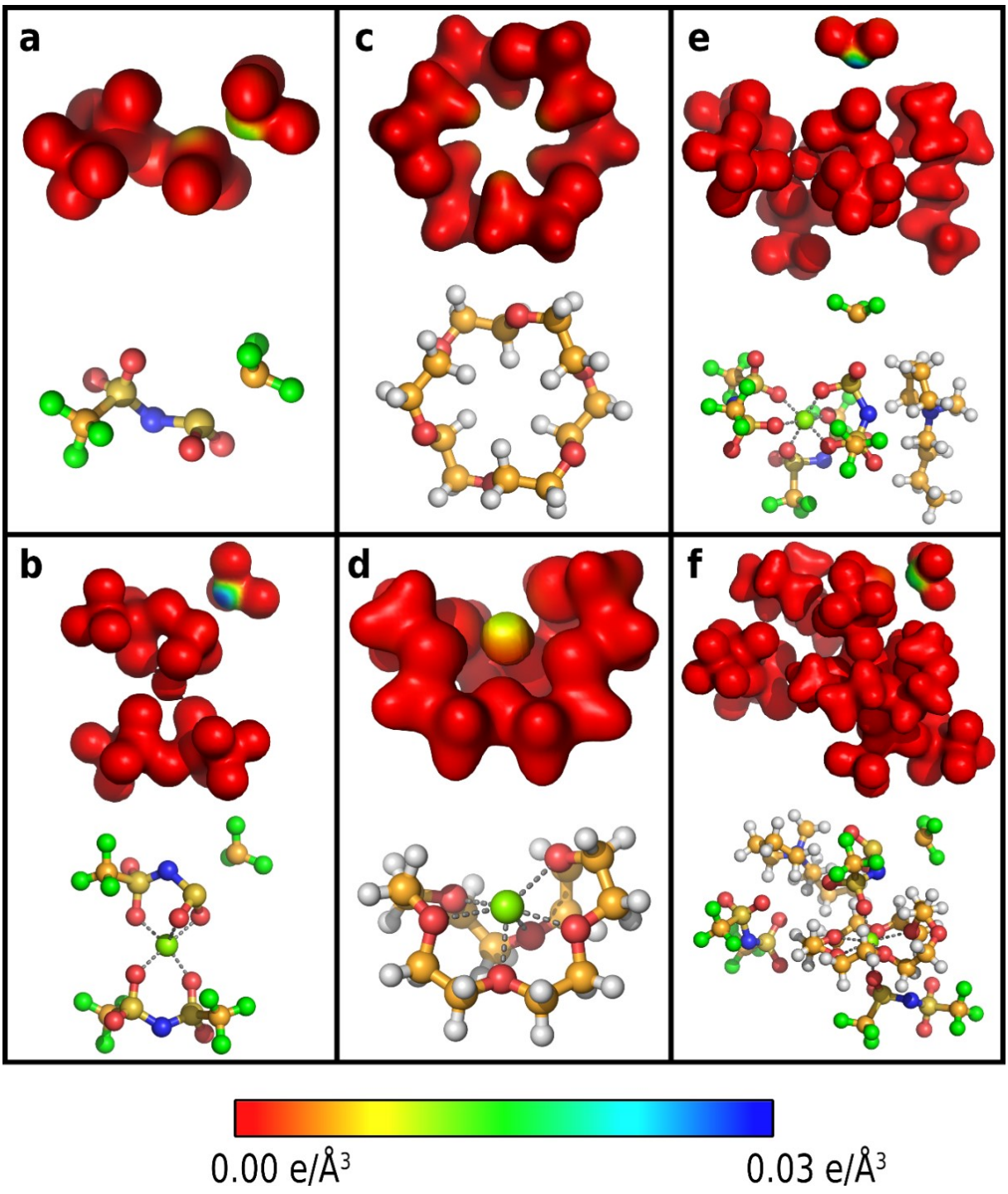

Figure S6-15. Color-coded spin density distribution displayed on the electron density isosurface (value of 0.04) of the reduced clusters a) $TFSI^{2-}$, b) $[MgTFSI_2]^-$, c) $[Mg^{2+} + 18c6]^-$, d) $[MgTFSI_2 + BMP\text{-}TFSI]^-$, e) $[MgTFSI_2 + 2\ BMP\text{-}TFSI]^-$, and d) $[MgTFSI_2 + 18c6 + BMP\text{-}TFSI]^-$ in their optimized geometries. Blue indicates an increased spin density, red areas are spin-free.

7. Summary and Conclusion

In this work, I have presented the results of my studies of the anode-electrolyte interactions in several model systems for lithium-ion batteries and, in one case, for secondary magnesium batteries, employing foremost cyclic voltammetry and (*ex situ*) X-ray photoelectron spectroscopy. This thesis offers detailed insights into the effects of the electrode structure and the solvent nature with respect to the formation processes of surface layers at the anode|electrolyte interface, which was achieved by comparing the results of both UHV-based surface science studies and electrochemical model studies using the same, well-defined substrates and simplified electrolyte compositions. Furthermore, these studies bridge the gap to real batteries by step-wise increasing the complexity of the model systems employed in the electrochemical investigations. Briefly, the systems under investigation are:

a) Substrates
   i. Highly oriented pyrolytic graphite (HOPG)
   ii. Binder-free graphite powder films
   iii. Binder-containing graphite powder films
   iv. Glassy carbon (GC)
   v. Mg

b) Solvents / Electrolytes
   i. $LiPF_6$-containing ethylene carbonate (EC) or dimethyl carbonate (DMC)
   ii. LP30 (1 M $LiPF_6$-containing EC/DMC, 1 : 1 v/v)
   iii. BMP-TFSI + Li^0
   iv. LiTFSI-containing BMP-TFSI
   v. $Mg(BH_4)_2$-, $MgTFSI_2$- and 18-crown-6-containing BMP-TFSI

In this final chapter, I will summarize the findings gained in these studies, emphasizing overarching effects. This will be complemented by an assessment of the strengths and weaknesses of the model systems employed.

Starting with the electrode materials mimicking the graphite anode of LIBs, HOPG – i.e., its basal plane, as employed in Chapter 3 of this thesis – is ideally suited for detailed surface science studies and enables both microscopic (STM / AFM) and spectroscopic experiments in UHV. Its well-defined surface is mechanically stable, easy-to-use, and requires no special preparation method aside from stripping the uppermost graphene layers to remove surface contaminants. It can be prepared and used in a similar manner for electrochemical studies at

standard reaction conditions. Its low surface defect site concentration, which largely hinders Li^+ (de-)intercalation, allows a focused view on the processes of electrolyte decomposition / SEI formation without interference from Li^+ (de-)intercalation currents, which, especially for the study using BMP-TFSI-based electrolyte in Chapter 5, facilitated the distinction of peaks in the cyclic voltammogram. At the same time, however, the low Li^+ insertion capability is a disadvantage that sets apart model and reality. It is not the only feature distinguishing the HOPG model substrate from realistic graphite electrodes: I found an activation effect (i.e., increasing currents for electrolyte decomposition) characteristic for the basal HOPG plane cycled in single-solvent carbonate electrolytes, most likely due to surface exfoliation. The absence of this activation effect in experiments on purposeful roughened HOPG electrodes showed that it is a special feature of HOPG with its low defect density. Thus, it has only little relevance for realistic, powder substrate-based systems.

The next step towards more realistic model electrodes was the use of binder-free (to still keep number of components in the system as low as possible) graphite powder film electrodes in EC- and DMC-based electrolyte. They are more elaborate in their use, as this includes the preparation of both the GC substrate and the aqueous suspension as well as the processes of deposition and subsequent drying. The resulting graphite powder films are very sensitive and sustain damage easily during cell assembly / disassembly due to the lack of binder; furthermore, cycling and rinsing procedures may lead to the loss of active material. In my experience, however, if treated carefully, the overall mechanical stability suffices for several potentiodynamic cycles as well as for follow-up XPS analysis. These powder film electrodes made of two different, realistic battery materials (commercial, artificial graphite (MAGE) and processed (spheroidized) natural graphite (SNG), see Chapter 4) allow staged, reversible Li^+ (de-)intercalation and also show slightly higher SEI formation potentials (e.g., 0.7 instead of 0.6 V vs. Li/Li^+ for EC-based electrolyte) and a much faster surface passivation / complete SEI formation in comparison to the HOPG electrodes. In line with their differing electrochemical characteristics I also found major differences in the overall composition of the SEIs formed on the different substrates. For example, *ex situ* XPS experiments on graphite powder electrodes revealed the presence of Li carbonates within the SEI, while none were found in the passivation layer formed on HOPG. Furthermore, LiF was found to be the main component of the SEI in the case of HOPG, while its amount within the SEI formed on the graphite powder film substrates was significantly lower. In addition, the film electrode-based SEI displayed a marked difference in LiF content depending on the scan rate, as well, while no major influence of the cycling speed was observed on the composition of the HOPG-based SEI. Interestingly, a

similar observation regarding the SEI's main component, i.e., LiF, as a function of the model substrate occurred when comparing the passivating interphase formed on HOPG cycled in LiTFSI-containing BMP-TFSI to the one formed on graphite powder film electrodes. The SEI formed on HOPG consisted mainly of LiF, while additional new species – most likely reduced $TFSI^-$ compounds – appeared in the SEI formed on the graphite film substrates. By comparing the HOPG and the graphite powder film model systems, thus, we were able to investigate the influence of the surface defect density of the substrate in greater detail.

The final section of the bridge between well-defined, surface-science model substrates (i.e., HOPG) and realistic battery anodes (containing active material, conductive carbon and binder) in this thesis was the use of binder-containing electrodes without conductive carbon. I studied two different graphite powder electrodes which were prepared by project partners via an established preparation and drying method from an electrode ink containing only the graphite material, solvent and the binder. The resulting electrodes are mechanically stable and easy-to-use but tend to crack during and/or after the cycling procedure, possibly due to a combination of the flexible Cu substrate and the thick (compared to the GC-based thin-film electrodes deposited from aqueous suspensions) graphite film. The influence of the binder itself, the higher loading and, subsequently, the higher inhomogeneity of the electrode on the electrochemical characteristics as compared to the binder-free graphite film electrodes, leads to a shift of the electrolyte decomposition potential to more negative values and higher current densities, as well as to a pronounced peak-broadening. While these differences may appear large at first glance, they do not suggest a major influence of the binder on the fundamental electrochemical characteristics of the model system. With regard to the *ex situ* XPS characterization of the deposited SEI, however, PVDF-containing substrates are less convenient due to the additional F 1s and C 1s signals caused by the binder which hamper the compositional analysis. In order to not complicate the already complex spectra even further, we selected binder-free substrates for XP spectroscopic post-cycling characterization.

As a model for different charge / discharge rates I used different scan speeds during SEI formation. While the SEI on HOPG in EC-based electrolyte consisted mainly of LiF both at slow and at fast scan rates, the composition of the SEI on binder-free graphite powder film models varied with the scan speed: if cycled at fast scan rates, the SEI also consisted mainly of LiF. At slow scan rates, however, the SEI layers contained a higher amount of carbon-containing (solvent) decomposition products. This compositional difference, and also differing trends within the depth profiles of the SEIs formed on different electrode materials, are

explained in a model in which the formation of a SEI takes place directly at the anode surface. Based on my results, the varying SEI compositions are caused by a more hindered transport of salt species than of solvent molecules through the porous passivation layer, leading, e.g., to a lower concentration of LiF / higher concentration of organic components after fast cycling, and vice versa. In addition, mass transport is further hindered due to the increasing thickness of the SEI. These transport limitations, along with the pore structure of the SEI depending on the solvent, are likely to influence the competition between salt transport and ion transport through the passivation layer.

In comparison to graphitic LIB model substrates, model systems for Mg-metal battery anodes require a very different set of characteristic properties: as no Mg^{2+} intercalation is required, easy-to-prepare electrodes like noble metal substrates (e.g., Pt) were widely employed in previous studies. Like HOPG, they may be used both in UHV and under conditions employed for electrochemical model studies. However, in the current work we employed glassy carbon (GC) substrates as they are rather inert, i.e., less likely to catalyze side reactions. In model studies on the Mg deposition / dissolution from ionic liquid we successfully observed (minor) Mg plating / stripping on GC (dependent on the electrolyte employed), but also pronounced surface passivation – likely due to side reactions such as Mg^{+}-induced $TFSI^{-}$ decomposition or BMP-TFSI reduction due to residual contaminations, e.g., O_2 or H_2O. These reactions very likely would have taken place on noble metal electrodes, as well.

We then moved on to Mg electrodes, which have the advantage of being the actual 'realistic' anode for secondary Mg-metal batteries. Unfortunately, the pristine Mg surface is highly reactive and, if one is able to remove the native passivation layer, instantaneously forms a new one when coming into contact with traces of air or water even in the glove box atmosphere. Consequently, it requires a complex preparation process which includes several polishing steps before cell assembly and, finally, an ill-defined roughening with a glass tip after the electrolyte has been filled into the cell. Of course, this strongly decreases the overall experimental reproducibility. Furthermore, both GC and Mg in our studies are passivated with ongoing cycling time, likely due to the passivation of the newly formed Mg layer. This passivation process is strongly enhanced on the Mg substrate due to its high reactivity. The most pronounced difference, however, is a high nucleation overpotential for Mg deposition on GC. Nevertheless, the GC substrate allows for a more easily reproduced electrochemical characterization of the model system in order to study the fundamental processes occurring at the anode|electrolyte interface and also to compare different electrolyte formulations – as was

the case in our study, with the different $Mg(BH_4)_2$, $MgTFSI_2$ and 18-crown-6 ether concentrations. Furthermore, any electrolyte tested and found inapplicable for Mg plating and stripping due to passivation of the newly formed Mg on GC will also not be suitable for realistic Mg batteries. Accordingly, we first employed GC electrodes and then moved on to Mg substrates in the search for promising systems.

In the following paragraphs, I will summarize the merits and challenges of the salt / solvent systems employed in this work.

An electrolyte which is used in real LIBs is a 1 : 1 (v/v) blend of EC/DMC and 1 M $LiPF_6$. It is often improved by additives for lower flammability, increased ionic conductivity and/or better SEI formation. However, in order to – for example – specifically tailor the characteristics of the passivating surface layer, a detailed knowledge of the individual interactions between solvent, salt and electrode components is crucial and accessible through simplified electrolytes. Ethylene carbonate may be used for UHV studies – where it adsorbs molecularly intact on HOPG – as well as for electrochemical model studies, despite its high viscosity and comparably low ion conductivity. Dimethyl carbonate, on the other hand, has not been studied under UHV conditions due to its high vapor pressure and, for the same reason, requires the use of a closed cell during potentiodynamic cycling.

As shown in Chapter 3, the electrochemical traits of HOPG substrates cycled in single-solvent electrolytes based on EC and DMC are very characteristic. The activation effect described above, for example, is far less pronounced in EC-based electrolytes compared to DMC-based electrolytes. Both on HOPG and the graphite powder film substrates employed in Chapter 4, the onset potential of SEI formation in EC-based electrolytes is more positive than the one found in DMC-based ones. Thus, in the former, the passivation process of the anode begins already at higher potentials and graphite exfoliation is inhibited already at an earlier stage than in the latter. In addition, complete surface passivation (i.e., SEI formation) took place immediately on substrates with a high surface defect concentration. This was not the case for DMC-based electrolyte, which allowed further graphite exfoliation with continued cycling. This applies both to the HOPG model substrate as well as to the graphite powder film anodes. In summary, our electrochemical model studies reveal that the EC single-solvent electrolyte possesses overall superior characteristics than DMC single-solvent electrolyte. In a mixed, EC/DMC-based electrolyte such as LP30 (as studied in this thesis on the binder-containing electrodes), SEI formation is dominated by the EC component, as indicated by the respective onset potentials of electrolyte decomposition.

As revealed by *ex situ* XPS, reductive decomposition of the solvents on HOPG results in products like PEO and semicarbonates like $(H_2COCO_2Li)_2$ for EC-based and H_3COCO_2Li and H_3COLi for DMC-based electrolyte. In addition, salt-decomposition products like LiF, Li_xPF_y and $Li_xPF_yO_z$ were observed in both cases. On the powder film substrates, a severe differential charging experienced with the DMC-cycled samples points towards significant differences in the product distribution of EC- and DMC-based electrolyte decomposition, respectively. This charging, unfortunately, prevented the evaluation of the XP spectra measured on graphite powder electrodes in DMC-based electrolytes. Another major challenge arising from the use of EC- and DMC-based electrolyte is the formation of a large variety of F-, O-, C-, P- and Li-containing species, which complicates the identification of individual compounds. This is often neglected when it comes to the analysis of the XP spectra. Furthermore, peak fitting is conducted seemingly without consideration of (quantitative) relations between the spectra of the constituting atoms. In my studies, I used a rigorous and comprehensive XPS peak fitting method, which considers these relations. Even with this approach I still cannot identify each and every SEI component unambiguously, but it nevertheless offers a strategical and consistent approach to the challenge.

The other electrolyte solvent used in the course of this work, the ionic liquid BMP-TFSI, is viewed as an example for novel and promising electrolytes for LIBs and secondary Mg batteries. For a combination of surface science and electrochemical model studies as presented in my thesis it enables a very close relation between these two worlds. In electrochemical experiments, for very fundamental studies (e.g., decomposition of the IL), it may even be used without any additional salt, so that the composition is exactly the same as in UHV. For more applied investigations, salts (e.g., Li^+ and Mg^{2+}) can be added (as LiTFSI or $MgTFSI_2$) without introducing another anion. Furthermore, in UHV experiments it is more practical than EC as it is more stable, less volatile and forms highly ordered adsorbate layers.

In electrochemical measurements, I observed irreversible electrolyte decomposition processes on the surface of both well-defined HOPG and graphite powder film substrates in LiTFSI-containing BMP-TFSI. A major difference between the carbonate- and $LiPF_6$-based electrolytes and the ionic liquid electrolyte is the fact that no staged Li^+ (de-)intercalation is observed, neither on the defect-low HOPG nor on the defect-rich graphite powder film electrodes. Thus, differently than with EC- and DMC-based electrolytes, reductive BMP-TFSI decomposition leads to a passivating interphase which does not allow Li^+ transport. Moreover, the resulting passivation layer also does not sufficiently protect the graphite against solvent co-

intercalation. XPS analysis reveals differences in the IL decomposition processes depending on the experimental conditions (UHV deposition vs. potentiodynamic cycling) and the nature of lithium present (Li^0 vs. Li^+): post-deposition of Li^0 on an adsorbed multilayer of BMP-TFSI in UHV leads to preferential BMP^+ decomposition, while the opposite (preferential $TFSI^-$ decomposition) occurs an electrochemical environment in the presence of LiTFSI, i.e., Li^+. The passivation layers formed in ILs are comprised of Li-containing nitrides, sulfites and sulfides (Li_3N, Li_xSO_x, Li_2S), as well as organic compounds of decomposed $TFSI^-$ and BMP^+ moieties. Like with the EC(DMC)-based model systems, the considerable amount of different salt and ionic liquid decomposition products and the possible presence of undecomposed and/or recombined species hampers an unambiguous compositional identification of the interphase formed on the IL|electrode model systems. These complications are aggravated when trying to assess the depth profile via argon sputtering, which is often disputed because it is difficult to distinguish between original SEI components and products formed during the ion bombardment. For the graphite|IL systems, we thus investigated the influence of sputtering on reference systems (LiTFSI, HOPG|IL@OCP) and observed, e.g., for LiTFSI the appearance of sputtering decomposition products like LiF already after a short time.

For the studies on the reversibility of Mg deposition / dissolution for rechargeable Mg-metal batteries, finally, $MgTFSI_2$-containing BMP-TFSI with $Mg(BH_4)_2$- or 18-crown-6 ether was employed in order to investigate the interactions between Mg^{2+} and the anions and additives present in the electrolyte. Like LiTFSI in BMP-TFSI, $MgTFSI_2$ dissolves well in the IL and also the additives (borohydride and crown ether) can be added in moderate concentrations without problems. I have shown that the formation of a passivating surface layer takes place during cycling of GC model anodes both in $MgTFSI_2$- and $Mg(BH_4)_2$-containing IL, much like in the LIB-related studies with LiTFSI-containing IL. The main reason for surface passivation in Mg-containing BMP-TFSI appears to be the detrimental interaction between Mg^+ and $TFSI^-$. Both the passivation layer formed in Li^+- and in Mg^{2+}-containing IL, however, block Li^+ and Mg^{2+} diffusion through the layer and impede both Li^+ (de-)intercalation and Mg^{2+} deposition / dissolution. Variation of the Mg salt component and $Mg(BH_4)_2$ and/or 18-crown-6 ether as additives omits the formation of this passivation layer and thus allows for improved Mg^{2+} plating / stripping, likely due to an interaction of the complexing cyclic ether within the coordination sphere of the Mg^{2+} cation. As shown by MD simulations and quantum chemical calculations performed by our project partners, this interaction is strong enough to lessen the detrimental Mg^+–$TFSI^-$ interactions, but also not strong enough to impede Mg deposition / dissolution – a concept comparable to the Sabatier Principle in catalysis.

Furthermore, the water-scavenging ability of the added borohydride is necessary to prevent passivation via MgO formation.

In summary, I have shown that cyclic voltammetry investigations of well-defined model systems are an ideal characterization tool. The simplicity of the models allows a direct link to other fundamental surface science and theoretical studies, which results in a deeper understanding of established processes and reactions. The details obtained here form the fundament of an indispensable and elemental understanding of interfaces in batteries and for further systematic investigations, aiming at a future design of safe and durable LIBs and secondary Mg-metal batteries.

8. Zusammenfassung und Fazit

In dieser Arbeit habe ich die Ergebnisse meiner Zyklovoltammetrie- und (ex situ) Röntgenphotonenspektroskopie-Untersuchungen der Anode-Elektrolyt-Wechselwirkungen in verschiedenen Modellsystemen für Lithium-Ionen-Batterien und, in einem Fall, für sekundäre Magnesium-Batterien, zusammengetragen. Sie bietet einen detaillierten Einblick in die Einflüsse, welche die Elektrodenstruktur und der Elektrolyt auf den Bildungsprozess der Oberflächenschicht an der Anode|Elektrolytgrenzfläche ausüben. Diese Erkenntnisse wurde mittels eines Vergleichs zwischen UHV-basierten Surface Science Studien und elektrochemischen Modellstudien auf denselben, wohl-definierten Substraten in simplifizierten Elektrolyten gewonnen. Darüber hinaus schlagen die elektrochemischen Untersuchungen eine Brücke zu realistischen Batterien, in dem die Komplexität der verwendeten Modellsysteme schrittweise erhöht wurde. Bei den untersuchten (Modell-)Systemen handelt es sich um:

a) Substrate
   i. Hochorientierter, pyrolytischer Graphit (HOPG)
   ii. Filme aus Graphitpulver, Binder-frei
   iii. Filme aus Graphitpulver, Binder-haltig
   iv. Glaskohlenstoff (GC)
   v. Magnesium
b) Solventien / Elektrolyte
   i. Ethylencarbonat (EC) oder Dimethylcarbonat mit $LiPF_6$
   ii. LP30 (EC/DMC, 1 : 1 v/v, mit 1 M $LiPF_6$)
   iii. BMP-TFSI + Li^0
   iv. BMP-TFSI mit LiTFSI
   v. BMP-TFSI mit $Mg(BH_4)_2$, $MgTFSI_2$ und/oder 18-Krone-6

In diesem letzten Kapitel werde ich die Ergebnisse der unterschiedlichen Studien zusammenfassen, übergreifende Effekte beleuchten und die verwendeten Modellsysteme hinsichtlich ihrer Stärken, Herausforderungen und Anwendbarkeit bewerten.

Um mit Elektrodenmaterialien, welche die Graphitanode von LIBs nachbilden, zu beginnen, ist HOPG – genauer gesagt, seine basale Oberfläche, wie in Kapitel 3 dieser Arbeit beschrieben – ein ideales Substrat für detaillierte Surface Science Studien und erlaubt sowohl mikroskopische (STM / AFM) als auch spektroskopische Experimente im UHV. Seine wohl-definierte Oberfläche ist mechanisch stabil und der Einsatz unkompliziert. Zur Vorbereitung der Messung werden lediglich die obersten Graphenschichten mittels Tesafilm abgelöst, um

Oberflächenkontaminationen zu entfernen. Dies gilt sowohl für UHV-basierte Untersuchungen als auch für elektrochemische Studien unter Standardbedingungen. HOPG besitzt eine geringe Oberflächendefektstellendichte, was Li^+ (De-)Interkalation größtenteils verhindert; und erlaubt daher einen fokussierten Blick auf den Prozess der Elektrolytzersetzung / SEI-Ausbildung ohne Li^+ (De-)Interkalationsströme. Besonders im Fall des BMP-TFSI-basierten Elektrolyten, welcher in Kapitel 5 verwendet wurde, erleichterte dies die Zuordnung der im Zyklovoltammogramm auftretenden Peaks. Gleichzeitig aber stellt die geringe Li^+ Insertionsfähigkeit, die das Modell deutlich von der Realität trennt, einen Nachteil dar. Auch ist es nicht die einzige Charakteristik, welche die HOPG Modellelektrode von realistischen Graphitelektroden unterscheidet: Im Laufe meiner Forschung fand ich einen Aktivierungseffekt (d.h., ansteigende Ströme für die Elektrolytzersetzung), welcher charakteristisch für die basale HOPG Oberfläche in Einzellösemittelelektrolyten (bestehend aus einem einzigen, carbonat-haltigen Solvens und $LiPF_6$) auftritt und sehr wahrscheinlich auf Oberflächenexfoliierung beruht. Die Tatsache, dass dieser Aktivierungseffekt nicht auftrat, sobald absichtlich aufgeraute bzw. angekratzte HOPG Elektroden für die Experimente verwendet wurden, zeigt, dass er eine Besonderheit der basalen HOPG Oberfläche mit seiner geringen Defektstellendichte ist. Der Effekt hat also nur geringe Relevanz für realistische Batteriesysteme mit Graphitpulverelektroden.

Im nächsten Schritt in Richtung realistischerer Modellelektroden wurden binder-freie Graphitpulverfilmelektroden in Einzellösemittelelektrolyten basierend auf EC und DMC verwendet. Der Binders wurde dabei weggelassen, um die Anzahl der Modellsystemkomponenten so gering wie möglich zu halten. Die Verwendung dieser Modellpulverfilmelektroden ist deutlich aufwändiger als die von HOPG, da diese zwangsläufig sowohl die Vorbereitung des GC-Trägers als auch die der wässrigen Suspension sowie die Abscheidungs- und abschließende Trocknungsprozedur der Filme beinhaltet. Die so hergestellten Pulverdünnschichtfilme sind durch den Mangel an Binder sehr empfindlich und können während des Ein- und Ausbaus in und aus der Zelle leicht beschädigt werden. Weiterhin kann der Zykel- und Reinigungsprozess zum Verlust des aktiven Materials führen. Meiner Erfahrung nach ist jedoch die mechanische Stabilität der Pulverfilme bei vorsichtiger Handhabung für eine Vielzahl von potentiodynamischen Zyklen und die nachfolgende XPS Analyse ausreichend. Die verwendeten Graphitpulverfilmelektroden, die aus zwei unterschiedlichen, realistischen Batteriematerialien hergestellt wurden (kommerzieller künstlicher Graphit, MAGE, und verarbeiteter (spheroidisierter) natürlicher Graphit, SNG, Kapitel 4), erlauben im Gegensatz zum HOPG mehrstufige, reversible Li^+ (De-)Interkalation.

Zudem beginnt die SEI-Bildung schon bei geringfügig höheren Potentialen (0.7 statt 0.6 V vs. Li/Li^+ für EC-basierten Elektrolyten) und die Oberflächenpassivierung / vollständige SEI-Ausbildung verläuft deutlich schneller. Passend zu ihren unterschiedlichen elektrochemischen Charakteristiken konnte ich außerdem bedeutende Unterschiede in der Zusammensetzung der auf den entsprechenden Substraten ausgebildeten SEIs beobachten. Zum Beispiel enthüllten *ex situ* XPS Experimente auf Graphitpulverfilmelektroden Lithiumcarbonate in der SEI, welche in der auf HOPG ausgebildeten Passivierungsschicht hingegen nicht gefunden wurden. Weiterhin wurde LiF als Hauptkomponente der auf HOPG ausgebildeten SEI identifiziert, während seine Konzentration in der SEI auf Graphitpulverfilmelektroden deutlich geringer war. Die LiF-Konzentration der SEI auf Graphitpulverfilmen wies außerdem eine Abhängigkeit von der Potentialvorschubgeschwindigkeit (Scanrate) der elektrochemischen Untersuchung auf, während keine offensichtliche Abhängigkeit der Zusammensetzung von der Scanrate bei HOPG-basierten SEIs gefunden wurde. Interessanterweise trat ein ähnlicher Zusammenhang hinsichtlich der SEI-Hauptkomponente als Funktion des Modellsubstrats auch beim Vergleich der Passivierungsschichten auf, welche durch Zykeln von HOPG und Graphitpulverfilmelektroden in LiTFSI-haltiger BMP-TFSI gebildet wurden. Die auf HOPG ausgebildete SEI bestand dort hauptsächlich aus LiF; während auf Graphitpulverfilmelektroden zusätzlich andere Spezies – wahrscheinlich reduzierte $TFSI^-$-Verbindungen – in der SEI auftraten. Durch Vergleiche der HOPG- und der Graphitpulverfilmmodelle konnten wir folglich den Einfluss der Oberflächendefektdichte der Substrate im Detail betrachten.

Der abschließende Abschnitt der Brücke zwischen den wohl-definierten Modellsubstraten (wie HOPG) und realistischen Batterieanoden (welche aktives Material, Leitruß und Binder enthalten) in dieser Arbeit war der Einsatz von binderhaltigen Graphitpulverfilmelektroden ohne Leitruß. Ich verwendete zwei unterschiedliche Graphitpulverfilmelektroden, welche von Projektpartnern durch einen etablierten Herstell- und Trocknungsprozess aus einer Elektrodentinte präpariert wurden welche lediglich das Graphit (aktives Material), ein Solvens und einen geringen Anteil an Binder enthielt. Diese Elektroden waren mechanisch stabil und ihre Verwendung vergleichsweise einfach (besonders im Vergleich mit binder-freien Graphitpulverfilmmodellelektroden). Jedoch neigen sie zum Bruch während und/oder nach dem Zykelprozess; möglicherweise aufgrund der Kombination des flexiblen Kupferfoliensubstrats und dem dicken (im Vergleich mit den aus wässriger Suspension abgeschiedenen, GC-geträgerten Dünnfilmelektroden) Graphitfilm. Der Einfluss des Binders selbst sowie die höhere Beladung und die resultierende stärkere Inhomogenität des binder-haltigen Elektrodenfilms auf die elektrochemischen Eigenschaften im Vergleich zur binder-

freien Graphitpulverfilmelektrode führt zu einer Verschiebung des Elektrolytzersetzungspotentials zu negativeren Werten, höheren Stromdichten und einer bedeutenden Peakverbreiterung. Diese Unterschiede erscheinen auf den ersten Blick sehr groß; dennoch deuten sie nicht auf einen übermäßig starken Einfluss des Binders auf die fundamentalen elektrochemischen Eigenschaften des Modellsystems hin. Hinsichtlich der *ex situ* XPS Charakterisierung der abgeschiedenen SEI wären die PVDF-(binder-)haltigen Substrate hingegen nachteilig, da sie zusätzliche F 1s und C 1s Signale im XP Spektrum aufweisen und so die Analyse der SEI-Zusammensetzung deutlich verkomplizieren. Um die Interpretation der ohnehin komplexen Spektren nicht weiter zu erschweren, wurden binderfreie Substrate für die XPS Charakterisierung verwendet.

Als Modell für unterschiedliche Lade- / Entladeraten verwendete ich unterschiedliche Potentialvorschubgeschwindigkeiten zur Ausbildung der SEI. Sowohl bei schnellen als auch bei langsamen Scanraten besteht diese auf HOPG in EC-basiertem Elektrolyten hauptsächlich aus LiF. Auf binder-freien Graphitpulverfilmelektroden hingegen variierte die SEI-Zusammensetzung mit der Zykelgeschwindigkeit: Bei schneller Scanrate bestand die SEI ebenfalls hauptsächlich aus LiF. Bei langsamer Scanrate wiederum enthielt sie einen höheren Anteil kohlenstoffhaltiger (Solvens-)Zersetzungsprodukte. Diese Unterschiede in der chemischen Zusammensetzung, ebenso wie die unterschiedlichen Trends in den Tiefenprofilen der auf unterschiedlichen Elektroden gebildeten SEIs, bilden die Grundlage für ein Modell, in dem die SEI-Bildung direkt an der Anodenoberfläche stattfindet. Basierend auf meinen Ergebnissen entstehen die Unterschiede in der SEI Zusammensetzung dadurch, dass der Massentransport der Salzspezies im Vergleich zum Massentransport der Solvensmoleküle durch die poröse Passivierungsschicht stärker behindert wird, was zu einer geringeren LiF Konzentration / höheren Konzentration organischer Komponenten bei schneller Scanrate führt (und umgekehrt bei langsamer Scanrate). Der Massentransport wird weiterhin durch die zunehmende Dicke der SEI behindert. Diese Einschränkung sowie die Porenstruktur der SEI in Abhängigkeit vom Solvens haben damit sehr wahrscheinlich einen signifikanten Einfluss auf die Konkurrenz zwischen Salz- und Ionentransport durch die Passivierungsschicht.

Anoden für sekundäre Mg Batterie-Modellsysteme benötigen deutlich andere Eigenschaften als graphitische LIB Modellsubstrate: Da keine Mg^{2+} Interkalation stattfindet, wurden bislang oft einfach zu präparierende Elektroden wie Edelmetalle (z.B. Pt) eingesetzt. Diese können, wie HOPG, sowohl im UHV als auch als unter elektrochemischen Standardbedingungen als Modellsubstrate verwendet werden. In der vorliegenden Arbeit wurde hingegen

Glaskohlenstoffsubstrate (GC) verwendet, da diese im Vergleich zu Platin inerter sind und weniger dazu neigen, Nebenreaktionen zu katalysieren. In Modellstudien zur Mg Abscheidung / Auflösung auf GC aus ionischer Flüssigkeit beobachteten wir (geringfügige) Mg Abscheidung / Auflösung in Abhängigkeit des verwendeten Elektrolyten. Gleichzeitig trat jedoch auch eine starke Oberflächenpassivierung auf, deren Ursprung in Mg^{+}-induzierter $TFSI^{-}$-Zersetzung oder durch Verunreinigungen (wie O_2/H_2O) katalysierte BMP-TFSI Zersetzung vermutet wird. Diese Reaktionen hätten sehr wahrscheinlich auch auf Edelmetallelektroden stattgefunden.

Schließlich wurden in dieser Arbeit Mg Elektroden verwendet, welche den Vorteil haben, dass Mg Metall die tatsächliche, „realistische“ Anode für wiederaufladbare Mg Batterien darstellt. Unglücklicherweise ist die reine Mg Oberfläche hochreaktiv und daher dauerhaft von einer natürlichen Passivierungsschicht überzogen. Gelingt es, diese zu entfernen, bildet sich bei Kontakt mit Spuren von Luft oder Wasser sofort eine neue Passivierungsschicht, selbst in der Atmosphäre der Glovebox. Entsprechend benötigen die Mg Anoden einen aufwändigen Präparationsprozess welcher aus mehreren Polierschritten schon vor dem Einbau der Anode in die Zelle und schließlich, nachdem der Elektrolyt in die Zelle gefüllt wurde, einen undefinierten Kratzprozess mit Hilfe einer Glasspitze beinhaltet. Damit verringert sich die Reproduzierbarkeit der Experimente deutlich. Darüber hinaus werden sowohl der verwendete GC wie auch das Mg mit zunehmender Zyklenzeit (wahrscheinlich) durch die Passivierung der neu abgeschiedenen Mg Schicht passiviert. Dieser Prozess tritt verstärkt auf dem hoch-reaktiven Mg Substrat auf. Der auffälligste Unterschied zwischen den beiden (Modell-)Substraten hingegen ist jedoch das hohe Nukleationsüberpotential für Mg Abscheidung auf GC. Dennoch erlaubt das Glaskohlenstoffsubstrat eine deutlich höhere Reproduzierbarkeit der elektrochemischen Charakterisierung der Modellsysteme um die grundlegenden Prozesse an der Anoden|Elektrolygrenzfläche zu untersuchen und um unterschiedliche Elektrolytzusammensetzungen zu vergleichen – im Fall dieser Arbeit mit unterschiedlichen Konzentrationen von $Mg(BH_4)_2$, $MgTFSI_2$ und 18-Krone-6. Abschließend gilt schließlich, dass jeder Elektrolyt, welcher zur Passivierung der frisch auf GC abgeschiedenen Magnesiumschicht führt, nicht für realistische Mg Batterien geeignet ist. Demzufolge haben wir bei der Suche nach vielversprechenden Elektrolytsystemen zunächst GC Elektroden eingesetzt, um dann zu Mg überzugehen.

Im nächsten Abschnitt werde ich die Vorteile und Herausforderungen der in dieser Arbeit zum Einsatz gekommenen Salz- / Solvenssysteme näher zusammenfassen.

Ein Elektrolyt, welcher auch in kommerziellen LIBs verwendet wird, ist eine 1 : 1 (v/v) Mischung aus EC/DMC und 1 M $LiPF_6$. Oft wird er durch die Zugabe von Additiven verbessert, z.B. durch Zusatzstoffe für geringere Entflammbarkeit, erhöhte ionische Leitfähigkeit und/oder für bessere SEI Ausbildung. Um jedoch – nur ein Beispiel unter vielen – gezielt die Eigenschaften der Passivierungsschicht beeinflussen zu können, benötigt man ein detailliertes Wissen über die individuellen Wechselwirkungen zwischen Solventien, Salz und Elektrodenkomponenten. Dieses ergibt sich zum Beispiel aus dem Studium von vereinfachten Elektrolyten. Ethylencarbonat kann, trotz seiner hohen Viskosität und vergleichsweise geringen Ionenleitfähigkeit, sowohl in UHV-Studien – in denen es als intaktes Molekül an der HOPG Oberfläche adsorbiert – als auch in elektrochemische Modellstudien eingesetzt werden. Dimethylcarbonat mit seinem hohen Dampfdruck hingegen fand bislang nicht in Surface Science Studien Verwendung und benötigt, aus demselben Grund, für elektrochemische Messungen eine geschlossene Zelle.

Wie in Kapitel 3 gezeigt sind die elektrochemischen Eigenschaften von EC- bzw. DMC-basierten Elektrolyten auf HOPG Substraten sehr charakteristisch. Der oben beschriebene Aktivierungseffekt, zum Beispiel, ist in Ersteren deutlich schwächer zu beobachten als in Letzteren. Außerdem ist sowohl für HOPG als auch für Graphitpulverfilmelektroden, wie sie in Kapitel 4 verwendet wurden, das Onsetpotential der SEI Ausbildung in EC-basierten deutlich positiver als in DMC-basierten Elektrolyten. In EC-basierten Elektrolyten beginnt der Passivierungsprozess der Anode also bereits bei höheren Potentialen, was dazu führt, dass Graphitexfoliierung bereits früher verhindert wird. Weiterhin ist auf Substraten mit einer hohen Oberflächendefektdichte sofortige, komplette Oberflächenpassivierung (also SEI Ausbildung) zu beobachten. Dies war für DMC-basierte Elektrolyte jedoch nicht der Fall, und während des weiteren Zykelns fand sowohl für HOPG als auch für Graphitpulverfilmsubstrate kontinuierliche Graphitexfoliierung statt. Zusammengefasst zeigen unsere elektrochemischen Modellstudien also deutlich die überlegenen Eigenschaften von EC-basierten Elektrolyten im Vergleich zu DMC-basierten. Auch in gemischten EC/DMC Systemen (wie LP30), wie jene mit den hier untersuchten, binder-haltigen Elektroden, zeigen die entsprechenden Onsetpotentiale der Elektrolytzersetzung die Dominanz der EC Komponente bei der SEI Ausbildung.

Ex situ XPS Studien haben gezeigt, dass die reduktive Zersetzung der Solventien auf HOPG zu Produkten wie PEO und Semicarbonaten wie $(H_2COCO_2Li)_2$ für EC-basierte und H_3COCO_2Li und H_3COLi für DMC-basierte Elektrolyte führt. Weiterhin wurden in beiden Fällen

Salzzersetzungsprodukte wie LiF, Li_xPF_y und $Li_xPF_yO_z$ beobachtet. Auf den Pulverfilmsubstraten deutet hingegen ein starker differenzieller Aufladungseffekt, welcher für die in DMC-basierten Elektrolyt gezykelten Substrate beobachtet wurde, auf signifikante Unterschiede in der Produktzusammensetzung zwischen beiden Elektrolyten hin. Leider verhinderte jedoch der Aufladungseffekt die Auswertung der in DMC-basierten Elektrolyten gezykelten Graphitpulverfilmelektroden. Eine weitere Herausforderung, welche sich aus der Verwendung von EC und DMC als Solvens ergibt, ist die Ausbildung einer Vielzahl von Zersetzungsprodukten mit F-, O-, C-, P- und Li-haltigen Bestandteilen, welche die genaue Identifizierung einzelner Spezies erschweren. Diese Tatsache wird bei der XP Spektrenanalyse oft vernachlässigt, und die Anpassung und Zuordnung der Signale in den Spektren erfolgt oft anscheinend ohne Beachtung der (quantitativen) Zusammenhänge zwischen den Spektren der beteiligten Atome. In meiner Arbeit habe ich eine strikte und umfassende XPS Peakfittingmethode verwendet, welche ebendiese Beziehungen beachtet. Zwar ist es auch mit diesem Ansatz kaum möglich, jede einzelne Spezies innerhalb der SEI zweifelsfrei zu identifizieren. Dennoch erlaubt sie eine strategische und einheitliche Herangehensweise an diese Herausforderung.

Ein weiterer Elektrolyt, welcher im Rahmen dieser Arbeit verwendet wurde – die ionische Flüssigkeit BMP-TFSI – wird oft als Beispiel für einen neuen, vielversprechenden Elektrolyten für LIBs und sekundäre Mg Batterien angesehen. Sie erlaubt eine enge Verknüpfung zwischen den Welten der Surface Science Studien und elektrochemische Modellstudien, wie sie hier präsentiert wurden, und kann in sehr grundlegenden elektrochemischen Studien (z.B. Zersetzung der IL) sogar ohne ein zusätzliches Salz verwendet werden. Um einen stärkeren Anwendungsbezug herzustellen kann das Leitsalz in Form von LiTFSI oder $MgTFSI_2$ hinzugegeben werden, ohne ein weiteres Fremdanion einzuführen. Schließlich ist BMP-TFSI in seiner Anwendung in UHV Experimenten deutlich praktischer als EC, da es stabiler ist, einen geringeren Dampfdruck hat und hochgeordnete Adsorbatlagen ausbildet.

In elektrochemischen Messungen beobachtete ich irreversible Elektrolytzersetzungsprozesse auf der Oberfläche von sowohl wohl-definiertem HOPG als auch Graphitpulverfilmelektroden in LiTFSI-haltiger IL. Einer der hervorstechenden Unterschiede zwischen den carbonat- und $LiPF_6$-haltigen Elektrolyten und den IL-basierten Elektrolyten ist die fehlende mehrstufige Li^+ (De-)Interkalation in der ionischen Flüssigkeit, die weder auf dem defekt-armen HOPG noch auf dem defekt-reichen Pulverfilmsubstrat auftritt. Im Gegensatz zu EC- und DMC-basierten Elektrolyten führt die reduktive BMP-TFSI Zersetzung folglich zu einer Passivierungsschicht,

welche keinen Li^+-Transport erlaubt und im weiteren Verlauf auch das Graphit nicht ausreichend gegen Solvens-Cointerkalation schützt. XPS Analysen zeigten Unterschiede in den IL-Zersetzungsprozessen in Abhängigkeit von den experimentellen Gegebenheiten (Abscheidung im UHV vs. Zyklovoltammetrie) und der Art des anwesenden Lithiums (Li^0 vs. Li^+): während die nachträgliche Abscheidung von Li^0 auf eine adsorbierte Multilage BMP-TFSI vorrangig zu BMP^+ Zersetzung führt, resultiert elektrochemische Zersetzung in der Gegenwart von Li^+ (LiTFSI) vorrangig in $TFSI^-$-Zersetzung. Die Passivierungsschichten, welche in der IL gebildet werden, bestehen sowohl aus Li-haltigen Nitriden, Sulfiten und Sulfiden (Li_3N, Li_xSO_x, Li_2S) als auch aus organischen Stoffen der zersetzten $TFSI^-$ und BMP^+ Bestandteile. Allerdings ist auch hier die beträchtliche Menge an unterschiedlichen Salz- und IL-Zersetzungsprodukten nicht zu unterschätzen, und auch bisher unzersetzte Spezies und/oder Rekombinationen aus Zersetzungsprodukten und Edukten können vorkommen. Die eindeutige Identifizierung der Zusammensetzung der Passivierungsschicht an der IL|Elektrodengrenzfläche in diesen Modellsystemen ist daher ebenso komplex wie die Identifizierung der SEI Zusammensetzung in carbonathaltigen, vereinfachten Elektrolyten. Der Versuch der Identifikation wird sogar noch weiter erschwert, wenn das Tiefenprofil der Passivierungsschicht durch Argon Sputtering analysiert wird. Da es zur Zersetzung vorhandener Spezies und Ausbildung neuer Bestandteile führt, ist Sputtern zu Recht umstritten. Aus diesem Grund untersuchten wir für die Graphit|IL Modellsysteme den Einfluss des Sputterns auf Referenzsysteme (LiTFSI, HOPG|IL@OCP) und beobachteten zum Beispiel bei LiTFSI schon nach kurzer Zeit das Auftreten von Zersetzungsprodukten, unter Anderem LiF.

Für die Untersuchungen der Reversibilität der Mg Abscheidung / Auflösung für wiederaufladbare Mg Metallbatterien schließlich lag mein Fokus auf den Wechselwirkungen zwischen $MgTFSI_2$-haltiger BMP-TFSI und $Mg(BH_4)_2$ oder 18-Krone-6, bzw. auf den Wechselwirkungen zwischen Mg^{2+} und den genannten, im Elektrolyt enthaltenen Anionen / Additiven. $MgTFSI_2$ löst sich, wie auch LiTFSI, gut in BMP-TFSI. Auch die Additive Borhydrid und Kronenether können in moderaten Konzentrationen problemlos hinzugegeben werden. Die Ausbildung einer Passivierungsschicht findet sowohl beim Zykeln von GC in $MgTFSI_2$- wie auch in $Mg(BH_4)_2$-haltiger IL statt, vergleichbar mit den LIB-bezogenen Untersuchungen von GC in LiTFSI-enthaltender BMP-TFSI. Der Hauptgrund für die Oberflächenpassivierung scheint hier eine schädliche Wechselwirkung zwischen Mg^+ und $TFSI^-$ zu sein, welche zur vorzeitigen $TFSI^-$-Zersetzung statt zur Mg Abscheidung führt. Jedoch blockieren beide – sowohl die in Li^+- wie auch die in Mg^{2+}-haltiger IL geformte – Passivierungsschichten den Transport der jeweiligen Kationen und Ladungsträger durch die

Schicht und verhindern so Li^+ (De-)Interkalation und Mg Abscheidung / Auflösung gleichermaßen. Eine Variation der Mg Salzkomponente und/oder die Zugabe von $Mg(BH_4)_2$ und 18-Krone-6 verhindert die Ausbildung der Passivierungsschicht und erlaubt verbesserte Mg Abscheidung / Auflösung; vermutlich aufgrund einer Wechselwirkung des komplexierenden zyklischen Ethers mit der Koordinationssphäre des Mg^{2+} Kations. MD Simulationen und quantenchemische Berechnungen, welche von unseren Projektpartnern durchgeführt wurden, zeigen, dass die o.g. Wechselwirkungen stark genug sind, um die schädlichen Mg^+–$TFSI^-$ Interaktion zu verringern. Gleichzeitig sind sie jedoch nicht so stark, dass die Mg Abscheidung / Auflösung verhindert würde – ein Konzept, welches mit dem Sabatier-Prinzip der Katalyse vergleichbar ist. Und schließlich fungiert das Borhydrid zusätzlich als Wasserfänger und verhindert so eine Oberflächenpassivierung via MgO Ausbildung.

Zum Abschluss meiner Arbeit fasse ich zusammen:

Zyklovoltammetrische Untersuchungen wohl-definierter Modellsysteme sind ein ideales Werkzeug zur Charakterisierung. Die Einfachheit der Modelle erlaubt eine direkte Verbindung zu Surface Science oder theoretischen Studien und kann so zu einem tieferen Verständnis bereits etablierter Prozesse und Reaktionen beitragen. Die Details, welche durch diese Untersuchungen gewonnen werden konnten, bilden das Fundament für ein unentbehrliches Verständnis von Grenzflächen in Batterien sowie für alle weiteren systematischen Untersuchungen mit dem Ziel, zukünftige LIB und Mg Metallbatteriesysteme sicher und langlebig zu gestalten.

9. Bibliography

1. Gross, E.; Moody, J.; Dimanchev, E.; Murphy, E.; Gençer, E.; Nunes, A.; Ghandi, A.; Oke, J. B.; Hsieh, I.-Y. L.; Sridhar, R.; Miller, I.; Weigl, D.; Morris, J. *Insights into Future Mobility*; MIT Energy Initiative: Cambridge, MA, Nov, **2019**.
2. Nishio, K.; Furukawa, N. Practical Batteries. In *Handbook of Battery Materials*, 2nd Ed.; Besenhard, J. O., Daniel, C., Eds.; John Wiley & Sons: Weinheim, **2012**; pp 27-85.
3. Berndt, D. Lead Oxides. In *Handbook of Battery Materials*, 2 ed.; Besenhard, J. O., Daniel, C., Eds.; John Wiley & Sons: Weinheim, **2012**; pp 169-196.
4. Reilly, J. J. Metal Hydride Electrodes. In *Handbook of Battery Materials*, 2 ed.; Besenhard, J. O., Daniel, C., Eds.; John Wiley & Sons: Weinheim, **2012**; pp 239-268.
5. Wyczalek, F. A. Market Mature 1998 Hybrid Electric Vehicles. *IEEE Aero. El. Sys. Mag.* **1999**, *14* (3), 41-44.
6. Whittingham, M. S. Electrical Energy Storage and Intercalation Chemistry. *Science* **1976**, *192* (4244), 1126-1127.
7. Tarascon, J. M.; Armand, M. Issues and Challenges Facing Rechargeable Lithium Batteries. *nature* **2001**, *414*, 359-367.
8. Rao, B. M. L.; Francis, R. W.; Christopher, H. A. Lithium–Aluminum Electrode. *J. Electrochem. Soc.* **1977**, *124* (10), 1490-1492.
9. Mohri, M.; Yanagisawa, N.; Tajima, Y.; Tanaka, H.; Mitate, T.; Nakajima, S.; Yoshida, M.; Yoshimoto, Y.; Suzuki, T.; Wada, H. Rechargeable Lithium Battery Based on Pyrolytic Carbon as a Negative Electrode. *J. Power Sources* **1989**, *26* (3-4), 545-551.
10. Dresselhaus, M. S.; Dresselhaus, G. Intercalation Compounds of Graphite. *Adv. Phys.* **1981**, *30* (2), 139-326.
11. Winter, M.; Besenhard, J. O.; Spahr, M. E.; Novák, P. Insertion Electrode Materials for Rechargeable Lithium Batteries. *Adv. Mater.* **1998**, *10* (10), 725-763.
12. NobelPrize.org Press Release: The Nobel Prize in Chemistry 2019. 2019.
13. Scrosati, B. Recent Advances in Lithium Ion Battery Materials. *Electrochim. Acta* **2000**, *45* (15-16), 2461-2466.
14. Armand, M.; Tarascon, J. M. Building Better Batteries. *nature* **2008**, *451* (7179), 652.
15. Scrosati, B.; Garche, J. Lithium Batteries: Status, Prospects and Future. *J. Power Sources* **2010**, *195* (9), 2419-2430.
16. Goodenough, J. B.; Kim, Y. Challenges for Rechargeable Li Batteries. *Chem. Mater.* **2010**, *22* (3), 587-603.
17. Barré, A.; Deguilhem, B.; Grolleau, S.; Gérard, M.; Suard, F.; Riu, D. A Review on Lithium-Ion Battery Ageing Mechanisms and Estimations for Automotive Applications. *J. Power Sources* **2013**, *241*, 680-689.
18. Lu, L.; Han, X.; Li, J.; Hua, J.; Ouyang, M. A Review on the Key Issues for Lithium-Ion Battery Management in Electric Vehicles. *J. Power Sources* **2013**, *226*, 272-288.
19. Hannan, M. A.; Lipu, M. S. H.; Hussain, A.; Mohamed, A. A Review of Lithium-Ion Battery State of Charge Estimation and Management System in Electric Vehicle Applications: Challenges and Recommendations. *Renew. Sust. Energ. Rev.* **2017**, *78*, 834-854.
20. Kim, T.; Song, W.; Son, D. Y.; Ono, L. K.; Qi, Y. Lithium-Ion Batteries: Outlook on Present, Future, and Hybridized Technologies. *J. Mater. Chem. A* **2019**, *7* (7), 2942-2964.
21. Xu, K. Nonaqueous Liquid Electrolytes for Lithium-Based Rechargeable Batteries. *Chem. Rev.* **2004**, *104* (10), 4303-4418.
22. Kalhoff, J.; Eshetu, G. G.; Bresser, D.; Passerini, S. Safer Electrolytes for Lithium–Ion Batteries: State of the Art and Perspectives. *ChemSusChem* **2015**, *8* (13), 2154-2175.

23. Ming, J.; Cao, Z.; Wu, Y.; Wahyudi, W.; Wang, W.; Guo, X.; Cavallo, L.; Hwang, J. Y.; Shamim, A.; Li, L. J.; Sun, Y. K.; Alshareef, H. N. New Insight on the Role of Electrolyte Additives in Rechargeable Lithium Ion Batteries. *ACS Energy Lett.* **2019**, *4* (11), 2613-2622.
24. Manthiram, A. A Reflection on Lithium-Ion Battery Cathode Chemistry. *Nature Commun.* **2020**, *11* (1), 1550.
25. Whittingham, M. S. Lithium Batteries and Cathode Materials. *Chem. Rev.* **2004**, *104* (10), 4271-4302.
26. Ellis, B. L.; Lee, K. T.; Nazar, L. F. Positive Electrode Materials for Li-Ion and Li Batteries. *Chem. Mater.* **2010**, *22* (3), 691-714.
27. Manthiram, A.; Muraliganth, T. Lithium Intercalation Cathode Materials for Lithium–Ion Batteries. In *Handbook of Battery Materials*, 2nd Ed.; Besenhard, J. O., Daniel, C., Eds.; John Wiley & Sons: Weinheim, **2012**; pp 343-375.
28. Nitta, N.; Wu, F.; Lee, J. T.; Yushin, G. Li-Ion Battery Materials: Present and Future. *Mater. Today* **2015**, *18* (5), 252-264.
29. Speirs, J.; Contestabile, M.; Houari, Y.; Gross, R. The Future of Lithium Availability for Electric Vehicle Batteries. *Renew. Sust. Energ. Rev.* **2014**, *35*, 183-193.
30. Moss, R. L.; Tzimas, E.; Willis, P.; Arendorf, J.; Thompson, P.; Chapman, A.; Morley, N.; Sims, E.; Bryson, R.; Peason, J. Critical Metals in the Path Towards the Decarbonisation of the EU Energy Sector - Assessing Rare Metals as Supply-Chain Bottlenecks in Low-Carbon Energy Technologies. *JRC Scientific and Policy Reports* **2013**, *25994*.
31. Xu, J.; Thomas, H. R.; Francis, R. W.; Lum, K. R.; Wang, J.; Liang, B. A Review of Processes and Technologies for the Recycling of Lithium-Ion Secondary Batteries. *J. Power Sources* **2008**, *177* (2), 512-527.
32. Zhang, X.; Li, L.; Fan, E.; Xue, Q.; Bian, Y.; Wu, F.; Chen, R. Toward Sustainable and Systematic Recycling of Spent Rechargeable Batteries. *Chem. Soc. Rev.* **2018**, *47* (19), 7239-7302.
33. Li, M.; Lu, J. Cobalt in Lithium-Ion Batteries. *Science* **2020**, *367* (6481), 979.
34. Christmann, P.; Gloaguen, E.; Labbé, J.-F.; Melleton, J.; Piantone, P. Global Lithium Resources and Sustainability Issues. In *Lithium Process Chemistry*, Chagnes, A., Swiatowska, J., Eds.; Elsevier: **2015**; pp 1-40.
35. Novák, P.; Joho, F.; Imhof, R.; Panitz, J. C.; Haas, O. In Situ Investigation of the Interaction Between Graphite and Electrolyte Solutions. *J. Power Sources* **1999**, *81-82*, 212-216.
36. Aurbach, D.; Gofer, Y.; Schechter, A.; Chusid, O.; Gizbar, H.; Cohen, Y.; Moshkovich, M.; Turgeman, R. A Comparison Between the Electrochemical Behavior of Reversible Magnesium and Lithium Electrodes. *J. Power Sources* **2001**, *97-98*, 269-273.
37. Shterenberg, I.; Salama, M.; Gofer, Y.; Levi, E.; Aurbach, D. The Challenge of Developing Rechargeable Magnesium Batteries. *MRS Bull.* **2014**, *39* (5), 453-460.
38. Mohtadi, R.; Mizuno, F. Magnesium Batteries: Current State of the Art, Issues and Future Perspectives. *Beilstein J. Nanotechnol.* **2014**, *5* (1), 1291-1311.
39. Bucur, C. B.; Gregory, T.; Oliver, A. G.; Muldoon, J. Confession of a Magnesium Battery. *J. Phys. Chem. Lett.* **2015**, *6* (18), 3578-3591.
40. Zhao-Karger, Z.; Fichtner, M. Magnesium–Sulfur Battery: Its Beginning and Recent Progress. *MRS Commun.* **2017**, *7* (4), 770-784.
41. Groß, A.; Ehrenberg, H.; Fichtner, M. *Energy Storage Beyond Lithium - New Storage Concepts for a Sustainable Future*; **2018**.
42. Fichtner, M. Motivation for a Magnesium Battery. In *Magnesium Batteries: Research and Applications*, 23rd Ed.; Fichtner, M., Ed.; Royal Society of Chemistry: **2019**; pp 1-16.
43. Liu, F.; Wang, T.; Liu, X.; Fan, L. Z. Challenges and Recent Progress on Key Materials for Rechargeable Magnesium Batteries. *Adv. Energy Mater.* **2020**, (2000787), 1-28.

44. Attias, R.; Salama, M.; Hirsch, B.; Goffer, Y.; Aurbach, D. Anode-Electrolyte Interfaces in Secondary Magnesium Batteries. *Joule* **2019**, *3* (1), 27-52.

45. Sagane, F.; Ogi, K.; Konno, A.; Egashira, M.; Kanamura, K. The Effect of the Cyclic Ether Additives to the Ethereal Electrolyte Solutions for Mg Secondary Battery. *Electrochemistry* **2016**, *84* (2), 76-78.

46. Sagane, F.; Ogi, K.; Konno, A.; Kanamura, K. The Effect of Cyclic Ethers on Mg Plating/Stripping Reaction in Ionic Liquid Electrolytes. *J. Electrochem. Soc.* **2019**, *166* (3), A5054-A5058.

47. Blake, I. C. Fiftieth Anniversary: The Anniversary Issue on Primary Cell Silver Chloride–Magnesium Reserve Battery. *J. Electrochem. Soc.* **1952**, *99* (8), 202C-203C.

48. Aurbach, D.; Gamolsky, K.; Markovsky, B.; Salitra, G.; Gofer, Y.; Heider, U.; Oesten, R.; Schmidt, M. The Study of Surface Phenomena Related to Electrochemical Lithium Intercalation into Li_xMO_y Host Materials (M= Ni, Mn). *J. Electrochem. Soc.* **2000**, *147* (4), 1322-1331.

49. Peled, E. The Electrochemical Behavior of Alkali and Alkaline Earth Metals in Nonaqueous Battery Systems - The Solid Electrolyte Interphase Model. *J. Electrochem. Soc.* **1979**, *126* (12), 2047-2051.

50. Aurbach, D.; Markovsky, B.; Weissman, I.; Levi, E.; Ein-Eli, Y. On the Correlation Between Surface Chemistry and Performance of Graphite Negative Electrodes for Li-Ion Batteries. *Electrochim. Acta* **1999**, *45* (1–2), 67-86.

51. Verma, P.; Maire, P.; Novák, P. A Review of the Features and Analyses of the Solid Electrolyte Interphase in Li-Ion Batteries. *Electrochim. Acta* **2010**, *55* (22), 6332-6341.

52. Ross, P. N. Catalysis and Interfacial Chemistry in Lithium Batteries: A Surface Science Approach. *Catal. Lett.* **2014**, *144* (8), 1370-1376.

53. Agubra, V. A.; Fergus, J. W. The Formation and Stability of the Solid Electrolyte Interface on the Graphite Anode. *J. Power Sources* **2014**, *268*, 153-162.

54. Gauthier, M.; Carney, T. J.; Grimaud, A.; Giordano, L.; Pour, N.; Chang, H. H.; Fenning, D. P.; Lux, S. F.; Paschos, O.; Bauer, C. Electrode–Electrolyte Interface in Li-Ion Batteries: Current Understanding and New Insights. *J. Phys. Chem. Lett.* **2015**, *6* (22), 4653-4672.

55. An, S. J.; Li, J.; Daniel, C.; Mohanty, D.; Nagpure, S.; Wood III, D. L. The State of Understanding of the Lithium-Ion Battery Graphite Solid Electrolyte Interphase (SEI) and its Relationship to Formation Cycling. *Carbon* **2016**, *105*, 52-76.

56. Peled, E.; Bar-Tow, D.; Merson, A.; Burstein, L. Microphase Structure of SEI on HOPG. *New Mat. Electrochem.* **2000**, *3* (4), 321-328.

57. Edström, K.; Herranen, M. Thermal Stability of the HOPG|Liquid Electrolyte Interphase Studied by *in situ* Electrochemical Atomic Force Microscopy. *J. Electrochem. Soc.* **2000**, *147* (10), 3628-3632.

58. Peled, E.; Bar-Tow, D.; Merson, A.; Gladkich, A.; Burstein, L.; Golodnitsky, D. Composition, Depth Profiles and Lateral Distribution of Materials in the SEI Built on HOPG - TOF-SIMS and XPS Studies. *J. Power Sources* **2001**, *97-98*, 52-57.

59. Peled, E.; Golodnitsky, D.; Ulus, A.; Yufit, V. Effect of Carbon Substrate on SEI Composition and Morphology. *Electrochim. Acta* **2004**, *50* (2–3), 391-395.

60. Eshkenazi, V.; Peled, E.; Burstein, L.; Golodnitsky, D. XPS Analysis of the SEI Formed on Carbonaceous Materials. *Solid State Ion.* **2004**, *170* (1-2), 83-91.

61. Lanz, P.; Novák, P. Combined In Situ Raman and IR Microscopy at the Interface of a Single Graphite Particle with Ethylene Carbonate/Dimethyl Carbonate. *J. Electrochem. Soc.* **2014**, *161* (10), A1555-A1563.

62. Aurbach, D.; Ein-Eli, Y.; Markovsky, B.; Zaban, A.; Luski, S.; Carmeli, Y.; Yamin, H. The Study of Electrolyte Solutions Based on Ethylene and Diethyl Carbonates for Rechargeable Li Batteries II: Graphite Electrodes. *J. Electrochem. Soc.* **1995**, *142* (9), 2882-2890.

63. Aurbach, D.; Zaban, A.; Ein-Eli, Y.; Weissman, I.; Chusid, O.; Markovsky, B.; Levi, M.; Levi, E.; Schechter, A.; Granot, E. Recent Studies on the Correlation Between Surface Chemistry,

Morphology, Three-Dimensional Structures and Performance of Li and Li-C Intercalation Anodes in Several Important Electrolyte Systems. *J. Power Sources* **1997**, *68* (1), 91-98.

64. Jeong, S. K.; Inaba, M.; Iriyama, Y.; Abe, T.; Ogumi, Z. Surface Film Formation on a Graphite Negative Electrode in Lithium-Ion Batteries: AFM Study on the Effects of Co-Solvents in Ethylene Carbonate-Based Solutions. *Electrochim. Acta* **2002**, *47* (12), 1975-1982.
65. Aurbach, D.; Talyosef, Y.; Markovsky, B.; Markevich, E.; Zinigrad, E.; Asraf, L.; Gnanaraj, J. S.; Kim, H. J. Design of Electrolyte Solutions for Li and Li-Ion Batteries: A Review. *Electrochim. Acta* **2004**, *50* (2–3), 247-254.
66. Nie, M.; Chalasani, D.; Abraham, D. P.; Chen, Y.; Bose, A.; Lucht, B. L. Lithium-Ion Battery Graphite Solid Electrolyte Interphase Revealed by Microscopy and Spectroscopy. *J. Phys. Chem. C* **2013,** *117* (3), 1257-1267.
67. Nie, M.; Abraham, D. P.; Seo, D. M.; Chen, Y.; Bose, A.; Lucht, B. L. Role of Solution Structure in Solid Electrolyte Interphase Formation on Graphite with $LiPF_6$ in Propylene Carbonate. *J. Phys. Chem. C* **2013**, *117* (48), 25381-25389.
68. Shen, C.; Wang, S.; Jin, Y.; Han, W. Q. In Situ AFM Imaging of Solid Electrolyte Interfaces on HOPG with Ethylene Carbonate and Fluoroethylene Carbonate-Based Electrolytes. *ASC Appl. Mater. Interfaces* **2015**, *7* (45), 25441-25447.
69. Aurbach, D.; Markovsky, B.; Shechter, A.; Ein-Eli, Y.; Cohen, H. A Comparative Study of Synthetic Graphite and Li Electrodes in Electrolyte Solutions Based on Ethylene Carbonate–Dimethyl Carbonate Mixtures. *J. Electrochem. Soc.* **1996**, *143* (12), 3809-3820.
70. Chu, A. C.; Josefowicz, J. Y.; Farrington, G. C. Electrochemistry of Highly Ordered Pyrolytic Graphite Surface Film Formation Observed by Atomic Force Microscopy. *J. Electrochem. Soc.* **1997**, *144* (12), 4161-4169.
71. Andersson, A. M.; Edström, K. Chemical Composition and Morphology of the Elevated Temperature SEI on Graphite. *J. Electrochem. Soc.* **2001**, *148* (10), A1100-A1109.
72. Leroy, S.; Martinez, H.; Dedryvère, R.; Lemordant, D.; Gonbeau, D. Influence of the Lithium Salt Nature over the Surface Film Formation on a Graphite Electrode in Li-Ion Batteries: An XPS Study. *Appl. Surf. Sci.* **2007**, *253* (11), 4895-4905.
73. Eshetu, G. G.; Diemant, T.; Grugeon, S.; Behm, R. J.; Laruelle, S.; Armand, M.; Passerini, S. In-Depth Interfacial Chemistry and Reactivity Focused Investigation of Lithium-Imide- and Lithium-Imidazole-Based Electrolytes. *ACS Appl. Mater. Interfaces* **2016**, *8*, 16087-16100.
74. Zhang, S. S. A Review on Electrolyte Additives for Lithium-Ion Batteries. *J. Power Sources* **2006**, *162* (2), 1379-1394.
75. Imhof, R.; Novák, P. *In Situ* Investigation of the Electrochemical Reduction of Carbonate Electrolyte Solutions at Graphite Electrodes. *J. Electrochem. Soc.* **1998**, *145* (4), 1081-1087.
76. Alliata, D.; Kötz, R.; Novák, P.; Siegenthaler, H. Electrochemical SPM Investigation of the Solid Electrolyte Interphase Film Formed on HOPG Electrodes. *Electrochem. Commun.* **2000**, *2* (6), 436-440.
77. Andersson, A. M.; Henningson, A.; Siegbahn, H.; Jansson, U.; Edström, K. Electrochemically Lithiated Graphite Characterised by Photoelectron Spectroscopy. *J. Power Sources* **2003**, *119*, 522-527.
78. Zhuang, G. V.; Xu, K.; Yang, H.; Jow, T. R.; Ross, P. N. Lithium Ethylene Dicarbonate Identified as the Primary Product of Chemical and Electrochemical Reduction of EC in 1.2 M $LiPF_6$/EC:EMC Electrolyte. *J. Phys. Chem. B* **2005**, *109* (37), 17567-17573.
79. Dedryvère, R.; Gireaud, L.; Grugeon, S.; Laruelle, S.; Tarascon, J. M.; Gonbeau, D. Characterization of Lithium Alkyl Carbonates by X-ray Photoelectron Spectroscopy: Experimental and Theoretical Study. *J. Phys. Chem. B* **2005**, *109* (33), 15868-15875.
80. Dedryvère, R.; Laruelle, S.; Grugeon, S.; Gireaud, L.; Tarascon, J. M.; Gonbeau, D. XPS Identification of the Organic and Inorganic Components of the Electrode|Electrolyte Interface Formed on a Metallic Cathode. *J. Electrochem. Soc.* **2005**, *152* (4), A689-A696.

81. Peled, E.; Golodnitsky, D.; Ardel, G. Advanced Model for Solid Electrolyte Interphase Electrodes in Liquid and Polymer Electrolytes. *J. Electrochem. Soc.* **1997**, *144* (8), L208-L210.

82. Kanamura, K.; Tamura, H.; Takehara, Z. XPS Analysis of a Lithium Surface Immersed in Propylene Carbonate Solution Containing Various Salts. *J. Electroanal. Chem.* **1992**, *333* (1–2), 127-142.

83. Kanamura, K.; Shiraishi, S.; Tamura, H.; Takehara, Z. X–ray Photoelectron Spectroscopic Analysis and Scanning Electron Microscopic Observation of the Lithium Surface Immersed in Nonaqueous Solvents. *J. Electrochem. Soc.* **1994**, *141* (9), 2379-2385.

84. Kanamura, K.; Tamura, H.; Shiraishi, S.; Takehara, Z. XPS Analysis of Lithium Surfaces Following Immersion in Various Solvents Containing $LiBF_4$. *J. Electrochem. Soc.* **1995**, *142* (2), 340-347.

85. Edström, K.; Herstedt, M.; Abraham, D. P. A New Look at the Solid Electrolyte Interphase on Graphite Anodes in Li-Ion Batteries. *J. Power Sources* **2006**, *153* (2), 380-384.

86. Malmgren, S.; Ciosek, K.; Hahlin, M.; Gustafsson, T.; Gorgoi, M.; Rensmo, H.; Edström, K. Comparing Anode and Cathode Electrode|Electrolyte Interface Composition and Morphology Using Soft and Hard X-ray Photoelectron Spectroscopy. *Electrochim. Acta* **2013**, *97*, 23-32.

87. Philippe, B.; Hahlin, M.; Edström, K.; Gustafsson, T.; Siegbahn, H.; Rensmo, H. Photoelectron Spectroscopy for Lithium Battery Interface Studies. *J. Electrochem. Soc.* **2015**, *163* (2), A178-A191.

88. Liebenow, C. Reversibility of Electrochemical Magnesium Deposition from Grignard Solutions. *J. Appl. Electrochem.* **1997**, *27* (2), 221-225.

89. Aurbach, D.; Weissman, I.; Gofer, Y.; Levi, El. Nonaqueous Magnesium Electrochemistry and its Application in Secondary Batteries. *Chem. Rec.* **2003**, *3* (1), 61-73.

90. Deivanayagam, R.; Ingram, B. J.; Shahbazian-Yassar, R. Progress in Development of Electrolytes for Magnesium Batteries. *Energy Storage Mater.* **2019**, *21*, 136-153.

91. Muldoon, J.; Bucur, C. B.; Gregory, T. Fervent Hype Behind Magnesium Batteries: An Open Call to Synthetic Chemists - Electrolytes and Cathodes Needed. *Angew. Chem. Int. Ed.* **2017**, *56* (40), 12064-12084.

92. Aurbach, D.; Weissman, I.; Schechter, A.; Cohen, H. X-ray Photoelectron Spectroscopy Studies of Lithium Surfaces Prepared in Several Important Electrolyte Solutions: A Comparison with Previous Studies by Fourier Transform Infrared Spectroscopy. *Langmuir* **1996**, *12* (16), 3991-4007.

93. Muldoon, J.; Bucur, C. B.; Oliver, A. G.; Sugimoto, T.; Matsui, M.; Kim, H. S.; Allred, G. D.; Zajicek, J.; Kotani, Y. Electrolyte Roadblocks to a Magnesium Rechargeable Battery. *Energ. Environ. Sci.* **2012**, *5* (3), 5941-5950.

94. Doe, R. E.; Han, R.; Hwang, J.; Gmitter, A. J.; Shterenberg, I.; Yoo, H. D.; Pour, N.; Aurbach, D. Novel Electrolyte Solutions Comprising Fully Inorganic Salts with High Anodic Stability for Rechargeable Magnesium Batteries. *Chem. Commun.* **2014**, *50* (2), 243-245.

95. See, K. A.; Chapman, K. W.; Zhu, L.; Wiaderek, K. M.; Borkiewicz, O. J.; Barile, C. J.; Chupas, P. J.; Gewirth, A. A. The Interplay of Al and Mg Speciation in Advanced Mg Battery Electrolyte Solutions. *J. Am. Chem. Soc.* **2016**, *138* (1), 328-337.

96. Guo, Y.; Zhang, F.; Yang, J.; Wang, F.; NuLi, Y.; Hirano, S. Boron-Based Electrolyte Solutions with Wide Electrochemical Windows for Rechargeable Magnesium Batteries. *Energy Environ. Sci.* **2012**, *5* (10), 9100-9106.

97. Carter, T. J.; Mohtadi, R.; Arthur, T. S.; Mizuno, F.; Zhang, R.; Shirai, S.; Kampf, J. W. Boron Clusters as Highly Stable Magnesium-Battery Electrolytes. *Angew. Chem. Int. Ed.* **2014**, *53* (12), 3173-3177.

98. Mohtadi, R.; Matsui, M.; Arthur, T. S.; Hwang, S.-J. Magnesium Borohydride: From Hydrogen Storage to Magnesium Battery. *Angew. Chem. Int. Ed.* **2012**, *51* (39), 9780-9783.

99. Herb, J. T.; Nist-Lund, C. A.; Arnold, C. B. A Fluorinated Alkoxyaluminate Electrolyte for Magnesium-Ion Batteries. *ACS Energy Lett.* **2016**, *1* (6), 1227-1232.

100. Zhao-Karger, Z.; Bardaji, M. E. G.; Fuhr, O.; Fichtner, M. A New Class of Non-Corrosive, Highly Efficient Electrolytes for Rechargeable Magnesium Batteries. *J. Mater. Chem. A* **2017**, *5* (22), 10815-10820.

101. Shterenberg, I.; Salama, M.; Yoo, H. D.; Gofer, Y.; Park, J. B.; Sun, Y. K.; Aurbach, D. Evaluation of $(CF_3SO_2)_2N$ (TFSI)-Based Electrolyte Solutions for Mg Batteries. *J. Electrochem. Soc.* **2015**, *162* (13), A7118-A7128.

102. Sakaebe, H.; Matsumoto, H. Application of Ionic Liquids to Li Batteries. In *Electrochemical Aspects of Ionic Liquids*, Ohno, H., Ed.; John Wiley & Sons: Hoboken, New Jersey, **2005**; p 173.

103. MacFarlane, D. R.; Forsyth, M.; Howlett, P. C.; Pringle, J. M.; Sun, J.; Annat, G.; Neil, W.; Izgorodina, E. I. Ionic Liquids in Electrochemical Devices and Processes: Managing Interfacial Electrochemistry. *Acc. Chem. Res.* **2007**, *40* (11), 1165-1173.

104. MacFarlane, D. R.; Seddon, K. R. Ionic Liquids – Progress on the Fundamental Issues. *Austr. J. Chem.* **2007**, *60* (1), 3-5.

105. Amir, N.; Vestfrid, Y.; Chusid, O.; Gofer, Y.; Aurbach, D. Progress in Nonaqueous Magnesium Electrochemistry. *J. Power Sources* **2007**, *174* (2), 1234-1240.

106. Lewandowski, A.; Swiderska-Mocek, A. Ionic Liquids as Electrolytes for Li-Ion Batteries – An Overview of Electrochemical Studies. *J. Power Sources* **2009**, *194* (2), 601-609.

107. Lovelock, K. R. J.; Villar-Garcia, I. J.; Maier, F.; Steinrück, H. P.; Licence, P. Photoelectron Spectroscopy of Ionic Liquid-Based Interfaces. *Chem. Rev.* **2010**, *110* (9), 5158-5190.

108. Li, Q.; Chen, J.; Fan, L.; Kong, X.; Lu, Y. Progress in Electrolytes for Rechargeable Li-Based Batteries and Beyond. *Green Energy Environ.* **2016**, *1* (1), 18-42.

109. Ohno, H. *Electrochemical Aspects of Ionic Liquids;* 1st Ed.; John Wiley & Sons: Hoboken, New Jersey, **2005**.

110. Galinski, M.; Lewandowski, A.; Stepniak, I. Ionic Liquids as Electrolytes. *Electrochim. Acta* **2006**, *51* (26), 5567-5580.

111. Menne, S.; Pires, J.; Anouti, M.; Balducci, A. Protic Ionic Liquids as Electrolytes for Lithium-Ion Batteries. *Electrochem. Commun.* **2013**, *31*, 39-41.

112. Eftekhari, A.; Liu, Y.; Chen, P. Different Roles of Ionic Liquids in Lithium Batteries. *J. Power Sources* **2016**, *334*, 221-239.

113. Bakkar, A.; Neubert, V. Electrodeposition onto Magnesium in Air and Water Stable Ionic Liquids: From Corrosion to Successful Plating. *Electrochem. Commun.* **2007**, *9* (9), 2428-2435.

114. Cheek, G. T.; O'Grady, W.; El Abedin, S. Z.; Moustafa, E. M.; Endres, F. Electrochemical Studies of Magnesium Deposition in Ionic Liquids. *ECS Trans.* **2007**, *3* (35), 269-279.

115. Cheek, G. T.; O'Grady, W. E.; El Abedin, S. Z.; Moustafa, E. M.; Endres, F. Studies on the Electrodeposition of Magnesium in Ionic Liquids. *J. Electrochem. Soc.* **2008**, *155* (1), D91-D95.

116. Kar, M.; Simons, T. J.; Forsyth, M.; MacFarlane, D. R. Ionic Liquid Electrolytes as a Platform for Rechargeable Metal–Air Batteries: A Perspective. *Phys. Chem. Chem. Phys.* **2014**, *16* (35), 18658-18674.

117. Shimamura, O.; Yoshimoto, N.; Matsumoto, M.; Egashia, M.; Morita, M. Electrochemical Co-Deposition of Magnesium with Lithium from Quaternary Ammonium-Based Ionic Liquid. *J. Power Sources* **2011**, *196* (3), 1586-1588.

118. Vardar, G.; Sleightholme, A. E. S.; Naruse, J.; Hiramatsu, H.; Siegel, D. J.; Monroe, C. W. Electrochemistry of Magnesium Electrolytes in Ionic Liquids for Secondary Batteries. *ACS Appl. Mater. Interfaces* **2014**, *6* (20), 18033-18039.

119. Watkins, T.; Kumar, A.; Buttry, D. A. Designer Ionic Liquids for Reversible Electrochemical Deposition/Dissolution of Magnesium. *J. Am. Chem. Soc.* **2016**, *138* (2), 641-650.

120. Giffin, G. A. Ionic Liquid-Based Electrolytes for "Beyond Lithium" Battery Technologies. *J. Mater. Chem. A* **2016,** *4* (35), 13378-13389.

121. Gao, X.; Mariani, A.; Jeong, S.; Liu, X.; Dou, X.; Ding, M.; Moretti, A.; Passerini, S. Prototype Rechargeable Magnesium Batteries Using Ionic Liquid Electrolytes. *J. Power Sources* **2019**, *423*, 52-59.

122. Uhl, B.; Buchner, F.; Alwast, D.; Wagner, N.; Behm, R. J. Adsorption of the Ionic Liquid [BMP][TFSA] on Au(111) and Ag(111): Substrate Effects on the Structure Formation Investigated by STM. *Beilstein J. Nanotech.* **2013**, *4* (1), 903-918.

123. Uhl, B.; Buchner, F.; Gabler, S.; Bozorgchenani, M.; Behm, R. J. Adsorption and Reaction of Sub-Monolayer Films of an Ionic Liquid on Cu(111). *Chem. Commun.* **2014**, *50* (62), 8601-8604.

124. Uhl, B.; Hekmatfar, M.; Buchner, F.; Behm, R. J. Interaction of the Ionic Liquid [BMP][TFSA] with Rutile TiO_2(110) and Coadsorbed Lithium. *Phys. Chem. Chem. Phys.* **2016**, *18* (9), 6618-6636.

125. Alwast, D.; Schnaidt, J.; Law, Y. T.; Behm, R. J. A Novel Approach for Differential Electrochemical Mass Spectrometry Studies on the Decomposition of Ionic Liquids. *Electrochim. Acta* **2016**, *197*, 290-299.

126. Law, Y. T.; Schnaidt, J.; Brimaud, S.; Behm, R. J. Oxygen Reduction and Evolution in an Ionic Liquid ([BMP][TFSA])-Based Electrolyte: A Model Study of the Cathode Reactions in Mg-Air Batteries. *J. Power Sources* **2016**, *333*, 173-183.

127. Buchner, F.; Forster-Tonigold, K.; Bozorgchenani, M.; Groß, A.; Behm, R. J. Interaction of a Self-Assembled Ionic Liquid Layer with Graphite(0001): A Combined Experimental and Theoretical Study. *J. Phys. Chem. Lett.* **2016**, *7* (2), 226-233.

128. Buchner, F.; Kim, J.; Adler, C.; Bozorgchenani, M.; Bansmann, J.; Behm, R. J. Intercalation and Deintercalation of Lithium at the Ionic Liquid–Graphite(0001) Interface. *J. Phys. Chem. Lett.* **2017**, *8* (23), 5804-5809.

129. Buchner, F.; Uhl, B.; Forster-Tonigold, K.; Bansmann, J.; Groß, A.; Behm, R. J. Structure Formation and Surface Chemistry of Ionic Liquids on Model Electrode Surfaces − Model Studies for the Electrode|Electrolyte Interface in Li-Ion Batteries. *J. Chem. Phys.* **2018**, *148* (19), 193821.

130. Buchner, F.; Forster-Tonigold, K.; Kim, J.; Adler, C.; Bansmann, J.; Groß, A.; Behm, R. J. Experimental and Computational Study on the Interaction of an Ionic Liquid Monolayer with Lithium on Pristine and Lithiated Graphite. *J. Phys. Chem. C* **2018**, *122* (33), 18968-18981.

131. Bozorgchenani, M.; Fischer, P.; Schnaidt, J.; Diemant, T.; Schwarz, R. M.; Marinaro, M.; Wachtler, M.; Jörissen, L.; Behm, R. J. Electrocatalytic Oxygen Reduction and Oxygen Evolution in Mg–Free and Mg–Containing Ionic Liquid 1-butyl–1–methylpyrrolidinium bis (trifluoromethanesulfonyl) imide. *ChemElectroChem* **2018**, *5* (18), 2600-2611.

132. Alwast, D.; Schnaidt, J.; Hancock, K.; Yetis, G.; Behm, R. J. Effect of Li^+ and Mg^{2+} on the Electrochemical Decomposition of the Ionic Liquid 1-butyl-1-methylpyrrolidinium bis (trifluoromethanesulfonyl) imide and Related Electrolytes. *ChemElectroChem* **2019**, *6* (12), 3009-3019.

133. Schnaidt, J.; Nguyen, T. L.; Jusys, Z.; Behm, R. J. How Many Electrons are Transferred During the Electrochemical O_2 Reduction in a Mg^{2+}-free/Mg^{2+}-containing Ionic Liquid? *Electrochim. Acta* **2019**, *299*, 372-377.

134. Jusys, Z.; Schnaidt, J.; Behm, R. J. O_2 Reduction on a Au Film Electrode in an Ionic Liquid in the Absence and Presence of Mg^{2+} Ions: Product Formation and Adlayer Dynamics. *J. Chem. Phys.* **2019**, *150* (4), 041724.

135. MacFarlane, D. R.; Meakin, P.; Sun, J.; Amini, N.; Forsyth, M. Pyrrolidinium Imides: A New Family of Molten Salts and Conductive Plastic Crystal Phases. *J. Phys. Chem. B* **1999**, *103* (20), 4164-4170.

136. Shamsipur, M.; Beigi, A. A. M.; Teymouri, M.; Pourmortazavi, S. M.; Irandoust, M. Physical and Electrochemical Properties of Ionic Liquids 1-ethyl-3-methylimidazolium tetrafluoroborate, 1-butyl-3-methylimidazolium trifluoromethanesulfonate and 1-butyl-1-methylpyrrolidinium bis (trifluoromethylsulfonyl) imide. *J. Mol. Liq.* **2010**, *157* (1), 43-50.

137. Uhl, B.; Huang, H.; Alwast, D.; Buchner, F.; Behm, R. J. Interaction of Ionic Liquids with Noble Metal Surfaces: Structure Formation and Stability of [OMIM][TFSA] and [EMIM][TFSA] on Au(111) and Ag(111). *Phys. Chem. Chem. Phys.* **2015,** *17* (37), 23816-23832.

138. Hausbrand, R.; Becker, D.; Jaegermann, W. A Surface Science Approach to Cathode|Electrolyte Interfaces in Li-Ion Batteries: Contact Properties, Charge Transfer and Reactions. *Progr. SolidStateChem.* **2014**, *42* (4), 175-183.

139. Heinze, J. Cyclic Voltammetry – "Electrochemical Spectroscopy". New Analytical Methods. *Angew. Chem. Int. Ed.* **1984**, *23* (11), 831-847.

140. Scholz, F. Voltammetric Techniques of Analysis: The Essentials. *ChemTexts* **2015**, *1* (4), 1-17.

141. Climent, V.; Feliu, J. M. Cyclic Voltammetry. In *Encyclopedia of Interfacial Chemistry*, Wandelt, K. Elsevier: Oxford, **2018**; pp 48-74.

142. Elgrishi, N.; Rountree, K. J.; McCarthy, B. D.; Rountree, E. S.; Eisenhart, T. T.; Dempsey, J. L. A Practical Beginner's Guide to Cyclic Voltammetry. *J. Chem. Educ.* **2017**, *95* (2), 197-206.

143. Bard, A. J.; Faulkner, L. R.; Leddy, J.; Zoski, C. G. *Electrochemical Methods: Fundamentals and Applications;* 2nd Ed.; John Wiley & Sons: New York, **1980**.

144. Smith, T. J.; Stevenson, K. J. Reference Electrodes. In *Handbook of Electrochemistry*, Elsevier: **2007**; pp 73-110.

145. Talaie, E.; Bonnick, P.; Sun, X.; Pang, Q.; Liang, X.; Nazar, L. F. Methods and Protocols for Electrochemical Energy Storage Materials Research. *Chem. Mater.* **2017**, *29* (1), 90-105.

146. Hui, J.; Gossage, Z. T.; Sarbapalli, D.; Hernández-Burgos, K.; Rodríguez-López, J. Advanced Electrochemical Analysis for Energy Storage Interfaces. *Anal. Chem.* **2018**, *91* (1), 60-83.

147. Moulder, J. F.; Stickle, W. F.; Sobol, P. E.; Bomben, K. D. *Handbook of X-ray Photoelectron Spectroscopy;* Perkin-Elmer Corp., Physical Electronics Division: Eden Prairie, MN, **1992**.

148. Leroy, S.; Blanchard, F.; Dedryvère, R.; Martinez, H.; Carre, B.; Lemordant, D.; Gonbeau, D. Surface Film Formation on a Graphite Electrode in Li–Ion Batteries: AFM and XPS Study. *Surf. Interface Anal.* **2005**, *37* (10), 773-781.

149. Lee, J. T.; Nitta, N.; Benson, J.; Magasinski, A.; Fuller, T. F.; Yushin, G. Comparative Study of the Solid Electrolyte Interphase on Graphite in Full Li-Ion Battery Cells Using X-ray Photoelectron Spectroscopy, Secondary Ion Mass Spectrometry, and Electron Microscopy. *Carbon* **2013**, *52*, 388-397.

150. Niehoff, P.; Passerini, S.; Winter, M. Interface Investigations of a Commercial Lithium Ion Battery Graphite Anode Material by Sputter Depth Profile X-ray Photoelectron Spectroscopy. *Langmuir* **2013**, *29* (19), 5806-5816.

151. Oswald, S. Binding Energy Referencing for XPS in Alkali Metal-Based Battery Materials Research (I): Basic Model Investigations. *Appl. Surf. Sci.* **2015**, *351*, 492-503.

152. Oswald, S.; Hoffmann, M.; Zier, M. Peak Position Differences Observed During XPS Sputter Depth Profiling of the SEI on Lithiated and Delithiated Carbon-Based Anode Material for Li-Ion Batteries. *Appl. Surf. Sci.* **2017**, *401*, 408-413.

153. Howlett, P. C.; Brack, N.; Hollenkamp, A. F.; Forsyth, M.; MacFarlane, D. R. Characterization of the Lithium Surface in N-methyl-N-alkylpyrrolidinium bis(trifluoromethanesulfonyl)amide Room-Temperature Ionic Liquid Electrolytes. *J. Electrochem. Soc.* **2006**, *153* (3), A595-A606.

154. Maibach, J.; Lindgren, F.; Eriksson, H.; Edström, K.; Hahlin, M. Electric Potential Gradient at the Buried Interface Between Lithium-Ion Battery Electrodes and the SEI Observed Using Photoelectron Spectroscopy. *J. Phys. Chem. Lett.* **2016**, *7* (10), 1775-1780.

155. Inaba, M.; Siroma, Z.; Funabiki, A.; Ogumi, Z.; Abe, T.; Mizutani, Y.; Asano, M. Electrochemical Scanning Tunneling Microscopy Observation of Highly Oriented Pyrolytic Graphite Surface Reactions in an Ethylene Carbonate-Based Electrolyte Solution. *Langmuir* **1996**, *12* (6), 1535-1540.

156. Inaba, M.; Siroma, Z.; Kawatate, Y.; Funabiki, A.; Ogumi, Z. Electrochemical Scanning Tunneling Microscopy Analysis of the Surface Reactions on Graphite Basal Plane in Ethylene Carbonate-Based Solvents and Propylene Carbonate. *J. Power Sources* **1997**, *68* (2), 221-226.

157. Funabiki, A.; Inaba, M.; Ogumi, Z. AC Impedance Analysis of Electrochemical Lithium Intercalation into Highly Oriented Pyrolytic Graphite. *J. Power Sources* **1997**, *68* (2), 227-231.

158. Bar-Tow, D.; Peled, E.; Burstein, L. A Study of Highly Oriented Pyrolytic Graphite as a Model for the Graphite Anode in Li–Ion Batteries. *J. Electrochem. Soc.* **1999**, *146* (3), 824-832.

159. Bozorgchenani, M.; Buchner, F.; Forster-Tonigold, K.; Kim, J.; Groß, A.; Behm, R. J. Adsorption of Ultrathin Ethylene Carbonate Films on Pristine and Lithiated Graphite and Their Interaction with Li. *Langmuir* **2018**, *34* (29), 8451-8463.

160. Jungblut, B.; Hoinkis, E. Diffusion of Lithium in Highly Oriented Pyrolytic Graphite at Low Concentrations and High Temperatures. *Phys. Rev. B* **1989**, *40* (16), 10810-10815.

161. Tran, T.; Kinoshita, K. Lithium Intercalation/Deintercalation Behavior of Basal and Edge Planes of Highly Oriented Pyrolytic Graphite and Graphite Powder. *J. Electroanal. Chem.* **1995**, *386* (1), 221-224.

162. Hitachi Hitachi Technology 2009 - 2010. Materials, Components & Others. **2010**; p 69.

163. Rapp, M.; Mundszinger, M.; Farsi, S.; Golla-Schindler, U.; Kaiser, U.; Wachtler, M. *Herstellung und Bewertung mechanisch gerundeter Graphie als Anodenmaterial für Lithium-Ionen-Batterien*; Apr 26, **2016**.

164. Rapp, M.; Mundszinger, M.; Farsi, S.; Golla-Schindler, U.; Kaiser, U.; Wachtler, M. Spheroidization of Graphite as Anode Material for Li-Ion Batteries: Spheroidization Process and Material Texture and Morphology **2016**; p 503.

165. Mundszinger, M.; Farsi, S.; Rapp, M.; Golla-Schindler, U.; Kaiser, U.; Wachtler, M. Morphology and Texture of Spheroidized Natural and Synthetic Graphites. *Carbon* **2017**, *111*, 764-773.

166. Weber, I.; Ingenmey, J.; Schnaidt, J.; Kirchner, B.; Behm, R. J. Influence of Complexing Additives on the Reversible Deposition / Dissolution of Magnesium in an Ionic Liquid. *ChemElectroChem* **2021**, *8 (2)*, 392-402.

167. Plimpton, S. Fast Parallel Algorithms for Short-Range Molecular Dynamics. *J. Comput. Phys.* **1995**, *117* (1), 1-19.

168. Jorgensen, W. L.; Maxwell, D. S.; Tirado-Rives, J. Development and Testing of the OPLS All-Atom Force Field on Conformational Energetics and Properties of Organic Liquids. *J. Am. Chem. Soc.* **1996**, *118* (45), 11225-11236.

169. Canongia Lopes, J. N.; Pádua, A. A. H. CL&P: A Generic and Systematic Force Field for Ionic Liquids Modeling. *Theor. Chem. Acc.* **2012**, *131* (3), 1129.

170. Brehm, M.; Kirchner, B. TRAVIS - A Free Analyzer and Visualizer for Monte Carlo and Molecular Dynamics Trajectories. *J. Chem. Inf. Model.* **2011**, *51* (8), 2007-2023.

171. Brehm, M.; Thomas, M.; Gehrke, S.; Kirchner, B. TRAVIS – A Free Analyzer For Trajectories From Molecular Simulation. *J. Chem. Phys.* **2020**, *152* (16), 164105.

172. Neese, F. The ORCA Program System. *WIREs Comput. Mol. Sci.* **2012**, *2* (1), 73-78.

173. Perdew, J. P. Density-Functional Approximation for the Correlation Energy of the Inhomogeneous Electron Gas. *Phys. Rev. B* **1986**, *33* (12), 8822-8824.

174. Becke, A. D. Density-Functional Exchange-Energy Approximation with Correct Asymptotic Behavior. *Phys. Rev. A* **1988**, *38* (6), 3098-3100.

175. Weigend, F.; Ahlrichs, R. Balanced Basis Sets of Split Valence, Triple Zeta Valence and Quadruple Zeta Valence Quality for H to Rn: Design and Assessment of Accuracy. *Phys. Chem. Chem. Phys.* **2005**, *7* (18), 3297-3305.

176. Grimme, S.; Antony, J.; Ehrlich, S.; Krieg, H. A Consistent and Accurate ab initioParametrization of Density Functional Dispersion Correction (DFT-D) For The 94 Elements H-Pu. *J. Chem. Phys.* **2010**, *132* (15), 154104.

177. Kruse, H.; Grimme, S. A Geometrical Correction for the Inter- and Intra-molecular Basis Set Superposition Error in Hartree-Fock and Density Functional Theory Calculations for Large Systems. *J. Chem. Phys.* **2012**, *136* (15), 154101.

178. Barone, V.; Cossi, M. Quantum Calculation of Molecular Energies and Energy Gradients in Solution by a Conductor Solvent Model. *J. Phys. Chem. A* **1998**, *102* (11), 1995-2001.

179. Huang, M. M.; Jiang, Y.; Sasisanker, P.; Driver, G. W.; Weingärtner, H. Static Relative Dielectric Permittivities of Ionic Liquids at 25 °C. *J. Chem. Eng. Data* **2011**, *56* (4), 1494-1499.

180. Pereiro, A. B.; Veiga, H. I. M.; Esperança, J. M. S. S.; Rodríguez, A. Effect of Temperature on the Physical Properties of Two Ionic Liquids. *J. Chem. Thermodyn.* **2009**, *41* (12), 1419-1423.

181. Borodin, O.; Behl, W.; Jow, T. R. Oxidative Stability and Initial Decomposition Reactions of Carbonate, Sulfone, and Alkyl Phosphate-Based Electrolytes. *J. Phys. Chem. C* **2013**, *117* (17), 8661-8682.

182. Qu, X.; Jain, A.; Rajput, N. N.; Cheng, L.; Zhang, Y.; Ong, S. P.; Brafman, M.; Maginn, E.; Curtiss, L. A.; Persson, K. A. The Electrolyte Genome Project: A Big Data Approach in Battery Materials Discovery. *Compu. Mater. Sci.* **2015**, *103*, 56-67.

183. Kazemiabnavi, S.; Zhang, Z.; Thornton, K.; Banerjee, S. Electrochemical Stability Window of Imidazolium-Based Ionic Liquids as Electrolytes for Lithium Batteries. *J. Phys. Chem. B* **2016**, *120* (25), 5691-5702.

184. Peljo, P.; Girault, H. H. Electrochemical Potential Window of Battery Electrolytes: The HOMO–LUMO Misconception. *Energy Environ. Sci.* **2018**, *11* (9), 2306-2309.

185. Weber, I.; Schnaidt, J.; Wang, B.; Diemant, T.; Behm, R. J. Model Studies on the Solid Electrolyte Interphase Formation on Graphite Electrodes in Ethylene Carbonate and Dimethyl Carbonate: Highly Oriented Pyrolytic Graphite. *ChemElectroChem* **2019**, *6*, 4977-4985.

186. Bruce, P. G.; Scrosati, B.; Tarascon, J. M. Nanomaterials for Rechargeable Lithium Batteries. *Angew. Chem. Int. Ed.* **2008**, *47* (16), 2930-2946.

187. Novák, P.; Panitz, J. C.; Joho, F.; Lanz, M.; Imhof, R.; Coluccia, M. Advanced In Situ Methods for the Characterization of Practical Electrodes in Lithium-Ion Batteries. *J. Power Sources* **2000**, *90* (1), 52-58.

188. Novák, P.; Joho, F.; Lanz, M.; Rykart, B.; Panitz, J. C.; Alliata, D.; Kötz, R.; Haas, O. The Complex Electrochemistry of Graphite Electrodes in Lithium-Ion Batteries. *J. Power Sources* **2001**, *97-98*, 39-46.

189. Peled, E.; Menkin, S. Review – SEI: Past, Present and Future. *J. Electrochem. Soc.* **2017**, *164* (7), A1703-A1719.

190. Wang, L.; Deng, X.; Dai, P. X.; Guo, Y. G.; Wang, D.; Wan, L. J. Initial Solid Electrolyte Interphase Formation Process of Graphite Anode in $LiPF_6$ Electrolyte: An In Situ EC-STM Investigation. *Phys. Chem. Chem. Phys.* **2012**, *14* (20), 7330-7336.

191. Kranz, T.; Kranz, S.; Miß, V.; Schepp, J.; Roling, B. Interrelation Between Redox Molecule Transport and Li^+ Ion Transport Across a Model Solid Electrolyte Interphase Grown on a Glassy Carbon Electrode. *J. Electrochem. Soc.* **2017**, *164* (14), A3777-A3784.

192. Cresce, A.; Russell, S. M.; Baker, D. R.; Gaskell, K. J.; Xu, K. In Situ and Quantitative Characterization of Solid Electrolyte Interphases. *Nano Lett.* **2014**, *14* (3), 1405-1412.

193. Aurbach, D.; Gnanaraj, J. S.; Levi, M. D.; Levi, E. A.; Fischer, J. E.; Claye, A. On the Correlation Among Surface Chemistry, 3D Structure, Morphology, Electrochemical and Impedance Behavior of Various Lithiated Carbon Electrodes. *J. Power Sources* **2001**, *97-98*, 92-96.

194. Aurbach, D.; Daroux, M.; Faguy, P.; Yeager, E. The Electrochemistry of Noble Metal Electrodes in Aprotic Organic Solvents Containing Lithium Salts. *J. Electroanal. Chem.* **1991**, *297* (1), 225-244.

195. Wagner, M. R.; Albering, J. H.; Moeller, K. C.; Besenhard, J. O.; Winter, M. XRD Evidence for the Electrochemical Formation of $Li^+(PC)_yC_n^-$ in PC-Based Electrolytes. *Electrochem. Commun.* **2005**, *7* (9), 947-952.

196. Chung, G. C.; Kim, H. J.; Yu, S. I.; Jun, S. H.; Choi, J. W.; Im, M. H. Origin of Graphite Exfoliation - An Investigation of the Important Role of Solvent Cointercalation. *J. Electrochem. Soc.* **2000**, *147* (12), 4391-4398.

197. Ensling, D.; Stjerndahl, M.; Nytén, A.; Gustafsson, T.; Thomas, J. O. A Comparative XPS Surface Study of Li_2FeSiO_4/C Cycled with LiTFSI-and $LiPF_6$-Based Electrolytes. *J. Mater. Chem.* **2009**, *19* (1), 82-88.

198. Xiao, A.; Yang, L.; Lucht, B. L.; Kang, S. H.; Abraham, D. P. Examining the Solid Electrolyte Interphase on Binder-Free Graphite Electrodes. *J. Electrochem. Soc.* **2009**, *156* (4), A318-A327.

199. Rendek, L. J.; Chottiner, G. S.; Scherson, D. A. The Reactivity of Linear Alkyl Carbonates Toward Metallic Lithium: X-ray Photoelectron Spectroscopy Studies in Ultrahigh Vacuum. *J. Electrochem. Soc.* **2002**, *149* (10), E408-E412.

200. Dedryvère, R.; Leroy, S.; Martinez, H.; Blanchard, F.; Lemordant, D.; Gonbeau, D. XPS Valence Characterization of Lithium Salts as a Tool to Study Electrode|Electrolyte Interfaces of Li-Ion Batteries. *J. Phys. Chem. B* **2006**, *110* (26), 12986-12992.

201. Zhuang, G. V.; Chen, Y.; Ross, P. N. The Reaction of Lithium with Dimethyl Carbonate and Diethyl Carbonate in Ultrahigh Vacuum Studied by X-ray Photoemission Spectroscopy. *Langmuir* **1999**, *15* (4), 1470-1479.

202. Weber, I.; Wang, B.; Bodirsky, C.; Chakraborty, M.; Wachtler, M.; Diemant, T.; Schnaidt, J.; Behm, R. J. Model Studies on Solid Electrolyte Interphase Formation on Graphite Electrodes in Ethylene Carbonate and Dimethyl Carbonate II: Graphite Powder Electrodes. *ChemElectroChem* **2020**, *7* (23), 4794-4809.

203. Massé, R. C.; Liu, C.; Li, Y.; Mai, L.; Cao, G. Energy Storage Through Intercalation Reactions: Electrodes for Rechargeable Batteries. *Natl. Sci. Rev.* **2017**, *4* (1), 26-53.

204. Jeong, S. K.; Inaba, M.; Mogi, R.; Iriyama, Y.; Abe, T.; Ogumi, Z. Surface Film Formation on a Graphite Negative Electrode in Lithium-Ion Batteries: Atomic Force Microscopy Study on the Effects of Film-Forming Additives in Propylene Carbonate Solutions. *Langmuir* **2001**, *17* (26), 8281-8286.

205. Zhang, J.; Yao, X.; Misra, R. K.; Cai, Q.; Zhao, Y. Progress in Electrolytes for Beyond-Lithium-Ion Batteries. *J. Mater. Sci. Technol.* **2020**, *44*, 237-257.

206. Selva Roselin, L.; Juang, R.-S.; Hsieh, C.-T.; Sagadevan, S.; Umar, A.; Selvin, R.; Hegazy, H. H. Recent Advances and Perspectives of Carbon-Based Nanostructures as Anode Materials for Li-Ion Batteries. *Materials* **2019**, *12* (8), 1229.

207. Xu, K.; von Cresce, A. Interfacing Electrolytes with Electrodes in Li-Ion Batteries. *J. Mater. Chem.* **2011**, *21* (27), 9849-9864.

208. Antonopoulos, B. K.; Maglia, F.; Schmidt-Stein, F.; Hoster, H. E.; Schmidt, J. P. Formation of the Solid Electrolyte Interphase at Constant Potentials: A Model Study on Highly Oriented Pyrolytic Graphite. *Batter. Supercaps* **2018**, *1* (3), 110-121.

209. Gossage, Z. T.; Hui, J.; Zeng, Y.; Flores-Zuleta, H.; Rodríguez-López, J. Probing the Reversibility and Kinetics of Li^+ During SEI Formation and (De)Intercalation on Edge Plane Graphite using Ion-Sensitive Scanning Electrochemical Microscopy. *J. Chem. Sci.* **2019**, *10* (46), 10749-10754.

210. Persson, K.; Sethuraman, V. A.; Hardwick, L. J.; Hinuma, Y.; Meng, Y. S.; van der Ven, A.; Srinivasan, V.; Kostecki, R.; Ceder, G. Lithium Diffusion in Graphitic Carbon. *J. Phys. Chem. Lett.* **2010**, *1* (8), 1176-1180.

211. Kang, S. H.; Abraham, D. P.; Xiao, A.; Lucht, B. L. Investigating the Solid Electrolyte Interphase Using Binder-Free Graphite Electrodes. *J. Power Sources* **2008**, *175* (1), 526-532.

212. Spahr, M. E.; Buqa, H.; Würsig, A.; Goers, D.; Hardwick, L.; Novák, P.; Krumeich, F.; Dentzer, J.; Vix-Guterl, C. Surface Reactivity of Graphite Materials and their Surface Passivation During the First Electrochemical Lithium Insertion. *J. Power Sources* **2006**, *153* (2), 300-311.

213. Novák, P.; Ufheil, J.; Buqa, H.; Krumeich, F.; Spahr, M. E.; Goers, D.; Wilhelm, H.; Dentzer, J.; Gadiou, R.; Vix-Guterl, C. The Importance of the Active Surface Area of Graphite Materials in the First Lithium Intercalation. *J. Power Sources* **2007**, *174* (2), 1082-1085.

214. Tang, M.; Lu, S.; Newman, J. Experimental and Theoretical Investigation of Solid Electrolyte Interphase Formation Mechanisms on Glassy Carbon. *J. Electrochem. Soc* **2012**, *159* (11), A1775.

215. Horstmann, B.; Single, F.; Latz, A. Review on Multi-Scale Models of Solid Electrolyte Interphase Formation. *Curr. Op. Electrochem.* **2019**, *13*, 61-69.

216. Ryu, G. Y.; Pyun, S. I. Passivation Kinetics of Surface Films Formed on Graphite Electrode in Organic Lithium Salt Solution as Function of Salt Anion Type. *J. Electroanal. Chem*. **1997**, *433 (1-2),* 97-105.

217. Dedryvère, R.; Martinez, H.; Leroy, S.; Lemordant, D.; Bonhomme, F.; Biensan, P.; Gonbeau, D. Surface Film Formation on Electrodes in a $LiCoO_2$/Graphite Cell: A Step by Step XPS Study. *J. Power Sources* **2007**, *174* (2), 462-468.

218. Wang, A.; Kadam, S.; Li, H.; Shi, S.; Qi, Y. Review on Modeling of the Anode Solid Electrolyte Interphase (SEI) for Lithium-Ion Batteries. *npj Compu. Mater.* **2018**, *4* (1), 1-26.

219. Weber, I.; Kim, J.; Buchner, F.; Schnaidt, J.; Behm, R. J. Surface Science and Electrochemical Model Studies on the Interaction of Graphite and Li–Containing Ionic Liquid. *ChemSusChem* **2020**, *13* (10), 2589-2601.

220. Ishikawa, M.; Sugimoto, T.; Kikuta, M.; Ishiko, E.; Kono, M. Pure Ionic Liquid Electrolytes Compatible with a Graphitized Carbon Negative Electrode in Rechargeable Lithium-Ion Batteries. *J. Power Sources* **2006**, *162* (1), 658-662.

221. Liu, H.; Liu, Y.; Li, J. Ionic Liquids in Surface Electrochemistry. *Phys. Chem. Chem. Phys.* **2010**, *12* (8), 1685-1697.

222. Hapiot, P.; Lagrost, C. Electrochemical Reactivity in Room-Temperature Ionic Liquids. *Chem. Rev.* **2008**, *108* (7), 2238-2264.

223. Martha, S. K.; Markevich, E.; Burgel, V.; Salitra, G.; Zinigrad, E.; Markovsky, B.; Sclar, H.; Pramovich, Z.; Heik, O.; Aurbach, D.; Exnar, I.; Buqa, H.; Drezen, T.; Semrau, G.; Schmidt, M.; Kovacheva, D.; Saliyski, N. A Short Review on Surface Chemical Aspects of Li Batteries: A Key for a Good Performance. *J. Power Sources* **2009**, *189* (1), 288-296.

224. Lombardo, L.; Brutti, S.; Navarra, M. A.; Panero, S.; Reale, P. Mixtures of Ionic Liquid – Alkylcarbonates as Electrolytes for Safe Lithium-Ion Batteries. *J. Power Sources* **2013**, *227*, 8-14.

225. Di Leo, R. A.; Marschilok, A. C.; Takeuchi, K. J.; Takeuchi, E. S. Battery Electrolytes Based on Saturated Ring Ionic Liquids: Physical and Electrochemical Properties. *Electrochim. Acta* **2013**, *109*, 27-32.

226. Lahiri, A.; Schubert, T. J. S.; Iliev, B.; Endres, F. LiTFSI in 1-butyl-1-methylpyrrolidinium bis (fluorosulfonyl) amide: A Possible Electrolyte for Ionic Liquid Based Lithium Ion Batteries. *Phys. Chem. Chem. Phys.* **2015**, *17* (17), 11161-11164.

227. Buchner, F.; Bozorgchenani, M.; Uhl, B.; Farkhondeh, H.; Bansmann, J.; Behm, R. J. Reactive Interaction of (Sub-)Monolayers and Multilayers of the Ionic Liquid 1-butyl-1-methylpyrrolidinium bis(trifluoro-methylsulfonyl) imide with Coadsorbed Lithium on Cu(111). *J. Phys. Chem. C* **2015**, *119* (29), 16649-16659.

228. Buchner, F.; Forster-Tonigold, K.; Kim, J.; Bansmann, J.; Groß, A.; Behm, R. J. Interaction Between Li, Ultrathin Adsorbed Ionic Liquid Films, and CoO(111) Thin Films: A Model Study of the Solid|Electrolyte Interphase Formation. *Chem. Mater.* **2019**, *31* (15), 5537-5549.

229. Kim, J.; Weber, I.; Buchner, F.; Schnaidt, J.; Behm, R. J. Surface Chemistry and Electrochemistry of an Ionic Liquid and Lithium on $Li_4Ti_5O_{12}$(111) – A Model Study of the Anode|Electrolyte Interface. *J. Chem. Phys.* **2019**, *151* (13), 134704.

230. Howlett, P. C.; MacFarlane, D. R.; Hollenkamp, A. F. High Lithium Metal Cycling Efficiency in a Room-Temperature Ionic Liquid. *Electrochem. Solid-State Lett.* **2004**, *7* (5), A97-A101.

231. Howlett, P. C.; Izgorodina, E. I.; Forsyth, M.; MacFarlane, D. R. Electrochemistry at Negative Potentials in bis (trifluoromethanesulfonyl) amide Ionic Liquids. *Z. Phys. Chem.* **2006**, *220* (10), 1483-1498.

232. Randström, S.; Appetecchi, G. B.; Lagergren, C.; Moreno, A.; Passerini, S. The Influence of Air and its Components on the Cathodic Stability of N-butyl-N-methylpyrrolidinium bis(trifluoromethanesulfonyl)imide. *Electrochim. Acta* **2007**, *53* (4), 1837-1842.

233. Randström, S.; Montanino, M.; Appetecchi, G. B.; Lagergren, C.; Moreno, A.; Passerini, S. Effect of Water and Oxygen Traces on the Cathodic Stability of N-alkyl-N-methylpyrrolidinium bis(trifluoromethanesulfonyl)imide. *Electrochim. Acta* **2008**, *53* (22), 6397-6401.

234. Shi, Y.; Yan, H. J.; Wen, R.; Wan, L. J. Direct Visualization of Nucleation and Growth Processes of Solid Electrolyte Interphase Film Using In Situ Atomic force microscopy. *ACS Appl. Mater. Interfaces* **2017**, *9* (26), 22063-22067.

235. Baranchugov, V.; Markevich, E.; Salitra, G.; Aurbach, D.; Semrau, G.; Schmidt, M. A. In Situ Raman Spectroscopy Study of Different Kinds of Graphite Electrodes in Ionic Liquid Electrolytes. *J. Electrochem. Soc.* **2008**, *155* (3), A217-A227.

236. O'Mahony, A. M.; Silvester, D. S.; Aldous, L.; Hardacre, C.; Compton, R. G. Effect of Water on the Electrochemical Window and Potential Limits of Room-Temperature Ionic Liquids. *J. Chem. Eng. Data* **2008**, *53* (12), 2884-2891.

237. De Vos, N.; Maton, C.; Stevens, C. V. Electrochemical Stability of Ionic Liquids: General Influences and Degradation Mechanisms. *ChemElectroChem* **2014**, *1* (8), 1258-1270.

238. Tulodziecki, M.; Tarascon, J. M.; Taberna, P. L.; Guéry, C. Catalytic Reduction of TFSI-Containing Ionic Liquid in the Presence of Lithium Cations. *Electrochem. Commun.* **2017**, *77*, 128-132.

239. Hu, X.; Chen, C.; Yan, J.; Mao, B. Electrochemical and In Situ Scanning Tunneling Microscopy Studies of bis(fluorosulfonyl)imide and bis(trifluoromethanesulfonyl)imide-Based Ionic Liquids on Graphite and Gold Electrodes and Lithium Salt Influence. *J. Power Sources* **2015**, *293*, 187-195.

240. Appetecchi, G. B.; Montanino, M.; Balducci, A.; Lux, S. F.; Winter, M.; Passerini, S. Lithium Insertion in Graphite from Ternary Ionic Liquid-Lithium Salt Electrolytes I: Electrochemical Characterization of the Electrolytes. *J. Power Sources* **2009**, *192* (2), 599-605.

241. Gasparotto, L. H. S.; Borisenko, N.; Bocchi, N.; El Abedin, S. Z.; Endres, F. In situ STM Investigation of the Lithium Underpotential Deposition on Au(111) in the Air-and Water-Stable Ionic Liquid 1-butyl-1-methylpyrrolidinium bis (trifluoromethylsulfonyl) amide. *Phys. Chem. Chem. Phys.* **2009**, *11* (47), 11140-11145.

242. Markevich, E.; Baranchugov, V.; Salitra, G.; Aurbach, D.; Schmidt, M. A. Behavior of Graphite Electrodes in Solutions Based on Ionic Liquids in In Situ Raman Studies. *J. Electrochem. Soc.* **2008**, *155* (2), A132-A137.

243. Markevich, E.; Sharabi, R.; Borgel, V.; Gottlieb, H.; Salitra, G.; Aurbach, D.; Semrau, G.; Schmidt, M. A. *In Situ* FTIR Study of the Decomposition of N-butyl-N-methylpyrrolidinium bis(trifluoromethanesulfonyl)amide Ionic Liquid During Cathodic Polarization of Lithium and Graphite Electrodes. *Electrochim. Acta* **2010**, *55* (8), 2687-2696.

244. Nádherná, M.; Reiter, J.; Moskon, J.; Dominko, R. Lithium bis(fluorosulfonyl)imide–PYR_{14}TFSI Ionic Liquid Electrolyte Compatible with Graphite. *J. Power Sources* **2011**, *196* (18), 7700-7706.

245. Zheng, H.; Jiang, K.; Abe, T.; Ogumi, Z. Electrochemical Intercalation of Lithium into a Natural Graphite Anode in Quaternary Ammonium-Based Ionic Liquid Electrolytes. *Carbon* **2006**, *44* (2), 203-210.

246. Cremer, T.; Stark, M.; Deyko, A.; Steinrück, H. P.; Maier, F. Liquid|Solid Interface of Ultrathin Ionic Liquid Films: $[C_1C_1Im][Tf_2N]$ and $[C_8C_1Im][Tf_2N]$ on Au(111). *Langmuir* **2011**, *27* (7), 3662-3671.

247. Ando, Y.; Kawamura, Y.; Ikeshoji, T.; Otani, M. Electrochemical Reduction of an Anion for Ionic Liquid Molecules on a Lithium Electrode Studied by First-Principles Calculations. *Chem. Phys. Lett.* **2014**, *612*, 240-244.

248. Xu, C.; Sun, B.; Gustafsson, T.; Edström, K.; Brandell, D.; Hahlin, M. Interface Layer Formation in Solid Polymer Electrolyte Lithium Batteries: An XPS Study. *J. Mater. Chem. A* **2014**, *2* (20), 7256-7264.

249. Park, K.; Yu, B.-C.; Goodenough, J. B. Li_3N as a Cathode Additive for High–Energy–Density Lithium–Ion Batteries. *Adv. Energy Mater.* **2016**, *6* (10), 1502534.

250. Olschewski, M.; Gustus, R.; Marschewski, M.; Höfft, O.; Endres, F. Spectroscopic Characterization of the Interaction of Lithium with Thin Films of the Ionic Liquid 1-octyl-3-methylimidazolium bis (trifluoromethylsulfonyl) amide. *Phys. Chem. Chem. Phys.* **2014**, *16* (47), 25969-25977.

251. MacFarlane, D. R.; Pringle, J. M.; Howlett, P. C.; Forsyth, M. Ionic Liquids and Reactions at the Electrochemical Interface. *Phys. Chem. Chem. Phys.* **2010**, *12* (8), 1659-1669.

252. Yamagata, M.; Nishigaki, N.; Nishishita, S.; Matsui, Y.; Sugimoto, T.; Kikuta, M.; Higashizaki, T.; Kono, M.; Ishikawa, M. Charge–Discharge Behavior of Graphite Negative Electrodes in bis(fluorosulfonyl)imide-Based Ionic Liquid and Structural Aspects of their Electrode|Electrolyte Interfaces. *Electrochim. Acta* **2013**, *110*, 181-190.

253. Giffin, G. A.; Moretti, A.; Jeong, S.; Passerini, S. Complex Nature of Ionic Coordination in Magnesium Ionic Liquid-Based Electrolytes: Solvates with Mobile Mg^{2+} Cations. *J. Phys. Chem. C* **2014**, *118* (19), 9966-9973.

254. Lahiri, A.; Carstens, T.; Atkin, R.; Borisenko, N.; Endres, F. In Situ Atomic Force Microscopic Studies of the Interfacial Multilayer Nanostructure of LiTFSI–$[Py_{1,4}]$ TFSI on Au(111): Influence of Li^+ Ion Concentration on the Au(111)|IL Interface. *J. Phys. Chem. C* **2015**, *119* (29), 16734-16742.

255. Rajput, N. N.; Seguin, T. J.; Wood, B. M.; Qu, X.; Persson, K. A. Elucidating Solvation Structures for Rational Design of Multivalent Electrolytes − A Review. In *Modeling Electrochemical Energy Storage at the Atomic Scale. Topics in Current Chemistry Collections*, Korth, M. Springer International Publishing: Cham, **2018**; pp 79-124.

256. Lu, Z.; Schechter, A.; Moshkovich, M.; Aurbach, D. On the Electrochemical Behavior of Magnesium Electrodes in Polar Aprotic Electrolyte Solutions. *J. Electroanal. Chem.* **1999**, *466* (2), 203-217.

257. Arthur, T. S.; Glans, P. A.; Singh, N.; Tutusaus, O.; Nie, K.; Liu, Y. S.; Mizuno, F.; Guo, J.; Alsem, D. H.; Salmon, N. J.; Mohtadi, R. Interfacial Insight from Operando XAS/TEM for Magnesium Metal Deposition with Borohydride Electrolytes. *Chem. Mater.* **2017**, *29* (17), 7183-7188.

258. Gao, T.; Hou, S.; Huynh, K.; Wang, F.; Eidson, N.; Fan, X.; Han, F.; Luo, C.; Mao, M.; Li, X. Existence of Solid Electrolyte Interphase in Mg Batteries: Mg/S Chemistry as an Example. *ACS Appl. Mater. Interfaces* **2018**, *10* (17), 14767-14776.

259. Lv, R.; Guan, X.; Zhang, J.; Xia, Y.; Luo, J. Enabling Mg Metal Anodes Rechargeable in Conventional Electrolytes by Fast Ionic Transport Interphase. *Natl. Sci. Rev.* **2019**, *7* (2), 333-341.

260. Connor, J. H.; Reid, W. E.; Wood, G. B. Electrodeposition of Metals from Organic Solutions: V. Electrodeposition of Magnesium and Magnesium Alloys. *J. Electrochem. Soc.* **1957**, *104* (1), 38-41.

261. Shao, Y.; Liu, T.; Li, G.; Gu, M.; Nie, Z.; Engelhard, M.; Xiao, J.; Lv, D.; Wang, C.; Zhang, J. G.; Liu, J. Coordination Chemistry in Magnesium Battery Electrolytes: How Ligands Affect Their Performance. *Sci. Rep.* **2013**, *3*, 3130.

262. Kar, M.; Ma, Z.; Azofra, L. M.; Chen, K.; Forsyth, M.; MacFarlane, D. R. Ionic Liquid Electrolytes for Reversible Magnesium Electrochemistry. *Chem. Commun.* **2016**, *52* (21), 4033-4036.

263. Ma, Z.; MacFarlane, D. R.; Kar, M. Mg Cathode Materials and Electrolytes for Rechargeable Mg Batteries: A Review. *Batter. Supercaps* **2019**, *2* (2), 115-127.

264. Tuerxun, F.; Yamamoto, K.; Hattori, M.; Mandai, T.; Nakanishi, K.; Choudhary, A.; Tateyama, Y.; Sodeyama, K.; Nakao, A.; Uchiyama, T.; Matsui, M.; Tsuruta, K.; Tamenori, Y.; Kanamura, K.;

Uchimoto, Y. Determining Factor on the Polarization Behavior of Magnesium Deposition for Magnesium Battery Anode. *ACS Appl. Mater. Interfaces* **2020**, *12* (23), 25775-25785.

265. Ha, S. Y.; Lee, Y. W.; Woo, S. W.; Koo, B.; Kim, J. S.; Cho, J.; Lee, K. T.; Choi, N. S. Magnesium(II) bis(trifluoromethanesulfonyl) imide-Based Electrolytes with Wide Electrochemical Windows for Rechargeable Magnesium Batteries. *ACS Appl. Mater. Interfaces* **2014**, *6* (6), 4063-4073.

266. Barile, C. J.; Spatney, R.; Zavadil, K. R.; Gewirth, A. A. Investigating the Reversibility of *In Situ* Generated Magnesium Organohaloaluminates for Magnesium Deposition and Dissolution. *J. Phys. Chem. C* **2014**, *118* (20), 10694-10699.

267. Fukutsuka, T.; Asaka, K.; Inoo, A.; Yasui, R.; Miyazaki, K.; Abe, T.; Nishio, K.; Uchimoto, Y. New Magnesium-Ion Conductive Electrolyte Solution Based on Triglyme for Reversible Magnesium Metal Deposition and Dissolution at Ambient Temperature. *Chem. Lett.* **2014**, *43* (11), 1788-1790.

268. Sa, N.; Rajput, N. N.; Wang, H.; Key, B.; Ferrandon, M.; Srinivasan, V.; Persson, K. A.; Burrell, A. K.; Vaughey, J. T. Concentration Dependent Electrochemical Properties and Structural Analysis of a Simple Magnesium Electrolyte: Magnesium bis (trifluoromethane sulfonyl) imide in diglyme. *RSC Adv.* **2016**, *6* (114), 113663-113670.

269. Terada, S.; Mandai, T.; Suzuki, S.; Tsuzuki, S.; Watanabe, K.; Kamei, Y.; Ueno, K.; Dokko, K.; Watanabe, M. Thermal and Electrochemical Stability of tetraglyme–magnesium bis(trifluoromethanesulfonyl)amide Complex: Electric Field Effect of Divalent Cation on Solvate Stability. *J. Phys. Chem. C* **2016**, *120* (3), 1353-1365.

270. Hebié, S.; Alloin, F.; Iojoiu, C.; Berthelot, R.; Leprêtre, J. C. Magnesium Anthracene System-Based Electrolyte as a Promoter of High Electrochemical Performance Rechargeable Magnesium Batteries. *ACS Appl. Mater. Interfaces* **2018**, *10* (6), 5527-5533.

271. Kang, S. J.; Kim, H.; Hwang, S.; Jo, M.; Jang, M.; Park, C.; Hong, S. T.; Lee, H. Electrolyte Additive Enabling Conditioning-Free Electrolytes for Magnesium Batteries. *ACS Appl. Mater. Interfaces* **2018**, *11* (1), 517-524.

272. Rajput, N. N.; Qu, X.; Sa, N.; Burrell, A. K.; Persson, K. A. The Coupling Between Stability and Ion Pair Formation in Magnesium Electrolytes from First-Principles Quantum Mechanics and Classical Molecular Dynamics. *J. Am. Chem. Soc.* **2015**, *137* (9), 3411-3420.

273. Lodovico, L.; Martins, V. L.; Benedetti, T. M.; Torresi, R. M. Electrochemical Behavior of Iron and Magnesium in Ionic Liquids. *J. Braz. Chem. Soc.* **2014**, *25* (3), 460-468.

274. Ma, Z.; Kar, M.; Xiao, C.; Forsyth, M.; MacFarlane, D. R. Electrochemical Cycling of Mg in $Mg[TFSI]_2$/tetraglyme Electrolytes. *Electrochem. Commun.* **2017**, *78*, 29-32.

275. Su, S.; NuLi, Y.; Wang, N.; Yusipu, D.; Yang, J.; Wang, J. L. Magnesium Borohydride-Based Electrolytes Containing 1-butyl-1-methylpiperidinium bis (trifluoromethyl sulfonyl) imide Ionic Liquid for Rechargeable Magnesium Batteries. *J. Electrochem. Soc.* **2016**, *163* (13), D682-D688.

276. Kuwata, H.; Matsui, M.; Imanishi, N. Passivation Layer Formation of Magnesium Metal Negative Electrodes for Rechargeable Magnesium Batteries. *J. Electrochem. Soc* **2017**, *164* (13), A3229-A3236.

277. Hu, J. Z.; Jaegers, N. R.; Chen, Y.; Han, K. S.; Wang, H.; Murugesan, V.; Mueller, K. T. Adsorption and Thermal Decomposition of Electrolytes on Nanometer Magnesium Oxide: An *In Situ* ^{13}C MAS NMR Study. *ACS Appl. Mater. Interfaces* **2019**, *11* (42), 38689-38696.

278. Mandai, T.; Tatesaka, K.; Soh, K.; Masu, H.; Choudhary, A.; Tateyama, Y.; Ise, R.; Imai, H.; Takeguchi, T.; Kanamura, K. Modifications in Coordination Structure of $Mg[TFSA]_2$-Based Supporting Salts for High-Voltage Magnesium Rechargeable Batteries. *Phys. Chem. Chem. Phys.* **2019**, *21* (23), 12100-12111.

279. Seguin, T. J.; Hahn, N. T.; Zavadil, K. R.; Persson, K. A. Elucidating Non-Aqueous Solvent Stability and Associated Decomposition Mechanisms for Mg Energy Storage Applications From First-Principles. *Front. Chem.* **2019**, *7*, 175.

280. Pedersen, C. J.; Frensdorff, H. K. Macrocyclic Polyethers and Their Complexes. *Angew. Chem. Int. Ed.* **1972**, *11* (1), 16-25.

281. Tuerxun, F.; Abulizi, Y.; NuLi, Y.; Su, S.; Yang, J.; Wang, J. L. High Concentration Magnesium Borohydride/tetraglyme Electrolyte for Rechargeable Magnesium Batteries. *J. Power Sources* **2015**, *276*, 255-261.

282. Canepa, P.; Gautam, G. S.; Malik, R.; Jayaraman, S.; Rong, Z.; Zavadil, K. R.; Persson, K.; Ceder, G. Understanding the Initial Stages of Reversible Mg Deposition and Stripping in Inorganic Nonaqueous Electrolytes. *Chem. Mater.* **2015**, *27* (9), 3317-3325.

283. Watkins, T.; Buttry, D. A. Determination of Mg^{2+} Speciation in a $TFSI^{-}$-Based Ionic Liquid with and without Chelating Ethers Using Raman Spectroscopy. *J. Phys. Chem. B* **2015**, *119* (23), 7003-7014.

284. Tutusaus, O.; Mohtadi, R.; Singh, N.; Arthur, T. S.; Mizuno, F. Study of Electrochemical Phenomena Observed at the Mg Metal|Electrolyte Interface. *ACS Energy Lett.* **2017**, *2* (1), 224-229.

285. Shao, Y.; Rajput, N. N.; Hu, J.; Hu, M.; Liu, T.; Wei, Z.; Gu, M.; Deng, X.; Xu, S.; Han, K. S.; Wang, J.-L.; Nie, Z.; Li, G.; Zavadil, K. R.; Xiao, J.; Wang, C.; Henderson, W. A.; Zhang, J. G.; Wang, Y.; Mueller, K. T.; Persson, K.; Liu, J. Nanocomposite Polymer Electrolyte for Rechargeable Magnesium Batteries. *Nano Energy* **2015**, *12*, 750-759.

286. Kitada, A.; Kang, Y.; Uchimoto, Y.; Murase, K. Room-Temperature Electrodeposition of Mg Metal from Amide Salts Dissolved in Glyme-Ionic Liquid Mixture. *J. Electrochem. Soc.* **2013**, *161* (3), D102-D106.

287. Matsui, M. Study on Electrochemically Deposited Mg Metal. *J. Power Sources* **2011**, *196* (16), 7048-7055.

288. Jankowski, P.; García Lastra, J. M.; Vegge, T. Structure of Magnesium Chloride Complexes in Ethereal Systems: Computational Comparison of THF and Glymes as Solvents for Magnesium Battery Electrolytes. *Batter. Supercaps* **2020**, *3 (12)* 1350-1359.

289. Samuel, D.; Steinhauser, C.; Smith, J. G.; Kaufman, A.; Radin, M. D.; Naruse, J.; Hiramatsu, H.; Siegel, D. J. Ion Pairing and Diffusion in Magnesium Electrolytes Based on Magnesium Borohydride. *ACS Appl. Mater. Interfaces* **2017**, *9* (50), 43755-43766.

290. Deetz, J. D.; Cao, F.; Wang, Q.; Sun, H. Exploring the Liquid Structure and Ion Formation in Magnesium Borohydride Electrolyte Using Density Functional Theory. *J. Electrochem. Soc.* **2018**, *165* (2), A61-A70.

291. Hu, J. Z.; Rajput, N. N.; Wan, C.; Shao, Y.; Deng, X.; Jaegers, N. R.; Hu, M.; Chen, Y.; Shin, Y.; Monk, J.; Chen, Z.; Qin, Z.; Mueller, K. T.; Liu, J.; Persson, K. A. ^{25}Mg NMR and Computational Modeling Studies of the Solvation Structures and Molecular Dynamics in Magnesium-Based Liquid Electrolytes. *Nano Energy* **2018**, *46*, 436-446.

292. Yu, Y.; Baskin, A.; Valero-Vidal, C.; Hahn, N. T.; Liu, Q.; Zavadil, K. R.; Eichhorn, B. W.; Prendergast, D.; Crumlin, E. J. Instability at the Electrode|Electrolyte Interface Induced by Hard Cation Chelation and Nucleophilic Attack. *Chem. Mater.* **2017**, *29* (19), 8504-8512.

293. Ta, K.; See, K. A.; Gewirth, A. A. Elucidating Zn and Mg Electrodeposition Mechanisms in Nonaqueous Electrolytes for Next-Generation Metal Batteries. *J. Phys. Chem. C* **2018**, *122* (25), 13790-13796.

10. Appendix

10.1. Data Acquisition Index

Table 10-1. List of figures (Fig.) appearing in the chapters (Ch.) of this work, along with the substrates (subst.) and solvent / salt (electrolyte) mixtures used, the type of data displayed (CV, XPS, accumulated charge (AC), SEM, TEM), the date of measurement (DoM) and the corresponding Origin files.

Ch.	Fig.	Subst.	Electrolyte	Data Type	DoM	File
3	3-1a	HOPG	EC + $LiPF_6$	CV	15.01.16	Thesis_IW_Ch3_Fig3-1
	3-1b	HOPG	DMC + $LiPF_6$	CV	05.07.16	
	3-2a-c	HOPG	EC + $LiPF_6$	CV	15.01.16, 20.11.15, 18.11.15	Thesis_IW_Ch3_Fig3-2
	3-2d-f	HOPG	DMC + $LiPF_6$	CV	05.07.16, 21.10.16, 04.08.16	
	3-3a	HOPG	EC + $LiPF_6$	CV	20.11.15, 13.05.16	Thesis_IW_Ch3_Fig3-3
	3-3b	HOPG	DMC + $LiPF_6$	CV	21.10.16, 07.06.18	
	3-4	HOPG	EC + $LiPF_6$ / DMC + $LiPF_6$	XPS	10.02.16, 05.08.16, 19.01.16, 18.08.16	Thesis_IW_Ch3_Fig3-4
	3-5a	HOPG	EC + $LiPF_6$	XPS	19.01.16, 10.02.16	Thesis_IW_Ch3_Fig3-5+3-6
	3-5b	HOPG	DMC + $LiPF_6$	XPS	22.07.16, 05.08.16	
	3-6a	HOPG	EC + $LiPF_6$	XPS	19.01.16, 10.02.16	
	3-6b	HOPG	DMC + $LiPF_6$	XPS	22.07.16, 05.08.16	
	3-7	HOPG	EC + $LiPF_6$ / DMC + $LiPF_6$	XPS	10.02.16, 05.08.16, 19.01.16, 18.08.16	Thesis_IW_Ch3_Fig3-7
	S3-1	HOPG		SEM	05.07.19	
	S3-2	HOPG	DMC + $LiPF_6$	CV	04.08.16, 15.08.16	Thesis_IW_Ch3_FigS3-2

Ch.	Fig.	Subst.	Electrolyte	Data Type	DoM	File
	S3-3a	HOPG	EC + $LiPF_6$	CV	15.11.16, 27.11.15, 18.11.15	Thesis_IW_Ch3_FigS3-3
	S3-3b	HOPG	DMC + $LiPF_6$	CV	05.07.16, 21.10.16, 04.08.16	
	S3-4a	HOPG	EC + $LiPF_6$	XPS	19.01.16, 10.02.16	Thesis_IW_Ch3_FigS3-4+3-5
	S3-4b	HOPG	DMC + $LiPF_6$	XPS	22.07.16, 05.08.16	
	S3-5a	HOPG	EC + $LiPF_6$	XPS	19.01.16, 10.02.16	
	S3-5b	HOPG	DMC + $LiPF_6$	XPS	22.07.16, 05.08.16	
	S3-6	HOPG	EC + $LiPF_6$	XPS	19.01.16	Thesis_IW_Ch3_FigS3-6
	S3-7	HOPG	DMC + $LiPF_6$	XPS	22.07.16	Thesis_IW_Ch3_FigS3-7
	S3-8a	HOPG	EC + $LiPF_6$	XPS	19.01.16	Thesis_IW_Ch3_FigS3-8
	S3-8b	HOPG	DMC + $LiPF_6$	XPS	22.07.16	
	S3-9	HOPG	EC + $LiPF_6$	XPS	10.02.16	Thesis_IW_Ch3_FigS3-9
	S3-10	HOPG	DMC + $LiPF_6$	XPS	05.08.16	Thesis_IW_Ch3_FigS3-10
	S3-11a	HOPG	EC + $LiPF_6$	XPS	10.02.16	Thesis_IW_Ch3_FigS-11
	S3-11b	HOPG	DMC + $LiPF_6$	XPS	05.08.16	
4	4-1	MAGE / SNG		TEM	09.03.17	
	4-2	MAGE/ SNG	EC + $LiPF_6$ / DMC + $LiPF_6$	CV	03.07.16, 29.08.16, 18.01.18, 03.03.17	Thesis_IW_Ch4_Fig4-2

Ch.	Fig.	Subst.	Electrolyte	Data Type	DoM	File
	4-3a	MAGE	EC + $LiPF_6$ / DMC + $LiPF_6$	CV	03.07.16, 22.06.16, 22.06.16, 29.08.16, 19.08.16, 10.08.16	Thesis_IW_Ch4_Fig4-3
	4-3b	SNG	EC + $LiPF_6$ / DMC + $LiPF_6$	CV	18.01.18, 17.08.16, 29.07.16, 03.03.17, 18.08.18, 17.04.18	
	4-4	MAGE, Mage + PVDF, SNG, SNG + PVDF	LP30	CV	21.08.16, 04.11.16, 18.08.16, 10.11.16	Thesis_IW_Ch4_Fig4-4
	4-5a	MAGE	EC + $LiPF_6$	XPS	22.03.19	Thesis_IW_Ch4_Fig4-5
	4-5b	SNG	EC + $LiPF_6$	XPS	22.02.17	
	4-6a	MAGE	EC + $LiPF_6$	XPS	22.03.19	Thesis_IW_Ch4_Fig4-6
	4-6b	SNG	EC + $LiPF_6$	XPS	22.02.17	
	4-7	MAGE / SNG	EC + $LiPF_6$	XPS	14.02.17, 22.03.19, 15.02.17, 22.02.17	Thesis_IW_Ch4_Fig4-7
	S4-1a, b	MAGE / SNG	EC + $LiPF_6$	CV	22.06.16, 27.05.16, 17.08.16, 29.07.16	Thesis_IW_Ch4_FigS4-1
	S4-1c, d	MAGE / SNG	DMC + $LiPF_6$	CV	28.07.16, 10.08.16, 20.04.18, 17.04.18	
	S4-2	MAGE / SNG + PVDF	LP30	CV	04.11.16, 10.11.16	Thesis_IW_Ch4_FigS4-2
	S4-3a	MAGE	EC + $LiPF_6$	XPS	05.08.16	Thesis_IW_Ch4_FigS4-3
	S4-3b	SNG	EC + $LiPF_6$	XPS	15.02.17	
	S4-4a	MAGE	EC + $LiPF_6$	XPS	05.08.16	Thesis_IW_Ch4_FigS4-4
	S4-4b	SNG	EC + $LiPF_6$	XPS	15.02.17	
	S4-5	MAGE	EC + $LiPF_6$	XPS	22.03.19	Thesis_IW_Ch4_FigS4-5
	S4-6	MAGE	EC + $LiPF_6$	XPS	22.03.19	Thesis_IW_Ch4_FigS4-6

Ch.	Fig.	Subst.	Electrolyte	Data Type	DoM	File
	S4-7	SNG	EC + $LiPF_6$	XPS	22.02.17	Thesis_IW_Ch4_FigS4-7
	S4-8	SNG	EC + $LiPF_6$	XPS	22.02.17	Thesis_IW_Ch4_FigS4-8
	S4-9	Mage	EC + $LiPF_6$	XPS	14.02.17	Thesis_IW_Ch4_FigS4-9+10
	S4-10	MAGE	EC + $LiPF_6$	XPS	14.02.17	
	S4-11	SNG	EC + $LiPF_6$	XPS	15.02.17	Thesis_IW_Ch4_FigS4-11+12
	S4-12	SNG	EC + $LiPF_6$	XPS	15.02.17	
5	5-1a, c	HOPG	BMP-TFSI + LiTFSI	CV	03.12.18, 26.10.18, 29.10.18	Thesis_IW_Ch5_Fig5-1
	5-1b, d	MAGE	BMP-TFSI + LiTFSI	CV	04.12.18, 02.03.18, 22.02.18	
	5-2	HOPG, MAGE	BMP-TFSI, BMP-TFSI + LiTFSI	CV	18.11.16, 03.12.18, 04.12.18	Thesis_IW_Ch5_Fig5-2
	5-3a	HOPG	BMP-TFSI Multilayers	XPS	23.03.16	Thesis_IW_Ch5_Fig5-3
	5-3b	HOPG	BMP-TFSI Multilayers + Li^0	XPS	23.03.16	
	5-3c		LiTFSI	XPS	04.05.18	
	5-3d	HOPG	BMP-TFSI + LiTFSI@OCP	XPS	10.04.18	
	5-3e	HOPG	BMP-TFSI + LiTFSI	XPS	17.01.18	
	5-3f	MAGE	BMP-TFSI + LiTFSI	XPS	05.12.18	
	5-4	HOPG	LiTFSI, BMP-TFSI + LiTFSI	XPS	04.05.18, 10.04.18	Thesis_IW_Ch5_Fig5-4
	5-5	HOPG, MAGE	BMP-TFSI + LiTFSI	XPS	17.01.18, 17.05.18	Thesis_IW_Ch5_Fig5-5
	S5-1	HOPG	BMP-TFSI + LiTFSI	CV	31.10.18, 12.03.18	Thesis_IW_Ch5_FigS5-1
	S5-2	HOPG	BMP-TFSI + LiTFSI	CV	26.10.18, 29.10.18	Thesis_IW_Ch5_FigS5-2
	S5-3	HOPG, MAGE	BMP-TFSI + LiTFSI	CV	02.03.18, 22.02.18	Thesis_IW_Ch5_FigS5-3
	S5-4	HOPG, MAGE	BMP-TFSI, BMP-TFSI + LiTFSI	XPS	23.03.16, 04.05.18, 10.04.18, 17.01.18, 05.12.18	Thesis_IW_Ch5_FigS5-4

Ch.	Fig.	Subst.	Electrolyte	Data Type	DoM	File
	S5-5	HOPG, MAGE	BMP-TFSI, BMP-TFSI + LiTFSI	XPS	23.03.16, 04.05.18, 10.04.18, 17.01.18, 05.12.18	Thesis_IW_Ch5_FigS5-5
6	6-1	GC	BMP-TFSI + $Mg(BH_4)_2$ + 18c6	CV	18.09.2019	Thesis_IW_Ch6_Fig6-1
	6-2	GC	BMP-TFSI + $Mg(BH_4)_2$ + $MgTFSI_2$ + 18c6	CV	14.08.19, 18.09.19, 13.08.19, 26.09.19	Thesis_IW_Ch6_Fig6-2
	6-3	Mg	BMP-TFSI + $Mg(BH_4)_2$ + 18c6	CV	22.07.19	Thesis_IW_Ch6_Fig6-3
	6-4	Original data of calculations and figures by J. Ingenmey, Mulliken Center of Theoretical Chemistry, Bonn University				
	6-5					
	6-6					
	6-7					
	S6-1	GC	BMP-TFSI + $Mg(BH_4)_2$	CV	07.06.19	Thesis_IW_Ch6_FigS6-1
	S6-2	GC	BMP-TFSI + a) Mg/$CaTFSI_2$, b) Mg/$Ca(BH_4)_2$, c) Mg/$CaTFSI_2$ + Mg/$Ca(BH_4)_2$, d) Mg/$CaTFSI_2$ + 18c6, e) Mg/$Ca(BH_4)_2$ + 18c6	CV	Mg: 07.06.19, 18.09.19, 26.02.20, 27.02.20, 12.03.20; Ca: 16.12.19, 19.12.19, 17.01.20, 28.02.20	Thesis_IW_Ch6_FigS6-2
	S6-3	GC	a) BMP-TFSI + $MgTFSI_2$ + $Mg(BH_4)_2$, b) BMP-TFSI + $CaTFSI_2$ + $Ca(BH_4)_2$, c) BMP-TFSI + $MgTFSI_2$ + xM 18c6	CV	Mg: 05.12.19, 09.12.19, 27.02.20 Ca: 14.01.20, 03.03.20	Thesis_IW_Ch6_FigS6-3
	S6-4	GC	BMP-TFSI + $Mg(BH_4)_2$	AC	07.06.19	Thesis_IW_Ch6_FigS6-4
	S6-5	GC	BMP-TFSI + $Mg(BH_4)_2$ + 18c6	AC	18.09.19	Thesis_IW_Ch6_FigS6-5

Ch.	Fig.	Subst.	Electrolyte	Data Type	DoM	File
	S6-6	GC	BMP-TFSI + $Mg(BH_4)_2$ + $MgTFSI_2$ + 18c6	AC	14.08.19	Thesis_IW_Ch6_FigS6-6
	S6-7	GC	BMP-TFSI + $Mg(BH_4)_2$ + $MgTFSI_2$ + 18c6	CV	26.09.19	Thesis_IW_Ch6_FigS6-7
	S6-8	Original data of calculations and figures by J. Ingenmey, Mulliken Center of Theoretical Chemistry, Bonn University				
	S6-9					
	S6-10					
	S6-11					
	S6-12					
	S6-13					
	S6-14					
	S6-15					

10.2. Curriculum Vitae

Die folgende Seite wurde aus Datenschutzgründen entfernt.

Die folgende Seite wurde aus Datenschutzgründen entfernt.

10.3. List of Publications

01/21 Weber, I.; Ingenmey, J.; Schnaidt, J.; Kirchner, B.; Behm, R.J.

Influence of Complexing Additives on the Reversible Deposition/Dissolution of Magnesium in an Ionic Liquid

ChemElectroChem, **2021**, *8 (2)*, 390-402. DOI: 10.1002/celc.202001488

10/20 Weber, I.; Wang, B.; Bodirsky, C.; Chakraborty, Wachtler, M.; M.; Diemant, T.; Schnaidt, J.; Behm, R.J.

Model Studies on the Solid Electrolyte Interphase Formation on Graphite Electrodes in Ethylene Carbonate and Dimethyl Carbonate II: Graphite Powder Electrodes

ChemElectroChem, **2020**, *7 (23)*, 4794-4809. DOI: 10.1002/celc.202001328

03/20 Weber, I.; Kim, J.; Buchner, F.; Schnaidt, J.; Behm, R.J.

Surface Science and Electrochemical Model Studies on the Interaction of Graphite and Li-Containing Ionic Liquid

ChemSusChem, **2020**, *13 (10)*, 2589-2601. DOI: 10.1002/cssc.202000495

09/19 Kim, J.; Weber, I.; Buchner, F.; Schnaidt, J.; Behm, R.J.

Surface Chemistry and Electrochemistry of an Ionic Liquid and Lithium on $Li_4Ti_5O_{12}$(111) – A Model Study of the Anode|Electrolyte Interface

J.Chem.Phys., **2019**, *151 (13)*, 134704. DOI: 10.1063/1.5119765

08/19 Weber, I.; Schnaidt, J.; Wang, B.; Diemant, T.; Behm, R.J.

Model Studies on the Solid Electrolyte Interphase Formation on Graphite Electrodes in Ethylene Carbonate and Dimethyl Carbonate I: Highly Oriented Pyrolytic Graphite

ChemElectroChem, **2019**, *6 (19)*, 4977-4985. DOI: 10.1002/celc.201900909

11/18 Ulm Electrochemical Talks (UECT), Ulm

Poster **Spectro-electrochemical Studies of the Solid Electrolyte Interphase Formed on Graphite Model Electrodes in Single-solvent Electrolyte**

Weber, I.; Schnaidt, J.; Wang, B.; Schmid, D.; Diemant, T.; Behm, R.J.

09/18 GDCh Electrochemistry, Ulm

Poster **Surface Science and Electrochemical Model Studies on the Solid Electrolyte Interphase between Graphite and an Ionic Liquid for Li-Ion Batteries**

Weber, I.; Buchner, F.; Schnaidt, J.; Behm, R.J.

06/17 Summer School “Photo-Electrocatalysis at the Atomic Scale”, San Sebastián

Talk **Electrochemical Model Studies of Electrolyte Decomposition at the Anode|Electrolyte Interphase of Lithium-Ion Batteries**

Weber, I.; Schnaidt, J.; Bodirsky, C.; Chakraborty, M.; Diemant, T.; Behm, R.J.

03/17 Jahrestagung der Deutschen Physikalischen Gesellschaft, Dresden

Talk **Li-Ion Battery Anodes: Electrochemical Model Studies at the Electrode|Electrolyte Interphase**

Weber, I.; Schnaidt, J., Bodirsky, C.; Diemant, T.; Behm, R.J.

09/16 Weber, I.; Solla-Gullón, J.; Brimaud, S.; Feliu, J.M.; Behm, R.J.

Structure, Surface Chemistry and Electrochemical De-alloying of Bimetallic Pt_xAg_{100-x} Nanoparticles: Quantifying the Changes in the Surface Properties for Adsorption and Electrocatalytic Transformation Upon Selective Ag Removal

J.Electroanal.Chem., **2016**, *793*, 164-173. DOI: 10.1016/j.jelechem.2016.11.062

09/16 GDCh Electrochemistry, Goslar

Poster **Spectroscopic and Electrochemical Investigations of the SEI Formation on Graphite Model Electrodes**

Weber, I.; Schnaidt, J.; Bozorgchenani, M.; Buchner, F.; Diemant, T.; Behm, R.J.

Metrohm Poster Prize 2016

07/16 Ulm Electrochemical Talks (UECT), Ulm

Poster **Investigation of the SEI Formation of Ethylene Carbonate on Graphitic Model Electrodes**

Weber, I.; Schnaidt, J.; Diemant, T.; Behm, R.J.

03/15 Jahrestagung der Deutschen Physikalischen Gesellschaft, Berlin

Poster **Preparation, Characterization and Electrocatalytic Activity of Bimetallic Pt_xAg_y and Pd_xAg_y Nanocrystals**

Weber, I.; Brimaud, S.; Solla-Gullón, J.; Feliu, J.M.; Behm, R.J.

04/14 Brimaud, S.; Solla-Gullón, J.; Weber, I.; Feliu, J.M.; Behm, R.J.

Formic Acid Electrooxidation on Noble-Metal Electrodes: Role and Mechanistic Implications of pH, Surface Structure, and Anion Adsorption

ChemElectroChem, **2014**, *1* (6), 1075-1083. DOI: 10.1002/celc.201400011

10.4. Acknowledgements

Die folgende Seite wurde aus Datenschutzgründen entfernt.

10.5. Declaration of Autonomy

I, Isabella Katharina Weber, hereby declare that I have written this thesis by myself and with no other means than the cited literature and the mentioned resources. I have indicated any verbatim and contextually adopted content according to the statute of Ulm University for the protection of good scientific practice. I have indicated the contributions of the people who worked alongside me, be it in data collection, measurements conducted by members of different institutions, or in writing.

Ulm, den 29. April 2021 _____

Isabella Weber